

**Studies of and Methods for Electronic Properties of Large  
Chemical Systems**

by

Matthew Gregory Welborn

B.S., University of Texas at Austin (2011)

Submitted to the Department of Chemistry  
in partial fulfillment of the requirements for the degree of

Doctor of Philosophy in Physical Chemistry

at the

MASSACHUSETTS INSTITUTE OF TECHNOLOGY

June 2016

© Massachusetts Institute of Technology 2016. All rights reserved.

Author .....  
Department of Chemistry  
May 3, 2016

Certified by .....  
Troy Van Voorhis  
Professor  
Thesis Supervisor

Accepted by .....  
Robert W. Field  
Chairman, Department Committee on Graduate Theses



This doctoral thesis has been examined by a Committee of the Department of  
Chemistry as follows:

Professor Jianshu Cao .....  
Chairman, Thesis Committee  
Professor of Chemistry

Professor Troy Van Voorhis .....  
Thesis Supervisor  
Professor of Chemistry

Professor Robert W. Field .....  
Member, Thesis Committee  
Professor of Chemistry



# Studies of and Methods for Electronic Properties of Large Chemical Systems

by

Matthew Gregory Welborn

Submitted to the Department of Chemistry  
on May 3, 2016, in partial fulfillment of the  
requirements for the degree of  
Doctor of Philosophy in Physical Chemistry

## Abstract

In this thesis, we explore various approaches to modeling electronic properties of large chemical systems, a challenge for theoretical and computational chemistry.

We first model experimental systems with conventional electronic structure by excerpting a region of interest: a few amino acids near the reactive site of a protein, an exciplex dimer in a thin-film LED, and a few donor/acceptor molecules at an organic/organic interface. We find that these models work well for explaining experiments provided we can identify a local region that captures the property of interest.

Second, we consider a situation in which the property of interest is not local. We investigate the Anderson model of localization in disordered materials, using the tools of random matrix theory. We use free probability to approximately compute the density of states of a Hamiltonian matrix ensemble without exact diagonalization. We develop an error analysis for this method, and show that it is accurate to the eighth moment of the density of states. Finally, we apply the method to various extensions of the Anderson model, to good result.

Third, we develop a wavefunction-in-wavefunction embedding theory for strongly correlated systems. We base our work on Density Matrix Embedding Theory (DMET). We extend the original DMET equations to account for correlation in the bath via an antisymmetrized geminal power (AGP) wave function. The resulting formalism has a number of advantages. First, it allows one to properly treat the weak correlation limit of independent pairs, which DMET is unable to do with a mean-field bath. Second, it associates a size extensive correlation energy with a given density matrix (for the models tested), which AGP by itself is incapable of providing. Third, it provides a reasonable description of charge redistribution in strongly correlated but non-periodic systems. We then describe a new electronic embedding method based on DMET, dubbed "Bootstrap Embedding," a self-consistent wavefunction-in-wavefunction embedding theory that uses overlapping fragments to improve the description of fragment edges. We find Bootstrap Embedding converges rapidly with embedded fragment size, overcoming the surface-area-to-volume-ratio error typical of many embedding methods.

Fourth, we employ semiempirical neglect of diatomic differential overlap (NDDO) methods as force fields for liquid water. Using force matching, we design a reparameterized NDDO model and find that it qualitatively reproduces the experimental radial distribution function of water, as well as various monomer, dimer, and bulk properties that standard NDDO method do not. This suggests that the apparent limitations of NDDO models are primarily due to poor parameterization and not to the NDDO approximations themselves. We identify the physical parameters that most influence the condensed phase properties. These results help to elucidate the chemistry that a semiempirical molecular orbital picture of water must capture. We conclude that properly parameterized NDDO models could be useful for simulations that require electronically detailed explicit solvent, including the calculation of redox potentials and simulation of charge transfer and photochemistry.

Thesis Supervisor: Troy Van Voorhis

Title: Professor

# Acknowledgments

First and foremost, I am grateful to my advisor Prof. Troy Van Voorhis for his guidance, insight, support, patience, encouragement, generosity, and kindness. Troy is, of course, the reason this thesis exists.

I would like to thank my thesis committee, Prof. Jianshu Cao and Prof. Robert Field, for their advice and support. I thank my undergraduate research advisor, Prof. Graeme Henkelman, for sparking my interest in theoretical chemistry, and for pointing me toward Troy.

I thank Chi Zhang, Peng Dao, Prof. Brad Pentelute, Dan Congreve, Mengfei Wu, Prof. Marc Baldo, Georgios Markopoulos, Prof. Tim Swager, Mike Fusella, and Prof. Barry Rand for sharing their excellent science and bringing me in on experimental collaborations. You've taught me so much about a wide range of chemistry. I also thank our mathematical collaborators Ramis Movassagh and Prof. Alan Edelman for showing me the wonderful mathematics of Random Matrix Theory.

I would like to thank all of my officemates over the years. In particular, thank you Lee-Ping, Jiahao, James, and Takashi for your mentorship. Mike, Thomas, John, Dave, Javier, Alex and Nadav: thank you for your friendship. Jeremy, Liam, and Oleg: I appreciate your perspective. Ben, Tim, Shane, and Eric: you have been great examples. Nathan and Hongzhou: thanks for your curiosity and hard work. Valérie: thank you for your support, patience, and encouragement. Special thanks to Alex, Hongzhou, Nadav, Nathan, and Valérie for editing parts of this thesis.

My thanks also goes to Li Miao for shielding all of us from MIT's vast bureaucracy.

Finally, I thank my family: my parents Mark and Mary, and my sister Macartney. This thesis is dedicated to you.



*Dynamical correlation is like porn:*

*I know it when I see it.*

TROY VAN VOORHIS



# Contents

<b>1</b>	<b>Introduction</b>	<b>21</b>
1.1	Tools of the trade . . . . .	21
1.1.1	Quantum chemistry . . . . .	22
1.1.1.1	The Born-Oppenheimer approximation . . . . .	22
1.1.1.2	Representation of wavefunctions . . . . .	23
1.1.1.3	Hartree Fock . . . . .	25
1.1.1.4	Kohn-Sham density functional theory . . . . .	27
1.1.1.5	Constrained density functional theory (configuration interaction) . .	28
1.1.2	Molecular dynamics . . . . .	30
1.1.2.1	Ensemble averages . . . . .	31
1.1.2.2	Thermostats . . . . .	32
1.1.2.3	Force fields . . . . .	33
1.1.2.4	Force matching . . . . .	34
1.2	Exotic methods . . . . .	36
1.2.1	Free probability (chapters 3 and 4) . . . . .	36
1.2.1.1	Review of classical probability . . . . .	36
1.2.1.2	What is a random matrix? . . . . .	39
1.2.1.3	Free independence . . . . .	39
1.2.1.4	The R transform . . . . .	41
1.2.2	Schmidt decomposition (chapters 5 and 6) . . . . .	42
1.2.2.1	Schmidt decomposition of product wavefunctions . . . . .	44
1.2.3	Broken symmetry mean fields (chapter 5) . . . . .	46
1.2.3.1	Hartree-Fock-Bogoliubov . . . . .	46
1.2.3.2	Antisymmetrized geminal product . . . . .	50
1.2.3.3	AGP as number-projected HFB . . . . .	51
1.2.4	Semi-empirical molecular orbital theory (chapter 7) . . . . .	54
1.3	Structure of this thesis . . . . .	56

<b>2</b>	<b>Some applications to experiment</b>	<b>61</b>
2.1	$\pi$ -clamp mediated site-specific cysteine conjugation . . . . .	61
2.1.1	Introduction . . . . .	62
2.1.2	Molecular dynamics calculations of peptide structure . . . . .	64
2.1.3	Density functional calculations on the arylation reaction . . . . .	64
2.1.4	Accelerating the reaction . . . . .	67
2.1.5	Conclusions . . . . .	72
2.2	Organic electronics . . . . .	73
2.2.1	Exciplex-based blue organic light emitting diodes . . . . .	73
2.2.1.1	Computational details . . . . .	74
2.2.1.2	Donor-acceptor binding . . . . .	75
2.2.1.3	Exciplex color . . . . .	78
2.2.1.4	Conclusions . . . . .	82
2.2.2	Band-like charge transfer states in organic photovoltaics . . . . .	83
2.2.2.1	Introduction . . . . .	83
2.2.2.2	Computational model of the disordered bulk heterojunction . . . . .	84
2.2.2.3	Computational model of the ordered interface . . . . .	84
2.2.2.4	Computational details . . . . .	88
2.3	Looking forward . . . . .	89
2.4	Acknowledgments . . . . .	89
<b>3</b>	<b>Error analysis of free probability approximations to the density of states of disordered systems</b>	<b>91</b>
3.1	Introduction . . . . .	91
3.2	Comparing two PDFs . . . . .	92
3.3	The free convolution . . . . .	92
3.4	Decomposition of the Anderson Hamiltonian . . . . .	94
3.5	Numerical free convolution . . . . .	95
3.6	Analytic free convolution . . . . .	96
3.7	Comparison with other approximations . . . . .	98
3.8	Acknowledgments . . . . .	99
<b>4</b>	<b>Densities of states for disordered systems from free probability: live free or diagonalize!</b>	<b>101</b>
4.1	Introduction . . . . .	101
4.2	Free probability . . . . .	103
4.2.1	Free independence . . . . .	103

4.2.2	Free independence and the $R$ -transform . . . . .	105
4.3	Numerical results . . . . .	106
4.3.1	Computation of the Density of States and its Free Approximant . . . . .	106
4.3.2	One-dimensional chain . . . . .	108
4.3.3	One-dimensional lattice with non-neighbor interactions . . . . .	109
4.3.4	Square, hexagonal and cubic lattices . . . . .	109
4.3.5	Off-diagonal disorder . . . . .	110
4.4	Error analysis . . . . .	111
4.4.1	Systems with constant interactions . . . . .	112
4.4.2	Random interactions . . . . .	113
4.5	Conclusion . . . . .	115
4.6	Acknowledgments . . . . .	116
<b>5</b>	<b>Density matrix embedding in an antisymmetrized geminal product wavefunction</b>	<b>117</b>
5.1	Introduction . . . . .	117
5.2	Motivation: DMET and independent pairs . . . . .	120
5.2.1	DMET equations . . . . .	120
5.2.2	Independent pairs . . . . .	122
5.3	Theory . . . . .	124
5.3.1	The AGP wave function . . . . .	125
5.3.2	AGP schmidt decomposition . . . . .	126
5.3.3	HFB matrix elements . . . . .	127
5.4	Results and discussion . . . . .	129
5.4.1	Verification of embedding equations . . . . .	129
5.4.2	Results for model hamiltonians . . . . .	129
5.4.2.1	The Hubbard model . . . . .	129
5.4.2.2	Non-interacting AB Dimers . . . . .	130
5.4.2.3	ABAB Solid . . . . .	132
5.4.2.4	Hubbard-Anderson Model . . . . .	133
5.5	Conclusions . . . . .	135
5.6	Appendix: Second Quantized Matrix Elements for AGP Embedding . . . . .	136
5.7	Acknowledgments . . . . .	140
<b>6</b>	<b>Bootstrap embedding</b>	<b>141</b>
6.1	Introduction . . . . .	141
6.2	Theory . . . . .	143
6.3	Results . . . . .	147

6.4	Conclusions . . . . .	150
6.5	Acknowledgments . . . . .	150
<b>7</b>	<b>Why many semiempirical molecular orbital theories fail for liquid water and how to fix them</b>	<b>151</b>
7.1	Introduction . . . . .	151
7.2	Reparameterizing PM6 for water . . . . .	154
7.2.1	Force matching . . . . .	154
7.2.2	Comparison to experiment . . . . .	156
7.2.3	Why PM6 fails . . . . .	157
7.3	Conclusions . . . . .	160
7.4	Appendix: Force field parameters . . . . .	161
7.5	Appendix: Size extrapolation of static dielectric constants . . . . .	162
7.6	Acknowledgments . . . . .	163
<b>8</b>	<b>Conclusions</b>	<b>165</b>

# List of Figures

2-1	Site-specific conjugation at the $\pi$ -clamp in the presence of another competing cysteine peptide. . . . .	63
2-2	Mutation studies show that Phe-1, Pro-3 and Phe-4 are required for the observed reactivity. . . . .	63
2-3	Graphical summary of computational results for the FCPF and GCPG systems. . . . .	65
2-4	Arylation reaction rates for a panoply of mutations and in a variety of salt environments. . . . .	68
2-5	Schematic of the reduced binding model used for mutation and salt studies. . . . .	69
2-6	Linear free energy relationship between rate and ligand-side-chain binding energy across side chain mutations. . . . .	70
2-7	The salt effect linear free energy relationship. As before, the rate ( $k_i$ ) is determined experimentally, and the energy ( $\Delta\Delta G$ ) is computed as $\Delta G_i - \Delta G_0$ from a binding model. The terms $k_0$ and $\Delta G_0$ are referenced to NaCl. Data are given in Table 2.4. . . . .	71
2-8	Exciplex charge combination and emission schematic. . . . .	74
2-9	Acceptor and an example donor. . . . .	75
2-10	Dimer CDFT emission energies compared to experiment. . . . .	82
2-11	Geometry and charge transfer state of the representative dimer used to describe the disordered BHJ. . . . .	85
2-12	Reduced model of the $C_{60}$ /rubrene crystal interface. . . . .	86
2-13	An example four molecule excerpt from Figure 2-12. . . . .	86
2-14	Weighted density of states for the crystalline rubrene/ $C_{60}$ interface lattice model. . . . .	88
3-1	Density of states of the one-dimensional Anderson model computed by free convolution and compared to exact diagonalization over a range of noise levels. . . . .	95
3-2	Diagrammatic expansion of the leading order error for the free probability approximation of the density of states of the one-dimensional Anderson model. . . . .	96
3-3	Comparison of free probability and perturbation theory approximations for the density of states of the one-dimensional Anderson model. . . . .	97

4-1	Graphical overview of extensions to the one-dimensional Anderson model considered in this chapter. . . . .	104
4-2	Comparison of exact density of states with the free probability approximant for the lattices in Figure 4-1. . . . .	108
4-3	Diagrammatic representation of the leading order error for a two-dimensional square lattice with constant interactions and nearest neighbors and for the case of a one-dimensional chain with off-diagonal disorder. . . . .	114
5-1	A summary of the DMET algorithm. . . . .	121
5-2	A pair of infinitely separated minimal basis LiH molecules. One molecule is chosen to be the system, and the other serves as a bath. In this case, one obtains the same Hamiltonian in the Schmidt basis as in the full basis. . . . .	123
5-3	Comparison of AGP and HF embedding baths for the Hubbard model at various correlation strengths. . . . .	131
5-4	$\delta$ dependence of ground state energy of the non-interacting Hamiltonian (Eq. 5.44) at half-filling and correlation strength $U/t = 8$ . . . . .	133
5-5	$\delta$ dependence of ground state energy of $\hat{H}_{ABAB}$ (Eq. 5.45) at half-filling and correlation strength $U/t = 8$ . . . . .	134
5-6	AGP embedding energy as a function of correlation strength for the Hubbard-Anderson model. . . . .	135
6-1	Four different fragment partitionings (A, B, C, D) for the same molecule. In Bootstrap Embedding, all four partitionings are used and the overlapping portions of the fragments are constrained to match. . . . .	142
6-2	Illustration of the Bootstrap Embedding procedure for a lattice model. . . . .	145
6-3	Energy per site of the one-dimensional Hubbard model as a function of electron filling with strong correlation ( $U/t = 8$ ). . . . .	147
6-4	Convergence of DMET and Bootstrap Embedding for the one-dimensional Hubbard model. . . . .	148
6-5	One-dimensional Hubbard model energy error for various constraint schemes. . . . .	149
6-6	Population difference as a function of “electronegativity difference,” $\delta/t$ , for the 1D ABAB Hubbard model at a filling of $\langle n \rangle = 0.5$ . . . . .	149
7-1	Oxygen-oxygen pair distribution function for two popular NDDO water models compared to experimental results. . . . .	153
7-2	Water dimer binding potential energy landscape and hydrogen bonding structure for the PM6 and reparameterized models. . . . .	155

7-3	O-O, O-H, and H-H radial distribution functions for water as predicted by PM6, PM6-DH+, PM7, and this work. . . . .	158
7-4	Size extrapolation of the static dielectric of water from our method as well as three common NDDO Hamiltonians. . . . .	163
8-1	Comparison of methods for computing the density of states and localization length of excitons in metal-free phthalocyanine. . . . .	166



# List of Tables

2.1	Reaction energies for cysteine arylation. . . . .	67
2.2	Reaction barrier heights for peptide arylation. . . . .	67
2.3	Thermodynamic data for 2-6. . . . .	72
2.4	Thermodynamic data for 2-7. . . . .	72
2.5	Computed donor-acceptor and didonor dimer binding energies. . . . .	76
2.6	Electronic and emission properties of donor-acceptor complexes. . . . .	79
4.1	Coefficients of the leading-order error in the free probability approximation in the Edgeworth expansion (4.15d). . . . .	115
7.1	Calculated physical properties of PM6, PM6-DH+, PM7, and this work compared to experiment. . . . .	159
7.2	NDDO parameters from force matching compared to original PM6 parameters [311].	161



# Chapter 1

## Introduction

Historically, science has concerned itself with two activities: experiments, which measure reality, and theories, which explain and predict experiments. However, since the advent of modern physics, theories have become so mathematically complex that they cannot be solved analytically. Chemistry is a particularly severe case: the Schrödinger equation, a nearly-complete model for chemistry, has been around for nearly a century. Yet, from Hylleraas’s variational computations on Helium in 1929 [152] up to the present day, nearly all progress in theoretical chemistry has come in the form of better approximations, more efficient numerical algorithms, and faster computers. Even the name of the field bears out this fact: computational and theoretical chemistry are often used as synonyms.

This isn’t to say that progress hasn’t been made. At present, we can compute electronic properties to great accuracy for small to medium sized molecules using a range of electronic structure methods. For large molecules or collections of molecules, molecular dynamics/mechanics provides a description of structural properties and averages.

But, there is still a vast set of large systems whose electronic properties cannot be calculated directly. Disordered organic materials are actively studied for photovoltaic [102, 116, 117] and electroluminescent applications [65]. Photosystem II [339] is a huge protein that uses light to catalyze water splitting. Solvation, where configurational sampling is usually prohibitively expensive, can shift redox potentials [351], electron transfer rates [183], and catalytic properties [350] of solutes.

The standard approach to large systems is to only treat accurately small subsystems of interest or to map the system onto a simpler model. But there is still room for development of new methods as well. In this thesis, we will explore both.

### 1.1 Tools of the trade

In this section, we briefly introduce the core tools of computational chemistry. Throughout this thesis, we will either apply these tools to study chemical systems, or use them as a foundation to

build new methods.

We first focus on practical solutions to electronic structure: the problem of solving the Schrödinger equation for electrons in the presence of fixed nuclei. Then, we discuss a classical approximation to the motion of these nuclei, molecular dynamics.

### 1.1.1 Quantum chemistry

At its heart, chemistry is the quantum physics of nuclei and electrons interacting via the Coulomb potential. A chemical system — composed of point electrons and nuclei — is well-described by the non-relativistic, time-independent Schrödinger equation [285]. In the basis of the positions of these particles, it is given by

$$\hat{H}\Psi(r_1, r_2, \dots, r_N, R_1, R_2, \dots, R_M) = E\Psi(r_1, r_2, \dots, r_N, R_1, R_2, \dots, R_M) \quad (1.1)$$

where, mechanically,  $\hat{H}$  is an input specified by the properties of all particles in the system, while  $E$  and  $\Psi$  are variables to be solved for.  $E$  is the (scalar) energy associated with a given “wavefunction”,  $\Psi$ . The wavefunction contains all information about the state of the system, and is a function of the coordinates of all of the electrons,  $\{r_i\}$ , and of all of the nuclei,  $\{R_i\}$ . Finally,  $\hat{H}$  is the Hamiltonian, an operator that acts on the wavefunction. In atomic units ( $\hbar = 1$ ,  $q_{e^-} = -1$ ,  $m_{e^-} = 1$ ) [132], it is given by

$$\hat{H} = -\sum_{i=1}^N \frac{1}{2} \nabla_i^2 - \sum_{I=1}^M \frac{1}{2m_I} \nabla_I^2 - \sum_{i=1}^N \sum_{I=1}^M \frac{Z_I}{r_{iI}} + \sum_{i=1}^N \sum_{j>i}^N \frac{1}{r_{ij}} + \sum_{I=1}^M \sum_{J>I}^M \frac{Z_I Z_J}{r_{IJ}} \quad (1.2)$$

where  $i$  and  $j$  index electrons,  $N$  is the number of electrons,  $I$  and  $J$  index nuclei,  $M$  is the number of nuclei,  $Z_I$  is the charge of nucleus  $I$ , (electrons have charge -1),  $m_I$  is the mass of nucleus  $I$ , (electrons have mass 1),  $\nabla_x^2$  is the laplacian operator acting on the coordinates of particle  $x$ , and  $r_{xy}$  is the distance between particles  $x$  and  $y$ . The first two terms represent the kinetic energy of each particle, while the last three terms account for the Coulomb interaction between particles.

While the kinetic energy terms are by themselves separable, the potential energy terms couple all degrees of freedom in the system together. The result is an equation that cannot be solved analytically. As such, solutions to equation 1.1 must be approximated in practice, and we will spend the remainder of this chapter building up such approximations.

#### 1.1.1.1 The Born-Oppenheimer approximation

The first and most common approximation to the problem of molecular quantum mechanics is the Born-Oppenheimer approximation [37]. Qualitatively, we observe that an electron is 1836 times less massive than the lightest of nuclei. We thus expect that electrons will move far faster than nuclei, or,

equivalently, there will be a separation of timescales between nuclear and electronic motion. Because this timescale is so large, we make the approximation that electronic relaxation is instantaneous compared to nuclear motion. That is, the nuclei move on a potential energy surface generated by completely relaxed electrons (the long time limit of the motion of the electrons). Conversely, the electrons move in a potential energy generated by fixed nuclei (the short time limit of the motion of the nuclei).

In mathematical terms, this means that we can separate the Hamiltonian, energy, and wavefunction into distinct nuclear and electronic components

$$\hat{H} \approx \hat{H}_n + \hat{H}_e \quad (1.3)$$

$$E \approx E_n + E_e \quad (1.4)$$

$$\Psi(r_1, r_2, \dots, r_N, R_1, R_2, \dots, R_M) \approx \Psi_n(R_1, R_2, \dots, R_M) \Psi_e(r_1, r_2, \dots, r_N). \quad (1.5)$$

Equation 1.1 can then be separated into a nuclear and an electronic Schrödinger equation

$$\hat{H}_n \Psi_n(R_1, R_2, \dots, R_M) = E_n \Psi_n(R_1, R_2, \dots, R_M) \quad (1.6)$$

$$\hat{H}_e(r_1, r_2, \dots, r_N) = E_e \Psi_e(r_1, r_2, \dots, r_N). \quad (1.7)$$

where the electronic Hamiltonian is given by

$$\hat{H}_e = -\sum_{i=1}^N \frac{1}{2} \nabla_i^2 - \sum_{i=1}^N \sum_{I=1}^M \frac{Z_I}{r_{iI}} + \sum_{i=1}^N \sum_{j>i}^N \frac{1}{r_{ij}} \quad (1.8)$$

while the nuclear Hamiltonian is given by

$$\hat{H}_n = -\sum_{I=1}^M \frac{1}{2m_I} \nabla_I^2 + \sum_{I=1}^M \sum_{J>I}^M \frac{Z_I Z_J}{r_{IJ}} + E_e(R_1, R_2, \dots, R_M). \quad (1.9)$$

$E_e$  is the electronic energy computed by solving equation 1.7 at fixed nuclear positions  $R_1, R_2, \dots, R_M$ .

For the remainder of this section, we focus on approximating solutions to equation 1.7. In Section 1.1.2, we will discuss a classical approximation to the time-dependent version of equation 1.6.

### 1.1.1.2 Representation of wavefunctions

At the end of the day, we will want to solve equation 1.7 on a computer. A key step in adapting the equation for computation is discretization of the wavefunction; the computer cannot directly represent a continuous function. Instead, we approximate the wavefunction as a weighted sum of basis functions

$$\Psi(\tau) = \sum_i c_i \psi_i(\tau) \quad (1.10)$$

where  $\tau$  represents all relevant coordinates. For the sake of simplicity, we will choose basis functions that are orthonormal

$$\int \psi_i^*(\tau) \psi_j(\tau) d\tau \equiv \langle \psi_i | \psi_j \rangle = \delta_{ij} \quad (1.11)$$

where we have also introduced Dirac notation [81].

These basis functions are arbitrary, but it is most computationally efficient to choose basis functions that make the representation as compact as possible. To this end, two choices are usually made. First, the basis is composed of functions of the coordinates of a single electron at a time, called orbitals. Second, these orbitals are chosen to closely resemble the solutions to the electronic structure problem of the atoms in the system as though they were isolated. When both of these choices are made, the basis functions are called “atomic orbitals”.

We can construct wavefunctions by combining atomic orbitals. To account for the fermion statistics of electrons, a convenient formalism for such constructions is second quantization. In second quantization, the creation operator  $\hat{a}_i^\dagger$  creates an electron in orbital  $|\psi_i\rangle$

$$|\psi_i\rangle = \hat{a}_i^\dagger | \rangle \quad (1.12)$$

while the annihilation operator  $\hat{a}_i$  removes an electron from orbital  $|\psi_i\rangle$

$$\hat{a}_i |\psi_i\rangle = | \rangle \quad (1.13)$$

where  $| \rangle$  represents the vacuum containing no electrons. The vacuum is chosen to be normalized

$$\langle | \rangle = 1 \quad (1.14)$$

and is the null space of the annihilation operators

$$\hat{a}_i | \rangle = 0. \quad (1.15)$$

Fermion statistics are handled by the anticommutation relations of the second quantization operators

$$\left[ \hat{a}_i^\dagger, \hat{a}_j \right]_+ = \delta_{ij} \quad (1.16)$$

$$\left[ \hat{a}_i, \hat{a}_j \right]_+ = 0 \quad (1.17)$$

$$\left[ \hat{a}_i^\dagger, \hat{a}_j^\dagger \right]_+ = 0. \quad (1.18)$$

where  $[\cdot, \cdot]_+$  is the anticommutator

$$[\hat{A}, \hat{B}]_+ \equiv \hat{A}\hat{B} + \hat{B}\hat{A}. \quad (1.19)$$

In this chapter, we use second quantization operators  $\{\hat{a}_i, \hat{a}_i^\dagger\}$  and functions  $|\psi_i\rangle$  to denote general orbitals. To specifically denote atomic orbitals, we use second quantization operators  $\{\hat{c}_\mu, \hat{c}_\mu^\dagger\}$  and functions  $|\phi_\mu\rangle$ .

We can now rewrite the electronic Hamiltonian (equation 1.8) in the basis of atomic orbitals using the notation of second quantization

$$\hat{H}_e = \sum_{\mu\nu} h_{\mu\nu} \hat{a}_\mu^\dagger \hat{a}_\nu + \sum_{\mu\nu\lambda\sigma} V_{\mu\nu\lambda\sigma} \hat{a}_\mu^\dagger \hat{a}_\nu^\dagger \hat{a}_\sigma \hat{a}_\lambda \quad (1.20)$$

where  $\mathbf{h}$  is the matrix of so-called one-electron integrals for the set of basis functions  $\{\phi_\mu\}$

$$h_{\mu\nu} = \int \phi_\mu^*(r) \left[ -\frac{1}{2} \nabla^2 - \sum_{I=1}^M \frac{Z_I}{|r - R_I|} \right] \phi_\nu(r) dr \quad (1.21)$$

and  $\mathbf{V}$  is the four-tensor of two-electron integrals (in physicists' notation)

$$V_{\mu\nu\lambda\sigma} = \int \phi_\mu^*(r_1) \phi_\nu^*(r_2) \frac{1}{r_{12}} \phi_\lambda(r_1) \phi_\sigma(r_2) dr_1 dr_2. \quad (1.22)$$

With these ideas in hand, we can now discuss the Hartree-Fock approximation.

### 1.1.1.3 Hartree Fock

While already approximate, the electronic Schrödinger equation (equation 1.7) cannot be solved even numerically; the cost of computing its solution increases exponentially with the number of electrons. This exponential scaling comes from the form of the wavefunction. If we grid out each electron coordinate over  $m$  basis function, then  $N$  electrons will require  $m^N$  basis functions, and any computation that touches every element of the wavefunction must scale as at least  $\mathcal{O}(m^N)$ . Thus, we need an approximate form of the wavefunction.

Hartree-Fock theory [318] approximates the wavefunction by noticing that in the absence of two electron interactions, the Schrödinger equation is separable

$$\begin{aligned} \hat{H}(V=0) \Psi(r_1, r_2, \dots, r_N) &= E \Psi(r_1, r_2, \dots, r_N) \\ \hat{H}(V=0) \prod_{i=1}^N [\psi_i(r_i)] &= \left( \sum_{i=1}^N E_i \right) \left( \prod_{i=1}^N [\psi_i(r_i)] \right) \end{aligned} \quad (1.23)$$

(where for now we have dropped the  $e$  subscript and ignored the fermion statistics of electrons). In

this limit, the wavefunction becomes a product of one-electron orbitals. These so-called molecular orbitals  $\{\psi_i\}$  can be expanded in the basis of atomic orbitals  $\{\phi_\mu\}$

$$|\psi_i\rangle = \sum_{\mu}^m C_{i\mu} |\phi_\mu\rangle = \sum_{\mu}^m C_{i\mu} \hat{c}_\mu^\dagger | \rangle. \quad (1.24)$$

This equation introduces the coefficient matrix,  $\mathbf{C}$ , whose  $i$ th row specifies the expansion of  $\psi_i$  in terms of the atomic orbital basis functions  $\{\phi_\mu\}$ , and the second quantization operators for these atomic orbitals  $\{\hat{c}_\mu, \hat{c}_\mu^\dagger\}$ . Rewriting the wavefunction from equation 1.23 in the notation of second quantization gives us the form of the Hartree-Fock wavefunction (with correct fermion statistics)

$$|\Psi_{HF}\rangle = \prod_{i=1}^N \hat{a}_i^\dagger | \rangle = \prod_{i=1}^N \left( \sum_{\mu}^m C_{i\mu} \hat{c}_\mu^\dagger \right) | \rangle. \quad (1.25)$$

This form of the wavefunction is known as the Slater determinant [299]. Unlike the general wavefunction, this ansatz has only  $mN$  parameters. In practice, the size of the basis set scales linearly with the number of electrons, so the scaling of computations involving this wavefunction has a lower bound of  $\mathcal{O}(N^2)$ . This is of course far better than the exponential-scaling lower bound of the exact wavefunction.

With a wavefunction ansatz in hand, we now need a prescription for choosing the elements of  $\mathbf{C}$ . In quantum mechanics, the variational principle [118] states that the expectation value of the Hamiltonian with any wavefunction is an upper bound for the true ground state energy. Thus,

$$\langle \Psi_{HF} | \hat{H} | \Psi_{HF} \rangle \geq E_0. \quad (1.26)$$

This provides our prescription for choosing the  $C_{i\mu}$ . We expect that the wavefunction ansatz with an energy ( $\langle \Psi_{HF} | \hat{H} | \Psi_{HF} \rangle$ ) closest to the true ground state is the best description of our physical system. Therefore, we minimize the difference  $\langle \Psi_{HF} | \hat{H} | \Psi_{HF} \rangle - E_0$ . Because the first term is always greater than the second, we need only minimize  $\langle \Psi_{HF} | \hat{H} | \Psi_{HF} \rangle$ .

Putting all of this together,

$$\mathbf{C} = \arg \min_{\mathbf{C} \in U(m)} \langle \Psi_{HF}(\mathbf{C}) | \hat{H} | \Psi_{HF}(\mathbf{C}) \rangle \quad (1.27)$$

where  $U(m)$  is the group of  $m \times m$  unitary matrices. Using equation 1.20, the expectation value is given by [201, 158]

$$\langle \Psi_{HF} | \hat{H} | \Psi_{HF} \rangle = \sum_{\mu\nu} h_{\mu\nu} P_{\nu\mu} + \sum_{\mu\nu\lambda\sigma} (V_{\mu\nu\lambda\sigma} - V_{\mu\nu\sigma\lambda}) P_{\lambda\mu} P_{\nu\sigma} \quad (1.28)$$

where  $\mathbf{P} = \mathbf{C}\mathbf{C}^\dagger$  ( $P_{\mu\nu} \equiv \langle \Psi_{HF}(\mathbf{C}) | \hat{c}_\nu^\dagger \hat{c}_\mu | \Psi_{HF}(\mathbf{C}) \rangle$ ) and is called the density matrix. Note that like  $\mathbf{C}$ ,  $\mathbf{P}$  is a complete description of the HF wavefunction. Performing the minimization in equation

1.27, results in the matrix eigenvalue equation

$$\mathbf{FC} = \mathbf{C}\epsilon \quad (1.29)$$

where  $\epsilon$  is a diagonal matrix and the Fock matrix,  $\mathbf{F}$ , is given by

$$F_{\mu\nu} = h_{\mu\nu} + \sum_{\lambda\sigma} P_{\lambda\sigma} (2V_{\mu\sigma\nu\lambda} - V_{\mu\sigma\lambda\nu}). \quad (1.30)$$

Equations 1.29 and 1.30 can also be written in terms of individual molecular orbitals (in the position representation):

$$\left[ -\frac{1}{2}\nabla_1^2 - \sum_{I=1}^M \frac{Z_I}{|r_1 - R_I|} + \sum_{j=1}^N \int dr_2 \psi_j^*(r_2) \frac{1}{r_{12}} (1 - \mathcal{P}_{12}) \psi_j(r_2) \right] \psi_i(r_1) = \epsilon_i \psi_i(r_1) \quad (1.31)$$

where  $\mathcal{P}_{12}$  exchanges the labels of electron 1 and 2 [318]. This representation is presented for later comparison to Kohn-Sham density functional theory.

For purposes of day-to-day computations, Hartree-Fock has mostly been supplanted by density functional theory, which we introduce in the next section. However, in Chapters 5 and 6, we will build a wavefunction-in-wavefunction embedding theory on top of Hartree-Fock, and in Chapter 7 we will create a water model based on a stripped-down version of Hartree Fock.

#### 1.1.1.4 Kohn-Sham density functional theory

The wavefunction is a costly description of a chemical system, and Density Functional Theory (DFT) seeks to do away with it. In DFT, the  $N$ -dimensional (electron) density

$$P(r_1, r_2, \dots, r_N) \equiv \Psi^*(r_1, r_2, \dots, r_N) \Psi(r_1, r_2, \dots, r_N) \quad (1.32)$$

is replaced by the one-electron density

$$\rho(r) \equiv \int \Psi^*(r, r_2, \dots, r_N) \Psi(r, r_2, \dots, r_N) dr_2, \dots, dr_N, \quad (1.33)$$

the result of integrating out every electronic coordinate except one [248].

Hohenberg and Kohn showed that there exists a universal functional of the density  $F$ , which does not depend on the details of the system, and gives its energy [143]

$$E[\rho(r)] = \int v_n(r)\rho(r)dr + F[\rho(r)] \quad (1.34)$$

where  $v_n$  is the external Coulomb potential created by the nuclei. Remarkably, this energy functional

is minimized by the one-electron density of the ground state wavefunction. Because the density can be expanded in a basis (in the same manner as the wavefunction), the density provides a complete description of an  $N$  electron system with only  $\mathcal{O}(N)$  parameters.

Unfortunately, the exact functional  $F$  is not known and must be approximated. The primary difficulty in approximation of  $F$  comes from approximation of the kinetic energy functional. Thus, the vast majority of approximations for this functional are framed in the Kohn-Sham (KS) framework [179], due to its highly accurate treatment of the kinetic energy. In this formalism, a fictitious system of non-interacting electrons is created whose ground state density is the same as that of the physical system. Because these fictitious electrons do not interact, their wavefunction is completely specified by a Slater determinant of orthonormal orbitals  $\{\psi_i^{KS}\}$  and the density is given by

$$\rho(r) = \sum_{i=1}^N \psi_i^{KS*}(r)\psi_i^{KS}(r). \quad (1.35)$$

The kinetic energy of this wavefunction is readily evaluated, and turns out to be a very good approximation to the kinetic energy of the physical system [249]. These orbitals are found by solving the Kohn-Sham equations

$$\left[ -\frac{1}{2}\nabla_1^2 + v_n(r) + \int \frac{\rho(r_2)}{|r_1 - r_2|} dr_2 + v_{xc}(r) \right] \psi_i^{KS}(r_1) = \epsilon_i \psi_i^{KS}(r_1). \quad (1.36)$$

Note that this equation bears a striking resemblance to the Hartree Fock equation 1.31. New in the KS equations is the exchange-correlation potential,  $v_{xc}(r)$ , which becomes the missing piece that must be approximated. The price of this formalism is the introduction of the fictitious orbitals which increase the cost of the calculation from  $\mathcal{O}(N)$  to a cost similar to that of Hartree Fock. However, KS DFT has proven to be far more accurate than Hartree Fock at roughly the same cost.

Throughout Chapter 2, we will use KS DFT to study a variety of chemical systems.

### 1.1.1.5 Constrained density functional theory (configuration interaction)

Sometimes, a state other than the ground state is desired. For example, in electron transfer reactions we might desire a charge transfer state in which an excess electron is localized on one part of a chemical system (and correspondingly, a hole is localized on another part). Such a property can be described entirely through the one electron density by requiring that the density in one region of space integrate to a certain number of electrons. This hints at the possibility of a Density Functional Theory description of a charge transfer state.

Constrained Density Functional Theory (CDFT) provides just such a description [165]. In CDFT, energy is minimized subject to constraints on the density. This variation is performed by finding stationary points of the CDFT functional

$$W[\rho, \lambda] = E[\rho] + \lambda \left( \int w(r) \rho(r) dr - V \right) \quad (1.37)$$

where  $E$  is the energy functional from equation 1.34,  $\lambda$  is a Lagrange multiplier,  $w$  is a weight function that defines the desired constraint, and  $V$  is the desired value of the constraint. For example, if we wished to constrain the number of electrons in a region of space to a certain value  $N_e$ ,  $w$  would be a binary function defining this region and  $V$  would be  $N_e$ . For the purposes of our charge transfer reaction,  $w$  is a density-based charge partitioning function (e.g. the Löwdin population [199]) and  $V$  represents an excess electron on part of our system. An excellent description of the practical considerations of CDFT calculations is given in reference [164]).

We can now compute the energy of both the ground state (from DFT) and the charge transfer excited state (from CDFT) of an electron transfer reaction. In Section 2.2.1, we use these tools to compute the color of exciplexes that emit through charge annihilation.

Densities generated via CDFT represent diabatic states [336]. These states do not diagonalize the Hamiltonian, and the Hamiltonian matrix element between two such states,  $|\Psi_1\rangle$  and  $|\Psi_2\rangle$ , is called the ‘‘coupling’’

$$V \equiv \langle \Psi_1 | \hat{H} | \Psi_2 \rangle. \quad (1.38)$$

This coupling is important, e.g., for determining the rate of condensed phase electron transfer reactions in Marcus theory [205]. In Section 2.2.2, we will compute such a coupling in order to understand hole hopping in a rubrene crystal.

In the framework of CDFT, these couplings are given by [365]

$$V = \frac{1}{2}(E_1 + E_2) \langle \Psi_1 | \Psi_2 \rangle - \frac{1}{2} \langle \Psi_1 | \lambda_1 \hat{w}_1 + \lambda_2 \hat{w}_2 | \Psi_2 \rangle \quad (1.39)$$

where the  $E_i$  are the functional energies associated with the two constrained densities and the  $w_i$  and  $\lambda_i$  are the weight functions and Lagrange multipliers used to specify and apply the constraints to these densities. However, DFT does not define a wavefunction for the physical system, so we do not know  $|\Psi_1\rangle$  and  $|\Psi_2\rangle$ . That is to say, CDFT computes  $\rho_1$  and  $\rho_2$  which are the densities associated with  $|\Psi_1\rangle$  and  $|\Psi_2\rangle$

$$\rho_1 = |\Psi_1\rangle \langle \Psi_1| \quad (1.40)$$

$$\rho_2 = |\Psi_2\rangle \langle \Psi_2|, \quad (1.41)$$

but many wavefunctions map onto a single density, and we cannot determine the exact ground state wavefunction from the exact ground state density. Thus, an approximation must be made.

CDFT-CI approximates the exact wavefunctions by the fictitious non-interacting Kohn-Sham Slater determinant of equations 1.35 and 1.36. Equation 1.39 becomes

$$V \approx \frac{1}{2}(E_1 + E_2) \langle \Psi_1^{KS} | \Psi_2^{KS} \rangle - \frac{1}{2} \langle \Psi_1^{KS} | \lambda_1 \hat{w}_1 + \lambda_2 \hat{w}_2 | \Psi_2^{KS} \rangle. \quad (1.42)$$

It is this approximation that we will employ in Section 2.2.2.

### 1.1.2 Molecular dynamics

In Section 1.1.1.1, we partitioned the Schrödinger equation approximately into an electronic and a nuclear equation. So far, we've discussed methods for approximating the electronic equation. In this section, we approximate the nuclear equation classically.

Like the quantum nuclear Hamiltonian, the classical nuclear Hamiltonian partitions into a kinetic and potential energy piece

$$H = T + V \quad (1.43)$$

where we substitute the classical momentum,  $P_I$ , for the quantum momentum operator,  $-\nabla_I^2$ ,

$$T(P_1, P_2, \dots, P_M) = \sum_{I=1}^M \frac{1}{2m_I} P_I^2 \quad (1.44)$$

and collect the potential energy terms

$$V(R_1, R_2, \dots, R_M) = \sum_{I=1}^M \sum_{J>I}^M \frac{Z_I Z_J}{r_{IJ}} + E_e(R_1, R_2, \dots, R_M). \quad (1.45)$$

This classical approximation is valid when nuclei are heavy (and thus localized) and when zero-point energies do not change significantly with nuclear coordinates.

While molecules usually exist in a single electronic state (most often the electronic ground state), finite temperature causes the nuclei to move. Thus we are almost always interested in the dynamics corresponding to equation 1.43. These dynamics are given by Hamilton's equations of motion [111]

$$\frac{dP_I}{dt} = -\frac{\partial H}{\partial R_I} \quad (1.46)$$

$$\frac{dR_I}{dt} = \frac{\partial H}{\partial P_I}. \quad (1.47)$$

In practice, these equations are usually integrated using the Velocity-Verlet algorithm [104]. Taken together, solving the classical equations of motion of the nuclei is called Molecular Dynamics (MD).

### 1.1.2.1 Ensemble averages

For the purposes of this thesis, we are not explicitly concerned with the time dependent dynamics of a system, but rather an ensemble average of some property

$$\langle A \rangle_p = \frac{\int p(\tau) A(\tau) d\tau}{\int p(\tau) d\tau} \quad (1.48)$$

where  $\tau$  is a collective variable containing all of the nuclear coordinates,  $R_1, R_2, \dots, R_M$ , used here for the sake of brevity.  $A$  is an observable and  $A(\tau)$  is the value of that observable at a given nuclear geometry.  $p(\tau)$  is the probability of observing that geometry. The denominator normalizes  $p$  and is called the ‘‘configuration integral’’

$$Q[p] \equiv \int p(\tau) d\tau. \quad (1.49)$$

At constant energy, volume, and number of particles (the so-called NVE ensemble) and ignoring the possibility of electronic degeneracy,  $p$  is just a function that requires the energy of the system to be fixed at a constant value  $E$

$$p_{NVE}(\tau) = \delta[V(\tau) - E] \quad (1.50)$$

where  $\delta$  is the Kronecker delta function. We can relate an NVE ensemble average to MD by way of the ergodic hypothesis [214]

$$\langle A \rangle_p = \frac{1}{Q[p_{NVE}]} \int p_{NVE}(\tau) A(\tau) d\tau = \lim_{t \rightarrow \infty} \frac{1}{t} \int_0^t A(\tau(t'))|_{NVE} dt' \quad (1.51)$$

where  $\tau(t')|_{NVE}$  are the coordinates of the system at time  $t'$  evolving dynamically under the conditions of constant NVE. By running MD at energy  $E$ , we can compute the trajectory  $\tau(t')|_{NVE}$ . MD is a constant energy algorithm because Hamilton’s equations of motion (equation 1.47) conserve energy for a conservative potential (like  $V$ ).

A more experimentally relevant ensemble is the NVT ensemble, where we substitute constant energy for constant temperature. In this ensemble,  $p$  is the Boltzmann distribution

$$p_{NVT}(\tau) = \exp[-\beta V(\tau)] \quad (1.52)$$

where  $\beta$  is the inverse temperature

$$\beta \equiv \frac{1}{kT}. \quad (1.53)$$

In order to sample the NVT ensemble with MD, we would like an equation similar to 1.51 :

$$\frac{1}{Q[p_{NVT}]} \int p_{NVT}(\tau) A(\tau) d\tau = \lim_{t \rightarrow \infty} \frac{1}{t} \int_0^t A(\tau(t')|_{NVT}) dt' \quad (1.54)$$

While it's easy to compute an MD trajectory at constant NVE, we need to include additional physics in our model to simulate constant temperature.

### 1.1.2.2 Thermostats

In a real system, constant temperature is the result of energy transfer between the system and the outside universe (or bath). On a computer, we seek to simulate this effect using a thermostat.

In this thesis, we use the Nosé-Hoover thermostat [238, 145]. It represents the effect of coupling to a thermal bath by a single auxiliary degree of freedom,  $s$ . This results in the extended Hamiltonian [238]

$$H_{Nose} = \sum_{I=1}^M \frac{p_I^2}{m_I} + V(\tau) + (3M + 1) kT \ln s + \frac{p_s^2}{m_s} \quad (1.55)$$

where  $m_s$  is a fictitious mass associated with coordinate  $s$ .  $m_s$  determines how strongly the system is coupled to the thermal bath, and is a parameter of an NVT MD simulation. (As a reminder,  $M$  is the number of nuclei in the system.)

Using Hamilton's equations of motion (equation 1.47), the dynamics of the system is given by

$$\frac{dR_I}{dt} = \frac{p_I}{2m_I s^2} \quad (1.56)$$

$$\frac{dp_I}{dt} = -\frac{\partial V(\tau)}{\partial R_I} \quad (1.57)$$

$$\frac{ds}{dt} = \frac{p_s}{m_s} \quad (1.58)$$

$$\frac{dp_s}{dt} = \sum_{I=1}^M \frac{p_I^2}{2m_I s^2} - (3M + 1) \frac{kT}{s}. \quad (1.59)$$

These equations result in a trajectory for the system that samples the NVT ensemble. But it does so at the cost of a timestep for the simulation that fluctuates across iterations. Hoover noticed that this inconvenience could be removed via a change of variables [145]

$$\zeta \equiv \frac{p_s}{3M} \quad (1.60)$$

$$\frac{dR_I}{dt} = \frac{p_I}{m_i} \quad (1.61)$$

$$\frac{dp_I}{dt} = -\frac{\partial V(\tau)}{\partial R_I} - \zeta p_I \quad (1.62)$$

$$\frac{d\zeta}{dt} = \frac{1}{m_s} \left( \sum_{I=1}^M \frac{p_I^2}{m_I} - 3MkT \right) \quad (1.63)$$

This thermostat has the attractive property that it can be integrated much like the NVE equations. We will use it in MD simulations to compute NVT ensemble averages in Chapters 2 and 7.

### 1.1.2.3 Force fields

In order to sufficiently sample to converge averages like equation 1.54, we must run MD for a long time. As currently presented, MD is usually too costly for such calculations.

Integrating the classical equations of motion is computationally straightforward. The expensive part of an MD calculation is the evaluation of the force on each nucleus

$$\frac{dP_I}{dt} = -\frac{\partial H}{\partial R_I} = -\frac{\partial V}{\partial R_I} \quad (1.64)$$

$$\frac{\partial V}{\partial R_I} = -\sum_{I=1}^N \sum_{J>I}^M \frac{Z_I Z_J}{r_{IJ}^2} \hat{r}_{IJ} + \frac{\partial E_e(R_1, R_2, \dots, R_M)}{\partial R_I}. \quad (1.65)$$

Specifically, the expensive term is the derivative of the electronic energy with respect to the nuclear coordinates because it requires an electronic structure calculation. When MD is performed in this manner, it is called “ab-initio” or “Born-Oppenheimer” MD [21].

In order to massively speed up this calculation,  $E_e(R_1, R_2, \dots, R_N)$  is often approximated by a classical, phenomenological expression. The resulting approximate potential energy is called a force field.

$$E_E(R_1, R_2, \dots, R_M) + \sum_{I=1}^M \sum_{J>I}^M \frac{Z_I Z_J}{r_{IJ}} = V(R_1, R_2, \dots, R_M) \approx V_{FF}(R_1, R_2, \dots, R_M) \quad (1.66)$$

When MD is performed using a force field, it is called Molecular Mechanics (MM) [9, 104].

A simple molecular force field is composed of four terms [13]

$$\begin{aligned}
V_{FF} = & \sum_{I=1}^M \sum_{J>I}^M [V_{Coul}(r_{IJ}, I, J) + V_{NB}(r_{IJ}, I, J) + V_{bond}(r_{IJ}, I, J)] + \\
& \sum_{I=1}^M \sum_{J>I}^M \sum_{K>J}^M V_{angle}(\theta_{IJK}, I, J, K).
\end{aligned} \tag{1.67}$$

$V_{coul}$  is the Coulomb interaction between two atoms

$$V_{coul}(r, A, B) = \frac{Q_A Q_B}{r} \tag{1.68}$$

where  $Q_X$  is the charge of atom  $X$  and is a parameter for the force field. The non-bonded interaction,  $V_{NB}$ , usually describes both hard-core short-range interactions as well as long range dispersion. One popular form of this interaction is the Lennard-Jones potential

$$V_{LJ}(r, A, B) = 4\epsilon_{AB} \left[ \left( \frac{\sigma_{AB}}{r} \right)^{12} - \left( \frac{\sigma_{AB}}{r} \right)^6 \right] \tag{1.69}$$

where  $\sigma_{AB}$  and  $\epsilon_{AB}$  are empirical parameters.  $V_{bond}$  describes stretching of chemical bonds, and is most simply approximated by a harmonic potential

$$V_{bond}(r, A, B) = \frac{1}{2} k_{AB} (r - b_{AB})^2 \tag{1.70}$$

where  $k_{AB}$  and  $b_{AB}$  are parameters if atoms  $A$  and  $B$  are covalently bonded, and zero otherwise. Finally,  $V_{angle}$  represents the energy of angular bond vibration and might be approximated by

$$V_{angle}(\theta, A, B, C) = \frac{1}{2} k_{ABC} [\cos(\theta) - \cos(\phi_{ABC})]^2 \tag{1.71}$$

with  $k_{ABC}$  and  $\phi_{ABC}$  as parameters (again zero if  $B$  isn't bonded to both  $A$  and  $C$ ).

Looking at equations 1.68, 1.69, 1.70, and 1.71, we see that even a simple force field has many parameters. Because these parameters are the only thing that changes for different atoms and molecules, the MD description of a chemical system is very sensitive to our choice of force field parameters.

#### 1.1.2.4 Force matching

One choice of force field parameters is motivated by equation 1.66; we want force field parameters that best minimize the difference between the force field potential energy and the quantum potential energy surface

$$\{\pi_i\} = \arg \min_{\{\pi_i\}} |V(R_1, R_2, \dots, R_M) - V_{FF}(R_1, R_2, \dots, R_M; \{\pi_i\})|^2 \tag{1.72}$$

where  $\{\pi_i\}$  represents the set of parameters of the force field. This expression does not specify nuclear coordinates, however, and we must make another choice. From Section 1.1.2.1, we recall that we are often interested in computing ensemble averages. Thus, we can choose our coordinates to produce the force field that best reproduces averages in an ensemble. We do this by minimizing the ensemble average of the error (equation 1.72)

$$\{\pi_i\} = \arg \min_{\{\pi_i\}} \frac{1}{Q[p]} \int p(\tau) |V(\tau) - V_{FF}(\tau; \{\pi_i\})|^2 d\tau. \quad (1.73)$$

And we sample this average using MD. In practice, we also minimize error in the derivatives of the potential, resulting in a method called “force matching” [92, 153]. For simplicity, we will consider only matching the potential in this section. In Section 7.2.1, we expound the general case of simultaneous energy and force matching.

Assuming that we are interested in the NVT ensemble,  $p$  becomes the Boltzmann ensemble

$$p(\tau) = \exp[-\beta V(\tau)]. \quad (1.74)$$

Of course, we cannot afford to sample this average with MD because it requires many evaluations of the expensive quantum potential energy surface. Instead, we approximate  $V$  with the force field

$$p(\tau) \approx p_{FF}(\tau) = \exp[-\beta V_{FF}(\tau; \{\pi_i\})]. \quad (1.75)$$

To first order (in  $\beta V$ ), the error of this approximation is

$$\frac{1}{Q[p]} \int p(\tau) |p(\tau) - p_{FF}(\tau)|^2 d\tau \approx \frac{1}{Q[p]} \int p(\tau) \beta^2 |V(\tau) - V_{FF}(\tau)|^2 d\tau \quad (1.76)$$

which is proportional to our original force matching error (equation 1.73). Thus, as we improve the error of our force field at each point  $\tau$ , we also improve the error in our choice of which  $\{\tau\}$  we sample. A force-matched set of parameters then not only gives a better description of  $V$ , but also gives a better estimate of the error

$$\frac{1}{Q[p]} \int p(\tau) |p(\tau) - p_{FF}(\tau)|^2 d\tau \approx \frac{1}{Q_{FF}[p]} \int p_{FF}(\tau) |p(\tau) - p_{FF}(\tau)|^2 d\tau. \quad (1.77)$$

This last observation leads to the self-consistent force-matching algorithm [348]:

1. Choose an initial set of parameters  $\{\pi_i^{(0)}\}$
2. For a given set of parameters  $\{\pi_i^{(n)}\}$ , sample a set of independent coordinate snapshots  $\{\tau^{(n)}\}$  by running MD with the approximate potential  $V_{FF}(\tau, \{\pi_i^{(n)}\})$ .
3. Find a new set of parameters  $\{\pi_i^{(n+1)}\}$  by minimizing the error (equation 1.73). To save

computational time, only compute the error using a sparse set of  $\tau$ .<sup>1</sup>

4. Repeat steps 2 and 3 until the  $\{\pi_i\}$  and error converge.

In Chapter 7, we will apply this self-consistent force-matching algorithm to parameterize a force field for liquid water.

## 1.2 Exotic methods

The previous section introduced popular methods central to computational and theoretical chemistry. In this section, we will introduce more niche concepts that serve as background for later chapters. Because these methods can be narrow in scope, each section contains in its title the chapter(s) to which it corresponds.

### 1.2.1 Free probability (chapters 3 and 4)

In this section, we introduce free probability, the theory of non-commuting random variables. For purposes of this thesis, our non-commuting random variables of interest will be random matrices, finite-basis representations of random operators. We begin by reviewing definitions and results from the theory of commuting random variables, classical probability. We then summarize key definitions and results from free probability by analogy to their classical counterparts.

#### 1.2.1.1 Review of classical probability

Classical probability [98] concerns itself with commuting random variables. By chance, random variables take on different scalar values. Each value is associated with a corresponding probability of measuring the random variable to have that value. For a random variable  $r$ , the relationship between a value,  $x$ , and its probability,  $p_r(x)$ , is contained in the probability distribution function (p.d.f.),  $p_r$ .  $p_r$  is normalized, non-negative, and does not associate a probability large than 1 with any value:

$$\begin{aligned}\int p_r(x)dx &= 1 \\ 0 &\leq p_r(x) \\ 1 &\geq \int p_r(x)dx.\end{aligned}\tag{1.78}$$

---

<sup>1</sup>This is actually a good approximation. The MD snapshots are time-correlated, reducing the statistical significance of sampling the error at two points that are close together in time. We only lose accuracy in the error integral if our sparsified samples differ by more than the correlation time of the system. Typical correlation times are around 1ps, or  $10^4$  MD steps. Thus, we only need one electronic structure calculation per  $10^4$  MM calculations.

The expectation value, or mean, of  $r$  is defined as the average value of repeated measurements of  $r$  as the number of measurements goes to infinity. It is related to the p.d.f. by

$$\langle r \rangle = \int x p_r(x) dx \quad (1.79)$$

where we use angle brackets  $\langle \cdot \rangle$  to denote the expectation value. More generally, the  $k$ th moment of  $r$  is defined as the expectation value of  $r^k$ , where  $k$  is a non-negative integer. These moments also relate to the p.d.f.

$$\mu_k^{(r)} \equiv \langle r^k \rangle = \int x^k p_r(x) dx. \quad (1.80)$$

We are sometimes interested in a joint moment  $\langle r^k q^l \rangle$  of two random variables,  $r$  and  $q$ . When this joint moment can be factored into moments of  $r$  and  $q$  alone

$$\langle r^k q^l \rangle = \langle r^k \rangle \langle q^l \rangle \quad (1.81)$$

for all non-negative integers  $k$  and  $l$ ,  $r$  and  $q$  are said to be “independent”. Under these conditions, we can sample a value of  $r+q$  by independently sampling a value from each  $r$  and  $q$  and adding them together. Somewhat more formally, if we have a vector of samples of  $r$ ,  $\vec{x}^{(r)} = [x_1^{(r)}, x_2^{(r)}, x_3^{(r)}, \dots, x_n^{(r)}]$ , and similar vector of samples of  $q$ ,  $\vec{x}^{(q)}$ , we can generate a vector of samples of  $r+q$  with

$$\vec{x}^{(r+q)} = \vec{x}^{(r)} + \mathbf{\Omega} \vec{x}^{(q)} = \mathbf{\Omega} \vec{x}^{(r)} + \vec{x}^{(q)} = \mathbf{\Omega} \vec{x}^{(r)} + \mathbf{\Omega}' \vec{x}^{(q)} \quad (1.82)$$

where  $\mathbf{\Omega}$  is a random permutation matrix (a shuffle) and equality is in a statistical sense.

The p.d.f. corresponding to  $r+q$  can be computed with the (classical) convolution

$$p_{r+q}(x) = \int p_r(y) p_q(x-y) dy \equiv p_r(x) \star p_q(x). \quad (1.83)$$

While this integral can be computed directly, the convolution can also be performed stepwise. In doing so, we distill the essence of each independent p.d.f. First, we compute the Fourier transform of each p.d.f.

$$\hat{p}(k) = \int e^{ikx} p(x) dx. \quad (1.84)$$

The Fourier transform of the p.d.f. of the sum of two random variables is simply the product of the Fourier transforms of their corresponding p.d.f.s

$$\hat{p}_{r+q}(k) = \hat{p}_r(k) \hat{p}_q(k). \quad (1.85)$$

The desired p.d.f. can then be recovered by inverting the Fourier transform

$$p_{r+q}(x) = \frac{1}{2\pi} \int e^{-ikx} \hat{p}_{r+q}(k) dk. \quad (1.86)$$

We can understand the action of the Fourier transform by expanding the exponential in 1.84 in a power series

$$\begin{aligned} \hat{p}_r(k) &= \int \left[ 1 + ikx + \frac{(ik)^2}{2} x^2 + \frac{(ik)^3}{3!} x^3 + \dots \right] p_r(x) dx \\ &= \int p_r(x) dx + ik \int xp_r(x) dx + \frac{(ik)^2}{2} \int x^2 p_r(x) dx + \frac{(ik)^3}{3!} \int x^3 p_r(x) dx + \dots \\ &= 1 + ik\mu_1^{(r)} + \frac{(ik)^2}{2} \mu_2^{(r)} + \frac{(ik)^3}{3!} \mu_3^{(r)} + \dots \\ &= \sum_{n=0}^{\infty} \mu_n^{(r)} \frac{(ik)^n}{n!}. \end{aligned} \quad (1.87)$$

We can then obtain moments of  $r$  by taking an appropriate derivative of the Fourier-transformed p.d.f.

$$\mu_n^{(r)} = \left. \frac{d^n}{d(ik)^n} \hat{p}_r(k) \right|_{k=0}. \quad (1.88)$$

This Fourier-transformed p.d.f. is sometimes called the “moment generating function”.

For purposes of future analogy, we can modify equation 1.85 so that addition of  $r$  and  $q$  corresponds to addition in some representation

$$\hat{p}_{r+q}(k) = \exp[\ln(\hat{p}_r(k)) + \ln(\hat{p}_q(k))]. \quad (1.89)$$

The logarithm of the Fourier transform is thus fundamentally related to the addition of independent random variables: it is the property of these variables that adds. Its Taylor series expansion is given by

$$\ln(\hat{p}_r(k)) = \sum_{n=1}^{\infty} \kappa_n^{(r)} \frac{(ik)^n}{n!}. \quad (1.90)$$

$\kappa_n^{(r)}$  is the  $n$ th “cumulant” of  $r$  and is a combinatorial function of the first  $n$  moments of  $r$ . The log-Fourier transform of the p.d.f. is sometimes called the “cumulant generating function” and we can use it to generate cumulants in a manner analogous to equation 1.88.

When we add two log-Fourier-transformed p.d.f.s, we gather each power of  $ik$

$$\ln(\hat{p}_r(k)) + \ln(\hat{p}_q(k)) = \sum_{n=1}^{\infty} \kappa_n^{(r)} \frac{(ik)^n}{n!} + \sum_{n=1}^{\infty} \kappa_n^{(q)} \frac{(ik)^n}{n!} = \sum_{n=1}^{\infty} (\kappa_n^{(r)} + \kappa_n^{(q)}) \frac{(ik)^n}{n!}. \quad (1.91)$$

Thus, adding two independent random variables is equivalent to adding their cumulants.

### 1.2.1.2 What is a random matrix?

We now progress to non-commuting random variables. Our non-commuting objects of choice will be random matrices. At its most basic, a random matrix is a square matrix whose elements are random variables.

We now define some analogous properties of random matrices. There are many choices of what to map on to the various objects in classical probability; we use the spectral theory of random matrices. This formulation concerns itself with eigenvalues of random matrices. It concerns us because computational quantum mechanics is often an eigenvalue-seeking problem. (For a discussion on the choices made to construct this formalism as well as their implications, see reference [322].) These eigenvalues are in general complex.

The p.d.f.,  $P_{\mathbf{R}}(\lambda)$ , of an  $n \times n$  random matrix,  $\mathbf{R}$ , is the probability that  $\mathbf{R}$  has an eigenvalue equal to  $\lambda$ . As in equation 1.78, it is normalized, non-negative, and associates a probability of 1 or less to a given eigenvalue. It is given by

$$p_{\mathbf{R}}(\lambda) = \frac{1}{n} \left\langle \sum_{i=1}^n \delta(\lambda - \lambda_i^{(\mathbf{R})}) \right\rangle \quad (1.92)$$

where  $\delta$  is the Kronecker delta function,  $\{\lambda_i^{(\mathbf{R})}\}$  are the eigenvalues of  $\mathbf{R}$ , and  $\frac{1}{n}$  normalizes the p.d.f. Note that for a deterministic matrix, this object is the density of states.

The expectation value (mean) is now replaced by the mean eigenvalue of  $\mathbf{R}$

$$\langle \mathbf{R} \rangle \equiv \frac{1}{n} \langle \text{Tr} \mathbf{R} \rangle \quad (1.93)$$

where we have used the fact that the trace is the sum of the eigenvalues. We also overload the angle brackets to denote this matrix expectation value when their argument is a matrix. We can define the moments of  $\mathbf{R}$  by analogy to equation 1.80

$$\mu_k^{(\mathbf{R})} \equiv \langle \mathbf{R}^k \rangle = \frac{1}{n} \langle \text{Tr} \mathbf{R}^k \rangle. \quad (1.94)$$

### 1.2.1.3 Free independence

As with commuting random variables, random matrices have a notion of independence. Naively mapping onto equation 1.81, we might expect that two random matrices  $\mathbf{R}$  and  $\mathbf{Q}$  are independent when

$$\langle \mathbf{R}^k \mathbf{Q}^l \rangle = \langle \mathbf{R}^k \rangle \langle \mathbf{Q}^l \rangle. \quad (1.95)$$

However, equation 1.81 has implicitly used the commutativity of  $r$  and  $q$  to gather terms. For non-commuting random matrices, the equivalent (and far more general) condition is [340]

$$\left\langle \prod_{i=1}^{\infty} p_i(\mathbf{R}) p'_i(\mathbf{Q}) \right\rangle = 0 \quad (1.96)$$

where the  $\{p_i\}$  and  $\{p'_i\}$  are all polynomials such that

$$\begin{aligned} \langle p_i(\mathbf{R}) \rangle &= 0 \\ \langle p'_i(\mathbf{Q}) \rangle &= 0. \end{aligned} \quad (1.97)$$

When equation 1.96 is satisfied,  $\mathbf{Q}$  and  $\mathbf{R}$  are said to be “freely independent” or, more succinctly, “free”. When  $\mathbf{Q}$  and  $\mathbf{R}$  do commute, this condition is not equivalent to 1.95. Thus, free independence is not a generalization of (classical) independence, but rather a parallel statistical property. (Note however, that this is only the case for matrices. For commuting scalar random variables (or random matrices with  $n = 1$ ), equation 1.96 does reduce to equation 1.81).

An equivalent (and simpler) condition to equation 1.96 is that all centered joint moments vanish

$$\left\langle \overline{\mathbf{R}^{k_1} \mathbf{Q}^{l_1} \mathbf{R}^{k_2} \mathbf{Q}^{l_2} \dots \mathbf{R}^{k_\infty} \mathbf{Q}^{l_\infty}} \right\rangle = 0 \quad (1.98)$$

where  $\{k_i\}$  and  $\{l_i\}$  are arbitrary sequences of non-negative integers and the centered matrix is defined as

$$\overline{\mathbf{M}} \equiv \mathbf{M} - \langle \mathbf{M} \rangle. \quad (1.99)$$

This definition allows us to draw analogy back to equation 1.81, which we can rewrite as

$$\left\langle \overline{r^k q^l} \right\rangle = 0 \quad (1.100)$$

$$\left\langle \overline{r^{k_1} q^{l_1} r^{k_2} q^{l_2} \dots r^{k_\infty} q^{l_\infty}} \right\rangle = 0 \quad (1.101)$$

using the commutativity of  $r$  and  $q$  with

$$k \equiv \sum_{i=1}^{\infty} k_i \quad (1.102)$$

$$l \equiv \sum_{i=1}^{\infty} l_i. \quad (1.103)$$

In classical probability, we viewed independence of classical variables as a shuffling operation (equation 1.82). The free probability equivalent is a random rotation of eigenvectors. Given a diagonal matrix of eigenvalues sampled from  $\mathbf{R}$ ,

$$\Lambda^{(\mathbf{R})} \equiv \begin{pmatrix} \lambda_1^{(\mathbf{R})} & & & \\ & \lambda_1^{(\mathbf{R})} & & \\ & & \ddots & \\ & & & \lambda_1^{(\mathbf{R})} \end{pmatrix}, \quad (1.104)$$

and a similar object for  $\mathbf{Q}$ ,  $\Lambda^{(\mathbf{Q})}$ , the eigenvalues sampled from their sum are given by

$$\mathbf{V}\Lambda^{(\mathbf{R}+\mathbf{Q})}\mathbf{V}^\dagger = \Lambda^{(\mathbf{R})} + \mathbf{U}\Lambda^{(\mathbf{Q})}\mathbf{U}^\dagger = \mathbf{U}\Lambda^{(\mathbf{R})}\mathbf{U}^\dagger + \Lambda^{(\mathbf{Q})} = \mathbf{U}\Lambda^{(\mathbf{R})}\mathbf{U}^\dagger + \mathbf{U}'\Lambda^{(\mathbf{Q})}(\mathbf{U}')^\dagger. \quad (1.105)$$

$\mathbf{U}$  is a random unitary matrix of Haar measure [63], the equivalent of a uniform distribution for unitary matrices.  $\mathbf{V}$  is also a unitary matrix, indicating that  $\mathbf{V}\Lambda^{(\mathbf{R}+\mathbf{Q})}\mathbf{V}^\dagger$  must be diagonalized to sample the eigenvalues of  $\mathbf{R} + \mathbf{Q}$ . Because equality is meant in a statistical sense,  $\mathbf{V}$  is also of Haar measure. If we assume that our random matrices are Hermitian, as is often the case in quantum mechanics,

$$\mathbf{V}(\mathbf{R} + \mathbf{Q})\mathbf{V}^\dagger = \mathbf{R} + \mathbf{U}\mathbf{Q}\mathbf{U}^\dagger = \mathbf{U}\mathbf{R}\mathbf{U}^\dagger + \mathbf{Q} = \mathbf{U}\mathbf{R}\mathbf{U}^\dagger + \mathbf{U}'\mathbf{Q}(\mathbf{U}')^\dagger, \quad (1.106)$$

where we have used the fact that Hermitian matrices are diagonalized by unitary transformations and that the sum of Hermitian matrices is Hermitian.

#### 1.2.1.4 The $\mathbf{R}$ transform

In classical probability, the convolution allowed us to find the p.d.f. of the sum of two independent random variables (equation 1.83). In free probability, the free convolution serves the same purpose

$$p_{\mathbf{R}+\mathbf{Q}}(\lambda) = p_{\mathbf{R}}(\lambda) \boxplus p_{\mathbf{Q}}(\lambda). \quad (1.107)$$

Unlike the (classical) convolution, the free convolution does not have a pithy form. Instead, we define it implicitly via the  $\mathbf{R}$  transform, which is analogous to the log-Fourier transform of equation 1.89. We define it in two steps. First, we compute the Cauchy transform of the p.d.f. [340, 234]

$$G_{\mathbf{R}}(w) = \lim_{\epsilon \rightarrow 0^+} \int \frac{p_{\mathbf{R}}(\lambda)}{w - \lambda - i\epsilon} d\lambda. \quad (1.108)$$

In the same way that the Fourier transform of the p.d.f. is the moment-generating function of classical probability, the Cauchy transform is a moment-generating function for free probability [28]

$$G_{\mathbf{R}}(w) = \sum_{m=0}^{\infty} \mu_m^{(\mathbf{R})} \frac{1}{w^{m+1}}. \quad (1.109)$$

Second, we invert the Cauchy transform to get the R transform

$$R_{\mathbf{R}}(w) = G_{\mathbf{R}}^{-1}(w). \quad (1.110)$$

The R transform is the free analogy of the log-Fourier transform (equation 1.89) in that the R transforms of free random matrices add

$$R_{\mathbf{R}+\mathbf{Q}}(w) = R_{\mathbf{R}}(w) + R_{\mathbf{Q}}(w) - \frac{1}{w} \quad (1.111)$$

where the last term ensures normalization. As with the log-Fourier transform for cumulants, the R transform is the generating function of the “free cumulants”

$$R_{\mathbf{R}}(w) = \sum_{i=0}^{\infty} \chi_i^{(\mathbf{R})} w^{i-1} \quad (1.112)$$

which add for free random matrices like the cumulants do for independent random variables.

Finally, we can recover the p.d.f. by inverting  $R_{\mathbf{R}+\mathbf{Q}}$  and by noting that the Cauchy transform is an anti-involution [328]

$$G^{-1}(G(w)) = -1. \quad (1.113)$$

## 1.2.2 Schmidt decomposition (chapters 5 and 6)

In this section, we introduce the Schmidt decomposition [250], a tool for decomposing wavefunctions. We begin with a Hilbert space,  $\mathcal{H}$ , of dimension  $d$  and a wavefunction  $|\Psi\rangle$  that exists in that Hilbert space. We can partition this Hilbert space into two smaller Hilbert spaces

$$\mathcal{H} = \mathcal{H}_A \oplus \mathcal{H}_B, \quad (1.114)$$

where we choose the dimension of  $\mathcal{H}_A$ ,  $d_A$ , to be smaller than that of  $\mathcal{H}_B$ .  $\mathcal{H}_A$  and  $\mathcal{H}_B$  are spanned by sets of states  $\{|a_i\rangle\}$  and  $\{|b_i\rangle\}$ , which we will choose to be orthonormal. We can write  $|\Psi\rangle$  in terms of these states

$$|\Psi\rangle = \sum_{i=1}^{d_A} \sum_{j=1}^{d_B} X_{ij} |a_i\rangle \otimes |b_j\rangle \quad (1.115)$$

where  $\mathbf{X}$  is a (generally rectangular) matrix of overlaps between  $|\Psi\rangle$  and the basis states of our Hilbert spaces

$$X_{ij} = (\langle a_i | \otimes \langle b_j |) |\Psi\rangle. \quad (1.116)$$

$\mathbf{X}$  can be rewritten using the singular value decomposition (SVD) [146]

$$\mathbf{X} = \mathbf{U} \boldsymbol{\sigma} \mathbf{V}^\dagger \quad (1.117)$$

where  $\mathbf{U}$  is a  $d_A \times d_A$  orthogonal matrix,  $\boldsymbol{\sigma}$  is a  $d_A \times d_A$  diagonal matrix, and  $\mathbf{V}^\dagger$  is a  $d_A \times d_B$  matrix with orthogonal rows. The matrix multiplication can be expanded as a sum

$$X_{ij} = \sum_{k=1}^{d_A} U_{ik} \sigma_{kk} V_{kj}^\dagger \quad (1.118)$$

where we have used the fact that  $\boldsymbol{\sigma}$  is diagonal.

Rewriting equation 1.115,

$$|\Psi\rangle = \sum_{i=1}^{d_A} \sum_{j=1}^{d_B} \sum_{k=1}^{d_A} U_{ik} \sigma_{kk} V_{kj}^\dagger |a_i\rangle \otimes |b_j\rangle \quad (1.119)$$

and defining

$$\begin{aligned} |\alpha_k\rangle &\equiv \sum_{i=1}^{d_A} U_{ik} |a_i\rangle \\ |\beta_k\rangle &\equiv \sum_{j=1}^{d_B} V_{jk}^* |b_j\rangle, \end{aligned} \quad (1.120)$$

we find the Schmidt decomposition

$$|\Psi\rangle = \sum_{k=1}^{d_A} \sigma_{kk} |\alpha_k\rangle \otimes |\beta_k\rangle. \quad (1.121)$$

This remarkable result shows that the wavefunction can be represented using  $d_A$  states of  $\mathcal{H}_A$  and only  $d_A$  corresponding states of  $\mathcal{H}_B$ . In other words, we have described the wavefunction with a set  $\{|\alpha_k\rangle\}$  that spans  $\mathcal{H}_A$  and a set of  $\{|\beta_k\rangle\}$  that spans only a  $d_A$ -dimensional subspace of  $\mathcal{H}_B$ . The  $\sigma_{kk}$  are called “entanglements” and relate to the coherence of  $|\alpha_k\rangle$  and  $|\beta_k\rangle$ . They take values between 0 and 1. The total entanglement of the wavefunction in  $\mathcal{H}_A$  to that in  $\mathcal{H}_B$  is the “entanglement entropy” [156],

$$S_{\boldsymbol{\sigma}} = - \sum_{k=1}^{d_A} \sigma_{kk} \ln \sigma_{kk}. \quad (1.122)$$

We can also bring operators into this reduced subspace. Given an operator,  $\hat{O}$ , in  $\mathcal{H}$ , its Schmidt-

reduced form  $\hat{O}_{AB}$  is the result of projecting it into our reduced Hilbert space

$$\hat{O}_{AB} = \sum_{i=1}^{d_A} \sum_{j=1}^{d_A} \sum_{k=1}^{d_A} \sum_{l=1}^{d_A} (|\alpha_i\rangle \otimes |\beta_i\rangle) (\langle\alpha_j| \otimes \langle\beta_j|) \hat{O} (|\alpha_k\rangle \otimes |\beta_k\rangle) (\langle\alpha_l| \otimes \langle\beta_l|). \quad (1.123)$$

This operation maintains expectation values

$$\langle\Psi|\hat{O}|\Psi\rangle = \langle\Psi|\hat{O}_{AB}|\Psi\rangle. \quad (1.124)$$

(It is convenient to evaluate the right-hand side using the Schmidt decomposition of  $|\Psi\rangle$  from equation 1.121).

### 1.2.2.1 Schmidt decomposition of product wavefunctions

In the special case of product wavefunctions, the Schmidt decomposition is even more compact. For this section, we focus on the Hartree-Fock wavefunction of Section 1.1.1.3, but these ideas are generalized in Section 5.6 to the Hartree-Fock-Bogoliubov and Antisymmetrized Geminal Product wavefunctions which will be introduced in the next section.

The Hilbert space of Hartree-Fock is the  $N$ -electron Fock space, composed of products of orbitals. As in equation 1.114, we partition our Fock space

$$\mathcal{F} = \mathcal{F}_A \oplus \mathcal{F}_B \quad (1.125)$$

with  $d_A \leq d_B$ .

To reach the most compact decomposition of a Hartree-Fock wavefunction, we use a different procedure than the previous section, following reference [174]. Our goal is to replace the many-body states of equation 1.121 with single-body orbitals. We begin with a wavefunction  $|\Psi_{HF}\rangle$  and a projector onto the orbitals that span  $\mathcal{F}_A$ ,  $\hat{P}_A$ .  $|\Psi_{HF}\rangle$  is a product of  $N$  molecular orbitals

$$|\Psi_{HF}\rangle = \prod_{p=1}^N \hat{a}_p^\dagger | \rangle. \quad (1.126)$$

Define the  $N \times N$  overlap of  $|\Psi_{HF}\rangle$  with  $\mathcal{F}_A$  as

$$M_{pq} = \langle | \hat{a}_p \hat{P}_A \hat{a}_q | \rangle. \quad (1.127)$$

This matrix is Hermitian and can be diagonalized by a unitary transformation

$$\mathbf{M} = \mathbf{T} \mathbf{O} \mathbf{T}^\dagger.$$

Because  $\hat{P}_A$  has rank  $d_A$ ,  $\mathbf{M}$  has  $d_A$  non-zero eigenvalues (assuming  $d_A \leq N$ ). Because  $\mathbf{T}$  is unitary

and the Hartree-Fock wavefunction is invariant under unitary rotations, we can represent  $|\Psi_{HF}\rangle$  in a rotation of the molecular orbitals by  $\mathbf{T}$

$$\hat{\chi}_i^\dagger = \sum_{p=1}^N T_{pi} \hat{a}_p^\dagger \quad (1.128)$$

$$|\Psi_{HF}\rangle = \prod_{i=1}^N \hat{\chi}_i^\dagger |\rangle. \quad (1.129)$$

These orbitals partition into two types. The first are those that come from eigenvectors of  $\mathbf{V}$  corresponding to zero eigenvalues. These orbitals have no density in  $\mathcal{F}_A$  and are called “environment” orbitals. Separating them out gives

$$|\Psi_{HF}\rangle = \left( \prod_{i=1}^{d_A} \hat{\eta}_i^\dagger \right) \left( \prod_{i=1}^{N-d_A} \hat{\gamma}_i^\dagger \right) |\rangle. \quad (1.130)$$

where the  $\{\hat{\gamma}_i^\dagger\}$  correspond to these environment. Their complement, the  $\{\hat{\eta}_i^\dagger\}$ , can be partitioned into their components in  $\mathcal{F}_A$ ,  $\alpha$ , and in  $\mathcal{F}_B$ ,  $\beta$

$$|\Psi_{HF}\rangle = \left( \prod_{i=1}^{d_A} \left[ \sqrt{O_{ii}} \hat{\alpha}_i^\dagger + \sqrt{1 - O_{ii}} \hat{\beta}_i^\dagger \right] \right) \left( \prod_{i=1}^{N-d_A} \hat{\gamma}_i^\dagger \right) |\rangle. \quad (1.131)$$

Rewriting this expression in the notation of equation 1.121 [364], we see

$$|\Psi_{HF}\rangle = \sum_{i=1}^{d_A} O_{ii} |\alpha_i\rangle \otimes |\beta_i\rangle \otimes |core\rangle \quad (1.132)$$

where

$$\begin{aligned} |\alpha_i\rangle &= \hat{\alpha}_i^\dagger |\rangle \\ |\beta_i\rangle &= \hat{\beta}_i^\dagger |\rangle \\ |core\rangle &= \left( \prod_{i=1}^{N-d_A} \hat{\gamma}_i^\dagger \right) |\rangle. \end{aligned}$$

Instead of the many-body states of the Schmidt-decomposition, this equation partitions the Hartree-Fock state into  $d_A$  interacting orbitals on the  $A$  and  $B$  subspaces and  $N - d_A$  environment orbitals in subspace  $B$ . We can project operators into this subspace. Specifically, we will project the Hamiltonian. Because our subspace is defined by orbitals, this amounts to just an orbital rotation of the integrals

$$(\mathbf{H}_{AB})_{ij} = \sum_{ij=1}^{2d_A} (\tilde{h}_{ij} + \tilde{h}_{core}) \hat{\tau}_i^\dagger \hat{\tau}_j + \sum_{ijkl=1}^{2d_A} \tilde{V}_{ijkl} \hat{\tau}_i^\dagger \hat{\tau}_j^\dagger \hat{\tau}_l \hat{\tau}_k \quad (1.133)$$

where

$$\{\hat{\tau}_i^\dagger\} = \{\hat{\alpha}_i^\dagger\} \cup \{\hat{\beta}_i^\dagger\}. \quad (1.134)$$

$\tilde{\mathbf{h}}$  and  $\tilde{\mathbf{V}}$  are the one- and two-electron integrals rotated into the basis of the  $\{\hat{\tau}_i^\dagger\}$ .  $\tilde{\mathbf{h}}_{core}$  is the frozen-core [147, 280] contribution of the environment orbitals, also rotated into this basis. The unrotated form is given by

$$(\mathbf{h}_{core})_{pq} = \sum_{pqrs} V_{pqrs} \sum_{a=d_A+1}^N T_{ra} T_{as}^\dagger. \quad (1.135)$$

### 1.2.3 Broken symmetry mean fields (chapter 5)

The difference between the Hartree-Fock (section 1.1.1.3) energy and the exact energy is called “correlation”. In Hartree-Fock, each electron moves in the average potential of the other electrons, and thus correlations between electron motions are lost. Correlation is divided into two types, reflecting the two main shortcomings of Hartree-Fock. Dynamical correlation is the process we just described: electrons repel each other instantaneously. When two electrons meet, they reduce their interaction energy by pushing each other away. Static correlation arises when there are near degeneracies in the Hartree-Fock ground state. The Hartree-Fock approximation assumes that the ground state is primarily described by a single Slater determinant. When static correlation is present, the correct wavefunction will have significant contributions from more than one determinant.

In this section, we introduce two wavefunctions that address this second kind of correlation. They both have mean-field-like cost ( $\mathcal{O}(n^3 \log n)$  at most), but are not competitive for solving real chemical problems. In Chapter 5, we use these wavefunctions as an embedding bath.

#### 1.2.3.1 Hartree-Fock-Bogoliubov

Hartree-Fock-Bogoliubov (HFB) is a generalization of Hartree-Fock, formulated to describe nuclear structure and superconductivity [272]. It begins with the Hartree-Fock Slater determinant and then adds quasi-particle operators that represent low-lying excitations of the Hartree-Fock determinant. By mixing in low-lying (possibly near-degenerate) determinants, HFB attempts to patch up the static correlation problem in Hartree-Fock.

The quasi-particles are defined through their second quantization operators

$$\begin{aligned}
\hat{\beta}_i^\dagger &\equiv \sum_{\mu} (U_{\mu i} \hat{c}_{\mu}^\dagger + V_{\mu i} \hat{c}_{\mu}) \\
\hat{\beta}_i &\equiv \sum_{\mu} (U_{\mu i}^* \hat{c}_{\mu} + V_{\mu i}^* \hat{c}_{\mu}^\dagger)
\end{aligned} \tag{1.136}$$

where  $\mathbf{U}$  and  $\mathbf{V}$  are parameters of the HFB wavefunction akin to the coefficient matrix,  $\mathbf{C}$ , of the Hartree-Fock wavefunction. For later convenience, these parameters can be gathered into a single matrix

$$\begin{pmatrix} \hat{\beta} \\ \hat{\beta}^\dagger \end{pmatrix} = \begin{pmatrix} \mathbf{U}^\dagger & \mathbf{V}^\dagger \\ \mathbf{V}^\mathbf{T} & \mathbf{U}^\mathbf{T} \end{pmatrix} \begin{pmatrix} \hat{c} \\ \hat{c}^\dagger \end{pmatrix} \equiv \mathbf{W}^\dagger \begin{pmatrix} \hat{c} \\ \hat{c}^\dagger \end{pmatrix}. \tag{1.137}$$

(The unsubscripted operators stand in for a vector of  $N$  quasiparticle or electron second quantization operators.)

HFB is a mean-field quasi-particle product wavefunction

$$|\Psi_{HFB}\rangle = \prod_{i=1}^N \hat{\beta}_i | \rangle. \tag{1.138}$$

Notice that this is analogous to the Hartree-Fock wavefunction (equation 1.25), but we have replaced the electron creation operators  $\hat{c}_i^\dagger$  with the quasiparticle annihilation operators  $\hat{\beta}_i$ . (This seemingly counterintuitive choice is made so that the ground state wavefunction is the vacuum with respect to quasiparticles

$$\hat{\beta}_i |\Psi_{HFB}\rangle = 0 \quad \forall i \in [1, N] \tag{1.139}$$

This condition also sets the limit of the product to  $N$  quasiparticles corresponding to  $N$  electrons.)

Like electrons, the quasi-particles are chosen to be fermions,

$$\{ \hat{\beta}_i^\dagger, \hat{\beta}_j \} = \delta_{ij} \tag{1.140}$$

$$\{ \hat{\beta}_i, \hat{\beta}_j \} = 0 \tag{1.141}$$

$$\{ \hat{\beta}_i^\dagger, \hat{\beta}_j^\dagger \} = 0. \tag{1.142}$$

This choice imposes a constraint on the parameters of the wavefunction most easily expressed by requiring  $\mathbf{W}$  to be unitary

$$\mathbf{W}^\dagger \mathbf{W} = \mathbf{1}. \tag{1.143}$$

To understand the structure of the HFB wavefunction, we can examine its analog of the Hartree-

Fock density matrix. First, we note that the Hartree-Fock density matrix can be written as

$$\mathbf{P} = \mathbf{C} \begin{pmatrix} \mathbf{1}_N & 0 \\ 0 & 0 \end{pmatrix} \mathbf{C}^\dagger \quad (1.144)$$

where  $\mathbf{1}_N$  is an  $N \times N$  identity matrix representing unity occupation of the occupied molecular orbitals. The HFB equivalent is given by

$$\mathbf{R} = \mathbf{W} \begin{pmatrix} 0 & 0 \\ 0 & \mathbf{1}_N \end{pmatrix} \mathbf{W}^\dagger \equiv \begin{pmatrix} \mathbf{P} & \mathbf{K} \\ -\mathbf{K}^* & \mathbf{1} - \mathbf{P}^* \end{pmatrix} \quad (1.145)$$

where  $\mathbf{1}_N$  is now in the bottom-right corner due to the choice to use quasi-particle annihilation operators in place of electron creation operators (equation 1.138). Using equations 1.136 and 1.137 and noting that

$$R_{\mu\nu} = \langle |\hat{c}_\mu | \Psi_{HFB} \rangle \langle \Psi_{HFB} | \hat{c}_\nu^\dagger | \rangle, \quad (1.146)$$

we find

$$P_{\mu\nu} = \langle \Psi_{HFB} | \hat{c}_\nu^\dagger \hat{c}_\mu | \Psi_{HFB} \rangle \quad (1.147)$$

$$K_{\mu\nu} = \langle \Psi_{HFB} | \hat{c}_\nu \hat{c}_\mu | \Psi_{HFB} \rangle. \quad (1.148)$$

$\mathbf{P}$  is thus analogous to the density matrix from Hartree-Fock. But, we notice that it is not idempotent

$$\mathbf{P}\mathbf{P} - \mathbf{P} = -\mathbf{K}\mathbf{K}^\dagger \quad (1.149)$$

where we have used the fact that  $\mathbf{R}$  is idempotent by construction. In fact,  $\mathbf{P}$  can assume any structure. We will use this fact in Chapter 5 to match similar wavefunctions to the exact wavefunction.

$\mathbf{K}$  is called the “pairing matrix” and represents pair correlation of electrons. It contains the new physics of HFB; when  $\mathbf{K} = \mathbf{0}$ , the wavefunction reduces to Hartree-Fock. The presence of  $\mathbf{K}$  also exposes an approximation of HFB (as applied to molecules): the HFB state is not an eigenstate of the electron number operator. In other words, the HFB wavefunction describes a fluctuating number of electrons. In order to make physical sense of such a state, the HFB wavefunctions is usually constrained to have the correct number of electrons *on average*

$$\langle \Psi_{HFB} | \hat{N} | \Psi_{HFB} \rangle = \text{Tr}\mathbf{P} = N_e. \quad (1.150)$$

Using the definitions in equations 1.21 and 1.22, the energy of an HFB state is given by

$$\begin{aligned} \langle \Psi_{HFB} | \hat{H} | \Psi_{HFB} \rangle &= \sum_{\mu\nu} h_{\mu\nu} P_{\nu\mu} + \frac{1}{2} \sum_{\mu\nu\lambda\sigma} (V_{\mu\lambda\nu\sigma} - V_{\mu\lambda\sigma\nu}) P_{\mu\nu} P_{\lambda\sigma} + \\ &\quad \frac{1}{4} \sum_{\mu\nu\lambda\sigma} (V_{\mu\nu\lambda\sigma} - V_{\mu\nu\sigma\lambda}) K_{\mu\nu}^* K_{\lambda\sigma}. \end{aligned} \quad (1.151)$$

To variationally optimize the HFB state, we minimize the Lagrangian

$$L[\mathbf{R}] = \langle \Psi_{HFB} | \hat{H} | \Psi_{HFB} \rangle - \Lambda (\text{Tr} \mathbf{P} - N) \quad (1.152)$$

where the second term enforces equation 1.150 using Lagrange multiplier  $\Lambda$ . This results in a self-consistency equation for HFB theory

$$\mathbf{G}_{HFB} \mathbf{W} = \mathbf{W} \begin{pmatrix} \epsilon & 0 \\ 0 & -\epsilon \end{pmatrix} \quad (1.153)$$

where

$$\mathbf{G}_{HFB} = \begin{pmatrix} \mathbf{F}_{HFB} & \mathbf{\Delta} \\ \mathbf{\Delta} & \mathbf{F}_{HFB}^* \end{pmatrix}. \quad (1.154)$$

$\mathbf{F}_{HFB}$  is analogous to the Fock matrix (equation 1.30)

$$(F_{HFB})_{\mu\nu} = h_{\mu\nu} + \frac{1}{2} \sum_{\lambda\sigma} (V_{\mu\lambda\nu\sigma} - V_{\mu\lambda\sigma\nu}) P_{\lambda\sigma} + \Lambda \delta_{\mu\nu}. \quad (1.155)$$

$\mathbf{\Delta}$  contains the mean-field description of the pairing interaction

$$\Delta_{\mu\nu} = \frac{1}{4} \sum_{\lambda\sigma} (V_{\mu\nu\lambda\sigma} - V_{\mu\nu\sigma\lambda}) K_{\lambda\sigma}. \quad (1.156)$$

The HFB wavefunction has two issues that make it unattractive for electronic structure. The first is the aforementioned number symmetry breaking, which we have patched by constraining the wavefunction to have the correct number of electrons on average (equation 1.150). The second problem is that the pairing interaction always increases the energy for repulsive interactions [16]. Thus, for the molecular Hamiltonian (equation 1.8), minimizing the HFB energy results in the Hartree-Fock wavefunction. One approach to this problem is to switch the sign of the pairing energy [307].

### 1.2.3.2 Antisymmetrized geminal product

Hartree-Fock(-Bogoliubov) is based on an approximate wavefunction that is a product of one-electron (one-quasiparticle) functions. Observing that (in chemistry) electrons tend to pair up and that the interactions are pairwise, we build a wavefunction ansatz that is a product of two-electron functions. These functions, called geminals, take the form

$$\hat{g}_i^\dagger \equiv \sum_{\mu\nu} C_{\mu\nu}^{(i)} \hat{c}_\mu^\dagger \hat{c}_\nu^\dagger \quad (1.157)$$

where we use the overbar,  $\bar{\phantom{x}}$ , to denote that  $\mu$  and  $\nu$  are restricted to opposite spins. We can create a product of these geminals

$$|\Psi_{APG}\rangle = \prod_{i=1}^{N/2} \hat{g}_i^\dagger | \rangle, \quad (1.158)$$

called the Antisymmetrized Product of Geminals (APG) wavefunction [211]. Because each geminal contains 2 electrons, this product of  $N/2$  geminals contains  $N$  electrons. If desired, we can handle the case of an odd number of electrons by tacking on an orbital for the unpaired electron

$$\left| \Psi_{APG}^{(odd)} \right\rangle = \hat{a}^\dagger \prod_{i=1}^{N/2} \hat{g}_i^\dagger | \rangle. \quad (1.159)$$

This APG wavefunction is highly accurate [236, 298], but is also exponentially expensive to variationally optimize.

To combat this scaling, many subsets of the APG wavefunctions have been formulated [151, 187, 188, 150, 316]. We will focus on the Antisymmetrized Geminal Power (AGP) wavefunction [60, 61]. In Hartree-Fock, the orbitals are required to be different because each single-electron orbital is a fermion. Two-electron geminals, however, are bosons. Thus, we can build a wavefunction out of the same geminal repeated  $N/2$  times

$$|\Psi_{AGP}\rangle = (g^\dagger)^{N/2} | \rangle. \quad (1.160)$$

The AGP wavefunction has a number of attractive properties. Unlike HFB, it is an eigenstate of the number operator. It treats static correlation by implicitly including a Slater determinant and all of its even excitations [39]. Thus, it contains all low-level excitations, patching Hartree-Fock's static correlation problem. In addition, it can have any density matrix. In principle, this means that it has the flexibility to match the density matrix of the exact wavefunction. (Such flexibility is not available in Hartree-Fock.)

However, AGP comes with a number of drawbacks. First, the coefficients of its excitations are not variationally optimized, but are rather fixed by the geminal coefficient matrix  $\mathbf{C}$ . Second, like

any truncated configuration interaction, AGP is not size-consistent. In fact, its energy reduces to that of HFB in the limit of large  $N$  [216, 62].

### 1.2.3.3 AGP as number-projected HFB

When discussing HFB, we constrained the wavefunction to have the correct number of electrons on average. Another approach to HFB's number asymmetry problem is to project it onto the eigenstate of the number operator corresponding to the desired number of electrons. As we will see later, this turns out to be equivalent to the AGP wavefunction

$$|\Psi_{AGP}\rangle = \hat{P}_N |\Psi_{HFB}\rangle. \quad (1.161)$$

$\hat{P}_N$  is a projection operator that zeros out components of the wavefunction without  $N$  electrons. This projection operator can be written as an integral [272]

$$\hat{P}_N |\Psi_{HFB}\rangle = \frac{1}{2\pi} \int_0^{2\pi} \exp[i(\hat{N} - N)\theta] |\Psi_{HFB}\rangle d\theta. \quad (1.162)$$

To understand this projector, we expand  $|\Psi_{HFB}\rangle$  in a basis on number eigenstates

$$\begin{aligned} |\Psi_{HFB}\rangle &= \sum_{M=0} c_M |\Phi_M\rangle \\ \hat{N} |\Phi_M\rangle &= M |\Phi_M\rangle. \end{aligned} \quad (1.163)$$

Then, the integral becomes

$$\hat{P}_N |\Psi_{HFB}\rangle = \frac{1}{2\pi} \sum_{M=0} |\Phi_M\rangle \int_0^{2\pi} \exp[i(M - N)\theta] d\theta. \quad (1.164)$$

When  $M = N$ , the exponential is 1 and the integral evaluates to  $2\pi$ . Otherwise, the exponential is oscillatory and integrates to zero around the unit circle.

To evaluate the integral in practice, we operate the number operator on the HFB wavefunction to generate a new HFB wavefunction

$$|\Psi_{HFB}(\theta)\rangle \equiv \exp[i\hat{N}\theta] |\Psi_{HFB}\rangle. \quad (1.165)$$

If  $|\Psi_{HFB}\rangle$  is described by parameter matrix  $\mathbf{W}$ , then the parameter matrix of  $|\Psi_{HFB}(\theta)\rangle$ ,  $\mathbf{W}(\theta)$ , is [294, 289]

$$\mathbf{W}(\theta) = \exp[iN\theta] \mathbf{W} = \begin{pmatrix} e^{i\theta} \mathbf{1} & 0 \\ 0 & e^{-i\theta} \mathbf{1} \end{pmatrix} \mathbf{W} = \begin{pmatrix} e^{i\theta} \mathbf{U} & (e^{-i\theta} \mathbf{V})^* \\ e^{-i\theta} \mathbf{V} & (e^{i\theta} \mathbf{U})^* \end{pmatrix}. \quad (1.166)$$

The integral 1.162 can be evaluated by quadrature

$$|\Psi_{AGP}\rangle = \hat{P}_N |\Psi_{HFB}\rangle = \sum_i w_i |\Psi_{HFB}(\theta_i)\rangle. \quad (1.167)$$

The AGP wavefunction is then just a sum of HFB determinants. Because the integral is one-dimensional and periodic, this quadrature should scale as  $\mathcal{O}(\log N)$ .

In general, we will want to evaluate matrix elements for AGP wavefunctions. For example, the energy expectation

$$E_{AGP} = \frac{\langle \Psi_{AGP} | \hat{H} | \Psi_{AGP} \rangle}{\langle \Psi_{AGP} | \Psi_{AGP} \rangle}. \quad (1.168)$$

Using equation 1.167, this becomes

$$E_{AGP} = \frac{\sum_{ij} w_i^* w_j \langle \Psi_{HFB}(\theta_i) | \hat{H} | \Psi_{HFB}(\theta_j) \rangle}{\sum_{ij} w_i^* w_j \langle \Psi_{HFB}(\theta_i) | \Psi_{HFB}(\theta_j) \rangle}. \quad (1.169)$$

Thus, we see that matrix elements between AGP wavefunctions can be evaluated as matrix elements between HFB wavefunctions.

To evaluate such matrix elements, we introduce the Thouless form of the HFB wavefunction [326]

$$|\Psi_{HFB}\rangle = \exp \left[ \sum_{\mu\nu} Z_{\mu\nu} \hat{c}_\mu^\dagger \hat{c}_\nu^\dagger \right] | \rangle \quad (1.170)$$

where  $\mathbf{Z}$  parameterizes the wavefunction and is related to our previous representation by

$$\mathbf{Z} = \mathbf{V}^* (\mathbf{U}^*)^{-1}. \quad (1.171)$$

For purposes of number projection,

$$\mathbf{Z}(\theta) = (e^{-i\theta} \mathbf{V})^* \left[ (e^{i\theta} \mathbf{U})^* \right]^{-1} = e^{2i\theta} \mathbf{Z}. \quad (1.172)$$

In this form, we can see why HFB does not conserve number. Expanding the exponential in a Taylor series, and noting that  $\sum_{\mu\nu} Z_{\mu\nu} \hat{c}_\mu^\dagger \hat{c}_\nu^\dagger \equiv g_{HFB}^\dagger$  is a geminal, equation 1.170 becomes

$$|\Psi_{HFB}\rangle = \left[ 1 + g_{HFB}^\dagger + \frac{1}{2} (g_{HFB}^\dagger)^2 + \frac{1}{3!} (g_{HFB}^\dagger)^3 + \dots \right] | \rangle. \quad (1.173)$$

So, Hartree-Fock-Bogoliubov is a sum of AGP wavefunctions corresponding to the same geminal, but different numbers of electrons. (Looking back, this also justifies equation 1.172, which can in turn be used to prove equation 1.166.) Expanding  $|\Psi_{HFB}(\theta)\rangle$  exposes how  $\exp[i\hat{N}\theta]$  marks each AGP wavefunction with its number of particles

$$\begin{aligned}
|\Psi_{HFB}(\theta)\rangle &= \left[ 1 + e^{2i\theta} g_{HFB}^\dagger + \frac{1}{2} \left( e^{2i\theta} g_{HFB}^\dagger \right)^2 + \frac{1}{3!} \left( e^{2i\theta} g_{HFB}^\dagger \right)^3 + \dots \right] |\rangle \\
&= \left[ 1 + e^{2i\theta} g_{HFB}^\dagger + \frac{1}{2} e^{4i\theta} \left( g_{HFB}^\dagger \right)^2 + \frac{1}{3!} e^{6i\theta} \left( g_{HFB}^\dagger \right)^3 + \dots \right] |\rangle \quad (1.174)
\end{aligned}$$

which then maps onto our expansion in number eigenstates, equation 1.163 (where the AGP functions are the number eigenstates).

The overlap between two HFB states,  $|\Psi_{HFB}^{(1)}\rangle$  and  $|\Psi_{HFB}^{(2)}\rangle$ , described by  $\mathbf{Z}_1$  and  $\mathbf{Z}_2$  is given by the Onishi theorem [244]

$$\langle \Psi_{HFB}^{(1)} | \Psi_{HFB}^{(2)} \rangle = \text{Pf}[1 - \mathbf{Z}_1^* \mathbf{Z}_2] \quad (1.175)$$

where Pf is the Pfaffian [218], a generalization of the determinant. Unlike the determinant, the Pfaffian can be computationally tricky [241, 105]. Hamiltonian matrix elements between HFB states can be evaluated through a generalization of equation 1.151 [272]

$$\begin{aligned}
\frac{\langle \Psi_{HFB}^{(1)} | \hat{H} | \Psi_{HFB}^{(2)} \rangle}{\langle \Psi_{HFB}^{(1)} | \Psi_{HFB}^{(2)} \rangle} &= \sum_{\mu\nu} h_{\mu\nu} P_{\nu\mu}^{(21)} + \frac{1}{2} \sum_{\mu\nu\lambda\sigma} (V_{\mu\lambda\nu\sigma} - V_{\mu\lambda\sigma\nu}) P_{\mu\nu}^{(21)} P_{\lambda\sigma}^{(21)} + \\
&\quad \frac{1}{4} \sum_{\mu\nu\lambda\sigma} (V_{\mu\nu\lambda\sigma} - V_{\mu\nu\sigma\lambda}) \left( K_{\mu\nu}^{(12)} \right)^* K_{\lambda\sigma}^{(21)}. \quad (1.176)
\end{aligned}$$

where the density and pairing matrices have been replaced by the transition density and transition pairing matrices

$$\begin{aligned}
\mathbf{P}^{(21)} &= -\mathbf{Z}^{(2)} \left( \mathbf{1} - \left( \mathbf{Z}^{(1)} \right)^* \mathbf{Z}^{(2)} \right)^{-1} \left( \mathbf{Z}^{(1)} \right)^*, \\
\mathbf{K}^{(21)} &= \mathbf{Z}^{(2)} \left( \mathbf{1} - \left( \mathbf{Z}^{(1)} \right)^* \mathbf{Z}^{(2)} \right)^{-1}, \\
\left( \mathbf{K}^{(12)} \right)^* &= \left( \mathbf{1} - \left( \mathbf{Z}^{(1)} \right)^* \mathbf{Z}^{(2)} \right)^{-1} \left( \mathbf{Z}^{(1)} \right)^*. \quad (1.177)
\end{aligned}$$

Finally, there is some question about variation with a projected wavefunction. Naively, we might variationally optimize the HFB wavefunction, and then number-project it to find the corresponding AGP wavefunction. But, in this projection after variation (PAV) framework, we find that the AGP state is just the Hartree-Fock state; the HFB state reduces to Hartree-Fock before projection, and Hartree-Fock is an eigenstate of the number operator.

The alternative option is variation after projection (VAP) [276]. For AGP, we vary

$$E_{AGP}[\mathbf{Z}] = \frac{\langle \Psi_{HFB}(\mathbf{Z}) | \hat{P}_N^\dagger H \hat{P}_N | \Psi_{HFB}(\mathbf{Z}) \rangle}{\langle \Psi_{HFB}(\mathbf{Z}) | \hat{P}_N^\dagger \hat{P}_N | \Psi_{HFB}(\mathbf{Z}) \rangle} = \frac{\langle \Psi_{HFB}(\mathbf{Z}) | H \hat{P}_N | \Psi_{HFB}(\mathbf{Z}) \rangle}{\langle \Psi_{HFB}(\mathbf{Z}) | \hat{P}_N | \Psi_{HFB}(\mathbf{Z}) \rangle}. \quad (1.178)$$

In the denominator, we have used the fact that projectors are Hermitian and idempotent. In the numerator, we have additionally used the fact that the Hamiltonian commutes with the number projector because it conserves total electron number. This method results in the true variational AGP state.

## 1.2.4 Semi-empirical molecular orbital theory (chapter 7)

The previous section covered extensions to Hartree-Fock that add new physics at little additional cost. In this section, we move in the other direction; we remove physics from Hartree-Fock in order to significantly reduce its cost.

We explore the class of so-called semi-empirical molecular orbital theories. All of these methods proceed by making cheap approximations to Hartree-Fock with free parameters, and then fitting these parameters to recover accuracy. The first among these methods, CNDO, INDO, and NDDO [262, 263, 264, 261], fit their parameters to Hartree-Fock results. The next generation, including AM1 [78], PM3 [310] and PM6 [311], instead fit to experimental data. Finally, there is a class of methods parameterized for excited states which includes ZINDO [373] and SINDO [228, 161, 162].

In this section, we focus on PM6. PM6 begins with the three Neglect of Diatomic Differential Overlap (NDDO) approximations [262]. To understand the first approximation, we note that the basis functions chosen to represent the wavefunction overlap in general

$$\langle | \hat{c}_\mu \hat{c}_\nu^\dagger | \rangle \equiv S_{\mu\nu} \quad (1.179)$$

where  $\mu$  and  $\nu$  are basis functions and  $\mathbf{S}$  is dubbed the “overlap matrix”. In this general case, equation 1.29 becomes

$$\mathbf{FC} = \mathbf{SC}\epsilon. \quad (1.180)$$

Solving this self-consistency equation is more expensive. NDDO approximates it away by setting

$$\mathbf{S} \approx \mathbf{1} \quad (1.181)$$

for purposes of the self-consistency equation. For standard atomic orbital basis sets, this is equivalent to saying that basis functions on different atoms do not overlap. (Basis functions on the same atom are already mutually orthogonal.)

Second, NDDO approximates the one-electron integrals between different atoms by

$$h_{\mu\nu} = \beta_{\mu\nu}^{(AB)} S_{\mu\nu} \quad (1.182)$$

where  $A$  and  $B$  are the atoms on which basis functions  $\mu$  and  $\nu$  are centered, and  $\beta_{\mu\nu}$  is a parameter.  $S_{\mu\nu}$  is the actual overlap of basis functions  $\mu$  and  $\nu$  (equation 1.179); the approximation that the basis is orthogonal (equation 1.181) only applies to the self-consistency equation. In PM6,  $\beta_{AB}$  is further approximated as additive

$$\beta_{\mu\nu}^{(AB)} \approx \frac{\beta_{\mu}^{(A)} + \beta_{\nu}^{(B)}}{2}. \quad (1.183)$$

In this expression,  $\mu$  and  $\nu$  index only whether the basis function is s- or p-type (i.e. each atom  $A$  has two parameters:  $\beta_s^{(A)}$  and  $\beta_p^{(A)}$ ).

The one electron integrals involving only a single basis function are parameterized. For basis function  $\mu$  on atom  $A$ ,

$$h_{\mu\mu} = U_{\mu}^{(A)} + \sum_{B \neq A}^M V_{\mu}^{(B)}. \quad (1.184)$$

Again, there are two  $U_{\mu}$  per atom type:  $U_s$  and  $U_p$ . The second term is the potential energy experienced by an electron in orbital  $\mu$  on atom  $A$  due to all of the other nuclei in the system  $B$ . This term is not a parameter, but is instead calculated at run-time.

Until this point, the basis functions did not need to actually exist because all integrals involving them were replaced by parameters. However,  $\mathbf{S}$  and  $\mathbf{V}$  (in equations 1.182 and 1.184) require that the basis actually have orbitals. The basis is composed of Slater-type orbitals [300] of the form

$$\phi_{\mu}^{(A)}(r, \theta, \gamma) = N r^{n-1} \exp[-\zeta_{\mu}^{(A)} r] Y_l^m(\theta, \gamma) \quad (1.185)$$

where  $A$  is the atom on which  $\phi$  is centered,  $\mu$  can take values of  $s$  and  $p$ ,  $N$  is the normalization constant,  $n$ ,  $l$ , and  $m$  are principle quantum numbers,  $Y$  is the spherical harmonic, and  $\zeta_{\mu}^{(A)}$  is, of course, a parameter.

Third, NDDO throws away all two electron integrals that involve basis functions on more than two atoms. In PM6, main row elements are represented by a minimal set of three basis functions, named  $s$ ,  $p$ ,  $p'$ , where the first is s-type and the latter two are p-type [78]. Two-electron integrals involving basis functions that are all on the same atom are replaced by five parameters. Each of these parameters corresponds to a one-center two-electron integral,

$$\begin{aligned}
G_{ss}^{(A)} &\approx V_{ssss} \\
G_{sp}^{(A)} &\approx V_{sspp} \\
G_{pp}^{(A)} &\approx V_{pppp} \\
G_{p^2}^{(A)} &\approx V_{ppp'p'} \\
H_{sp}^{(A)} &\approx V_{spsp}.
\end{aligned}
\tag{1.186}$$

Each atom type  $A$  present in the system has its own values for these five parameters. Two-center two electron integrals between atoms  $A$  and  $B$  by a combination of the appropriate  $G$  parameters and the interatomic distance  $R_{AB}$ . These formulae, derived from a multipole approximation, are presented in reference [77].

Finally, PM6 introduces a force-field-like core-core repulsion between each pair of atoms [311]

$$E_n(R_{AB}, A, B) = Z^{(A)} Z^{(B)} V_{s^{(A)}s^{(A)}s^{(B)}s^{(B)}} \left( 1 + x^{(AB)} \exp \left[ -\alpha^{(AB)} (R_{AB} + 0.0003R_{AB}^6) \right] \right).
\tag{1.187}$$

$Z^{(A)}$  and  $Z^{(B)}$  are the numbers of *valence* electrons on atoms  $A$  and  $B$ .  $x^{(AB)}$  and  $\alpha^{(AB)}$  are diatomic parameters for each unique pair of atoms. The last term in the exponential is a small dispersion correction.

PM6 also adds d-type functions on some atoms. Myriad other approximations are added for special cases where PM6 would otherwise perform poorly. They are detailed in reference [311].

### 1.3 Structure of this thesis

As with this chapter, the remainder of this thesis partitions into two broad categories: application of existing methods to experimental systems and efforts toward development of new methods. The former is covered in Chapter 2. The latter spans Chapters 3 through 7.

At the end of the day, the purpose of any theory is to explain and predict natural phenomena. Chapter 2 presents three applications of standard computational methods from Section 1.1 to help explain novel experimental results. We begin in Section 2.1 examining a protein labelling reaction. We employ classical molecular dynamics to study the structural landscape of a short peptide, and then examine reactions of this peptide with a fluoroaromatic ligand using density functional theory. In Section 2.2, we explore electronic process in organic semiconductors. Specifically, we look at exciplex-based organic light-emitting diodes in Section 2.2.1 and a crystalline organic photovoltaic cell in Section 2.2.2. We finish in Section 2.3 by discussing similar experimental systems that

are challenging for standard methods, motivating future method development in the following five chapters.

We then shift our focus to methods development. In Section 2.2.2, we will consider a completely ordered organic-organic interface. Central to our model will be a single lattice Hamiltonian whose eigenstates and energies completely describe the experiment. However, this ordered interface is rare: the vast majority of organic molecular solids and organic-organic heterojunctions are disordered. In such a case, we require a Hamiltonian for each sample of the disordered system’s configurations. Then, this collection of Hamiltonians would together model the disordered system of interest. To distill this information, such a collection can be viewed as a set of samples of a matrix with random elements. The mathematical field of Random Matrix Theory (RMT) concerns itself with such matrices. In Chapters 3 and 4, we employ a tool from RMT, free probability, to understand simple random matrix models of disordered materials, focusing on the Anderson model [10].

In Chapter 3, we explore application of RMT to the one-dimensional Anderson model. Theoretical studies of localization, anomalous diffusion and ergodicity breaking require solving the electronic structure of disordered systems. We use free probability to approximate the ensemble-averaged density of states without exact diagonalization. We present an error analysis that quantifies the accuracy using a generalized moment expansion, allowing us to distinguish between different approximations. We identify an approximation that is accurate to the eighth moment across all noise strengths, and contrast this with the perturbation theory and isotropic entanglement theory.

In Chapter 4, we investigate how free probability allows us to approximate the density of states in tight binding models of disordered electronic systems. Extending our previous studies of the Anderson model in one dimension with nearest-neighbor interactions (Chapter 3 and Reference [54]), we find that free probability continues to provide accurate approximations for systems with constant interactions on two- and three-dimensional lattices or with next-nearest-neighbor interactions, with the results being visually indistinguishable from the numerically exact solution. For systems with disordered interactions, we observe a small but visible degradation of the approximation. To explain this behavior of the free approximation, we develop and apply an asymptotic error analysis scheme to show that the approximation is accurate to the eighth moment in the density of states for systems with constant interactions, but is only accurate to sixth order for systems with disordered interactions. The error analysis also allows us to calculate asymptotic corrections to the density of states, allowing for systematically improvable approximations as well as insight into the sources of error without requiring a direct comparison to an exact solution.

Random Matrix Theory provides tools to study the electronic structure of systems where global properties of the entire system are important. Often in chemistry, only a small subset of a system is directly of interest. For example, active sites of enzymes are of great interest for understanding catalysis, but the remainder of the protein is only important inasmuch as it supports the active site.

When simulating such a system, we would prefer to only perform expensive electronic structure calculations on the subsystem of interest. Embedding theories promise this: they partition the system into a fragment of interest, which is treated at a high level, and a remaining “bath”, which is treated at a low level. Furthermore, a sufficiently accurate and internally-consistent embedding theory can be used in a fragment embedding paradigm. Taking a divide-and-conquer approach, the whole system is completely partitioned into a set of fragments (with associated baths), high level calculations are performed on each fragment, and the final wavefunction is stitched together from its constituent fragments. In Chapters 5 and 6, we develop embedding methods. First, we build on a previously existing theory: Density Matrix Embedding Theory [175, 176]. Second, we exploit properties of fragment embedding to develop improved internal-consistency conditions.

In Chapter 5, we examine and expand upon one such embedding theory. Density matrix embedding theory (DMET) has emerged as a powerful tool for performing wave function-in-wave function embedding for strongly correlated systems. In traditional DMET, an accurate calculation is performed on a small impurity embedded in a mean field bath. Here, we extend the original DMET equations to account for correlation in the bath via an antisymmetrized geminal power (AGP) wave function. The resulting formalism has a number of advantages. First, it allows one to properly treat the *weak* correlation limit of independent pairs, which DMET is unable to do with a mean-field bath. Second, it associates a *size extensive* correlation energy with a given density matrix (for the models tested), which AGP by itself is incapable of providing. Third, it provides a reasonable description of charge redistribution in strongly correlated but non-periodic systems. Thus, AGP-DMET appears to be a good starting point for describing electron correlation in molecules, which are aperiodic and possess both strong and weak electron correlation.

Strong correlation poses a difficult problem for electronic structure theory, with computational cost scaling quickly with system size. Fragment embedding is an attractive approach to this problem. By dividing a large complicated system into smaller manageable fragments "embedded" in an approximate description of the rest of the system, we can hope to ameliorate the steep cost of correlated calculations. While appealing, these methods often converge slowly with fragment size because of small errors at the boundary between fragment and bath. In Chapter, 6, we describe a new electronic embedding method, dubbed "Bootstrap Embedding," a self-consistent wavefunction-in-wavefunction embedding theory that uses overlapping fragments to improve the description of fragment edges. We apply this method to the one dimensional Hubbard model and a translationally-asymmetric variant, and find that it performs very well for energies and populations. We find Bootstrap Embedding converges rapidly with embedded fragment size, overcoming the surface-area-to-volume-ratio error typical of many embedding methods. We anticipate that this method may find lead to a low-scaling, high accuracy treatment of electron correlation in large molecular systems.

Chapters 3 through 6 consider relatively homogenous systems. Chapter 7 by contrast considers

a common situation in chemistry: solvation. As with Chapters 3 and 4, a solution is a disordered system; the liquid solvent adopts many configurations and each influences the solute in a different way. To model this disorder, we explicitly sample solvent configurations. This necessitates computationally inexpensive methods for treating large numbers of solvent molecules. It also calls back to the embedding of Chapters 5 and 6. The solvent is a bath for the solute; as before, we care about the details of the solute and would prefer to treat the solvent as cheaply as possible. These considerations usually lead to treatment of the solvent at the molecular mechanics level. In Chapter 7, we develop a hybrid electronic structure/molecular mechanics method for liquid water, the so-called “universal solvent”.

Water is an extremely important liquid for chemistry and the search for more accurate force fields for liquid water continues unabated. Neglect of diatomic differential overlap (NDDO) molecular orbital methods provide an intriguing generalization of classical force fields in this regard because they can account both for bond breaking and electronic polarization of molecules. However, we show that most standard NDDO methods fail for water because they give an incorrect description of hydrogen bonding, water’s key structural feature. Using force matching, we design a reparameterized NDDO model and find that it qualitatively reproduces the experimental radial distribution function of water, as well as various monomer, dimer, and bulk properties that PM6 does not. This suggests that the apparent limitations of NDDO models are primarily due to poor parameterization and not to the NDDO approximations themselves. Finally, we identify the physical parameters that most influence the condensed phase properties. These results help to elucidate the chemistry that a semiempirical molecular orbital picture of water must capture. We conclude that properly parameterized NDDO models could be useful for simulations that require electronically detailed explicit solvent, including the calculation of redox potentials and simulation of charge transfer and photochemistry.

In Chapter 8, we propose some future directions for the work presented in this thesis.



## Chapter 2

# Some applications to experiment

At the end of the day, the purpose of any theory is to explain and predict natural phenomena. This chapter presents three applications of standard computational methods from section 1.1 to help explain novel experimental results. We begin in section 2.1 examining a protein labelling reaction. We employ classical molecular dynamics to study the structural landscape of a short peptide. We then examine reactions of this peptide with a fluoroaromatic ligand using density functional theory. In section 2.2, we explore electronic process in organic semiconductors. Specifically, we look at exciplex-based organic light-emitting diodes in subsection 2.2.1 and a crystalline organic photovoltaic cell in subsection 2.2.2. We finish in section 2.3 by discussing similar experimental systems that pose a challenge for standard methods, motivating future method development in the following five chapters.

### 2.1 $\pi$ -clamp mediated site-specific cysteine conjugation

Recent experimental results [374] reveal an exciting chemistry that allows for site-specific modifications of proteins. Surrounded by a particular four amino acid sequence (FCPF), cysteine can be selectively arylated. In this section, we employ standard computational tools to understand this selectivity. First, we explore the configurational space of an experimentally-proven ten amino acid peptide containing the FCPF sequence using molecular dynamics. Taking relevant structures from this simulation, we compute — as proxies for the reaction rate — reaction energies and barriers for the arylation reaction using non-local density functional theory. In its most reactive form, the FCPF block of the peptide adopts a “ $\pi$ -clamp” geometry in which the phenylalanine rings surround and activate the cysteine sulfur for nucleophilic aromatic substitution. In the transition state and product, these phenylalanines also stack with the fluoroaromatic ligand, stabilizing it. We compare to a non-reactive control peptide (GCPG) and find that FCPF has a 5 kcal/mol lower reaction energy and a 3 kcal/mol lower reaction barrier, in agreement with experimental results.

Further experimental studies sought to accelerate the arylation reaction by mutating the phenylalanine residues to non-natural amino acids and by adding salts to the reaction mixture. To reduce computational and conceptual complexity, we employ a simple model of the chemistry. At the density functional theory level, we examine binding of the ligand to the side chains of the various mutant amino acids tested in experiment. We model added salts by directly incorporating an ion into the binding complex. We then construct linear free energy relations to correlate these binding events with experimental rates and find good agreement across many classes of side chains. These results show that dispersive interactions are predictive of rate, and that  $\pi$ - $\pi$  stacking is not required, as was previously thought.

### 2.1.1 Introduction

Site-selective functionalization of proteins [48, 123, 267, 305] is important for studying protein structure and function [334], as well as an approach to drug delivery [315]. Previous methods fall into two main categories. In orthogonal chemistries [301, 6], a protein is prepared with only a single reactive residue for a specific ligand. All other residues must be unreactive with this ligand. In catalyst recognition [194, 56, 302, 251, 358, 253], a specific catalyst must recognize the desired reactive site. Both of the methods impose constraints on which proteins can be selectively conjugated.

In nature, proteins adopt conformations that promote specific reactivity at an active residue while suppressing reactivity at similar residues in other parts of the protein. Inspired by this, work was carried out to identify amino acid sequences that would selectively bind a particular ligand at a specific cysteine residue, leaving other cysteines unchanged [374]. It was found (Figure 2-1) that the peptide sequence FCPF (**1E**) (phenylalanine, cysteine, proline, phenylalanine) was uniquely reactive with a fluoroaromatic ligand (**2**) under standard biological conditions. Follow-up point-mutation studies on each of the three amino acid residues surrounding the cysteine of interest (Figure 2-2) demonstrated that this specific sequence is necessary for the reaction to complete. Based on simple molecular models of the FCPF sequence, it was hypothesized that the phenylalanine side chains form a “ $\pi$ -clamp” around the cysteine sulfur. This clamp was proposed to serve a dual purpose: first, to activate the sulfur for nucleophilic aromatic substitution; second, to stabilize the transition state and product of the arylation reaction by  $\pi$ - $\pi$  stacking with the fluoroaromatic ligand.

In order to understand the structure and reactivity of the  $\pi$ -clamp system, we employ a combined molecular dynamics (MD) and electronic structure approach. First, MD is used to test whether the reactive  $\pi$ -clamp complex forms under ambient conditions, as well as to generate candidate reactant structures. These structures are then examined using density functional theory in order to calculate both binding energies and reaction barriers for the addition of the fluoroaromatic ligand to the cysteine residue.

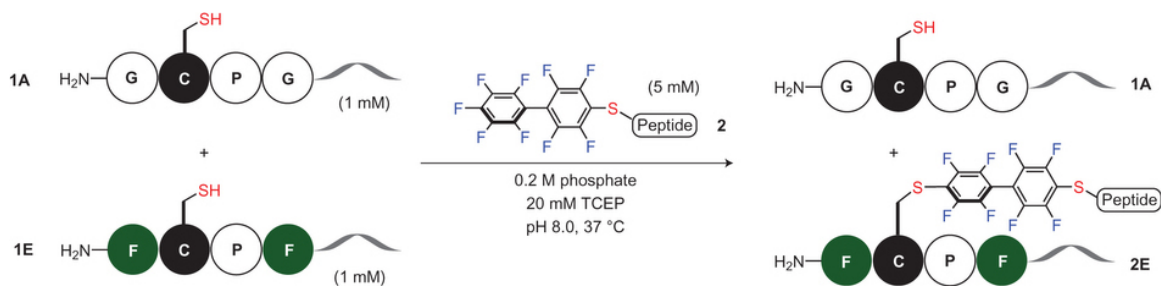


Figure 2-1: Site-specific conjugation at the  $\pi$ -clamp in the presence of another competing cysteine peptide.  $\pi$ -Clamp peptide **1E** was fully converted to the arylated product **2E** while a competing cysteine peptide **1A** remained unmodified. (Reproduced with permission from reference [374].)

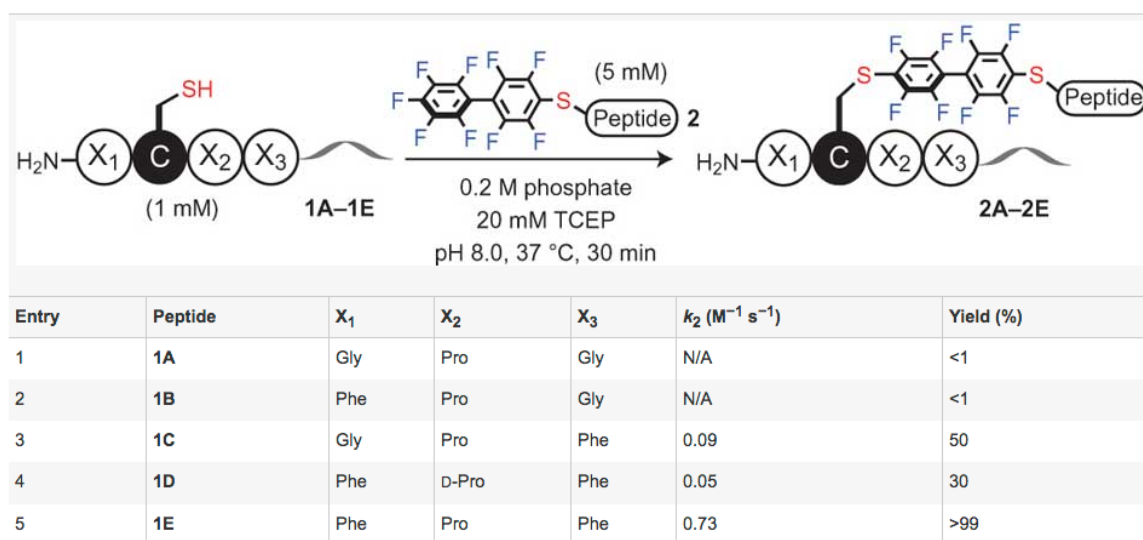


Figure 2-2: Mutation studies show that Phe-1, Pro-3 and Phe-4 are required for the observed reactivity. (Reproduced with permission from reference [374].)

### 2.1.2 Molecular dynamics calculations of peptide structure

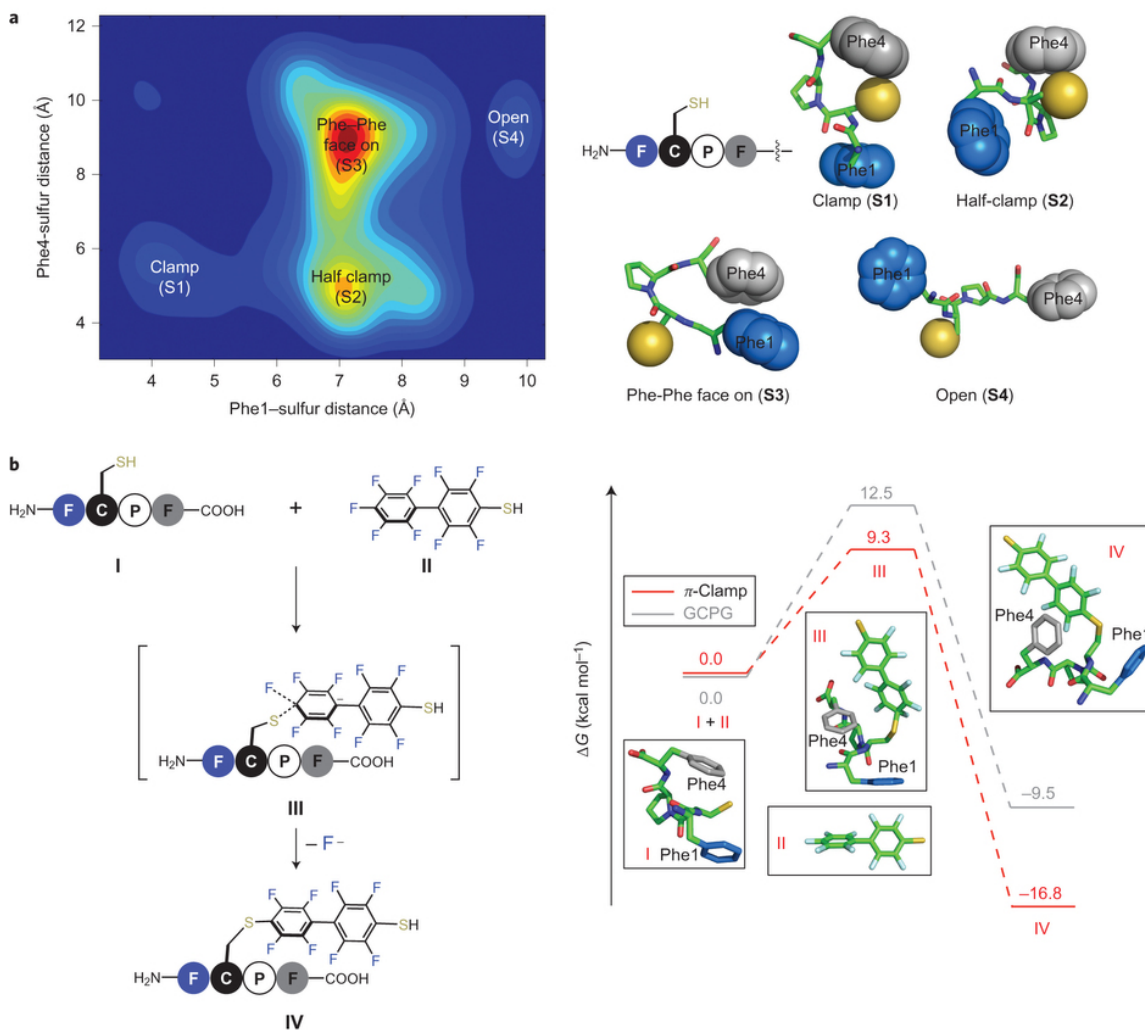
We perform molecular dynamics calculations on a model ten amino acid peptide originally found to be reactive in experiment, FCPFGLLKNK (Figure 2-2 **1E**) with proline in its *cis* conformation. These calculations first establish that the reactive  $\pi$ -clamp complex forms thermodynamically, and then are used to generate candidate structures for study with density functional theory (DFT). In addition, we simulate GCPGGLLKNK (Figure 2-2 **1A**) as an unreactive control.

Calculations were performed using the GROMACS 4.6.5 [139] molecular dynamics package. The peptide was described by the AMBER 2003 [84] force field. This force field was chosen because it best reproduced the Ramachandran plot of *cis*-proline, a key structural feature in the  $\pi$ -clamp sequence, when compared to CHARMM 2.7 [42], OPLS-AA [159, 167], and GROMOS96 45A3 [286]. In addition, it has been shown to be accurate for dispersive interactions between phenylalanine and sulfur [142, 180], the main interaction in the  $\pi$ -clamp. The peptide was solvated in 3382 explicit TIP3P [202] waters. Periodic boundary conditions were employed in a  $(4.3\text{nm})^3$  simulation box. Simulations were performed in the NVT ensemble with temperature set to 300K and enforced by the Nose-Hoover thermostat [238, 145]. Simulations were run for 500 ns with a time step of 2 fs. The linear peptide ( $\phi = \psi = 180^\circ$ ) was used as the initial configuration and equilibrated for a burn-in period of 50 ns. For purposes of Figure 2-3, configurations were sampled at 10 ps intervals.

We choose PHE1-CYS2 and PHE4-CYS2 distances as order parameters. Specifically, we measure the distance between the center of each PHE ring and the CYS sulfur atom. We choose these specific order parameters because we expect the interaction of the PHE rings with the CYS sulfur to directly mediate the reaction. The peptide adopts four primary forms under ambient conditions (Figure 2-3): a  $\pi$ -clamp structure with the PHE1 and PHE4 aromatic rings interacting face-on (**S1**) with the CYS2 sulfur; a “half-clamp” structure where only the PHE4 ring interacts with said sulfur (**S2**); a structure in which the PHE1 and PHE4 rings stack, leaving the CYS2 sulfur exposed to solution (**S3**); and an open configuration where all three of these groups are too far apart to interact (**S4**). MD simulation for FCPF... peptide (**1E**) with a *trans*-proline indicated two “open” structures with the cysteine thiol not interacting with a PHE residue and one structure with only the PHE4 side chain interacting with the CYS2 thiol.

### 2.1.3 Density functional calculations on the arylation reaction

With these MD structures in hand, we use density functional theory (DFT) to investigate the nucleophilic aromatic substitution pathway for structures with a *cis*-proline. First, we compute the reaction energy (*BE*) with the peptide in each of the four aforementioned conformations. All DFT computations were carried out using the Q-Chem 4.1 [291] software package. To reduce the computational cost, we truncated the peptide sequence to the four active amino acids in the  $\pi$ -



clamp: FCPF. The binding energy ( $BE$ ) was calculated as:  $BE = E_{Product} + E_{HF} - E_{Peptide} - E_{Perfluoroaromatic}$ . We extracted snapshots from MD simulations for different starting structures of peptides in DFT calculations. For the product’s starting structure, we manually added the ligand to the peptide.

In each case, four gas-phase geometry optimizations were performed on structures sampled from the MD trajectory, using the B3LYP exchange-correlation functional [23] in the 6-31G\* basis set [131]. To account for  $\pi$ - $\pi$  interactions, we also include Grimme’s DFT-D3 empirical dispersion correction [119] for the optimization. Once a potential energy minimum was located, we refined the energy by performing a single point energy calculation with the more accurate combination of the rPW86 exchange functional [225], the PBE local correlation functional [256], and the VV10 non-local correlation functional [344] to accurately handle the long-range dispersions critical to the  $\pi$ - $\pi$  interaction. For these calculations, we also employed the larger 6-31G\*\* basis set [185] and a large non-local integration grid (Lebedev 75,302 [191]). We then calculated the binding energies in both the gas phase and in water. We approximate the latter by the polarizable continuum model (PCM) [67]. We used 302 PCM grid points and a dielectric of 78.39 (corresponding to that of water).

The binding energy results are shown in Table 2.1. We found that the half-clamp structure (**S2**) stabilized the arylation product by  $\sim 5$  kcal/mol compared to the double glycine mutant, indicating the important role of PHE4 in promoting the arylation reaction. This is consistent with mutation studies showing that PHE4 alone can partially mediate the arylation reaction (Figure 2-2, table row 3). The product generated from the open structure (**S4**) has a similar free energy to that of the double glycine mutant, further substantiating the hypothesis that the two phenylalanine side chains are important for the arylation reaction with perfluoroaryl groups. The most stable product was observed with the  $\pi$ -clamp structure (**S1**), for which the free energy was  $\sim 7$  kcal/mol lower than that of the double glycine mutant. The energy and structure of this product are shown in Figure 2-3b.

We next compute reaction barriers for GCPG and clamp-structure FCPF. Transition state searches were performed at the B3LYP/DFT-D3/6-31G\* level of theory, using a Hessian eigenvector following method [17]. Following the TS search, we carried out a vibration frequency calculation at the same level of theory to confirm the structure was a first-order saddle point. All single point calculations were performed using the long-range corrected version (LC-VV10) of the method we used previously for binding energy single-point calculations in both gas phase and PCM water.

The reaction barrier results are shown in Table 2.2. The activation energy for the formation of the transition state (**III** in Figure 2-3b) was decreased by  $\sim 3$  kcal/mol when the  $\pi$ -clamp (**S1**) was present compared to the GCPG mutant, presumably because of the phenyl rings recognizing the perfluoroaryl group and activating the cysteine sulfur before conjugation. Collectively, these DFT calculations indicated that the  $\pi$ -clamp offers both a kinetic advantage (lower activation energy)

Final Configuration	Gas Phase Energy (kcal/mol)	PCM Energy (kcal/mol)
Clamp	-12.97	-15.22
Clamp	-12.60	-15.61
Clamp	-17.22	-19.61
Clamp	-13.20	-16.62
Average	-14.00	-16.76
Half-Clamp 1	-11.89	-14.57
Half-Clamp 1	-11.80	-14.81
Half-Clamp 1	-11.32	-15.80
Average	-11.67	-15.06
Half-Clamp 2	-9.41	-11.01
Half-Clamp 2	-12.27	-13.43
Half-Clamp 2	-11.06	-13.03
Average	-10.91	-12.49
Open	-7.16	-9.36
Open	-5.69	-9.78
Average	-6.43	-9.57
GCPG	-6.83	-9.48

Table 2.1: Reaction energies for cysteine arylation in gas phase and in PCM implicit solvent. All rows correspond to the FCPF system except for the last row which corresponds to GCPG.

Peptide	Gas Phase Barrier (kcal/mol)	PCM Barrier (kcal/mol)
FCPF	0.56	9.29
GCPG	5.84	12.50
Difference	5.28	3.21

Table 2.2: Reaction barrier heights for FCPF and GCPG arylation in gas phase and PCM implicit solvent.

and a thermodynamic advantage (lower free energy) over the double glycine mutant for selective reaction with the perfluoroaryl reagent.

### 2.1.4 Accelerating the reaction

In the previous section, we examined a single  $\pi$ -clamp peptide in great detail and found it to be reactive. Its rate of arylation reaction, however, is too slow for biological application. Searching for a more reactive peptide, mutations studies were carried out in which the PHE residues at the 1 and 4 positions were replaced with a series of non-natural — but readily available — amino acids. Results of this study are shown in Figure 2-4, where it can be seen that certain substitutions can lead to a hundredfold increase in rate. Additionally, the reaction rate is dramatically altered by the addition of certain salts. In the remainder of this section, we develop a computational model to explain the observed trends in reactivity.

Previously, we took a detailed and painstaking approach to understanding the reactivity of the

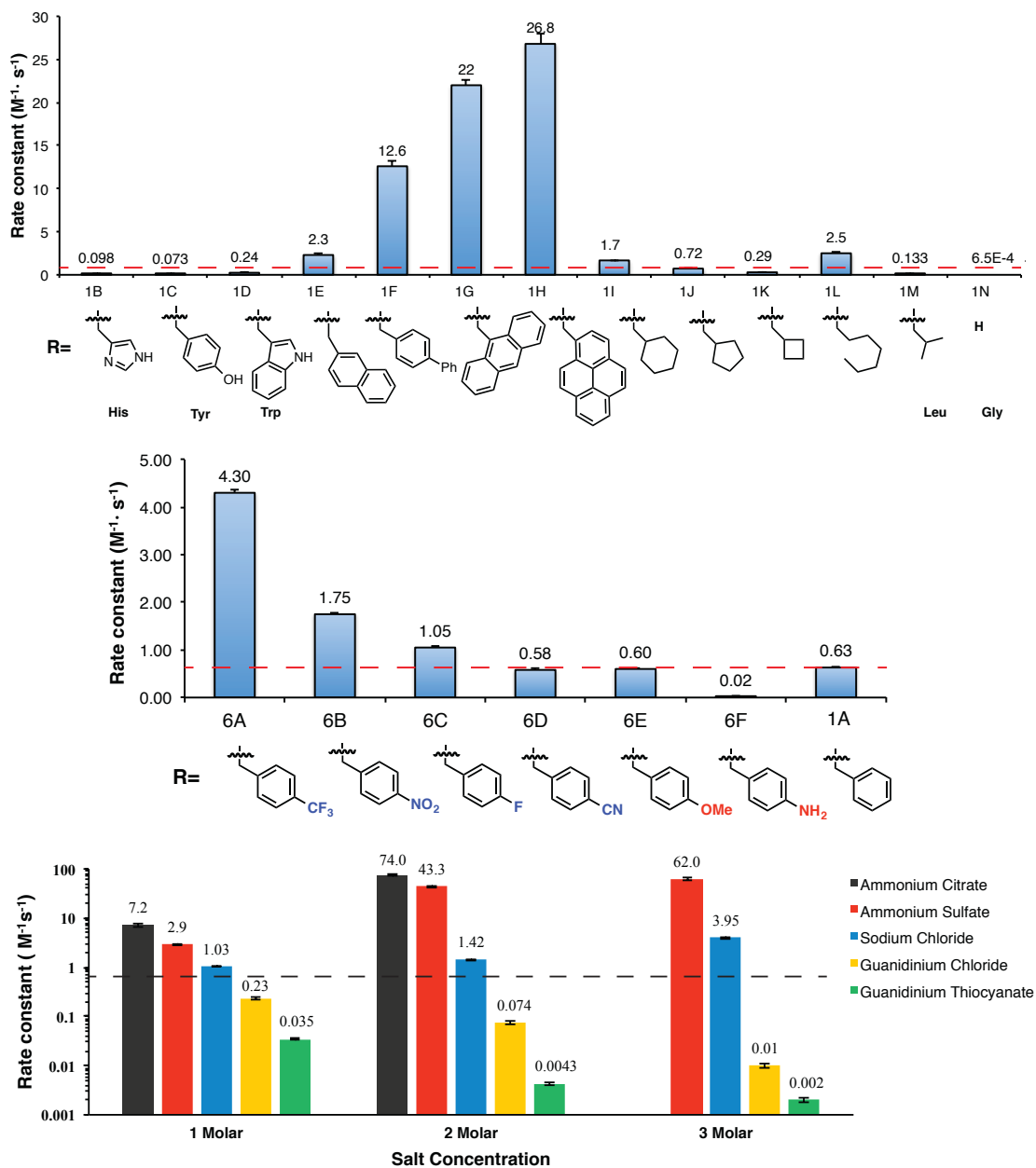


Figure 2-4: Top: Arylation reaction rates for a panoply of mutations. The PHE residues at the 1 and 4 positions on the peptide were replaced with residues whose side chains are shown on the x-axis. The red dotted line represents the reaction rate of FCPF (here labelled “PHE”). Bottom: arylation reaction rates of the standard FCPF peptide in various added concentrations of various salts. The black dotted line represents the reaction rate of the peptide in just the standard 200mM phosphate buffer. Note the logarithmic y-scale. (Reproduced with permission from [72]).

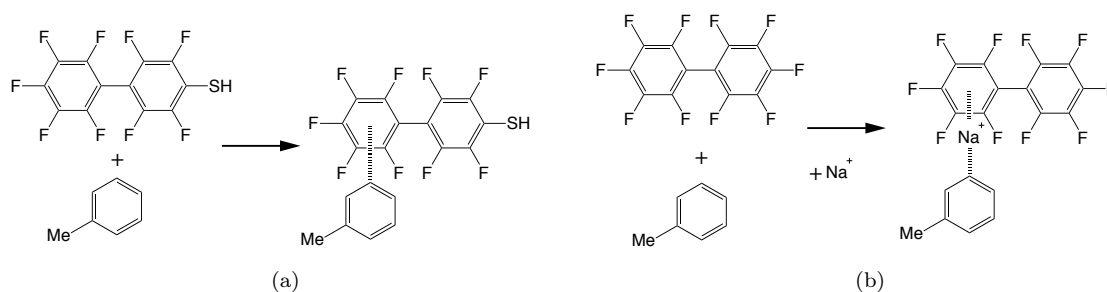


Figure 2-5: A schematic for binding energy models used for (a) phenylalanine clamp-like binding and (b) the same binding in the presence of salt. In each case, the  $\Delta G$  of the reaction scheme was calculated. In (b), the thiol group was omitted due to geometric distortions from strong sulfur-ion effects which are not present in the full protein system.

$\pi$ -clamp system. We employed detailed density functional calculations on the entire reactive site of the peptide to simulate the reactants, products, and transition state in great detail. However, this type of calculation is prohibitively expensive to apply to all of the mutants in Figure 2-4.

Instead, we build a reduced model of the reaction that abstracts away all but the most relevant details of the reaction. Our hypothesis is that the binding interactions between the perfluoroaryl ligand and the side chain of the amino acids at the 1 and 4 positions are responsible for the change in rate seen when the phenylalanine moieties are substituted with other motifs, or when the salt solution is changed. That is to say that when the phenylalanine group is positively modified, the binding of the clamp becomes stronger, leading to an increase in the rate of reaction. The model which we employ is therefore based on binding events, designed to measure to changes in the strength of the clamp interaction across substitutions. We compute the free energy ( $\Delta G$ ) of association between an abstracted version of the perfluoroaryl probe and the phenylalanine or its substituent (Figure 2-5a). To capture salt effects, we use explicit salt ions to mediate the binding interaction (Figure 2-5b). Similar models have seen great success elsewhere in the literature [103].

As in the previous section, energies were determined by high-level density functional theory calculations which account for van der Waals effects using the QCHEM 4.3 software package [290]. An initial coarse geometry optimization was performed with the B3LYP functional [23] using Grimme’s D1 corrections [119] in a 6-311+g\* basis set [58, 185]. Then a final optimization was performed using the VV10 [344] (rpw86/PBE) functional [256] in a 6-311+g\* basis with a B term of 5.9, a C term of 0.0093 and an SG1 non-local grid [109]. A Lebedev (75, 302) [191] exchange-correlation grid was used. Again, the conducting polarizable continuum model (with a dielectric of 78.4) was used to implicitly model the effects of solvation in water [329]. We also included zero-point energy and vibrational entropy within the harmonic approximation. A variety of initial structures were used to ensure an appropriate sampling of the free energy landscape, all of which would be compatible with the situation in vivo (where bulky proteins are attached).

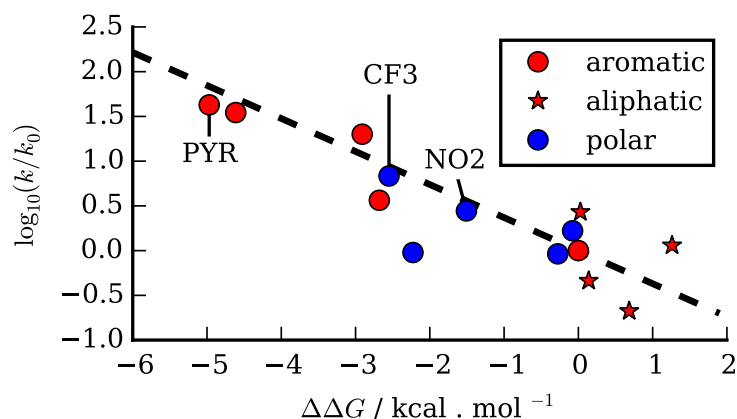


Figure 2-6: Linear free energy relationship between rate and ligand-side-chain binding energy across side chain mutations. The rate ( $k_i$ ) is determined experimentally, and the energy ( $\Delta\Delta G$ ) is computed as  $\Delta G_i - \Delta G_0$  from a binding model. The terms  $k_0$  and  $\Delta G_0$  are referenced to phenylalanine. Highlighted moieties are discussed in the text. Full data are given in Table 2.3.

Despite the apparent simplicity of this model, the change in the dimerization free energy under phenylalanine mutation was well-correlated to the rate for both aliphatic and aromatic synthetic amino acids substitutions (Figure 2-6). This is consistent with our hypothesis that stronger binding gives rise to improved rate across this series. We find that the strength of binding from van der Waals forces and induction is strongly related to the size of the binding groups i.e. the number of carbon atoms in the chain or ring systems. These intermolecular interactions form one part of a description for changing hydrophobicity near the reaction center. However, we have not attempted to explicitly model hydrophobicity (or other protein effects) because we find our approach sufficient to find a linear behavior which we believe would have appropriate predictive accuracy.

In order to understand how the binding energy can be so well correlated to the overall reaction rate, we will take a short detour and describe Linear Free Energy Relationships (LFERs). LFERs are commonly employed in organic chemistry and chemical biology in an attempt to gain mechanistic understanding of a reaction [47]. In particular, they are a means by which thermodynamic quantities, namely free energy changes between stable reaction intermediates, can be used to understand and rationalize trends in kinetic data. When looking at rate changes across a series of homologous structures, it is typical to seek a common chemistry. LFERs allow the kinetic trends to be explained in terms of thermochemical values.

For a set of rate constants  $k$ , the most commonly used relationship is

$$\begin{aligned} \ln\left(\frac{k}{k_0}\right) &= \alpha \ln\left(\frac{K}{K_0}\right) + \beta, \\ &= \alpha(\Delta G - \Delta G_0) + \beta, \end{aligned} \tag{2.1}$$

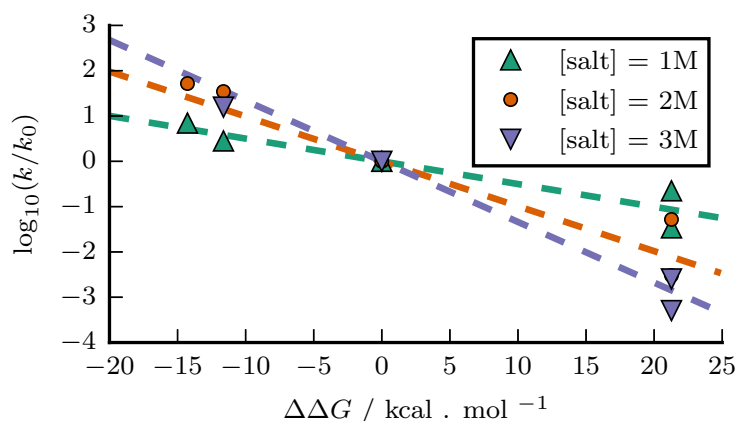


Figure 2-7: The salt effect linear free energy relationship. As before, the rate ( $k_i$ ) is determined experimentally, and the energy ( $\Delta\Delta G$ ) is computed as  $\Delta G_i - \Delta G_0$  from a binding model. The terms  $k_0$  and  $\Delta G_0$  are referenced to NaCl. Data are given in Table 2.4.

where parameters  $\alpha$  and  $\beta$  are found by regression [128]. Here, the thermodynamic quantities  $K$  and  $\Delta G$  respectively are equilibrium constants and free energies of a model or abstracted reaction which represent the essential chemistry contained in the kinetic series of interest. The correlate is commonly thought of as an important component of the physical basis for the mechanism as a whole, but this is not necessary for the utility of linear free energy relationships.

A significant finding of our LFER is that the trend seems consistent as the chemical nature of the substitution is changed. Referring again to Figure 2-6, we can compare the aromatic and electronic series. In the aromatic series the dominant change is the size of the aromatic system, with the largest array of rings (labelled PYR) being the most binding. However, when the mutation is electronic in nature, such as a para-substitution with  $\text{CF}_3$  and  $\text{NO}_2$  (labelled  $\text{CF}_3$  and  $\text{NO}_2$ ), these also lie on the trend line. Since our solvent model does not account for hydrogen bonds, the moieties which have strong hydrogen bonding with water do not lie on the LFER constructed here.

Building on the success of our model for phenylalanine substitution, we turn our attention to the salt effect. Figure 2-7 shows the linear free energy relationship we find here. We note that other studies have found that free energies of binding are correlated with free energies of solution [103], which are consistent with our data showing that it is possible for a binding energy to form a sufficient physical picture of this rate enhancement.

The number of salts used here is not sufficient to probe an ion pair effect [103, 64]. Instead, we simply deal with the complication arising from the presence of a cation and an anion in the salt by selecting the strongest bound ion as the one that is dominantly affecting the rate; we are therefore unable to explain changes in counter ions alone for the pair of guanidinium salts.

Our physical interpretation of the energetic study is that clamp-like binding is being enhanced

Residue	$\log(k/k_0)$	$\Delta\Delta G/$ kcal.mol <sup>-1</sup>
PYR ( <b>1H</b> )	-4.9703	1.6288
ANTH ( <b>1G</b> )	-4.6132	1.5431
BIP ( <b>1F</b> )	-2.9103	1.3010
CF3 ( <b>6A</b> )	-2.5496	0.8341
NAL ( <b>1E</b> )	-2.6797	0.5624
NO2 ( <b>6B</b> )	-1.5072	0.4437
CHA ( <b>1I</b> )	0.0268	0.4311
F ( <b>6C</b> )	-0.0778	0.2218
CPA ( <b>1J</b> )	1.2611	0.0580
PHE ( <b>1A</b> )	0.0000	0.0000
OME ( <b>6E</b> )	-2.2267	-0.0212
CN ( <b>6D</b> )	-0.2773	-0.0359
CBA ( <b>1K</b> )	0.1388	-0.3369
TRP* ( <b>1D</b> )	-1.9135	-0.4191
LEU ( <b>1M</b> )	0.6841	-0.6755
HIS* ( <b>1B</b> )	-0.0910	-0.8081
TYR* ( <b>1C</b> )	-0.2466	-0.9360
NH2* ( <b>6F</b> )	-1.7887	-1.4983

Table 2.3: Thermodynamic data for 2-6. \*= over-bound outliers due to neglect of H bond effects. Residue names refer to CHARMM/SwissSidechain [108] naming. Parenthetical bolded names refer to Figure 2-4.

Salt	$\Delta\Delta G/$ kcal.mol <sup>-1</sup>
Citrate*	-67.97
Cl	-25.58
Guanidinium	-32.42
Na*	-53.69
SCN	-27.80
SO <sub>4</sub> *	-65.32

Table 2.4: Thermodynamic data for 2-7. \*= strongest bound ion.

both by substitution of the phenylalanine and by the presence of Hofmeister salts. The binding affects the transition state, and it is stabilized relative to the reactants. The idea of the transition state being structurally more clamp-like than the reactants follows from the Hammond postulate, which makes it a late transition state. However, it is also possible that the binding happens as a pre-equilibrium, and we are not able to infer which of these is most likely. In either viewpoint, the upshot is that the energy of the transition state is lowered relative to the reactants by binding interactions leading to the rate enhancements seen here.

### 2.1.5 Conclusions

Site-specific protein conjugation is a useful tool in molecular biology. Previous work demonstrated a novel  $\pi$ -clamp architecture that allowed for reaction with a specific cysteine embedded in the amino acid sequence FCPF. We employed MD calculations to find candidate structures for the FCPF

peptide folding. We then studied the reaction energies of these structures with DFT and found the “ $\pi$ -clamp” confirmation to be most strongly binding. Further, the “open” configuration exhibited the same reaction energy as the glycine double mutant control peptide, supporting the importance of the  $\pi$ -clamp confirmation to specific reactivity. Transition state searches revealed the  $\pi$ -clamp conformer of the FCPF peptide to have a lower reaction barrier than the GCPG control.

A later study examined the enhancement to the reaction rate by mutating the phenylalanine residues to a variety of non-natural amino acids. A second study demonstrated the efficacy of addition of salts to the reaction mixture. To model these effects, we employed a reduced model of the binding event between the ligand and clamp side chain. This model proved effective in explaining the experimental data, producing a linear free energy relation between binding energy and the logarithm of reaction rate.

## 2.2 Organic electronics

With energy demand expected to expand 56% by 2050 [5, 193], cheap, renewable, and efficient energy sources are the focus of much research. At the same time, it is equally important to produce efficient and affordable electronics that consume this energy. Organic electronics are promising candidates in both categories.

Solar cells harvest perhaps the most abundant and renewable source of energy available: the sun. So abundant is solar energy that even inefficient cells could meet the world’s energy demand if they covered only one thousandth of the Earth’s landmass [116, 117]. However, existing technologies are simply too expensive to replace existing fossil fuel power generation [14]. Organic photovoltaics (OPVs) are a candidate to solve this problem [170, 247]. Because they are made of simple organic molecules and can be fabricated readily, they are much cheaper than traditional inorganic technologies [102]. However, these devices lag behind in efficiency [239]. In Section 2.2.2, we discuss simulations of a new OPV which may circumvent a key efficiency loss process.

On the other end of the wire, devices that consume electricity must also be efficient and affordable. For example, commercial lighting consumes an estimated 10% of all power produced [5]. Light-emitting diodes offer great increases in efficiency over traditional lighting, but are currently too expensive to impact the market. As with OPVs for light harvesting, organic light-emitting diodes (OLEDs) could offer an inexpensive alternative [65]. Additionally, due to their ease of fabrication, OLEDs could see application in mobile devices, where inefficient pixels currently tax battery life.

### 2.2.1 Exciplex-based blue organic light emitting diodes

For LEDs, blue is hard. So hard, in fact, the the 2014 Nobel Prize in physics was awarded to an inorganic blue LED [1]. Blue LEDs are critical in lighting applications and display applications,

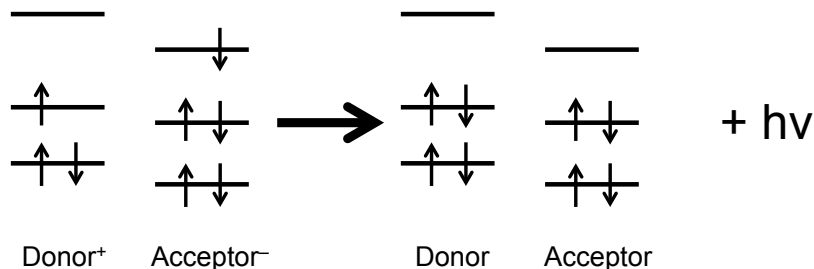


Figure 2-8: Exciplex charge combination and emission schematic.

where blue is the missing primary color needed for these devices to span the visible spectrum. OLEDs have been used in phone displays, but the lifetime of these displays has been limited by the lifetime of the blue OLED pixels. Further because of their inefficiency, some displays require blue OLEDs that dwarf their red and green counterparts in size.

Exciplexes are candidate materials for improved OLEDs [166]. In LEDs, charges recombine to form light. In an exciplex, this process is bimolecular. A dimer of two molecules is formed with an electron on the “acceptor” and a hole on the “donor” (so named for the reverse process in which the neutral excited donor donates an electron to the acceptor). These charges combine to form an exciton, which decays to emit light. A scheme is shown in Figure 2-8. Because the process is bimolecular, exciplex emission wavelengths can be tuned by individually tuning the electronic structures of the donor and acceptor. Specifically, the difference between the ionization potential of the donor and the electron affinity of the acceptor is a proxy for the emission energy.

As with all things, exciplex-based OLEDs have a key draw back. The charge annihilation rate — and therefore light production efficiency — is limited by the strength of donor-acceptor binding. When the donor and acceptor bind weakly, they are rarely in their dimer form, necessary for emission. To circumvent this, synthetic work [208] was carried out to produce donor-acceptor pairs that bind strongly, while still emitting blue light. The key idea was to create a lock-key geometry for the donor and acceptor that would maximize binding of the two via van der Waals interactions (Figure 2-9). In this section, we study the binding strength of these dimers as well as the color of their emission using density functional theory.

### 2.2.1.1 Computational details

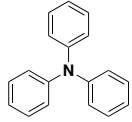
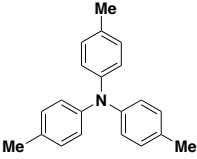
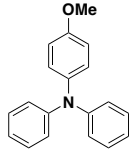
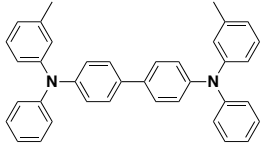
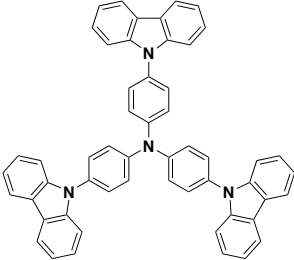
Density functional theory calculations were performed with the QChem 4.3 software package [290] using the b3lyp functional [23] with Grimme’s dispersion corrections [119]. A Lebedev (75, 302) exchange-correlation grid was used [191]. Geometry optimizations were performed using a 6-31+g\* basis set [185]. Binding energies, HOMOs, and IPs were computed in an aug-cc-pVDZ basis set [86]. Ionization potentials were computed by vertical detachment of an electron. Electron affinities were computed by vertical attachment of an electron.

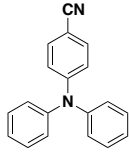
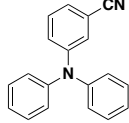
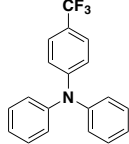
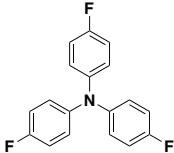
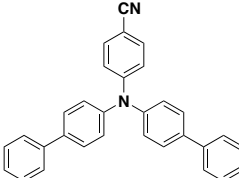
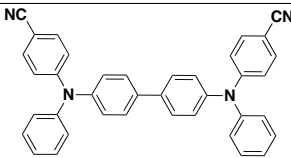
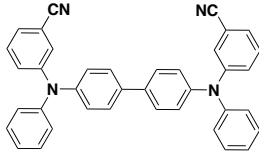


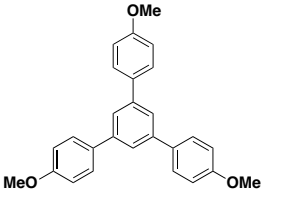
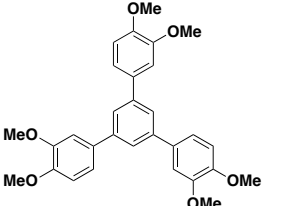
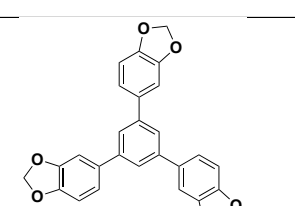
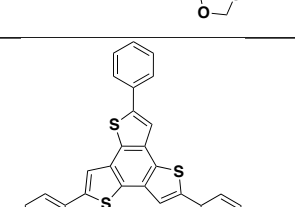
the gas phase. We see that the binding strength is correlated to the amount of available aromatic surface area on the core donor, consistent with dispersive interactions between the donor and the core of the acceptor. The strongest of the binders additionally contains wings that bind to the wings of the acceptor.

The same mechanism that binds the donor to the acceptor also binds the donor to itself and binds the acceptor to itself. Thus, we expect that there could be correlation (and therefore competition) between the strength of donor-acceptor binding and donor-donor binding. To examine this possibility, we perform the same optimization and binding energy calculations from before, but now on the acceptor dimer and each donor dimer. Results are presented in the third and fourth columns of Table 2.5. Only the sulfur compound energetically prefers the donor-acceptor dimer over didonor and diacceptor (though most relative binding energies do not differ within DFT error).

Table 2.5: Computed donor-acceptor and didonor dimer binding energies. The diacceptor dimer has a binding energy of -45.3 kcal/mol. Relative binding energies are the reaction energy of  $\frac{1}{2}D_2 + \frac{1}{2}A_2 \rightarrow DA$ .

Donor	Donor-acceptor binding energy (kcal/mol)	Didonor binding energy (kcal/mol)	Relative binding energy (kcal/mol)
	-24.8	-17.2	6.4
	-28.6	-18.8	3.4
	-31.3	-18.3	0.5
	-37.9	N/A	N/A
	-45.8	N/A	N/A

	-30.4	-17.8	1.1
	-27.6	-18.1	4.1
	-30.3	-19.1	1.9
	-30.2	-17.6	1.2
	-28.8	-17.9	2.8
	-27.7	-17.7	3.8
	-41.1	N/A	N/A
	-34.0	N/A	N/A
	-37.3	N/A	N/A

	-34.3	-28.7	2.7
	-38.8	N/A	N/A
	-36.5	-33.3	2.8
	-38.4	-29.5	-1.0

### 2.2.1.3 Exciplex color

These exciplex molecules were designed with two goals in mind: strong binding energy and blue emission. We now focus on the latter.

In an OLED, current is pushed through the device, creating charged  $D^+A^-$  pairs. When these charges combine, light is emitted. The simplest model of this emission is energy gap between the Highest Occupied Molecular Orbital (HOMO) of the donor and the Lowest Unoccupied Molecular Orbital (LUMO) of the acceptor. (Note that these names are in reference to the neutral state of these molecules.) In this model, the excess electron on the acceptor anion resides in its LUMO and a hole exists in the HOMO of the donor. During charge recombination, the electron moves from the LUMO of the acceptor to annihilate the hole in the HOMO of the donor (Figure 2-8). If the HOMO of the donor is at a lower energy than the LUMO of the acceptor, light is emitted with photon energy corresponding to this energy difference. HOMO-LUMO gaps for the donor-acceptor dimers are given in Table 2.6, column 2.

While effective, the HOMO-LUMO gap is a crude model with a major flaw. The Kohn-Sham

virtual orbitals (in particular, the acceptor LUMO) have no physical meaning [248]. The HOMO-LUMO gap is used as a stand-in for the process of removing an electron from the acceptor and placing it on the donor. In its place, we can simply compute the steps of this process. The energy of removing an electron from the acceptor anion is the negative of its electron affinity (EA). The energy of adding an electron to the donor cation is its ionization potential (IP). We can compute the IP and EA as vertical electron detachment and attachment energies, respectively. These donor-acceptor IP-EA gaps are listed in the third column of Table 2.6, and correlate well to the HOMO-LUMO gaps.

The HOMO-LUMO and IP-EA gaps are instructive proxies for the energy of charge recombinations, but they require that the donor and acceptor be considered separately as monomers; we lose information about the electronic effect of the close binding of these molecules in the dimers. Using CDFT, we can constrain the acceptor to have an excess electron, resulting in the  $D^+A^-$  charge-transfer configuration. We can then directly compare this energy to that of the unconstrained  $DA$  dimer. Because dimers were geometry optimized in their ground state, this energy corresponds to an absorption rather than an emission.

To correct for the Stokes shift, we consider the Stokes shifts of the donor and acceptor in isolation, due to the numerical difficulty of performing a CDFT geometry optimization. Stokes shifts are computed using the four point rule:

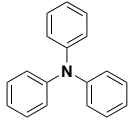
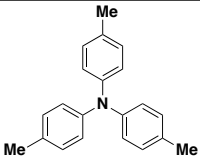
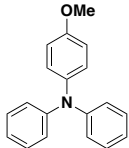
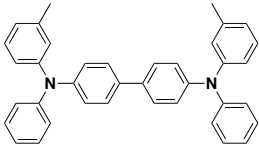
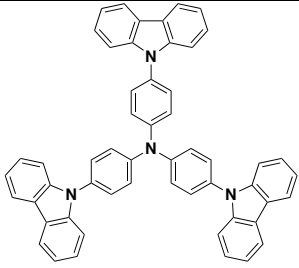
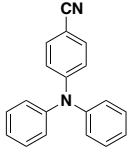
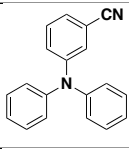
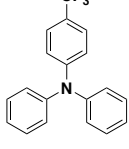
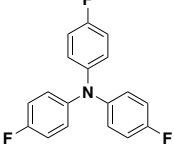
$$\begin{aligned} S_D &= [E(D^+)_D - E(D)_D] - [E(D^+)_{D^+} - E(D)_{D^+}] \\ S_A &= [E(A^-)_A - E(A)_A] - [E(A^-)_{A^-} - E(A)_{A^-}] \end{aligned} \quad (2.2)$$

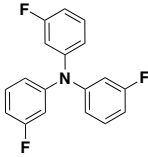
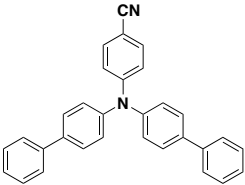
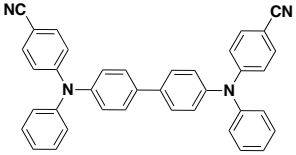
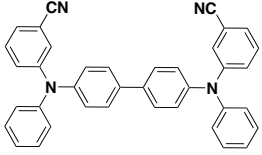
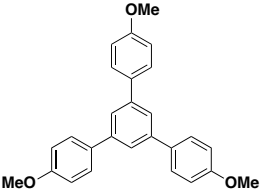
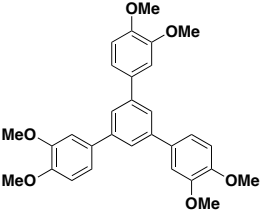
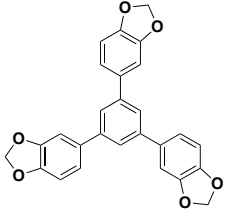
where  $E(X)_Y$  denotes the energy of species  $X$  in the optimal geometry of species  $Y$ . These two Stokes shifts are then added (with appropriate sign) to the CDFT absorption energy to give the CDFT emission energy. These emission energies are given in Table 2.6, column 4.

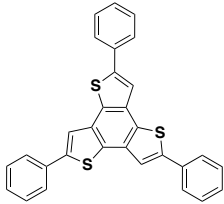
Figure 2-10 shows a comparison of computed CDFT emission energies to experiment. We see that the computed and experimental emission energies are only loosely correlated. As such, we cannot use computation to directly predict the color of candidate donor-acceptor dimers. However, CDFT emission energies may still be useful as a coarse computational screen to find donors that whose emission energies are in the right ballpark.

Table 2.6: Electronic and emission properties of donor-acceptor complexes.

Donor	HOMO-LUMO gap (eV)	EA-IP gap (eV)	CDFT-CI emission (eV)
-------	-----------------------	-------------------	--------------------------

	3.24	5.69	2.60
	2.97	5.33	2.37
	3.05	5.46	2.30
	2.94	4.99	N/A
	3.27	5.20	N/A
	3.70	6.10	2.92
	3.65	6.06	2.77
	3.59	6.02	2.81
	3.46	5.92	3.40

	3.73	6.17	2.86
	3.59	6.03	2.75
	3.56	5.73	2.66
	3.56	5.58	N/A
	3.43	5.47	N/A
	3.70	5.92	2.59
	3.84	6.00	2.98
	3.73	5.90	3.41

	3.62	5.81	3.13
---	------	------	------

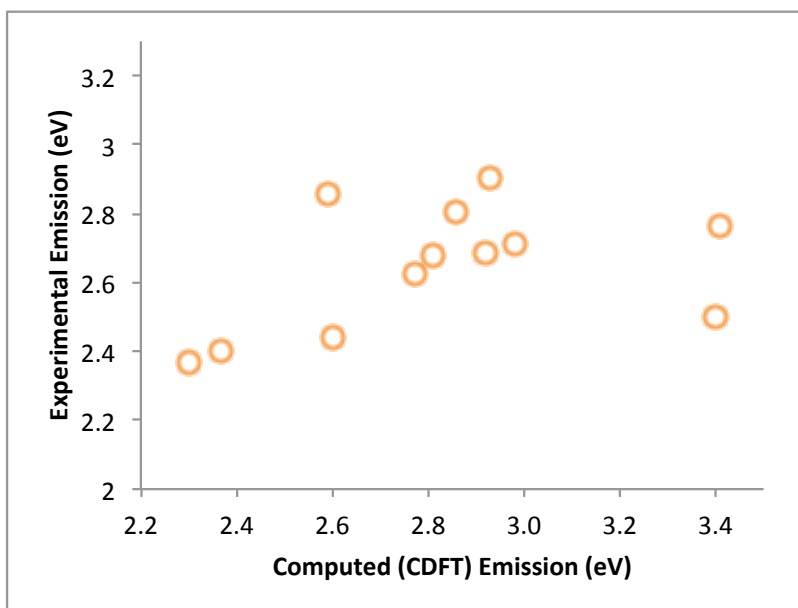


Figure 2-10: Dimer CDFT emission energies compared to experiment (where available) for the molecules in Table 2.6.

#### 2.2.1.4 Conclusions

Exciplexes are a candidate for OLEDs that traditionally suffer from weak emission. A new class of exciplexes for OLEDs (Figure 2-9) was proposed to be more effective due to strong donor-acceptor binding. We computed the binding energies of these exciplexes as well as their emission energies. The emission energies were found to correlate only loosely with experiment. There is not yet experimental data available for the efficiency of devices incorporating these exciplexes; once available, it can be compared to binding energies.

In this section, we considered the emission of organic molecules in a disordered thin-film medium. In the next section, we flip these conditions and look at absorption of a pair of stacked organic crystals.

## 2.2.2 Band-like charge transfer states in organic photovoltaics

Organic photovoltaics are attractive alternatives to traditional inorganic cells due to their ease of manufacture and low cost. However, they suffer from low efficiency due in part to their disordered nature. In this section, we examine computationally a novel crystalline rubrene/ $C_{60}$  device and compare it to its disordered counterpart. We compute charge transfer energies and couplings, and build a lattice model for the crystalline device. We see excellent agreement in both energy and band shape between our model and experiment. We determine that the crystalline device has a far lower barrier to charge separation, suggesting that it is more efficient than the disordered cell. Finally, we consider alternative crystalline geometries and find that the experimental cell is uniquely efficient for solar applications.

### 2.2.2.1 Introduction

Organic photovoltaics (OPV) have shown promise as solar materials. Because they comprise a disordered mixture of organic molecules, they are cheap and easy to manufacture, transport, and install [102]. However, OPVs are currently inefficient compared to existing inorganic technologies; the best OPVs only reach 11% efficiency compared to 46% efficiency of the best inorganic cells [239]. This inefficiency stems from many causes, including inferior charge generation.

In OPVs, absorption of light creates a bound electron-hole pair, called an exciton. This exciton must separate into an unbound hole and electron in order to generate current. This process is hindered by two main factors. First, organic materials have small dielectric constants, leading to a large attractive coulombic potential between the electron and hole. Second, charge transport hopping integrals between organic molecules are low, decreasing the rate of charge separation. This problem is exacerbated by the disordered nature of OPVs: even when favorable transport pathways are available, molecules are rarely aligned correctly to take advantage of them. The result of these factors is a large dissociation barrier (on the order of tenths of eV). Inorganic materials, meanwhile, do not have these problems. They feature high dielectric constants and large charge conductivity, leading to facile charge dissociation at room temperature.

Leaving aside the first problem, attempts have been made to solve the second problem. Crystalline rubrene is an excellent conductor of holes. However, this conductivity is contingent on crystallinity and the rubrene thin films used in OPVs are disordered. Recent work has demonstrated a technique that induces crystallization in such films [338]. Extending on this technique, the h00 face of a thin film of crystalline rubrene was used to template a  $C_{60}$  film, which was also shown to be crystalline.

Electroluminescence (EL) measurements were carried out on this so-called crystal planar heterojunction (PHJ) cell, as well as a typical disordered rubrene/ $C_{60}$  bulk heterojunction (BHJ). The BHJ cell exhibited a typical Marcus Gaussian lineshape and emitted isotropic light, both indicative

of a disordered emitter. The crystal PHJ cell, however, displayed an atypical EL peak and emitted anisotropic light, indicating emission from an ordered system.

In this chapter, we seek to model this crystalline PHJ and to understand its unique EL spectrum. We begin with a control calculation on the BHJ. Then, we develop a model for the crystalline PHJ. Finally, we compare the resulting computational picture of the two.

### 2.2.2.2 Computational model of the disordered bulk heterojunction

The BHJ presents a computational problem: it is composed of a disordered blend of rubrene and  $C_{60}$ . In order to completely model the EL spectrum of the BHJ, we would need to explicitly sample the possible configurations of such a disordered system. Calculations of this size are outside of the scope of this work as our main focus is the PHJ rather than the BHJ. Rather than attempt to completely model the BHJ, we instead will use it as a check on the applicability of our model to the experimental system. To do this, we identify a representative (most likely) configuration and then test whether its computed CT energy matches experiment.

In order to choose such a sample, we rely on three approximations. First, we assume that the CT excitation is primarily governed by the electronic structure of a single rubrene/ $C_{60}$  pair. (This assumption is in part justified by the disorder of the system. It is unlikely that the CT state can coherently delocalize.) As such, we model the surrounding rubrene/ $C_{60}$  blend as a continuum dielectric model. The dielectric constant of this model was 2.9, resulting from Clausius-Mossotti mixing [Shin1989] of the dielectric constants of rubrene and  $C_{60}$ , 1.8 [323] and 5 [168] respectively. Second, we expect that the most optically active CT excitations have the least charge separation and thus will occur between an adjacent pair of rubrene and  $C_{60}$  molecules. Finally, we assume that the most likely configuration of such a dimer (that can be determined in this dimer model) is its minimum energy geometry.

The geometry and charge transfer state of this representative dimer are shown in Figure 2-11. This state has a calculated CT energy of 1.6 eV versus the neutral dimer. This compares favorably to the center of the experimental EL peak at 1.48 eV. We note that we expect an error of approximately 0.2 eV on such a calculation.

To compute the binding energy of this electron-hole pair, we also consider a dissociated state in the BHJ. This state is modeled by two calculations: the rubrene cation and the  $C_{60}$  anion, each embedded in a dielectric of 2.9. This CT state has energy of 2.3 eV relative to the neutral molecules.

### 2.2.2.3 Computational model of the ordered interface

X-ray crystallography provided information about the crystal structure of the rubrene and  $C_{60}$  and also identified which crystal faces were parallel to the interface. However, the exact alignment of the rubrene and  $C_{60}$  crystal faces was not provided by these data. To find this structure, we built a

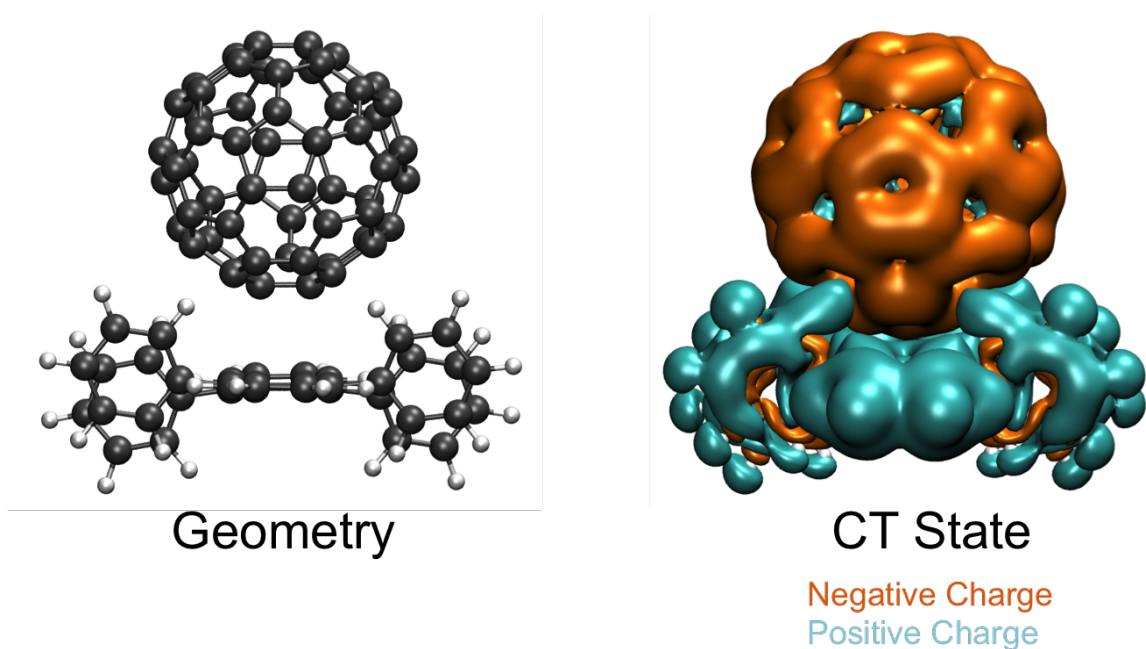


Figure 2-11: Geometry and charge transfer state of the representative dimer used to describe the disordered BHJ.

molecular mechanics model of the interface and minimized its energy. The rubrene and  $C_{60}$  molecules were frozen in their experimental lattice positions and geometries, but the two crystals were allowed to slide and rotate relative to each other.

The cost of quantum mechanical calculations requires that we choose a much smaller model of the interface. In practice, we can afford to compute 4 molecules at the level of theory used. Because we are seeking to simulate a possible band-like CT state, we first determine which part of the system shows the greatest intermolecular nearest-neighbor coupling for either electron or hole hopping (in  $C_{60}$  or rubrene, respectively). The  $C_{60}$  crystal is face-centered cubic and thus has only one choice of nearest neighbor. We compute a  $C_{60}$ - $C_{60}$  electron hopping coupling of 0.02 eV. Rubrene has three distinct crystal axes. We compute rubrene-rubrene hole hopping couplings of 0.02 eV, 0.05 eV, and 0.14 eV for the  $a$ ,  $b$ , and  $c$  axes of the rubrene crystal. Because of its much larger hopping integral, we expect that the rubrene  $c$  axis plays the most important role in a potential band-like state. We thus consider a model of a negatively charged  $C_{60}$  and a wire of rubrenes aligned along the  $c$  crystal axis (Figure 2-12).

From this reduced model, we excerpt one  $C_{60}$  and three rubrenes at a time. (One such excerpt is shown in Figure 2-13.) For each four-molecule excerpt, we compute the CT state energies (with the hole localized on each rubrene) and the hopping integral for moving the hole between first and second nearest neighbor rubrenes. We also compute the transition dipole moment for the CT to neutral transition.

We then combine these results into a lattice model for the hole in rubrene. Each lattice site

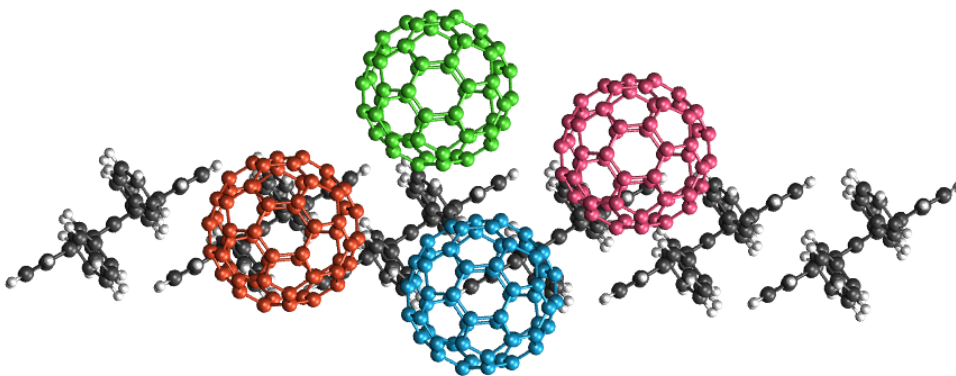


Figure 2-12: Reduced model of the  $C_{60}$ /rubrene crystal interface. CT states and hole hopping couplings were computed by excerpting one  $C_{60}$  and three adjacent rubrenes at a time.  $C_{60}$  colors correspond to the sticks in Figure 2-14.

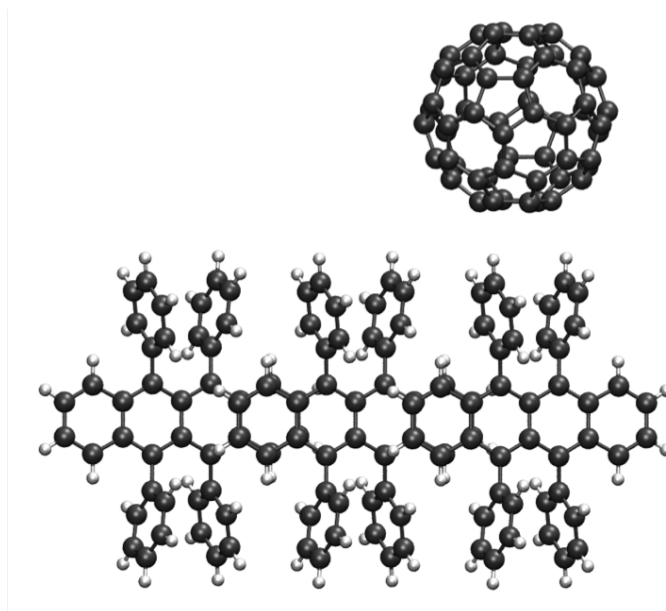


Figure 2-13: An example four molecule excerpt from Figure 2-12.



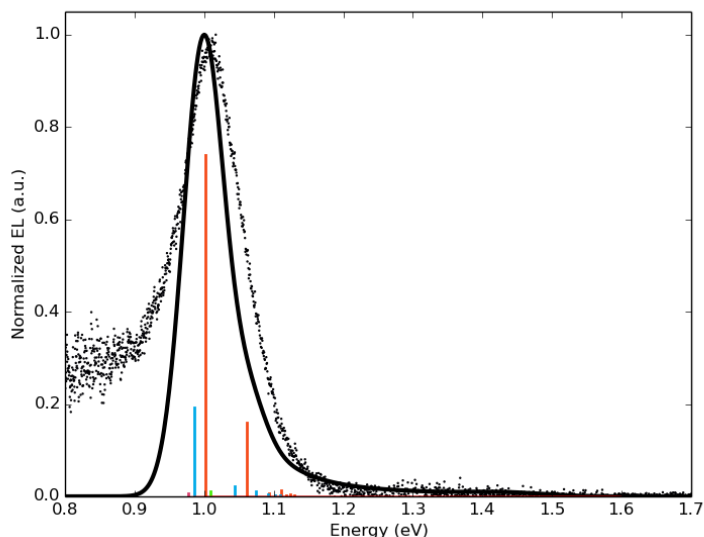


Figure 2-14: Weighted density of states for the lattice model (solid black) compared to experimental electroluminescence data (black points). Each stick denotes an eigenstate of the lattice model at a given energy. Heights of the sticks are in proportion to their optical weight (square of the transition dipole moment). Colors of sticks correspond to the anionic  $C_{60}$  (matched to colors in Figure 2-12). The stick spectrum is smoothed into a continuous peak using Kernel Density Estimation [293].

derstand the role of interfacial geometry in these devices. We see that both exciton binding energy and optical transition intensity are governed by the distance between rubrene molecules in the direction of the interface: more closely packed rubrenes lead to a lower exciton binding energy and higher optical strength. At the same time, closer packing of rubrenes creates higher hole mobility. Thus, the experimental interface realized in this work is optimal because it aligns the close-packed, highly-conductive  $c$ -axis of rubrene along the interface.

These results in concert with experiments establish a novel mode of charge generation in OPVs. This delocalization opens up a pathway for efficient charge separation, an advantage previously available only in inorganic solar cells. Further details can be found in an upcoming work.

#### 2.2.2.4 Computational details

Density functional theory calculations were performed using the Q-Chem 4.3 package [290] with the B3LYP functional [23] in a 6-31g\* basis set [185]. Charge transfer state energies, couplings, and transition dipole moments were computed using Constrained Density Functional Theory Configuration Interaction (CDFT-CI) [365]. We expect CT state energies computed with CDFT-CI to be accurate to within 0.2 eV. Dielectric effects were simulated using the conducting Polarizable Continuum Model [57].

Molecular mechanics calculations were performed using the GROMACS package [3]. The Lennard-

Jones parameters for carbon were  $\sigma = 0.3431$  and  $\epsilon = 0.4396$ . The Lennard-Jones parameters for hydrogen were  $\sigma = 0.2571$  and  $\epsilon = 0.1842$ .

## 2.3 Looking forward

In this chapter, we applied readily available, time-tested methods. Each section presented a different application and extensions to each section suggest new directions for methods development.

In Section 2.2.2, we examined charge delocalization in a highly crystalline planar heterojunction, constructing a single model Hamiltonian for the entire crystal. For the disordered bulk heterojunction, we made simplifying assumptions about charge localization in order to avoid building a model Hamiltonian for each configuration of the disordered system. In Chapters 3 and 4, we introduce a tool for studying such collections of disordered Hamiltonians, Random Matrix Theory. We then apply this tool to the study of toy models of localization in disordered systems.

In Section 2.1, we examined the binding of a ligand to a protein. In principle, we would like to simulate the entire protein, but computational cost prevents such a complete model. We create a reduced model of the binding by truncating away all but the most relevant parts of the protein. Another, more satisfying approach would be to retain the rest of the protein, but treat it using a much cheaper theory. Such a set up is called embedding; in Chapters 5 and 4, we develop an embedding method.

Finally, throughout this chapter, we treated the effects of solvent implicitly. Explicit treatment of solvation requires an accurate and cheap solvent model. In Chapter 7, we build a model for liquid water.

## 2.4 Acknowledgments

The work in Section 2.1 was done with Chi Zhang, Peng Dai, Tianyu Zhu, James Shepherd and Bradley Pentelute. They are listed as coauthors in reference [374] and on a submitted manuscript. The experimental work described in Section 2.2.1 was carried out by Georgios Markopoulos and Tim Swager. The experimental work in Section 2.2.2 was performed by Michael Fussella, Alyssa Bridgeman, Geoffrey Purdum, Richard Schaller, Yun-Hui Lin, Ross Kerner, Yueh-Lin Loo, Noel Giebink, and Barry Rand. They are listed as coauthors on a manuscript currently in review.



## Chapter 3

# Error analysis of free probability approximations to the density of states of disordered systems

Theoretical studies of localization, anomalous diffusion and ergodicity breaking require solving the electronic structure of disordered systems. We use free probability to approximate the ensemble-averaged density of states without exact diagonalization. We present an error analysis that quantifies the accuracy using a generalized moment expansion, allowing us to distinguish between different approximations. We identify an approximation that is accurate to the eighth moment across all noise strengths, and contrast this with the perturbation theory and isotropic entanglement theory.

### 3.1 Introduction

Disordered materials have long been of interest for their unique physics such as localization [327, 95], anomalous diffusion [38, 296] and ergodicity breaking [246]. Their properties have been exploited for applications as diverse as quantum dots [19, 308], magnetic nanostructures [138], disordered metals [88, 85], and bulk heterojunction photovoltaics [254, 80, 370]. However, conventional electronic structure theories require diagonalization of many explicit sampled Hamiltonians, making such calculations expensive. Alternatively, free probability theory allows a powerful nonperturbative method for computing of eigenvalues of sums of certain matrices without re-diagonalizing the matrix sums [342]. This has been proposed as an approximation for general random matrices [28]; however, we are not aware of any rigorous study of its accuracy. This motivates us to describe herein a general framework for quantifying the error in terms of discrepancies in the moments of the probability distribution functions (PDFs).

## 3.2 Comparing two PDFs

We propose to quantify the deviation between two PDFs using moment expansions. [53] These are widely used to describe deviations from normality in the form of Gram–Charlier and Edgeworth series [314, 34]. The general case applies also to non-Gaussian reference PDFs. For two PDFs  $w(\xi)$  and  $\tilde{w}(\xi)$  with finite cumulants  $\kappa_1, \kappa_2, \dots$  and  $\tilde{\kappa}_1, \tilde{\kappa}_2, \dots$ , and moments  $\mu_1, \mu_2, \dots$  and  $\tilde{\mu}_1, \tilde{\mu}_2, \dots$  respectively, we can define a formal differential operator which transforms  $\tilde{w}$  into  $w$  [346, 314]:

$$w(\xi) = \exp \left[ \sum_{n=1}^{\infty} \frac{\kappa_n - \tilde{\kappa}_n}{n!} \left( -\frac{d}{d\xi} \right)^n \right] \tilde{w}(\xi). \quad (3.1)$$

This operator is parameterized completely by the cumulants of both distributions. The resulting Edgeworth series is asymptotic and only conditionally convergent [69].

The first  $k$  for which the cumulants  $\kappa_k$  and  $\tilde{\kappa}_k$  differ then allows us to define a degree to which the approximation  $w \approx \tilde{w}$  is valid. Expanding the exponential and using the well-known relationships between cumulants and moments allows us to state that if the first  $k - 1$  cumulants agree, but the  $k$ th cumulants differ, then

$$w(\xi) = \tilde{w}(\xi) + \frac{\mu_k - \tilde{\mu}_k}{k!} (-1)^k \tilde{w}^{(k)}(\xi) + O(\tilde{w}^{(k+1)}). \quad (3.2)$$

This series inherits the same asymptotic convergence properties as the original Edgeworth series [69, 124]. Nevertheless, it is sufficient to use the leading order correction solely to quantify the error incurred by approximating one PDF by another.

## 3.3 The free convolution

We now take the PDFs to be densities of states (DOSs) of random matrices. The DOS of a random matrix  $X$  is defined using the eigenvalues  $\{\lambda_n^{(m)}\}$  of the  $M$  samples  $X_1, \dots, X_m, \dots, X_M$  by

$$\rho^{(X)}(\xi) = \lim_{M \rightarrow \infty} \frac{1}{M} \sum_{m=1}^M \frac{1}{N} \sum_{n=1}^N \delta(\xi - \lambda_n^{(m)}). \quad (3.3)$$

To approximate DOSs with free probability, we split the Hamiltonian

$$H = A + B \quad (3.4)$$

into two matrices  $A$  and  $B$  whose DOSs,  $\rho^{(A)}$  and  $\rho^{(B)}$  respectively, can be determined easily. In general, it is not possible to calculate the eigenvalues of  $H$  by adding the eigenvalues of  $A$  and  $B$  together; the general problem is complicated by  $A$  and  $B$  not commuting [177]. In contrast,

free probability tells us that for certain noncommuting matrices  $A$  and  $B$ , the exact DOS becomes the free convolution  $A \boxplus B$ , i.e.  $\rho^{(H)} \approx \rho^{(A \boxplus B)}$ , a “sum” which can be calculated without exact diagonalization of  $H$  [340]. We calculate the free convolution numerically by diagonalizing the free approximant [79]

$$Z = A + Q^{-1} B Q, \quad (3.5)$$

where  $Q$  is a  $N \times N$  random matrix of Haar measure. For real symmetric matrices  $A$  and  $B$  it is sufficient to consider orthogonal matrices  $Q$ , which can be generated from the  $QR$  decomposition [112] of a Gaussian orthogonal matrix [79]. (This can be generalized readily to unitary and symplectic matrices for complex and quaternionic Hamiltonians respectively.) The similarity transformation  $Q^{-1} \cdot Q$  applies a random rotation to the basis of  $B$  with respect to  $A$ . In the  $N \rightarrow \infty$  limit, the DOS  $\rho^{(Z)}$  converges to the free convolution  $A \boxplus B$  [342, 343].

The moment expansion above provides an error analysis via discrepancies between the  $k$ th moment of the exact DOS,  $\mu_k^{(H)}$ , and the free approximant,  $\mu_k^{(A \boxplus B)}$ . By definition, the exact moments are [215]

$$\mu_k^{(H)} = \mu_k^{(A+B)} = \langle (A+B)^k \rangle, \quad (3.6)$$

where  $\langle Z \rangle = \mathbb{E} \text{Tr} (Z) / N$  denotes the normalized expected trace (NET) of the  $N \times N$  matrix  $Z$ . Expanding the (noncommutative) binomial produces a sum of joint moments  $\langle A^{n_1} B^{m_1} \dots A^{n_r} B^{m_r} \rangle$  with the positive integer exponents  $n_s, m_s$  summing to  $\sum_{s=1}^r (n_s + m_s) = k$ . The approximation of freeness implies that the joint moments must obey, by definition [235], relations of the form

$$0 = \langle \prod_{s=1}^r (A^{n_s} - \langle A^{n_s} \rangle) (B^{m_s} - \langle B^{m_s} \rangle) \rangle \quad (3.7a)$$

$$= \langle \prod_{s=1}^r A^{n_s} B^{m_s} \rangle + \text{lower order terms}, \quad (3.7b)$$

where the second equality results from the linearity of the NET. Testing for  $\mu_k^{(A+B)} \neq \mu_k^{(A \boxplus B)}$  then reduces to testing whether each centered joint moment of the form in (3.7a) is statistically nonzero. Enumerating all unique joint moments of degree  $k$  is equivalent to the combinatorics of binary necklaces, which can be generated efficiently [281].

The procedure we have described ascribes a degree  $k$  to the approximation  $\rho^{(H)} \approx \rho^{(A \boxplus B)}$  given the splitting  $H = A + B$ . For each positive integer  $n$ , we generate all unique centered joint moments of degree  $n$ , and test if they are statistically nonzero. The lowest  $n$  for which there is at least one such term is the degree of approximation  $k$ . This is our main result.

### 3.4 Decomposition of the Anderson Hamiltonian

As a concrete example, we focus on the Anderson Hamiltonian [10]

$$H = \begin{pmatrix} h_1 & J & & \\ J & h_2 & \ddots & \\ & \ddots & \ddots & J \\ & & J & h_N \end{pmatrix}, \quad (3.8)$$

where  $J$  is constant and the diagonal elements  $h_i$  are identically and independently distributed (iid) random variables with PDF  $p_h(\xi)$ . This is a real, symmetric tridiagonal matrix with circulant (periodic) boundary conditions on a one-dimensional chain. Unless otherwise stated, we assume that  $h_i$  are normally distributed with mean 0 and variance  $\sigma^2$ . We note that  $\sigma/J$  gives us a dimensionless order parameter to quantify the strength of disorder.

So far, we have only required of the decomposition scheme  $H = A+B$  that  $\rho^{(A)}$  and  $\rho^{(B)}$  be easily computable. Are certain choices intrinsically superior to others? For the Anderson Hamiltonian, we consider two reasonable partitioning schemes:

$$H = A_1 + B_1 = \begin{pmatrix} h_1 & & & \\ & h_2 & & \\ & & h_3 & \\ & & & \ddots \end{pmatrix} + \begin{pmatrix} 0 & J & & \\ J & 0 & J & \\ & J & 0 & \ddots \\ & & \ddots & \ddots \end{pmatrix} \quad (3.9a)$$

$$H = A_2 + B_2 = \begin{pmatrix} h_1 & J & & \\ J & 0 & & \\ & & h_3 & J \\ & & J & 0 \\ & & & \ddots \end{pmatrix} + \begin{pmatrix} 0 & & & \\ & h_2 & J & \\ & J & 0 & \\ & & & h_4 & \cdots \\ & & & \vdots & \ddots \end{pmatrix}. \quad (3.9b)$$

We refer to these as Scheme I and II respectively. In Scheme I, we have  $\rho_{A_1} = p_h$  since  $A_1$  is diagonal with each nonzero matrix element being iid.  $B_1$  is simply  $J$  multiplied by the adjacency matrix of a one-dimensional chain, and therefore has eigenvalues  $\lambda_n = 2J \cos(2n\pi/N)$  [313]. The DOS of  $B_1$  is  $\rho_{B_1}(\xi) = \sum_{n=1}^N \delta(\xi - \lambda_n)$  which converges as  $N \rightarrow \infty$  to the arcsine distribution with PDF  $p_{AS}(\xi) = 1/(\pi\sqrt{4J^2 - \xi^2})$  on the interval  $[-2|J|, 2|J|]$ . In Scheme II, we have that  $\rho_{A_2} = \rho_{B_2} = \rho_X$  where  $\rho_X$  is the DOS of  $X = \begin{pmatrix} h_1 & J \\ J & 0 \end{pmatrix}$ . The matrix  $X$  has eigenvalues

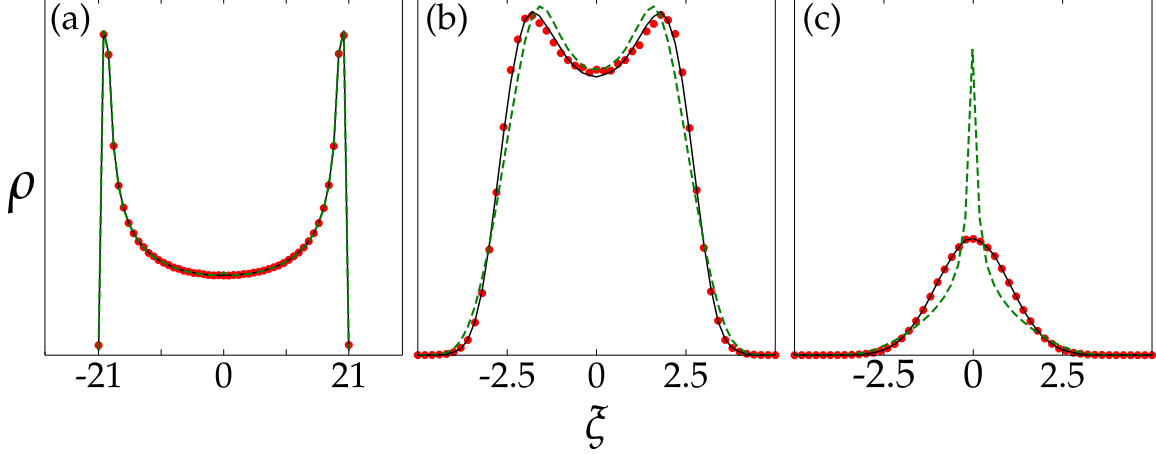


Figure 3-1: Calculation of the DOS,  $\rho(\xi)$ , of the Hamiltonian  $H$  of (3.8) with  $M = 5000$  samples of  $2000 \times 2000$  matrices for (a) low, (b) moderate and (c) high noise ( $\sigma/J=0.1, 1$  and  $10$  respectively with  $\sigma = 1$ ). For each figure we show the results of free convolution defined in Scheme I ( $\rho^{(A_1 \boxplus B_1)}$ ; black solid line), Scheme II ( $\rho^{(A_2 \boxplus B_2)}$ ; green dashed line) and exact diagonalization ( $\rho^{(H)}$ ; red dotted line).

$\epsilon_{\pm}(\xi) = h_1(\xi)/2 \pm \sqrt{h_1^2(\xi)/4 + J^2}$  and so

$$\rho_X(\xi) = \left(1 + \frac{J^2}{\xi^2}\right) p_h\left(\xi - \frac{J^2}{\xi}\right). \quad (3.10)$$

### 3.5 Numerical free convolution

We now calculate the free convolution  $A \boxplus B$  numerically by sampling the distributions of  $A$  and  $B$  and diagonalizing the free approximant (3.5). The exact DOS  $\rho^{(A+B)}$  and free approximant  $\rho^{(A \boxplus B)}$  are plotted in Figure 3-1(a)–(c) for both schemes for low, moderate and high noise regimes ( $\sigma/J = 0.1, 1, 10$  respectively). For Scheme I, we observe excellent agreement between  $\rho^{(H)}$  and  $\rho^{(A_1 \boxplus B_1)}$  across all values of  $\sigma/J$ , which is evident from visual inspection; in contrast, Scheme II shows variable quality of fit. We can understand this difference using the procedure outlined above to analyze the accuracy of the approximations  $\rho^{(H)} \approx \rho^{(A_1 \boxplus B_1)}$  and  $\rho^{(H)} \approx \rho^{(A_2 \boxplus B_2)}$ . For Scheme I, the approximation (3.2) is of degree  $k = 8$ ; the discrepancy lies solely in the term  $\langle (A_1 B_1)^4 \rangle$  [260]. Free probability expects this term to vanish, but its true value is nonzero. The matrix  $A_1$  weights each path by a factor of  $h$ , while  $B_1$  weights each path by  $J$  and requires a hop to an adjacent site. The explicit products of matrix elements can then be expressed diagrammatically with closed paths as shown in Figure 3-2. Consequently, we can write explicitly

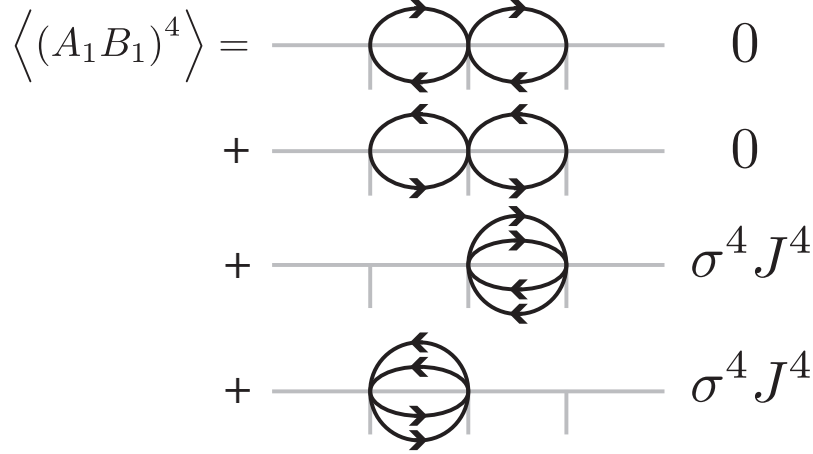


Figure 3-2: Diagrammatic expansion of the term  $\langle A_1 B_1 A_1 B_1 A_1 B_1 A_1 B_1 \rangle$  in terms of allowed paths dictated by the matrix elements of  $A_1$  and  $B_1$  of Scheme I in (3.9a).

$$\begin{aligned}
\langle (A_1 B_1)^4 \rangle &= \langle h_i J h_{i-1} J h_i J h_{i+1} J \rangle + \langle h_i J h_{i+1} J h_i J h_{i-1} J \rangle \\
&\quad + \langle h_i J h_{i-1} J h_i J h_{i-1} J \rangle + \langle h_i J h_{i+1} J h_i J h_{i+1} J \rangle \\
&= 2J^4 \mathbb{E}(h_i)^2 \mathbb{E}(h_i^2) + 2J^4 \mathbb{E}(h_i^2)^2 = 0 + 2J^4 \sigma^4, \tag{3.11}
\end{aligned}$$

where the second equality follows from the independence of the  $h_i$ 's. This explains why the agreement between the free and exact PDFs is so good, as the leading order correction is in the eighth derivative of  $\rho^{(A_1 \boxplus B_1)}$  with coefficient  $2\sigma^4 J^4 / 8! = (\sigma J)^4 / 20160$ . In contrast, Scheme II is correct only to degree  $k = 4$ , where the discrepancy lies in  $\langle A_2^2 B_2^2 \rangle$ . Free probability expects this to be equal to  $\langle A_2^2 B_2^2 \rangle = \langle A_2^2 \rangle \langle B_2^2 \rangle = \langle X^2 \rangle^2 = (J^2 + \sigma^2 / 2)^2$ , whereas the exact value of this term is  $J^2 (J^2 + \sigma^2)$ . Therefore, the error is in the fourth derivative of  $\rho^{(A \boxplus B)}$  with coefficient  $(-\sigma^4 / 4) / 4! = -\sigma^4 / 96$ .

### 3.6 Analytic free convolution

Free probability allows us also to calculate the limiting distribution of  $\rho^{(A \boxplus B)}$  in the macroscopic limit  $N \rightarrow \infty$  and  $M \rightarrow \infty$ , allowing the cost of numerical sampling and matrix diagonalization to be sidestepped entirely. The key tool is the  $R$ -transform  $r(w) = g^{-1}(w) - w^{-1}$  [340], where  $g^{-1}$  is defined implicitly via the Cauchy transform (i.e. its retarded Green function)

$$w = \lim_{\epsilon \downarrow 0} \int_{\mathbb{R}} \frac{\rho^{(A_1)}(\xi)}{g^{-1}(w) - (\xi + i\epsilon)} d\xi. \tag{3.12}$$

For freely independent  $A$  and  $B$ , the  $R$ -transforms linearize the free convolution, i.e.  $R^{(A \boxplus B)}(w) = R^{(A)}(w) + R^{(B)}(w)$ , and the PDF can be recovered from the Plemelj–Sokhotsky inversion formula

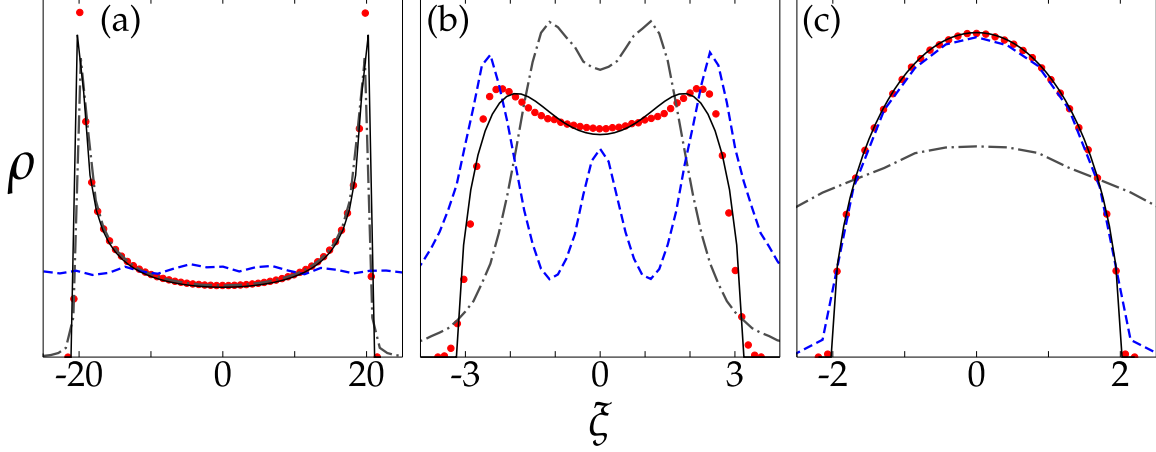


Figure 3-3: DOS,  $\rho(\xi)$ , of the Hamiltonian (3.8) with  $M = 5000$  samples of  $2000 \times 2000$  matrices with (a) low, (b) moderate and (c) high semicircular on-site noise ( $\sigma/J=0.1, 1$  and  $10$  respectively with  $\sigma = 1$ ), as calculated with exact diagonalization (red dotted line), free convolution (black solid line), and perturbation theory with  $A_1$  as reference (blue dashed line) and  $B_1$  as reference (gray dash-dotted line). The partitioning scheme is Scheme I of (3.9a).

by

$$\rho^{(A \boxplus B)}(\xi) = \frac{1}{\pi} \text{Im} \left( \left( g^{(A \boxplus B)} \right)^{-1}(\xi) \right) \quad (3.13a)$$

$$g^{(A \boxplus B)}(w) = R^{(A \boxplus B)}(w) + w^{-1}. \quad (3.13b)$$

We apply this to Scheme I with each iid  $h_i$  following a Wigner semicircle distribution with PDF  $p_W(\xi) = \sqrt{4 - \xi^2}/4\pi$  on the interval  $[-2, 2]$ . (The analytic calculation is considerably easier than for Gaussian noise.) First, calculate the Green function  $G^{(A_1)}(z) = (z - \sqrt{z^2 - 4})/2$ . Next, take the functional inverse  $g^{(A_1)}(w) = (G^{(A_1)})^{-1}(w) = w + 1/w$ . Subtracting  $1/w$  finally yields the  $R$ -transform  $r^{(A)}(w) = w$ . Similarly with  $\rho^{(B_1)} = p_{AS}$ , we find its Cauchy transform  $G^{(B_1)}(z) = 1/\sqrt{z^2 - 4J^2}$ , its functional inverse  $g^{(B_1)}(w) = (\sqrt{1 + 4J^2w^2})/w$ , and the  $R$ -transform  $R^{(B_1)}(w) = (-1 + \sqrt{1 + 4J^2w^2})/w$ .

To perform the free convolution analytically, we add the  $R$ -transforms to get  $R^{(A_1 \boxplus B_1)}(w) = R^{(A_1)}(w) + R^{(B_1)}(w)$ , from which we obtain  $g^{(A_1 \boxplus B_1)}(w) = w + (\sqrt{1 + 4J^2w^2})/w$ . The final steps are to calculate the functional inverse  $(g^{(A_1 \boxplus B_1)})^{-1}$  and take its imaginary part to obtain  $\rho^{(A_1 \boxplus B_1)}$ . Unfortunately,  $(g^{(A_1 \boxplus B_1)})^{-1}$  cannot be written in a compact closed form; nevertheless, the inversion can be calculated numerically. We present calculations of the DOS as a function of noise strength  $\sigma/J$  in Figure 3-3, showing again that the free convolution is an excellent approximation to the exact DOS.

### 3.7 Comparison with other approximations

We compare the free approximations to the results of standard second-order matrix perturbation theory [146], as shown in Figure 3-3. Unsurprisingly, perturbation theory produces results that vary strongly with  $\sigma/J$ , and that the different series, based on whether  $A$  is considered a perturbation of  $B$  or vice versa, have different regimes of applicability. Furthermore, it is clear even from visual inspection that the second moment of the DOS calculated using second-order perturbation theory is not always correct. In contrast, the free convolution produces results with a more uniform level of accuracy across the entire range of  $\sigma/J$ , and that we have at least the first three moments being correct [222].

It is also natural to ask what mean field theory, another standard tool, would predict. Interestingly, the limiting behavior of Scheme I as  $N \rightarrow \infty$  is equivalent to both the coherent potential approximation (CPA) [229, 230, 231] in condensed matter physics, and the Blue's function formalism in quantum chromodynamics for calculating one-particle irreducible self-energies [372]. The breakdown in the CPA in the term  $\langle (A_1 B_1)^4 \rangle$  is known [32, 327]; however, to our knowledge, the magnitude of the deviation was not explained. Our error analysis framework provides such a quantitative explanation.

Finally, we discuss the predictions of isotropic entanglement (IE) theory, which linearly interpolates the fourth cumulant between the classical convolution  $\rho^{(A*B)}(\xi) = \int_{-\infty}^{\infty} \rho^{(A)}(\xi) \rho^{(B)}(x - \xi) dx$  and the free convolution  $\rho^{(A\boxplus B)}(\xi)$  [222, 223]. Given the eigenvalues  $\Lambda_A, \Lambda_B$  of the matrices  $A$  and  $B$ , the classical convolution  $\rho^{(A*B)}(\xi)$  can be computed from the eigenvalues of the random matrix  $Z_{cl} = \Lambda_A + \Pi^{-1} \Lambda_B \Pi$ , where  $\Pi$  is a  $N \times N$  random permutation matrix. This compares with the free convolution sampled from  $Z' = \Lambda_A + Q^{-1} \Lambda_B Q$ , which has the same eigenvalues as the free approximant 3.5 by orthogonal invariance of the Haar measure of  $Q$ . As discussed previously, the lowest three moments of  $Z$  and  $H$  are identical; this turns out to be true also for  $Z_{cl}$  [222]. Therefore, IE proposes to interpolate via the fourth cumulant, with interpolation parameter  $p$  defined as

$$p = \frac{\kappa_4^{(H)} - \kappa_4^{(A\boxplus B)}}{\kappa_4^{(A*B)} - \kappa_4^{(A\boxplus B)}} \quad (3.14)$$

For Scheme I, IE always favors the free convolution limit ( $p = 0$ ) over the classical limit ( $p = 1$ ); this follows from our previous analysis that  $\kappa_4^{(H)} = \kappa_4^{(A_1 \boxplus B_1)}$ . In Scheme II, however, we observe the unexpected result that  $p$  is always negative regardless of the noise strength  $\sigma/J$ . From our previous analysis,  $\kappa_4^{(A_2+B_2)} - \kappa_4^{(A_2 \boxplus B_2)} = -\sigma^4/4$ . Additionally,  $\kappa_4^{(A_2*B_2)} \neq \kappa_4^{(A_2 \boxplus B_2)}$  where the only discrepancy lies is in the so-called departing term  $\langle A_2 B_2 A_2 B_2 \rangle$  [222, 223]. This term contributes 0 to  $\kappa_4^{(A\boxplus B)}$  but has value  $\langle A_2^2 \rangle \langle B_2^2 \rangle = (J^2 + \sigma^2/2)^2$  in  $\kappa_4^{(A_2*B_2)}$ , since for the classical convolution,  $\langle \Pi_{s=1}^r (A_2^{n_s} B_2^{m_s}) \rangle = \langle A_2^{\sum_{s=1}^r n_s} \rangle \langle B_2^{\sum_{s=1}^r m_s} \rangle$ . Thus  $p = -2 \left( 2 \left( \frac{\sigma}{J} \right)^{-2} + 1 \right)^{-2}$  which is manifestly negative.

In conclusion, the accuracy of approximations using the free convolution depend crucially on the way the Hamiltonian is partitioned. Scheme I describes an unexpectedly accurate approximation for the DOS of disordered Hamiltonians for all system sizes  $N$  and noise strengths  $\sigma/J$ . Our error analysis explains why this approximation is correct to degree 8, and also provides a general framework for understanding the performance of other approximations. We expect our results to be generally applicable to arbitrary Hamiltonians, and pave the way toward constructing even more accurate approximations using free probability with rigorous error bars. Our results represent an optimistic beginning to the use of powerful and highly accurate nonperturbative methods for studying the electronic properties of disordered condensed matter systems regardless of the strength of noise present. Thus, we expect these methods to be especially useful for studying the unique physics enabled by noise.

### 3.8 Acknowledgments

The work described in this chapter was carried out in collaboration with Jiahao Chen, Eric Hontz, Jeremy Moix, Alberto Suarez, Ramis Movassagh, and Alan Edelman. They are listed as co-authors in reference [54].



## Chapter 4

# Densities of states for disordered systems from free probability: live free or diagonalize!

We investigate how free probability allows us to approximate the density of states in tight binding models of disordered electronic systems. Extending our previous studies of the Anderson model in one dimension with nearest-neighbor interactions [54], we find that free probability continues to provide accurate approximations for systems with constant interactions on two- and three-dimensional lattices or with next-nearest-neighbor interactions, with the results being visually indistinguishable from the numerically exact solution. For systems with disordered interactions, we observe a small but visible degradation of the approximation. To explain this behavior of the free approximation, we develop and apply an asymptotic error analysis scheme to show that the approximation is accurate to the eighth moment in the density of states for systems with constant interactions, but is only accurate to sixth order for systems with disordered interactions. The error analysis also allows us to calculate asymptotic corrections to the density of states, allowing for systematically improvable approximations as well as insight into the sources of error without requiring a direct comparison to an exact solution.

### 4.1 Introduction

Disordered matter is ubiquitous in nature and in manmade materials [377]. Random media such as glasses [120, 101, 76], disordered alloys [221, 332], and disordered metals [122, 88, 85] exhibit unusual properties resulting from the unique physics produced by statistical fluctuations. For example, disordered materials often exhibit unusual electronic properties, such as in the weakly bound electrons

in metal–ammonia solutions [184, 51, 209], or in water [345, 275]. Paradoxically, disorder can also enhance transport properties of excitons in new photovoltaic systems containing bulk heterojunction layers [254, 213, 370] and quantum dots [19, 308], producing anomalous diffusion effects [38, 296, 133] which appear to contradict the expected effects of Anderson localization [10, 327, 25]. Accounting for the effects of disorder in electro-optic systems is therefore integral for accurately modeling and engineering second-generation photovoltaic devices [80].

Disordered systems are challenging for conventional quantum methods, which were developed to calculate the electronic structure of systems with perfectly known crystal structures. Determining the electronic properties of a disordered material thus necessitates explicit sampling of relevant structures from thermodynamically accessible regions of the potential energy surface, followed by quantum chemical calculations for each sample. Furthermore, these materials lack long-range order and must therefore be modeled with large supercells to average over possible realizations of short-range order and to minimize finite-size effects. These two factors conspire to amplify the cost of electronic structure calculations on disordered materials enormously.

To avoid such expensive computations, we consider instead calculations where the disorder is treated explicitly in the electronic Hamiltonian. The simplest such Hamiltonian comes from the Anderson model [10, 95], which is a tight binding lattice model of the electronic structure of a disordered electronic medium. Despite its simplicity, this model nonetheless captures the rich physics of strong localization and can be used to model the conductivity of disordered metals [327, 25, 83]. However, the Anderson model cannot be solved exactly except in special cases [125, 198], which complicates studies of its excitation and transport properties. Studying more complicated systems thus requires accurate, efficiently computable approximations for the experimental observables of interest. While other methods exist to accurately treat similar tight binding models efficiently [135, 136, 317], they still require explicit sampling of many realizations of the disorder.

Random matrix theory offers new possibilities for developing accurate approximate solutions to disordered systems [361, 24, 7] by treating the ensemble of disordered Hamiltonians all at once rather than first sampling this ensemble and then averaging observables. In this chapter, we focus on using random matrix theory to construct efficient approximations for the density of states of a random medium. The density of states is one of the most important quantities that characterize an electronic system, and a large number of physical observables can be calculated from it [172], including band structure, precursors to absorption spectra [136, 210], chemisorption properties [127] and in turn catalysis on surfaces [321, 265], and transition rates from Fermi’s Golden Rule [40]. In disordered electronics, the shape of the density of states is a key predictor of charge carrier mobility [240, 324], and has found such application in organic photovoltaics [212], bulk heterojunctions [269], and organic/polymer transistors [330, 319, 325]. Furthermore, it only depends on the eigenvalues of the Hamiltonian and is thus simpler to approximate, as information about the eigenvectors is not

needed.

The density of states is not a complete description of a physical system. Other interesting observables, such as correlation functions and transport properties require knowledge of eigenvectors. While not a solved problem, the application of random matrix methods to eigenvectors remains an active area of research [26]. Some intriguing results that suggest it may be possible to calculate some transport properties, such as localization lengths, solely from eigenvalue statistics [35]. Nonetheless, the calculation of the density of states for real systems is already a sufficiently challenging problem, and we focus on more complex models in this chapter, leaving open the future possibility of applying free probability to more complex classes of observables in these models.

We have previously shown that highly accurate approximations can be constructed using free probability theory for the simplest possible Anderson model, i.e. on a one-dimensional lattice with constant nearest-neighbor interactions [54]. However, it remains to be seen if similar approximations are sufficient to describe more complicated systems, and in particular if the richer physics produced by more complicated lattices and by off-diagonal disorder can be captured using such free probabilistic methods.

In this chapter, we present a brief, self-contained introduction to free probability theory in Section 4.2. We then develop approximations from free probability theory in Section 4.3 that generalize our earlier study [54] in three ways. First, we develop analogous approximations for systems with long range interactions, specializing to the simplest such extension of a one-dimensional lattices with next-nearest-neighbor interactions. Second, we study lattices in two and three dimensions. We consider square and hexagonal two-dimensional lattices to investigate the effect of coordination on the approximations. Third, we also make the interactions random and develop approximations for these systems as well. These cases are summarized graphically in Figure 4-1 and are representative of the diversity of disorder systems described above. Finally, we introduce an asymptotic error analysis which allows us to quantify and analyze the errors in the free probability approximations in Section 4.4.

## 4.2 Free probability

### 4.2.1 Free independence

In this section, we briefly introduce free probability by highlighting its parallels with (classical) probability theory. One of the core ideas in probability theory [98] is how to characterize the relationship between two (scalar-valued) random variables  $x$  and  $y$ . They may be correlated, so that the joint moment  $\langle xy \rangle$  is not simply the product of the individual expectations  $\langle x \rangle \langle y \rangle$ , or they may be correlated in a higher order moment, i.e. there are some smallest positive integers  $m$  and  $n$  for which  $\langle x^m y^n \rangle \neq \langle x^m \rangle \langle y^n \rangle$ . If neither case holds, then they are said to be independent, i.e. that

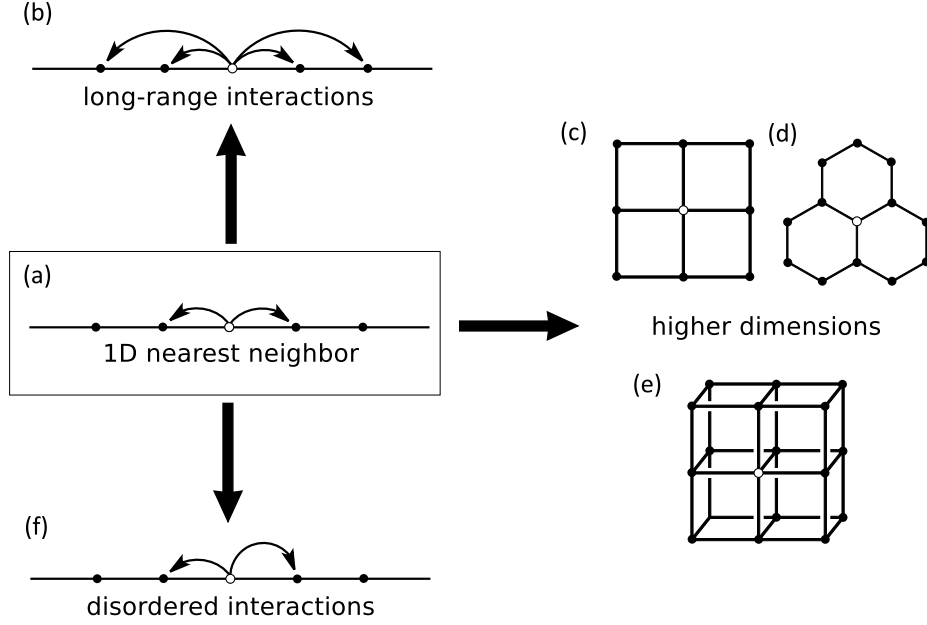


Figure 4-1: The lattices considered in this chapter: (a) one-dimensional chain with nearest neighbor interactions, (b) one-dimensional chain with many neighbors, (c) two-dimensional square lattice, (d) two-dimensional hexagonal (honeycomb) lattice, (e) three-dimensional cubic lattice, and (f) one dimensional-chain with disordered interactions.

all their joint moments of the form  $\langle x^m y^n \rangle$  factorize into products of the form  $\langle x^m y^n \rangle = \langle x^m \rangle \langle y^n \rangle$ . For random matrices, similar statements can be written down if the expectation  $\langle \cdot \rangle$  is interpreted as the normalized expectation of the trace, i.e.  $\langle \cdot \rangle = \frac{1}{N} \mathbb{E} \text{Tr} \cdot$ , where  $N$  is the size of the matrix. However, matrices in general do not commute, and therefore this notion of independence is no longer unique: for noncommuting random variables, one cannot simply take a joint moment of the form  $\langle A^{m_1} B^{n_1} \dots A^{m_k} B^{n_k} \rangle$  and assert it to be equal in general to  $\langle A^{m_1 + \dots + m_k} B^{n_1 + \dots + n_k} \rangle$ . The complications introduced by noncommutativity give rise to a different theory, known as free probability theory, for noncommuting random variables [234]. This theory introduces the notion of free independence, which is the noncommutative analogue of (classical) independence. Specifically, two noncommutative random variables  $A$  and  $B$  are said to be freely independent if for all positive integers  $m_1, \dots, m_k, n_1, \dots, n_k$ , the centered joint moment vanishes, i.e.

$$\langle \overline{A^{m_1}} \overline{B^{n_1}} \dots \overline{A^{m_k}} \overline{B^{n_k}} \rangle = 0, \quad (4.1)$$

where we have introduced the centering notation  $\overline{A} = A - \langle A \rangle$ . This naturally generalizes the notion of classical independence to noncommuting variables, as the former is equivalent to requiring that all the centered joint moments of the form  $\langle \overline{x^m} \overline{y^n} \rangle$  vanish. If the expectation  $\langle A \rangle$  is reinterpreted as the normalized expectation of the trace of a random matrix  $A$ , then the machinery of free independence can be applied directly to random matrices [342].

## 4.2.2 Free independence and the $R$ -transform

One of the central results of classical probability theory is that if  $x$  and  $y$  are independent random variables with distributions  $p_X(x)$  and  $p_Y(y)$  respectively, then the probability distribution of their sum  $x + y$  is given by the convolution of the distributions, i.e. [98]

$$p_{X+Y}(y) = \int_{-\infty}^{\infty} p_X(x) p_Y(x - y) dx. \quad (4.2)$$

An analogous result holds for freely independent noncommuting random variables and is known as the (additive) free convolution; this is most conveniently defined using the  $R$ -transform [234, 341, 304]. For a probability density  $p(x)$  supported on  $[a, b]$ , its  $R$ -transform  $R(w)$  is defined implicitly via

$$G(z) = \lim_{\epsilon \rightarrow 0^+} \int_a^b \frac{p(x)}{z - (x + i\epsilon)} dx \quad (4.3a)$$

$$R(w) = G^{-1}(w) - \frac{1}{w}. \quad (4.3b)$$

These quantities have natural analogues in Green function theory:  $p(x)$  is the density of states, i.e. the distribution of eigenvalues of the underlying random matrix;  $G(z)$  is the Cauchy transform of  $p(x)$ , which is the retarded Green function; and  $G^{-1}(w) = R(w) + 1/w$  is the self-energy. The  $R$ -transform allows us to define the free convolution of  $A$  and  $B$ , denoted  $A \boxplus B$ , by adding the individual  $R$ -transforms

$$R_{A \boxplus B}(w) := R_A(w) + R_B(w). \quad (4.4)$$

This finally allows to state that if  $A$  and  $B$  are freely independent, then the sum  $A + B$  must satisfy

$$R_{A+B}(w) = R_{A \boxplus B}(w). \quad (4.5)$$

In general, random matrices  $A$  and  $B$  are neither classically independent nor freely independent. However, we can always construct combinations of them that are always freely independent. One such combination is  $A + Q^\dagger B Q$ , where  $Q$  is a random orthogonal (unitary) matrix of uniform Haar measure, as applied to real symmetric (Hermitian)  $A$  and  $B$  [89]. The similarity transform effected by  $Q$  randomly rotates the basis of  $B$ , so that the eigenvectors of  $A$  and  $B$  are always in generic position, i.e. that any eigenvector of  $A$  is uncorrelated with any eigenvector of  $B$  [7]. This is the main result that we wish to exploit. While in general  $A$  and  $B$  are not freely independent, and hence (4.5) fails to hold exactly, we can nonetheless make the approximation that (4.5) holds *approximately*, and use this as a way to calculate the density of states of a random matrix  $H$  using only its decomposition into a matrix sum  $H = A + B$ . Our application of this idea to the Anderson model is described

below.

## 4.3 Numerical results

### 4.3.1 Computation of the Density of States and its Free Approximant

We now wish to apply the framework of free probability theory to study Anderson models beyond the one-dimensional nearest-neighbor model which was the focus of our initial study [54]. It is well-known that more complicated Anderson models exhibit rich physics that are absent in the simplest case. First, the one-dimensional Anderson Hamiltonian with long range interactions has delocalized eigenstates at low energies and an asymmetric density of states, features that are absent in the simplest Anderson model [70, 74, 75, 204, 273]. These long range interactions give rise to slowly decaying interactions in many systems, such as spin glasses [101, 30] and ionic liquids [259]. Second, two-dimensional lattices can exhibit weak localization [4], which is responsible for the unusual conductivities of low temperature metal thin films [82, 27]. The hexagonal (honeycomb) lattice is of particular interest as a tight binding model for nanostructured carbon allotropes such as carbon nanotubes [278] and graphene [141, 50], which exhibit novel electronic phases with chirally tunable band gaps [126, 279] and topological insulation [49, 220]. Third, the Anderson model in three dimensions exhibits nontrivial localization phases that are connected by the metal–insulator transition [10, 284]. Fourth, systems with off-diagonal disorder, such as substitutional alloys and Frenkel excitons in molecular aggregates [377, 100], exhibit rich physics such as localization transitions in lattices of any dimension [12], localization dependence on lattice geometry [148], Van Hove singularities [41], and asymmetries in the density of states [100]. Despite intense interest in the effects of off-diagonal disorder, such systems have resisted accurate modeling [32, 178, 94, 91, 320, 31, 295, 288, 287]. We are therefore interested to find out if our approximations as developed in our initial study [54] can be applied also to all these disordered systems.

The Anderson model can be represented in the site basis by the matrix with elements

$$H_{ij} = g_i \delta_{ij} + J_{ij} \tag{4.6}$$

where  $g_i$  is the energy of site  $i$ ,  $\delta_{ij}$  is the usual Kronecker delta, and  $J_{ij}$  is the matrix of interactions with  $J_{ii} = 0$ . Unless otherwise specified, we further specialize to the case of constant interactions between connected neighbors, so that  $J_{ij} = JM_{ij}$  where  $J$  is a scalar constant representing the interaction strength, and  $M$  is the adjacency matrix of the underlying lattice. Unless specified otherwise, we also apply vanishing (Dirichlet) boundary conditions, as this reduces finite-size fluctuations in the density of states relative to periodic boundary conditions. For concrete numerical calculations, we also choose the site energies  $g_i$  to be iid Gaussian random variables of variance  $\sigma^2$  and mean

0. With these assumptions, the strength of disorder in the system can be quantified by a single dimensionless parameter  $\sigma/J$ .

The particular quantity we are interested in approximating is the density of states, which is one of the most important descriptors of electronic band structure in condensed matter systems [172]. It is defined as the distribution

$$\rho_H(x) = \left\langle \sum_j \delta(x - \epsilon_j) \right\rangle \quad (4.7)$$

where  $\epsilon_j$  is the  $j$ th eigenvalue of a sample of  $H$  and the expectation  $\langle \cdot \rangle$  is the ensemble average.

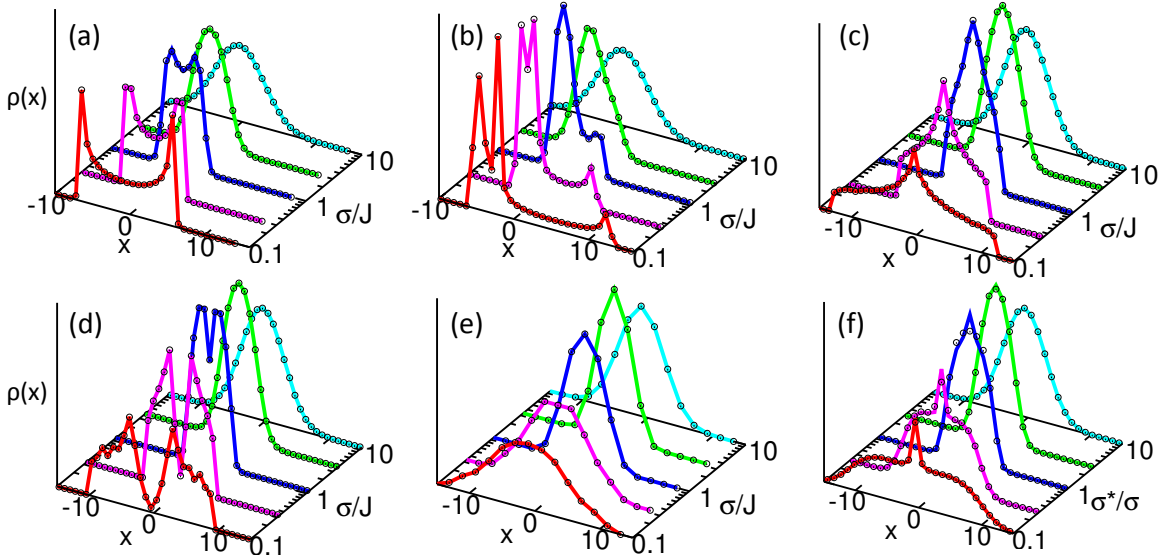
To apply the approximations from free probability theory, we partition our Hamiltonian matrix into its diagonal and off-diagonal components  $A$  and  $B$ . The density of states of  $A$  is simply a Gaussian of mean 0 and variance  $\sigma^2$ , and for many of our cases studied below, the density of states of  $B$  is proportional to the adjacency matrix of well-known graphs [313] and hence is known analytically. We then construct the free approximant

$$H' = A + Q^T B Q \quad (4.8)$$

where  $Q$  is a random orthogonal matrix of uniform Haar measure as discussed in Section 4.2.2, and find its density of states  $\rho_{H'}$ . Specific samples of  $Q$  can be generated by taking the orthogonal part of the QR decomposition [112] of matrix from the Gaussian orthogonal ensemble (GOE) [79]. We then average the approximate density of states over many realizations of the Hamiltonian and  $Q$  and compare it to the ensemble averaged density of states generated from exact diagonalization of the Hamiltonian. We choose the number of samples to be sufficient to converge the density of states with respect to the disorder in the Hamiltonian.

While this method is more costly than diagonalization of the exact Hamiltonian, it provides a general and robust test for the quality of the free approximation for this exploratory study. A far more efficient method would be to numerically compute the free convolution directly. The Cauchy transform of the densities of states of  $A$  and  $B$  (equation 4.3a) can be computed via a series expansion [242]. With careful numerics, the functional inverses of the Cauchy transform can be computed, giving the R-transforms, which are then added (equations 4.3b and 4.4) [243]. This process is then inverted, where the inverse Cauchy transform is computed using Plemelj's lemma [137]. While this process is fairly straightforward, it has proven numerically challenging. As such, we use equation 4.8 as a general and accurate test of the quality of the free approximation, anticipating that further work could use the more efficient free convolution once the numerical issues are solved.

Figure 4-2: Comparison of exact density of states (lines) with free probability approximant (circles) for the lattices in Figure 4-1, with (b) showing the case of  $n = 4$  neighbors. Data are shown for multiple values of a dimensionless parameter quantifying the strength of disorder to show the robustness of this approximation. For (a-e), this parameter is  $\sigma/J$ , the ratio of the noisiness of diagonal elements to the strength of off-diagonal interaction. In (f), the axis is chosen to be the relative strength of off-diagonal disorder to diagonal disorder,  $\sigma^*/\sigma$ , with  $\sigma/J = 1$ .



### 4.3.2 One-dimensional chain

We now proceed to apply the theory of the previous section to specific examples of the Anderson model on various lattices. Previously, we had studied the Anderson model on the one-dimensional chain [54]:

$$H_{ij} = g_i \delta_{ij} + J(\delta_{i,j+1} + \delta_{i,j-1}), \quad (4.9)$$

which is arguably the simplest model of a disordered system. Despite its simple tridiagonal form, this Hamiltonian does not have an exact solution for its density of states, and many approximations for it have been developed [369]. However, unlike the original Hamiltonian, the diagonal and off-diagonal components each have a known density of states when considered separately. To calculate the density of states of the Hamiltonian, we diagonalized 1000 samples of  $1000 \times 1000$  matrices, so that the resulting density of states is converged with respect to both disorder and finite-size effects. The results are shown in Figure 4-2(a), demonstrating that the free approximation to the density of states is visually indistinguishable from the exact result over all the entire possible range of disorder strength  $\sigma/J$ .

### 4.3.3 One-dimensional lattice with non-neighbor interactions

Going beyond tridiagonal Hamiltonians, we next study the Anderson model on a one-dimensional chain with constant interactions to  $n$  neighbors. The Hamiltonian then takes the form:

$$H_{ij}^{1D} = g_i \delta_{ij} + J \left[ \sum_{k=1}^n \delta_{i,j+k} + \delta_{i+k,j} \right]. \quad (4.10)$$

where we use the superscript to distinguish the one-dimensional many-neighbor Hamiltonian from its higher dimensional analogs. Unlike the nearest-neighbor interaction case above, the density of states is known to exhibit Van Hove singularities at all but the strongest disorder [327, 377].

We average over 1000 samples of  $1000 \times 1000$  Hamiltonians, which as before ensures that the density of states is numerically converged with respect to statistical fluctuations and finite-size effects. We looked at the case of  $n = 2, \dots, 6$  neighbors with identical interaction strengths, and also interaction strengths that decayed linearly with distance to better model the decay of interactions with distance in more realistic systems. The free approximant is of similar quality in all cases. As shown in Figure 4-2(b) for  $n = 4$  neighbors, the free approximant reproduces these singular features of the density of states, unlike perturbative methods which are known to smooth them out [8, 134]. The reproduction of singularities by the free approximant parallels similar observations found in other applications of free probability to quantum information theory [223].

### 4.3.4 Square, hexagonal and cubic lattices

We now investigate the effect of dimensionality on the accuracy of the free approximant in three lattices. First, we consider the Anderson model on the square lattice, with Hamiltonian:

$$H^{2D} = B^{1D} \otimes I + I \otimes B^{1D} + A \quad (4.11)$$

where  $B^{1D}$  is the off-diagonal part of the  $H^{1D}$  defined in equation (4.10),  $I$  is the identity matrix with the same dimensions as  $B^{1D}$ ,  $A$  is the diagonal matrix of independent random site energies of appropriate dimension, and  $\otimes$  is the Kronecker (direct) product. We have found that a square lattice of  $50 \times 50 = 2500$  sites is the smallest lattice with negligible finite size fluctuations in the density of states. As such, we calculated the density of states for 500 samples of  $3600 \times 3600$  Hamiltonians. We find that for both nearest-neighbors (shown in Figure 4-2(c)) and non-nearest-neighbors (specifically,  $n = 2, \dots, 6$ ), the free approximation is again visually identical to the exact answer.

Second, we consider the honeycomb (hexagonal) lattice, which has a lower coordination number than the square lattice. Its adjacency matrix does not have a simple closed form, but can nonetheless be easily generated. For this lattice, we averaged over 1000 samples of matrices of size  $968 \times 968$ , and applied periodic boundary conditions to illustrate their effect. As in the square case of the two

dimensional grid model, the density of states of the honeycomb lattice with any number of coupled neighbor shells is well reproduced by the free approximant (Figure 4-2(d)), even reproducing the Van Hove singularities at low to moderate site disorder. Additionally, we see that the finite-size oscillations at low disorder ( $\sigma/J \sim 0.1$ ) are also reproduced by the free approximation.

Third, we consider the Anderson model on a cubic lattice, whose Hamiltonian is:

$$H^{3D} = (B^{1D} \otimes I \otimes I) + (I \otimes B^{1D} \otimes I) + (I \otimes I \otimes B^{1D}) + A \quad (4.12)$$

Figure 4-2(e) shows the approximate and exact density of states calculated from 1000 samples of  $1000 \times 1000$  matrices. This represents a  $10 \times 10 \times 10$  cubic lattice which is significantly smaller in linear dimension than the previously considered lattices. We therefore observed oscillatory features in the density of states arising from finite-size effects. Despite this, the free approximant is still able to reproduce the exact density of states quantitatively. In fact, if the histogram in Figure 4-2(e) is recomputed with finer histogram bins to emphasize the finite-size induced oscillations, we still observe that the free approximant reproduces these features.

### 4.3.5 Off-diagonal disorder

Up to this point, all of the models we have considered have only site disorder, with no off-diagonal disorder. Free probability has thus far provided a qualitatively correct approximation for all these lattices. To test the robustness of this approximation, we now investigate systems with random interactions. The simplest such system is the one-dimensional chain, with a Hamiltonian of the form:

$$H_{ij} = g_i \delta_{ij} + h_i (\delta_{i,j+1} + \delta_{i,j-1}). \quad (4.13)$$

Unlike in the previous systems, the interactions are no longer constant, but are instead new random variables  $h_i$ . We choose them to be Gaussians of mean  $J$  and variance  $(\sigma^*)^2$ . There are now two order parameters to consider:  $\sigma^*/J$ , the relative disorder in the interaction strengths, and  $\sigma^*/\sigma$ , the strength of off-diagonal disorder relative to site disorder. As in the prior one-dimensional case, we average over 1000 realizations of  $1000 \times 1000$  matrices.

We now observe that the quality of the free approximation is no longer uniform across all values of the order parameters. Instead, it varies with  $\sigma^*/\sigma$ , but not  $\sigma^*/J$ . In Figure 4-2(f), we demonstrate the results of varying  $\sigma^*/\sigma$  with  $\sigma/J = 1$ . In the limits  $\sigma^*/\sigma \gg 1$  and  $\sigma^*/\sigma \ll 1$ , the free approximation matches the exact result well; however, there is a small but noticeable discrepancy between the exact and approximate density of states for moderate relative off-diagonal disorder, though the quality of the approximation is mostly unaffected by the centering of the off-diagonal disorder. In the next section, we will investigate the nontrivial behavior of the approximation with

the  $\sigma^*/\sigma$  order parameter.

## 4.4 Error analysis

In our numerical experiments, we have found that the accuracy of the free approximation remains excellent for systems with only site disorder, regardless of the underlying lattice topology or the number of interactions that each site has. Details such as finite-size oscillations and Van Hove singularities are also captured when present. However, when off-diagonal disorder is present, the quality of the approximation does vary qualitatively with the ratio of off-diagonal disorder to site disorder  $\sigma^*/\sigma$  as illustrated in Section 4.3.5, and the error is greatest when  $\sigma^* \approx \sigma$ . To understand the reliability of the free approximant (4.8) in all these situations, we apply an asymptotic moment expansion to calculate the leading order error terms for the various systems. In general, a probability density  $\rho$  can be expanded with respect to another probability density  $\tilde{\rho}$  in an asymptotic moment expansion known as the Edgeworth series [53, 314]:

$$\rho(x) = \exp\left(\sum_{m=1}^{\infty} \frac{\kappa^{(m)} - \tilde{\kappa}^{(m)}}{m!} \left(-\frac{d}{dx}\right)^m\right) \tilde{\rho}(x) \quad (4.14)$$

where  $\kappa^{(m)}$  is the  $m$ th cumulant of  $\rho$  and  $\tilde{\kappa}^{(m)}$  is the  $m$ th cumulant of  $\tilde{\rho}$ . When all the cumulants exist and are finite, this is an exact relation that allows for the distribution  $\tilde{\rho}$  to be systematically corrected to become  $\rho$  by substituting in the correct cumulants. If the first  $(n-1)$  cumulants of  $\rho$  and  $\tilde{\rho}$  match, but not the  $n$ th, then we can calculate the leading-order asymptotic correction to  $\tilde{\rho}$  as:

$$\rho(x) = \exp\left(\frac{\kappa^{(n)} - \tilde{\kappa}^{(n)}}{n!} \left(-\frac{d}{dx}\right)^n + \dots\right) \tilde{\rho}(x) \quad (4.15a)$$

$$= \left(1 + \frac{\kappa^{(n)} - \tilde{\kappa}^{(n)}}{n!} \left(-\frac{d}{dx}\right)^n + \dots\right) \tilde{\rho}(x) \quad (4.15b)$$

$$= \tilde{\rho}(x) + \frac{(-1)^n}{n!} (\kappa^{(n)} - \tilde{\kappa}^{(n)}) \frac{d^n \tilde{\rho}}{dx^n}(x) + \mathcal{O}\left(\frac{d^{n+1} \tilde{\rho}}{dx^{n+1}}\right) \quad (4.15c)$$

$$= \tilde{\rho}(x) + \frac{(-1)^n}{n!} (\mu^{(n)} - \tilde{\mu}^{(n)}) \frac{d^n \tilde{\rho}}{dx^n}(x) + \mathcal{O}\left(\frac{d^{n+1} \tilde{\rho}}{dx^{n+1}}\right) \quad (4.15d)$$

where on the second line we expanded the exponential  $e^X = 1 + X + \dots$ , and on the fourth line we used the well-known relationship between cumulants  $\kappa$  and moments  $\mu$  and the fact that the first  $n-1$  moments of  $\rho$  and  $\tilde{\rho}$  were identical by assumption.

We can now use this expansion to calculate the leading-order difference between the exact density of states  $\rho_H = \rho_{A+B}$ , and its free approximant  $\rho_{H'} = \rho_{A\boxplus B}$  by setting  $\tilde{\rho} = \rho_{H'}$  and  $\rho = \rho_H$  in (4.15d). The only additional data required are the moments  $\mu_H^{(n)} = \langle H^n \rangle$  and  $\mu_{H'}^{(n)} = \langle (H')^n \rangle$ ,

which can be computed from the sampled data or recursively from the joint moments of  $A$  and  $B$  as detailed in the previous chapter. This then gives us a way to detect discrepancies, which is to calculate successively higher moments of  $H$  and  $H'$  to determine whether the difference in moments is statistically significant, and then for the smallest order moment that differs, calculate the correction using (4.15d).

The error analysis also yields detailed information about the source of error in the free approximation. The  $n$ th moment of  $H$  is given by

$$\mu_H^{(n)} = \langle H^n \rangle = \langle (A + B)^n \rangle = \sum_{\substack{m_1, n_1, \dots, m_k, n_k \\ \sum_{j=1}^k m_j + n_j = n}} \langle A^{m_1} B^{n_1} \dots A^{m_k} B^{n_k} \rangle, \quad (4.16)$$

where the last equality arises from expanding  $(A + B)^n$  in a noncommutative binomial series. If  $A$  and  $B$  are freely independent, then each of these terms must satisfy recurrence relations that can be derived from the definition (4.1) [53]. Exhaustively enumerating and examining each of the terms in the final sum to see if they satisfy (4.1) thus provides detailed information about the accuracy of the free approximation.

We now apply this general error analysis for the specific systems we have studied. It turns out that the results for systems with and without off-diagonal disorder exhibit different errors, and so are presented separately below.

#### 4.4.1 Systems with constant interactions

We have previously shown that for the one-dimensional chain with nearest-neighbor interactions, the free approximant is exact in the first seven moments, and that the only term in the eighth moment that differs between the free approximant and the exact  $H$  is  $\langle (AB)^4 \rangle$  [54]. The value of this joint moment can be understood in terms of discretized hopping paths on the lattice [361]. Writing out the term  $\langle (AB)^4 \rangle$  explicitly in terms of matrix elements and with Einstein's implicit summation convention gives:

$$\langle (AB)^4 \rangle = \frac{1}{N} \mathbb{E} (A_{i_1 i_2} B_{i_2 i_3} A_{i_3 i_4} B_{i_4 i_5} A_{i_5 i_6} B_{i_6 i_7} A_{i_7 i_8} B_{i_8 i_1}) \quad (4.17a)$$

$$= \frac{1}{N} \mathbb{E} ((g_{i_1} \delta_{i_1 i_2}) (JM_{i_2 i_3}) (g_{i_3} \delta_{i_3 i_4}) (JM_{i_4 i_5}) (g_{i_5} \delta_{i_5 i_6}) (JM_{i_6 i_7}) (g_{i_7} \delta_{i_7 i_8}) (JM_{i_8 i_1})) \quad (4.17b)$$

$$= \frac{1}{N} \mathbb{E} (g_{i_1} g_{i_2} g_{i_3} g_{i_4} J^4 M_{i_1 i_2} M_{i_2 i_3} M_{i_3 i_4} M_{i_4 i_1}). \quad (4.17c)$$

From this calculation, we can see that each multiplication by  $A$  weights each path by the site energy of a given site,  $g_i$ , and each multiplication by  $B$  weights the path by  $J$  and causes the path to hop to

a coupled site. The sum therefore reduces to a weighted sum over returning paths on the lattice that must traverse exactly three intermediate sites. The only paths on the lattice with nearest-neighbors that satisfy these constraints are shown in Figure 3(a), namely  $(i_1, i_2, i_3, i_4) = (k, k + 1, k, k + 1)$ ,  $(k, k + 1, k + 2, k + 1)$ ,  $(k, k - 1, k, k - 1)$ , and  $(k, k - 1, k - 2, k - 1)$  for some starting site  $k$ . The first path contributes weight  $\mathbb{E}(g_k^2 g_{k+1}^2) J^4 = \mathbb{E}(g_k^2) \mathbb{E}(g_{k+1}^2) J^4 = \sigma^4 J^4$  while the second term has weight  $\mathbb{E}(g_k g_{k+1}^2 g_{k+2}) J^4 = \mathbb{E}(g_k) \mathbb{E}(g_{k+1}^2) \mathbb{E}(g_{k+2}) J^4 = 0$ . Similarly, the third and fourth paths also have weight  $\sigma^4 J^4$  and 0 respectively. Finally averaging over all possible starting sites, we arrive at the final result that  $\langle (AB)^4 \rangle = 2\sigma^4 J^4$  with periodic boundary conditions and  $\langle (AB)^4 \rangle = 2(1 - 1/N) \sigma^4 J^4$  with vanishing boundary conditions. We therefore see when  $N$  is sufficiently large, the boundary conditions contribute a term of  $\mathcal{O}(1/N)$  which can be discarded, thus showing the universality of this result regardless of the boundary conditions.

Applying the preceding error analysis, we observe that the result from the one-dimensional chain generalizes all the other systems with constant interactions that we have studied; the only difference being that the coefficient 2 is simply replaced by  $n$ , the number of sites accessible in a single hop from a given lattice site. In order to keep the effective interaction felt by a site constant as we scale  $n$ , we can choose  $J$  to scale as  $\frac{1}{\sqrt{n}}$ . In this case, the free approximation converges to the exact result as  $\frac{1}{n}$ .

We can generalize the argument presented above to explain why  $\langle (\overline{AB})^4 \rangle$  is the first nonzero joint centered moment, and thus why the approximation does not break down before the eighth moment. Consider centered joint moments of the form:

$$\langle \overline{A^{a_1} B^{b_1} A^{a_2} B^{b_2} \dots A^{a_n} B^{b_n}} \rangle \quad (4.18)$$

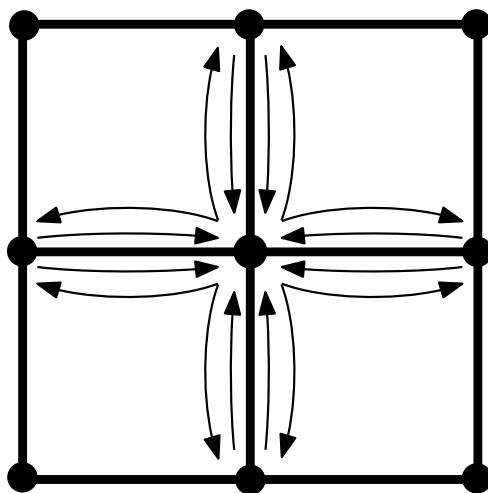
for positive integers  $\{a_i, b_i\}$  such that  $\sum_i (a_i + b_i) \leq 8$ . Since  $A$  is diagonal with iid elements, all powers of  $A^n$  are also diagonal with iid elements, and so  $\overline{A^n} = 0$ . Centered higher powers of  $B$ ,  $\overline{B^n}$ , couple each site to other sites with interaction strengths  $J^n$ , but after centering, the diagonal elements of  $\overline{B^n}$  are zero and multiplication by  $\overline{B^n}$  still represents a hop from one site to a different coupled site. Therefore, the lowest order nonzero joint centered moment requires at least four hops, so  $n \geq 4$  is the smallest possible nonzero term, but but the only term of this form of eighth order or lower is the one with  $a_i = b_i = 1$ , i.e. the term  $\langle (AB)^4 \rangle$ .

#### 4.4.2 Random interactions

When the off-diagonal interactions are allowed to fluctuate, the free approximation breaks down in the sixth moment, where the joint centered moment  $\langle (\overline{AB^2})^2 \rangle$  fails to vanish. We can understand this using a generalization of the hopping explanation from before. In this case,  $\overline{B^2}$  contains nonzero diagonal elements, which corresponds to a nonzero weight for paths that stay at the same site. Thus,

Figure 4-3: (a) Diagrammatic representation of the four paths that contribute to the leading order error for the case of a two-dimensional square lattice with constant interactions and nearest neighbors. Dots contribute a factor of  $g_i$  for site  $i$ . Solid arrows represent a factor of  $J$ . Each path contributes  $J^4 \langle g_a^2 \rangle \langle g_b^2 \rangle = \sigma^4 J^4$  to the error. (b) Build up of the diagrammatic representation the leading order error in the case of a 1D chain with off-diagonal disorder. The two dashed arrows contribute a factor of  $\mu_4 - \mu_2^2$ . Because of the disorder in the interactions, multiplication by  $\overline{B^2}$  allows loops back to the same site. The first of these loops,  $\langle \overline{AB^2} \rangle$ , has zero expectation value because it contains an independent random variable of mean zero as a factor. Once two loops are present, the expectation value instead contains this random variable squared, which has nonzero expectation value.

(a)



(b)

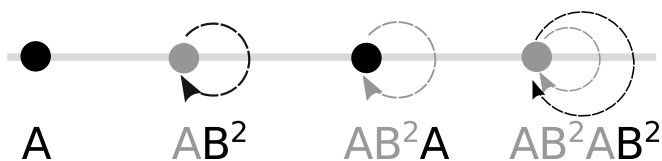


Table 4.1: Coefficients of the leading-order error in the free probability approximation in the Edgeworth expansion (4.15d).

	Order	Term	Coefficient
1D	8	$(AB)^4$	$\tilde{J}^4 \sigma^4 / (2 \cdot 8!)$
2D square	8	$(AB)^4$	$\tilde{J}^4 \sigma^4 / (4 \cdot 8!)$
2D honeycomb	8	$(AB)^4$	$\tilde{J}^4 \sigma^4 / (3 \cdot 8!)$
3D cube	8	$(AB)^4$	$\tilde{J}^4 \sigma^4 / (6 \cdot 8!)$
1D with $n$ nearest-neighbors	8	$(AB)^4$	$\tilde{J}^4 \sigma^4 / (2n \cdot 8!)$
1D with off-diagonal disorder	6	$(AB^2)^2$	$\sigma^2 (\mu_4 - \mu_2^2) / 6!$

$(\overline{AB^2})^2$  contains a path of nonzero weight that starts at a site and loops back to that site twice (shown in Figure 3(b)). The overall difference in the moment of the exact distribution from that in the free distribution is  $2\sigma^2 (\mu_4 - \mu_2^2)$ , where  $\mu_4$  and  $\mu_2$  are the fourth and second moments of the off-diagonal disorder. As above, the  $\sigma^2$  component of this difference can be understood as the contribution of the two  $A$ s in the joint centered moment. The other factor,  $2 (\mu_4 - \mu_2^2)$ , is the weight of the path of two consecutive self-loops. The sixth moment is the first to break down because, as before, we must hop to each node on our path twice in order to avoid multiplying by the expectation value of mean zero, and  $(AB^2)^2$  is the lowest order term that allows such a path.

We summarize the the leading order corrections and errors in Table 4.1. At this point, we introduce the quantity  $\tilde{J} = \sqrt{2n}J$ , which is an aggregate measure of the interactions of any site with all its  $2n$  neighbors. As can be seen, the discrepancy occurs to eighth order for all the studied systems with constant interactions, with a numerical prefactor indicative of the coordination number of the lattice, and the factor of  $1/8!$  strongly suppresses the contribution of the error terms. Furthermore, for any given value of the total interaction  $\tilde{J}$ , the error decreases quickly with coordination number  $2n$ , suggesting that the free probability approximation is exact in the mean field limit of  $2n \rightarrow \infty$  neighbors. This is consistent with previous studies of the Anderson model employing the coherent potential approximation.[327, 230, 231] In contrast, the system with off-diagonal disorder has a discrepancy in the sixth moment, which has a larger coefficient in the Edgeworth expansion (4.15d). This explains the correspondingly poorer performance of our free approximation for systems with off-diagonal disorder. Furthermore, the preceding analysis shows that only the first and second moments of the diagonal disorder  $\sigma$  contribute to the correction coefficient, thus showing that this behavior is universal for disorder with finite mean and standard deviation.

## 4.5 Conclusion

Free probability provides accurate approximations to the density of states of a disordered system, which can be constructed by partitioning the Hamiltonian into two easily-diagonalizable ensembles and then free convolving their densities of states. The previous chapter showed that this approxi-

mation worked well for the one-dimensional Anderson model partitioned into its diagonal and off-diagonal components. Our numerical and theoretical study described above demonstrates that the same approximation scheme is widely applicable to a diverse range of systems, encompassing more complex lattices and more interactions beyond the nearest-neighbor. The quality of the approximation remains unchanged regardless of the lattice as long as the interactions are constant, with the free approximation being in error only in the eighth moment of the density of states. When the interactions fluctuate, the quality of the approximation worsens, but remains exact in the first five moments of the density of states.

Our results strongly suggest that free probability has the potential to produce high-quality approximations for the properties of disordered systems. In particular, our theoretical analysis of the errors reveals universal features of the quality of the approximation, with the error being characterized entirely by the moments of the relevant fluctuations and the local topology of the lattice. This gives us confidence that approximations constructed using free probability will give us high-quality results with rigorous error quantification. This also motivates future investigations towards constructing fast free convolutions using numerical methods for  $R$ -transforms,[243] which would yield much faster methods for constructing free approximations. Additionally, further studies will be required to approximate more complex observables beyond the density of states, such as conductivities and phase transition points. These will require further theoretical investigation into how free probability can help predict properties of eigenvectors, which may involve generalizing some promising initial studies linking the statistics of eigenvectors such as their inverse participation ratios to eigenvalue statistics such as the spectral compressibility [173, 35].

## 4.6 Acknowledgments

The work described in this chapter was carried out in collaboration with Jiahao Chen. He is listed as a coauthor in reference [356].

## Chapter 5

# Density matrix embedding in an antisymmetrized geminal product wavefunction

Density matrix embedding theory (DMET) has emerged as a powerful tool for performing wave function-in-wave function embedding for strongly correlated systems. In traditional DMET, an accurate calculation is performed on a small impurity embedded in a mean field bath. Here, we extend the original DMET equations to account for correlation in the bath via an antisymmetrized geminal power (AGP) wave function. The resulting formalism has a number of advantages. First, it allows one to properly treat the *weak* correlation limit of independent pairs, which DMET is unable to do with a mean-field bath. Second, it associates a *size extensive* correlation energy with a given density matrix (for the models tested), which AGP by itself is incapable of providing. Third, it provides a reasonable description of charge redistribution in strongly correlated but non-periodic systems. Thus, AGP-DMET appears to be a good starting point for describing electron correlation in molecules, which are aperiodic and possess both strong and weak electron correlation.

### 5.1 Introduction

Accurate description of the electron correlation of molecules and materials is crucial for predicting their physical and chemical properties. Kohn-Sham Density Functional Theory (DFT)[143, 179] has enjoyed great success for large, weakly correlated systems, and has been routinely used as a compromise between accuracy and cost. However, it is now well known that most DFT approximations fail to describe strong correlation: for example, almost all DFT functionals break down for Mott insulators and transition metal oxides [255, 59]. Certain wave function methods, on the other hand, are

more reliable for treating strong correlation in small molecular systems [282, 360, 52, 283, 274, 44]. Unfortunately, they have significant limitations due to their steep computational scaling and thus cannot easily be applied to large and bulk systems. In particular, all correlated wave function methods will face an inevitable challenge in solids because of the computational effort required to evaluate the integration over the Brillouin zone [140]. Hence, it has become important to find new reliable and feasible descriptions of both weak and strong correlations for large systems.

In the last decade, much progress has been made on this problem, and it has attracted widespread attention. The central motivation is that electron correlation is *local* [266, 277, 15, 130]. This fact makes it possible to treat the whole system by decomposing it into a small local system (sometimes called an impurity) and its extended environment (sometimes called a bath) where the former is accurately treated under the influence of the latter. In other words, a small, tractable impurity system is *embedded* in the rest of system, where the impurity and bath interact with each other in some approximate but self-consistent manner. This system-bath breakup is the basis for a number of important forms of embedding.

On the one hand, subsystem DFT[66, 359] achieves this breakup at the level of densities - the density for the system is decomposed into an impurity (the subsystem) and a bath such that  $\rho_{imp}(\mathbf{r}) + \rho_{bath}(\mathbf{r}) = \rho_{total}(\mathbf{r})$ . Although the method was originally conceived as a route to DFT-in-DFT embedding with the expectation of linear scaling computational cost, it has more recently found success as a wave function-in-DFT embedding scheme. The energy of  $\rho_{imp}(\mathbf{r})$  is then computed using a high level of theory while  $\rho_{bath}(\mathbf{r})$  can be treated at a lower level of theory. In this case, the high level calculation is subject to a constraint potential  $v_{imp}(\mathbf{r})$  that forces the correlated density to match  $\rho_{imp}(\mathbf{r})$ . The resulting wavefunction-in-DFT embedding scheme can quite successfully describe systems where the subsystem has little correlation or coherence with the bath. For example, it has been used to describe molecules at surfaces [115], proteins [154], organic molecular crystals [232], and molecules in solution [20].

An alternative approach to the density embedding scenario is dynamical mean-field theory (DMFT) [217, 203, 107, 106]. Here, instead of embedding densities, one embeds the Green's function. A local impurity Green's function is constructed self-consistently with a larger bath Green's function. The local Green's function is determined by employing a quantum impurity solver (usually with high-level many-body theories or full configuration interaction (FCI)). The impurity Green's function is then used to construct the corresponding local self-energy. Self-consistency is obtained by performing this calculation on each fragment (with the other fragments as a bath) and iterating until the self energy converges. DMFT has been applied to solids with great success [219, 252, 29, 206, 73], and was recently extended to finite systems as well [155, 197, 333].

In practice, DMFT can be quite demanding, owing to the frequency integrals implicit in the Green's function formalism. Recently, Density Matrix Embedding Theory (DMET) has been pro-

posed as a simplified version of DMFT that still captures the same basic physics [175, 176]. Instead of using the Green’s function, DMET employs a frequency-independent variable: the one-particle density matrix (DM),  $\langle \hat{a}_i^\dagger \hat{a}_j \rangle$ . The information of the wave function is mapped onto its DM, and self-consistency is achieved by matching the DMs between the impurity solver and mean-field bath wave function, i.e. Hartree-Fock (HF). In this sense, DMET is intermediate between subsystem DFT and DMFT: it attempts to maintain the simple matching conditions of subsystem DFT while still incorporating the important strong correlation physics of DMFT. DMET accomplishes this feat by rigorously defining the impurity and bath in Fock space through Schmidt decomposition of the mean-field wave function [258, 257]. Importantly, the Schmidt decomposition represents the bath using the same number of states as the impurity, and thus greatly reduces the size of the active space for the quantum impurity solver. Despite its simplicity, DMET is accurate for the 1- and 2-dimensional Hubbard models [175] and simple chemical models such as hydrogen rings [176]. It has been further simplified by Bulik et al. to density embedding theory (DET) [46], where only the electron density is matched, with impressive performance on realistic infinite systems [45].

In this chapter, we will extend the original DMET to include a correlated bath. The original DMET, hereafter called HF-DMET, uses a HF bath (i.e. FCI-in-HF embedding) and thus the bath density matrix is not flexible enough to represent correlated systems because it must always be idempotent. This can cause convergence problems as well as unexpected wrong behaviors in the non-interacting limit (as we will discuss later), essentially because the DM cannot be matched exactly even when the embedding should be exact. To remedy this problem, we specifically use the antisymmetrized geminal power (AGP) [227, 33, 60, 187] wave function for the bath. Because AGP can obtain any N-representable one particle density matrix [211] FCI-in-AGP embedding can enforce *exact* density matrix matching even though the bath is only approximate. This feature has significant benefits for making DMET robust and well-behaved. As a side benefit, because the DMET scheme becomes exact in the limit of FCI-in-FCI, it is expected that using a correlated bath (FCI-in-AGP in our case) will lead to a systematic improvement of the approximation.

We organize this chapter as follows. We will first discuss the shortcomings of HF-DMET in more detail in Section 5.2. In Section 5.3 we outline the steps required for AGP-DMET, noting that AGP can be viewed as number-projected Hartree-Fock-Bogoliubov (PHFB) [39, 355], where HFB’s broken electron number symmetry is restored by a projection operator [294, 289]. Therefore, one can rely on the mean field nature of HFB to significantly ease the complexity of employing an AGP bath. Section 5.4 shows our results on illustrative examples of the Hubbard model and its variants, including an alternating ABAB Hubbard model and a stochastic Hubbard-Anderson model. Finally, we conclude this chapter and discuss future directions for DMET in Section 5.5.

## 5.2 Motivation: DMET and independent pairs

### 5.2.1 DMET equations

Given a decomposition of  $N$  orbitals into  $N_{\text{imp}}$  “impurity” (or system) orbitals and  $N - N_{\text{imp}}$  “bath” (or environment) orbitals, any many particle wave function (including the exact ground state wave function) can be decomposed as a sum over products of impurity states ( $\alpha$ ) times bath states ( $\beta$ ):

$$|\Psi\rangle = \sum_{I=1}^M \lambda_I |\alpha_I\rangle |\beta_I\rangle \quad (5.1)$$

This decomposition is known as the Schmidt decomposition of the wave function [258, 257]. The intriguing thing about this decomposition is that the length of the expansion ( $M$ ) is limited by the *lesser* of two things: the number of states available to the impurity and the number of states available to the bath. Thus, in the common scenario where the impurity has a very small number of states available to it, the Schmidt decomposition is very compact, even for a complicated  $|\Psi\rangle$  and a large bath.

In practice, it is very difficult to get the bath states without knowing the full wave function to begin with. Thus, DMET takes the pragmatic path of approximating the bath states using a low level of theory, typically mean field. In this case, the action of the full Hamiltonian

$$\hat{H} \equiv \sum_{pq=1}^N h_{pq} \hat{a}_p^\dagger \hat{a}_q + \sum_{pqrs=1}^N v_{pqrs} \hat{a}_p^\dagger \hat{a}_q^\dagger \hat{a}_s \hat{a}_r \quad (5.2)$$

in the Schmidt space can be exactly reproduced by the action of a reduced Hamiltonian

$$\hat{H}_{red} \equiv \sum_{pq=1}^{2N_{\text{imp}}} \bar{h}_{pq} \hat{c}_p^\dagger \hat{c}_q + \sum_{pqrs=1}^{2N_{\text{imp}}} \bar{v}_{pqrs} \hat{c}_p^\dagger \hat{c}_q^\dagger \hat{c}_s \hat{c}_r \quad (5.3)$$

in a space of fictitious quasiparticles [175, 176]. The first  $N_{\text{imp}}$  of the creation/destruction operators  $\hat{c}_p^\dagger/\hat{c}_p$  are identical to the corresponding creation/destruction operators in the impurity. The remaining operators are linear combinations of the bath creation/destruction operators defined in such a way that whenever  $p$  is occupied in the Schmidt decomposition of  $\Psi$ ,  $p + N_{\text{imp}}$  is empty and vice versa. More details on the algebra of how these quasi-operators are defined for a Hartree-Fock state can be found in Ref. [46].

Now, for small numbers of impurity orbitals, the ground state wavefunction corresponding to the Hamiltonian of Eq. 5.3 can be found either exactly using CI[318, 175], or very accurately using coupled cluster[22, 45] or density matrix renormalization group [360] methods. Thus, the flow in DMET is: 1) Pick a good mean field description for the bath; 2) Construct the corresponding reduced Hamiltonian; (Eq. 5.3) 3) Solve for the ground state of  $\hat{H}_{\text{imp}}$ ; 4) Report the energy of the impurity (with no bath) as the expectation value of

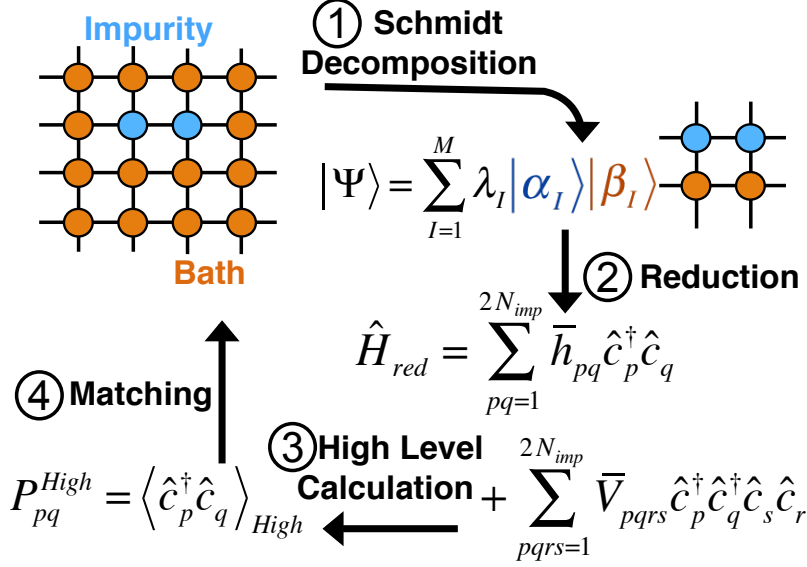


Figure 5-1: A summary of the DMET algorithm.

$$\hat{H}_{imp} \equiv \sum_{p=1}^{N_{imp}} \left[ \sum_{q=1}^{2N_{imp}} \bar{h}_{pq} \hat{c}_p^\dagger \hat{c}_q + \sum_{qrs=1}^{2N_{imp}} \bar{v}_{pqrs} \hat{c}_p^\dagger \hat{c}_q^\dagger \hat{c}_s \hat{c}_r \right]. \quad (5.4)$$

For an aperiodic system, one can break the system up into disjoint subsystems, perform DMET on each subsystem, and then reconstruct the total energy by adding up the impurity energies (Eq. 5.4) for each fragment.

The only uncertain piece of the DMET algorithm is how one picks a “good” mean field description of the bath. Physically, one expects that a good mean field description of a given subsystem will be one that resembles what one would have obtained by doing DMET on the same subsystem. That is,  $\Psi_{MF} \approx \Psi_{DMET}$ , at least locally. Different DMET algorithms choose to enforce this approximate condition in different ways [175, 176, 45], all of which focus on the DM in the Schmidt space

$$P_{pq} = \langle \hat{c}_q^\dagger \hat{c}_p \rangle. \quad (5.5)$$

One can then match either the full matrix, impurity-impurity block of the matrix, or the diagonal elements of the matrix (with the latter being referred to as density embedding theory, or DET[45, 46]). For the duration of this chapter we will consider only DMET matching the impurity-impurity block

$$(P_{pq}^{MF} \equiv \langle \hat{a}_q^\dagger \hat{a}_p \rangle_{MF} = \langle \hat{a}_q^\dagger \hat{a}_p \rangle_{CI} \equiv P_{pq}^{CI}) \quad (5.6)$$

for simplicity. Similar results and arguments can be found with the other matching conditions.

In order to enforce the matching condition, DMET borrows from subsystem DFT and adds an

additional (nonlocal) potential  $\hat{v}_{\text{imp}}$  to each impurity

$$\hat{v}_{\text{imp}} = \sum_{pq=1}^{N_{\text{imp}}} v_{pq}^{\text{imp}} \hat{a}_p^\dagger \hat{a}_q. \quad (5.7)$$

The mean field wave function is chosen to be the ground state of the original  $\hat{H}$  plus this impurity potential

$$\Psi_{MF} = \min_{\Phi \in \{\text{Determinants}\}} \langle \hat{H} + \hat{v}_{\text{imp}} \rangle. \quad (5.8)$$

The impurity Hamiltonian then depends on  $\hat{v}_{\text{imp}}$  in two ways. First, there is a direct dependence, as the matrix elements involving bath states are computed using  $\hat{v}_{\text{imp}}$ . Second, there is an indirect dependence that arises because the Schmidt states are determined by  $\Psi_{MF}$ , which in turn depends on  $\hat{v}_{\text{imp}}$ .

We thus have that both  $P^{MF}$  and  $P^{CI}$  depend on  $\hat{v}_{\text{imp}}$ , so that the matching condition becomes

$$P_{pq}^{MF}(\hat{v}_{\text{imp}}) = P_{pq}^{CI}(\hat{v}_{\text{imp}}) \quad [p, q \in \text{Impurity}]. \quad (5.9)$$

The number of parameters (in  $\hat{v}_{\text{imp}}$ ) is exactly equal to the number of unknowns (in  $P^{MF}$ ) and thus the proper adjustment of  $\hat{v}_{\text{imp}}$  in practice can lead to exact fulfillment of the matching conditions. In some ways, Eq. 5.9 can be thought of as a self-consistency condition: one chooses the potential so that the impurity DM used in the Schmidt decomposition exactly matches the impurity DM obtained from doing an exact calculation in this Schmidt space. Putting all the pieces together, the resulting DMET algorithm is summarized in Figure 5-1.

## 5.2.2 Independent pairs

Now, let us consider a system of two noninteracting electron pairs in a minimal basis - for example, two LiH/STO-3G molecules (with frozen cores) infinitely far from each other. Consider the situation illustrated in Figure 5-2 where one runs DMET on this system with two impurity sites. In this case, the Schmidt decomposition is fairly easy: the impurity orbitals are just the orbitals on one of the LiH molecules and the bath quasi-orbitals are just the physical orbitals on the other LiH molecule. Thus, the Schmidt Hamiltonian is exactly equal to the full Hamiltonian and DMET with two impurity orbitals should be exact for this case.

However, to this point we have neglected the effects of self-consistent density matching. It is clear from the argument above that DMET is exact if the impurity potential ( $\hat{v}_{\text{imp}}$ ) is zero. Unfortunately, it is in general *not zero* when the bath is a mean field so that DMET fails to be exact in this simple case. To see why this is so, note that because the two orbital pairs are infinitely far apart, the one particle DM will be block diagonal. Both for the CI

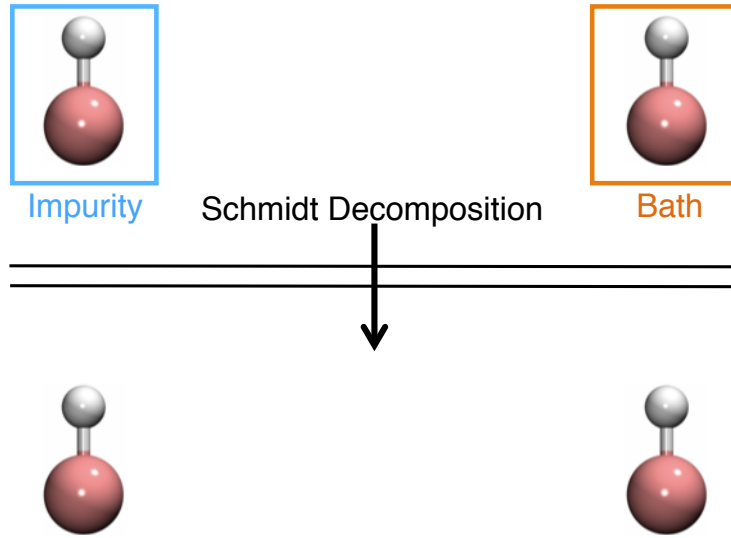


Figure 5-2: A pair of infinitely separated minimal basis LiH molecules. One molecule is chosen to be the system, and the other serves as a bath. In this case, one obtains the same Hamiltonian in the Schmidt basis as in the full basis.

$$\mathbf{P}^{\text{CI}} = \begin{pmatrix} \mathbf{P}_{\text{ii}}^{\text{CI}} & \mathbf{0} \\ \mathbf{0} & \mathbf{P}_{\text{bb}}^{\text{CI}} \end{pmatrix} \quad (5.10)$$

and the mean field

$$\mathbf{P}^{\text{MF}} = \begin{pmatrix} \mathbf{P}_{\text{ii}}^{\text{MF}} & \mathbf{0} \\ \mathbf{0} & \mathbf{P}_{\text{bb}}^{\text{MF}} \end{pmatrix} \quad (5.11)$$

the DM consists of impurity-impurity and bath-bath blocks. The matching condition that we want to satisfy is then

$$\mathbf{P}_{\text{ii}}^{\text{MF}}(\hat{v}_{\text{imp}}) = \mathbf{P}_{\text{ii}}^{\text{CI}}(\hat{v}_{\text{imp}}) \quad (5.12)$$

In order for DMET to be exact, this condition would need to be satisfied when  $\hat{v}_{\text{imp}} = 0$ . However, this cannot be because the mean field DM must be idempotent ( $\mathbf{P}\mathbf{P} = \mathbf{P}$ ) whereas the CI density matrix will generally be sub-idempotent ( $\mathbf{P}\mathbf{P} < \mathbf{P}$ ). In general, there exists no potential that can make the CI density idempotent, and so *the exact matching condition cannot be satisfied* for the simple case of noninteracting pairs.

In order for Eq. 5.12 to be satisfied even in a least squares sense, one needs to apply an impurity potential to the system. This potential will perturb the DMET solution, leading to an incorrect result for non-interacting pairs. We note that a similar but weaker condition holds for DET. It is

possible to apply a potential so that the densities of the MF and CI states match on the impurity. However, once again, this potential will typically not be zero so that DET is not exact for this case either.

To illustrate the inexact nature of DMET for noninteracting pairs, we consider a simple four site Hubbard Hamiltonian [149, 93]

$$\hat{H} = \sum_{ij,\sigma} h_{ij} \hat{a}_{i\sigma}^\dagger \hat{a}_{j\sigma} + \sum_i U \hat{n}_{i\uparrow} \hat{n}_{i\downarrow} \quad (5.13)$$

where the first term includes all one electron terms and the second describes on-site electron repulsion with strength  $U$ . The one electron Hamiltonian takes the form

$$\mathbf{h} \equiv \begin{pmatrix} \epsilon & t & 0 & 0 \\ t & 0 & 0 & 0 \\ 0 & 0 & \epsilon & t \\ 0 & 0 & t & 0 \end{pmatrix} \quad (5.14)$$

which describes two identical noninteracting pairs (1,2) and (3,4). The orbitals are coupled within a pair by a hopping term  $t$  and the odd orbitals are higher in energy by an amount  $\epsilon$  compared to the even orbitals. The model mimics our example of two LiH/STO-3G molecules (with frozen cores) infinitely far from one another. For a particular set of parameters ( $t=1$ ,  $\epsilon=0.3$ ,  $U=8$ ) it is easy to show that the exact answer for this system is  $E_{\text{CI}} = -0.086$  (per site), which is identical to what DMET gives when  $\hat{v}_{\text{imp}} = 0$ . However, once the matching condition is satisfied,  $\hat{v}_{\text{imp}} \neq 0$  and we find  $E_{\text{DMET}} = -.416$  so that DMET is clearly *not* exact for this case.

### 5.3 Theory

In order to allow DMET to be exact for noninteracting pairs, it is clear that we need more flexibility in the DM. Specifically, we need to describe the environment by a correlated wave function, so that the DM can be sub-idempotent. With this in mind, it becomes clear that the AGP wave function [227, 187, 60] is an ideal candidate for the environment. The AGP wave function is compact [61], its computational scaling is similar to that of HF, it is easy to compute matrix elements between AGP states [289], and most importantly, a suitably chosen AGP wave function can reproduce *any* physical DM [211]. In what follows, we start by briefly reviewing the basic properties of an AGP wave function.

### 5.3.1 The AGP wave function

The AGP wave function is built out of a single two-electron function (the geminal). Because it describes two electrons, this geminal can be expanded in terms of orbital products:

$$g(x_1, x_2) \equiv \sum_{ij} c_{ij} \phi_i(x_1) \bar{\phi}_j(x_2). \quad (5.15)$$

The AGP wavefunction for  $2M$  electrons can then be succinctly written as [227]

$$\Psi_{AGP}(x_1, x_2, x_3, \dots, x_M) \equiv \mathcal{A}[g(x_1, x_2) g(x_3, x_4) \dots g(x_{2M-1}, x_{2M})] \quad (5.16)$$

where  $\mathcal{A}$  is the antisymmetrizer. The resulting wave function clearly resembles  $g^M$ , motivating the geminal power name.

For our purposes, the real space expression for  $\Psi_{AGP}$  is inconvenient, as it is not clearly related to any mean field state, making the Schmidt decomposition tedious. Toward this end, we note that the  $\Psi_{AGP}$  is closely related to the HFB wave function [39, 355, 307]. In HFB, one mixes the creation and destruction operators to create new quasi-particle operators

$$\begin{aligned} \hat{\gamma}_i &\equiv \sum_j^N \left( U_{ji} \hat{a}_j + V_{ji} \hat{a}_j^\dagger \right) \\ \hat{\gamma}_i^\dagger &\equiv \sum_j^N \left( U_{ji}^* \hat{a}_j^\dagger + V_{ji}^* \hat{a}_j \right). \end{aligned} \quad (5.17)$$

One then creates a mean field out of these quasi-particles

$$|\Psi_{HFB}\rangle \equiv \prod_{i=1}^{N/2} \hat{\gamma}_i |0\rangle \quad (5.18)$$

where  $|0\rangle$  is the true vacuum containing no electrons. Note that because the quasi-operators mix creation and destruction operators,  $\Psi_{HFB}$  will not typically have a well-defined number of electrons.

The AGP wave function can be obtained from the HFB wave function by projecting it on to the desired number of electrons [39, 355]

$$|\Psi_{AGP}\rangle = \hat{P}_M |\Psi_{HFB}\rangle. \quad (5.19)$$

Here  $\hat{P}_M$  is an operator that multiplies all states with  $M$  electrons by 1 and multiplies all other states by 0. It has been known for several decades [272] that this projection can be efficiently written as an integral

$$\begin{aligned}
\hat{P}_M |\Psi_{HFB}\rangle &= \frac{1}{2\pi} \int_0^{2\pi} e^{i(\hat{N}-M)\theta} |\Psi_{HFB}\rangle d\theta \\
&= \frac{1}{2\pi} \int_0^{2\pi} e^{-iM\theta} |\Psi_{HFB}(\theta)\rangle d\theta
\end{aligned} \tag{5.20}$$

where  $\hat{N}$  is the number operator and on the second line we have used the fact that  $e^{i\hat{N}\theta} |\Psi_{HFB}\rangle$  can be written as a new HFB wave function  $|\Psi(\theta)\rangle$  with  $U_{ij} \rightarrow U_{ij}e^{i\theta}$  and  $V_{ij} \rightarrow V_{ij}e^{-i\theta}$ . Finally, one notes that the integral over  $\theta$  can be evaluated by quadrature to give

$$|\Psi_{AGP}\rangle = \sum_j w_j |\Psi_{HFB}(\theta_j)\rangle. \tag{5.21}$$

Thus the AGP wave function can be exactly written as a sum of mean-field HFB wave functions.

### 5.3.2 AGP schmidt decomposition

We are now in a position to write out the Schmidt decomposition for the AGP state. First, we note that each Schmidt state can be obtained from the parent wave function by an appropriate operator

$$|\alpha_I\rangle |\beta_J\rangle = \hat{P}_{IJ} |\Psi\rangle. \tag{5.22}$$

For example, with one impurity orbital and a state that conserves particle number

$$\begin{aligned}
|1\rangle |1\rangle &= \mathcal{N}_1 \hat{n}_{i\uparrow} \hat{n}_{i\downarrow} |\Psi\rangle \\
|1\rangle |1\rangle &= \mathcal{N}_2 \hat{n}_{i\uparrow} (1 - \hat{n}_{i\downarrow}) |\Psi\rangle \\
|1\rangle |1\rangle &= \mathcal{N}_3 (1 - \hat{n}_{i\uparrow}) \hat{n}_{i\downarrow} |\Psi\rangle \\
|1\rangle |1\rangle &= \mathcal{N}_4 (1 - \hat{n}_{i\uparrow}) (1 - \hat{n}_{i\downarrow}) |\Psi\rangle
\end{aligned} \tag{5.23}$$

where the  $\mathcal{N}_i$  are appropriate normalization constants.

Note that we are now using a more general basis than in equation 5.1. We have included cross terms for two reasons. First, by including these terms, we can write the Hamiltonian in the Schmidt space as a second quantized two body operator, which allows us to use standard full CI algorithms. Second, we are using the Schmidt decomposition of the AGP bath wavefunction as an approximation to the Schmidt space of the full CI wavefunction. We then perform a full CI calculation to refine this approximation. By including the cross terms (i.e.  $I \neq J$ ), we give the full CI wavefunction greater variational flexibility.

We can combine Eq. 5.22 with our expansion of the AGP wave function to write the matrix

elements of the Hamiltonian in the AGP Schmidt basis as

$$\begin{aligned}
\langle \alpha_I | \langle \beta_J | \hat{H} | \alpha_K \rangle | \beta_L \rangle &= \langle \Psi_{AGP} | \hat{\mathcal{P}}_{IJ} \hat{H} \hat{\mathcal{P}}_{KL} | \Psi_{AGP} \rangle \\
&= \sum_i w_i \langle \Psi_{HFB}(\theta_i) | \hat{\mathcal{P}}_{IJ} \hat{H} \hat{\mathcal{P}}_{KL} \sum_j w_j | \Psi_{HFB}(\theta_j) \rangle \\
&= \sum_{ij} w_i w_j \langle \Psi_{HFB}(\theta_i) | \hat{\mathcal{P}}_{IJ} \hat{H} \hat{\mathcal{P}}_{KL} | \Psi_{HFB}(\theta_j) \rangle
\end{aligned} \tag{5.24}$$

so that the matrix elements of  $\hat{H}$  in the AGP Schmidt basis can be efficiently computed as a weighted sum of matrix elements between *mean field* HFB states. The matrix elements between the HFB states can in turn be computed using a reduced Hamiltonian akin to Eq. 5.3 as we now show.

### 5.3.3 HFB matrix elements

We now need three key pieces of information in order to evaluate the matrix elements in Eq. 5.24. First, we need to decompose the state into its Schmidt components, i.e.  $\hat{\mathcal{P}}_{IJ} | \Psi_{HFB} \rangle$ . Second, we need the Hamiltonian matrix elements between two arbitrary HFB states. To simplify the discussion, we present a set of equations specific to the case of one impurity site. Finally, we need to rotate the HFB state,  $| \Psi_{HFB}(\theta) \rangle = e^{-i\theta \hat{N}} | \Psi_{HFB} \rangle$ . A lengthier discussion of the general case can be found in Appendix 5.6.

For one-site, the four electron configurations of the Schmidt space of an HFB wave function can be written by applying number operators:

$$|1\rangle |1\rangle = \hat{n}_{i\uparrow} \hat{n}_{i\downarrow} | \Psi_{HFB} \rangle \tag{5.25}$$

$$|1\rangle |0\rangle = \hat{n}_{i\uparrow} (1 - \hat{n}_{i\downarrow}) | \Psi_{HFB} \rangle \tag{5.26}$$

$$|0\rangle |1\rangle = \hat{n}_{i\downarrow} (1 - \hat{n}_{i\uparrow}) | \Psi_{HFB} \rangle \tag{5.27}$$

$$|0\rangle |0\rangle = (1 - \hat{n}_{i\uparrow}) (1 - \hat{n}_{i\downarrow}) | \Psi_{HFB} \rangle \tag{5.28}$$

These wave functions are not easy to evaluate using the standard form of the HFB wave function, but the Thouless form proves useful. The Thouless form of the HFB wave function is given by [326]:

$$| \Psi_{HFB} \rangle = \exp \left( \frac{1}{2} \sum_{kl} Z_{kl} a_{k\uparrow}^\dagger a_{l\downarrow}^\dagger \right) |0\rangle \tag{5.29}$$

where the  $\mathbf{Z}$  is a matrix of coefficients, defined as  $\mathbf{V}^* \mathbf{U}^{*-1}$ . In this form, we can readily remove an alpha or beta electron from the wave function by deleting a row or column (respectively) of the  $\mathbf{Z}$

matrix. Let  $\mathbf{Z}^{(\mu\bar{\nu})}$  denote a  $\mathbf{Z}$  matrix with row  $\mu$  and column  $\nu$  set to zero. Then, for example:

$$| \rangle | 1 \rangle = (1 - \hat{n}_{i1}) (1 - \hat{n}_{i\bar{l}}) | \Psi_{\text{HFB}} \rangle = \exp \left( \frac{1}{2} \sum_{kl} Z_{kl}^{(i\bar{i})} a_{k\uparrow}^\dagger a_{l\bar{l}}^\dagger \right) | 0 \rangle. \quad (5.30)$$

We can now construct the basis in Eqs. 5.25-5.28 as a linear combination of these ‘‘truncated’’ HFB states:

$$| \rangle | 1 \rangle = (1 - \hat{n}_{i1}) (1 - \hat{n}_{i\bar{l}}) | \Psi_{\text{HFB}} \rangle \equiv | \Psi_{\text{HFB}}^{(i\bar{i})} \rangle \quad (5.31)$$

$$| 1 \rangle | \rangle = (1 - \hat{n}_{i1}) | \Psi_{\text{HFB}} \rangle - | \Psi_{\text{HFB}}^{(i\bar{i})} \rangle \equiv | \Psi_{\text{HFB}}^{(\bar{i})} \rangle - | \Psi_{\text{HFB}}^{(i\bar{i})} \rangle \quad (5.32)$$

$$| \rangle | 1 \rangle = (1 - \hat{n}_{i1}) | \Psi_{\text{HFB}} \rangle - | \Psi_{\text{HFB}}^{(i\bar{i})} \rangle \equiv | \Psi_{\text{HFB}}^{(i)} \rangle - | \Psi_{\text{HFB}}^{(i\bar{i})} \rangle \quad (5.33)$$

$$| 1 \rangle | \rangle = | \Psi_{\text{HFB}} \rangle - | \Psi_{\text{HFB}}^{(i)} \rangle - | \Psi_{\text{HFB}}^{(\bar{i})} \rangle + | \Psi_{\text{HFB}}^{(i\bar{i})} \rangle \quad (5.34)$$

where we have introduced  $| \Psi_{\text{HFB}}^{(k\bar{l})} \rangle$  to mean the truncated state without an alpha electron in  $k$  and a beta electron in  $l$ .

In order to evaluate matrix elements between two HFB states, we employ the generalized Wick’s Theorem [272]. Given two HFB states,  $|\Phi\rangle$  and  $|\Psi\rangle$ , whose Thouless coefficient matrices are  $\mathbf{Z}^\Phi$  and  $\mathbf{Z}^\Psi$ ,

$$\frac{\langle \Phi | \hat{H} | \Psi \rangle}{\langle \Phi | \Psi \rangle} = \sum_{pq} h_{pq} P_{qp}^{\Psi\Phi} + \frac{1}{2} \sum_{pqrs} v_{pqrs} P_{rp}^{\Psi\Phi} P_{sq}^{\Psi\Phi} + \frac{1}{4} \sum_{pqrs} v_{pqrs} \kappa_{pq}^{\Psi\Phi*} \kappa_{sr}^{\Psi\Phi}, \quad (5.35)$$

where the transition density matrix and pairing matrix are defined as

$$\mathbf{P}^{\Psi\Phi} = -\mathbf{Z}^\Psi (\mathbf{1} - \mathbf{Z}^{\Phi*} \mathbf{Z}^\Psi)^{-1} \mathbf{Z}^{\Phi*}, \quad (5.36)$$

$$\boldsymbol{\kappa}^{\Psi\Phi} = \mathbf{Z}^\Psi (\mathbf{1} - \mathbf{Z}^{\Phi*} \mathbf{Z}^\Psi)^{-1}, \quad (5.37)$$

$$\boldsymbol{\kappa}^{\Phi\Psi*} = (\mathbf{1} - \mathbf{Z}^{\Phi*} \mathbf{Z}^\Psi)^{-1} \mathbf{Z}^{\Phi*}. \quad (5.38)$$

The norm overlap is given by the Onishi theorem [244, 272]:

$$\langle \Phi | \Psi \rangle = \pm \sqrt{\det [\mathbf{1} - \mathbf{Z}^{\Phi*} \mathbf{Z}^\Psi]}. \quad (5.39)$$

Note that the sign of the square root is undetermined in this form. However, we are using a singlet-pairing HFB reference with real orbitals, which allows us to rewrite Eq. 5.39 as:

$$\langle \Phi | \Psi \rangle = \det [\mathbf{1} + \mathbf{z}^{\Phi(T)} \mathbf{z}^\Psi] \quad (5.40)$$

where the lowercase letter indicates the  $\alpha\beta$  block of the coefficient matrix, i.e.:

$$\mathbf{Z} = \begin{pmatrix} \mathbf{0} & \mathbf{z} \\ -\mathbf{z}^T & \mathbf{0} \end{pmatrix}. \quad (5.41)$$

This result now has a well-defined phase.

Finally, in order to Schmidt decompose a number-projected HFB state (as in Eq. 5.24), we need to know how to produce the rotated HFB state in the Thouless form. Due to its exponential form, the rotation is facile in this representation:

$$|\Psi_{\text{HFB}}(\theta)\rangle = e^{i\hat{N}\theta} |\Psi_{\text{HFB}}\rangle = \exp\left(\frac{1}{2} \sum_{kl} e^{2i\theta} Z_{kl} c_{k\uparrow}^\dagger c_{l\downarrow}^\dagger\right) |0\rangle. \quad (5.42)$$

Combining these equations, we reach the central result of this section: a means of evaluating the matrix elements in Eq. 5.24 in terms of Wicks theorem involving a two-body operator in the impurity+entangled space for one impurity site.

## 5.4 Results and discussion

### 5.4.1 Verification of embedding equations

We verified the accuracy of our code for evaluating the matrix elements between Schmidt states by using a house-built Full CI code. Specifically, for a small number of total sites ( $N < 15$ ), one can represent the state  $|\Psi\rangle$  as a vector in the many electron Hilbert space. A state like  $\hat{n}_i \hat{n}_j |\Psi\rangle$  can then be directly evaluated by operating successive one electron operators (e.g.  $\hat{n}_i$ ) on the vector that represents  $|\Psi\rangle$ . Finally, matrix elements between states (e.g.  $\langle \Phi | \hat{n}_i (1 - \hat{n}_j) \hat{H} \hat{n}_i \hat{n}_j | \Psi \rangle$ ) can be evaluated using standard Full CI energy evaluation routines. By implementing this, we are able to verify that our equations are correct for a random  $\hat{H}$  and random left and right states, providing a powerful proof of the accuracy both of the derivation and the implementation.

### 5.4.2 Results for model hamiltonians

#### 5.4.2.1 The Hubbard model

To evaluate the performance of our AGP embedding method, we look at a number of extensions to the Hubbard model [149, 93], a simple lattice model of electron correlation. The Hubbard Hamiltonian is given in the lattice site basis by:

$$\hat{H}_{\text{Hub}} = -t \sum_{\langle i,j \rangle} \sum_{\sigma \in \{\uparrow, \downarrow\}} \hat{a}_{i\sigma}^\dagger \hat{a}_{j\sigma} + U \sum_i \hat{n}_i \uparrow \hat{n}_i \downarrow. \quad (5.43)$$

The first term creates nearest-neighbor one electron hopping, while the second term is an on-site two electron repulsion. The model is governed by one dimensionless parameter,  $U/t$ , that determines correlation strength: as this parameter increases, the system becomes more strongly correlated.

The one dimensional Hubbard model can be solved exactly via the Bethe Ansatz [196]. However, in what follows we will also be interested in variations of this model that can only be solved numerically by, for example, DMRG [52]. For the sake of consistency, then, we use a one-dimensional Hubbard lattice with 30 sites with periodic boundary conditions. This allows us to strike a compromise: we can use DMRG as a sufficiently “exact” answer, while still having a large enough lattice to be bulk-like. We employ the BLOCK DMRG code [292] with  $M=2000$  to obtain our reference numbers.

Results for the Hubbard model at various fillings and correlation strengths are shown in Figure 5-3, where for HF-DMET we have used one and two impurity sites, respectively denoted as HF(1) and HF(2). At low correlation strengths ( $U/t = 1$ ), the AGP bath, like its HF counterpart, is visually indistinguishable from the exact answer. As correlation strength increases, the AGP and HF results diverge: HF embedding performs better for medium fillings, while AGP outperforms at low and high fillings. Perhaps most importantly, AGP embedding is numerically exact for every value of  $U$  and every number of sites when there are only two electrons. This result is to be expected, as the AGP and FCI wave functions are identical in this case.

In general, one expects that the quality of DMET results should improve as the bath wave function improves. As can be proven mathematically, DMET is exact for FCI-in-FCI embedding, while it is only approximate for FCI-in-HF embedding [176]. As the AGP wave function is clearly closer to FCI than HF is, one might expect AGP-DMET to always be better than HF-DMET. The fact that this is not the case suggests there is some cancellation of errors in HF-DMET for this case. Nonetheless, both methods perform fairly well for this model.

#### 5.4.2.2 Non-interacting AB Dimers

Now that we have established that the AGP-DMET prescription is at least as accurate as HF-DMET for the crucial case of the Hubbard model, we turn our attention to noninteracting pairs of sites as discussed in section 5.2.2. To connect this to the Hubbard model that we know works well, we create noninteracting pairs by adding two terms to Eq. 5.43: we add an alternating coupling term to zero out the hopping interaction between every second site and a potential bias  $\delta$  on alternating

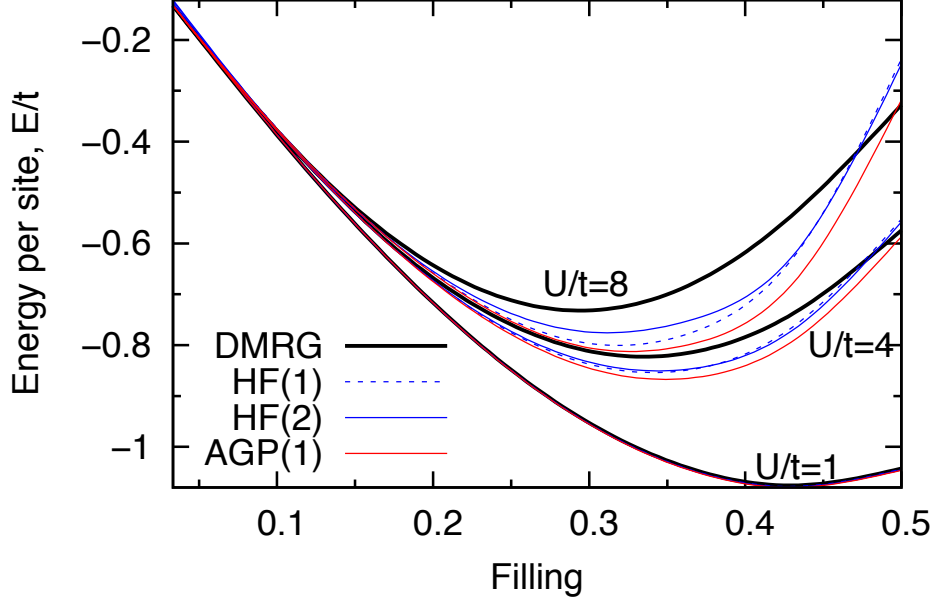


Figure 5-3: Filling dependence of the ground state energy of the Hubbard Hamiltonian (Eq. 5.43) at various correlation strengths. AGP and HF denote the bath wave function, and numbers in parenthesis are the number of sites in the impurity. We use DMRG as an exact answer to account for finite size effects, though the Bethe Ansatz [196] is visually identical on this scale.

sites:

$$\hat{H}_{ABAB} = \hat{H}_{\text{Hub}} + t \sum_{\langle i \text{ even}, j \rangle} \sum_{\sigma \in \{1, \downarrow\}} \hat{a}_{i\sigma}^\dagger \hat{a}_{j\sigma} + \delta \sum_{i \text{ even}} \sum_{\sigma \in \{1, \downarrow\}} \hat{n}_{i\sigma}, \quad (5.44)$$

This Hamiltonian describes an infinite number of noninteracting AB dimers and is identical to Eq. 5.14 when  $N = 4$ . The model now has two dimensionless parameters,  $U/t$  and  $\delta/t$ . This new parameter introduces a one-electron potential on every second site, creating pairs of adjacent “A” and “B” sites.

Within a dimer, the potential difference between the “A” site and the “B” site leads to unequal charge sharing, similar to what would be observed in an ionic bond. Between dimers, the interaction is zeroed out by the removal of the hopping term. Again, just like the example in the introduction, DMET will be exact for this as long as the self-consistency conditions are ignored.

This model is interesting because we do not know the electron populations on each site *a priori*, as opposed to  $\hat{H}_{\text{Hub}}$  where all the lattice sites are equally occupied. If we use two sites in our impurity, then the total number of electrons becomes well-defined. But for one site embedding (which might be preferred for computational reasons) the ABAB model presents a challenge: does the density matrix matching condition result in correct populations? In order to solve this problem for one-site embedding, we modify the original DMET to have two equal and opposite fictitious bath potentials: one that repeats on every A site and one on every B site. We then perform the

embedding calculation twice, once each for an A site and a B site. Finally, the two bath potentials are optimized to satisfy the DMET matching condition for both sites.

Results for this model are shown in Figure 5-4. Looking first at the one-site data, both HF-DMET and AGP-DMET give reasonable though not exact energies. The AGP data are somewhat better, but the trends are both good. For two site embedding, AGP-DMET becomes exact (not shown). Meanwhile, for two sites, HF-DMET fails to find an exact match for the density matrix and the least squares solution gives qualitatively incorrect behavior: the energies are poor and the slope is inaccurate. [Note: The two-site DMET does give the correct answer for the case of  $\delta = 0$ , but for the wrong reason; it still fails to converge, but the correct initial guess is a local (and perhaps global) minimum.] We thus see the problem outlined in the introduction clearly laid out: for weakly interacting systems, the self-consistency condition in HF-DMET can actually make the results significantly worse. AGP-DMET essentially fixes this problem - the results are acceptable with one site and exact for two site embedding (as they should be).

We note that these results also suggest size-extensivity of our method: we have tested AGP-DMET on strongly ( $\delta = 1$ ) and weakly ( $\delta = 0$ ) interacting infinite systems and recovered an extensive correlation energy for both. We can make an argument about how our method achieves size-extensivity. The total energy in DMET is the sum of the energies of the embedded fragments. Thus, the total energy will be size extensive as long as the correlation energy of each embedded fragment is non-vanishing. This should be the case if the fragments are chosen to be localized, where practically any impurity solver will give a finite correlation energy. Because the fragments are finite in size (and required to be small by computational limitations), even a non-size-extensive correlation method (e.g. CISD, AGP) will give a finite correlation energy, resulting in a size-extensive total energy.

### 5.4.2.3 ABAB Solid

Next, we examine a hybrid of the previous two examples: a Hubbard model with broken translational symmetry:

$$\hat{H}_{\text{ABAB}} = \hat{H}_{\text{Hub}} + \delta \sum_{i \text{ even}}^N \sum_{\sigma \in \{1,1\}} \hat{n}_{i\sigma}, \quad (5.45)$$

but again with periodic boundary conditions. Physically, this Hamiltonian could be crudely analogized to a one dimensional ionic solid.

Results for this model from embedding in a HF and an AGP bath are shown in Figure 5-5. Again, the one site embeddings are quite good: AGP-DMET is slightly better, but the slopes are essentially correct. At first blush, two site embedding for HF-DMET appears to improve matters. The one-

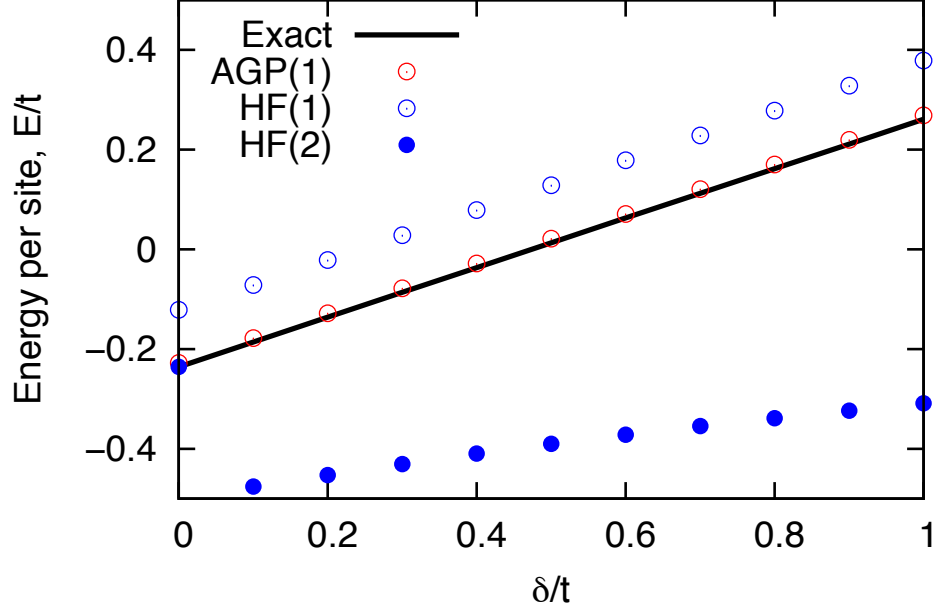


Figure 5-4:  $\delta$  dependence of ground state energy of the non-interacting Hamiltonian (Eq. 5.44) at half-filling and correlation strength  $U/t = 8$ .

and two-site results are essentially indistinguishable for  $\delta = 0$  (which corresponds to the original Hubbard model) and the two site results get closer to the exact results when  $\delta \neq 0$ . However, similar behavior is seen for the non-interacting limit (the  $\delta \neq 0$  energies are systematically lower than  $\delta = 0$ ) and in that case the  $\delta \neq 0$  results are clearly wrong. The drop in energy when  $\delta \neq 0$  is more muted here, but is likely coming from the same source - the self-consistent density is systematically worse than the non-self-consistent density for  $\delta \neq 0$ . The only reason the energies are better is cancellation of errors - the initial energy is too high, and the error lowers the energy. Because DMET is not variational, a lower energy does not imply a better approximation to the ground state. As a result, in this case we see that the flaws of the HF-DMET matching condition even have an impact on a strongly interacting system where the matching can be performed exactly.

#### 5.4.2.4 Hubbard-Anderson Model

Finally, in order to test the limits of our AGP embedding method, we turn to the Hubbard-Anderson model[11]. This model combines the two electron correlation of the Hubbard Hamiltonian with the site disorder of the Anderson model:

$$\hat{H}_{ABAB} = \hat{H}_{Hub} + \sum_i^N g_i(0, \sigma^2) \sum_{\sigma \in \{1, \downarrow\}} \hat{a}_{i\sigma}^\dagger \hat{a}_{i\sigma} \quad (5.46)$$

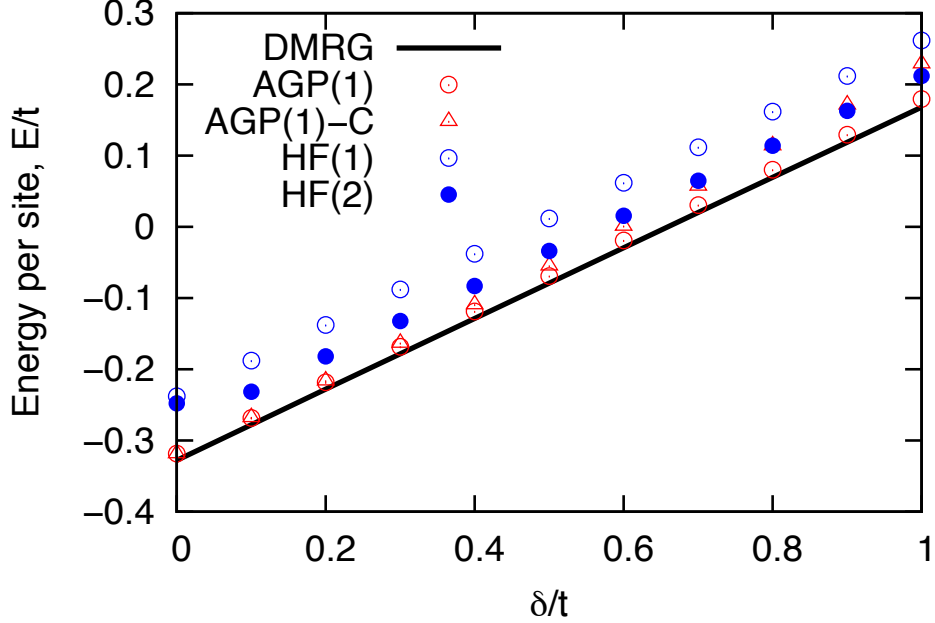


Figure 5-5:  $\delta$  dependence of ground state energy of  $\hat{H}_{\text{ABAB}}$  (Eq. 5.45) at half-filling and correlation strength  $U/t = 8$ . The “AGP(1)-C” series were produced by a constrained embedding as described in the text of the *Hubbard-Anderson Model* section.

where the  $g_i$  are normally distributed random site energies with mean 0 and variance  $\sigma^2$ . We use this model to show the benefits of embedding over an AGP treatment of correlation. We note that because of the random  $g_i$ , the Hubbard-Anderson model is not a single Hamiltonian but an *ensemble* of many Hamiltonians. In this context, it only makes sense to consider results that have been obtained by sampling many, many such Hamiltonians.

Results for  $\sigma = 2$  with  $M = 26$  are shown in Figure 5-6. For the purposes of this model, it is not computationally feasible to perform a self-consistent optimization of the embedding wave function at each site for every realization of the Hamiltonian. Instead, we perform a more limited simulation where the embedded wave function is constrained to match the populations of the overall AGP embedding wave function, in a scheme we will call AGP-C. This approximation is reasonably accurate. For example, in the ABAB Hubbard model from the previous section, AGP-C is essentially the same as full AGP-DMET for  $\delta < 0.4$  and clearly better than HF-DMET for all  $\delta < 1$ . (See Figure 5-5) We thus expect that the AGP-C numbers here will be representative of the results of full AGP-DMET embedding for this problem.

In Figure 5-6 we show the average energies of the AGP-C and DMRG calculations as a function of  $U/t$ . Clearly the trends observed for the pure Hubbard model are maintained even when a random, non-symmetric potential is added. Finally, we also plot the standard AGP wave function result to show that embedding dramatically improves the correlation energy; as correlation strength,  $U/t$ , increases, the bare AGP gives increasingly poor results. This is to be expected because the AGP

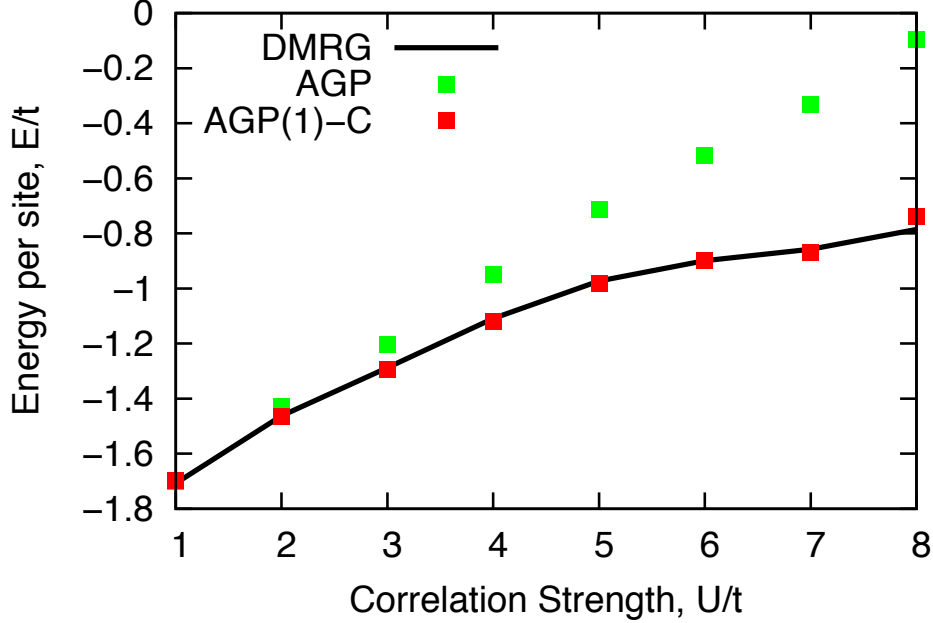


Figure 5-6:  $U$  strength dependence of the Hubbard-Anderson model (equation 5.46) with  $\sigma = 2$  and 26 electrons. AGP is the standard AGP wave function. AGP(1) is one-site embedding in AGP. The data series show the mean of 500 samples. Each data point has a standard deviation of  $\sim 0.06$ .

correlation energy is not size consistent, while AGP-DMET is. Thus, even though AGP and AGP-DMET are based on the same density matrix here, the correlation energy per site in AGP is very small, while the correlation energy from AGP-DMET for these randomly selected Hamiltonians is clearly very accurate at any correlation strength.

The Hubbard-Anderson model also provides an opportunity to examine the computational scaling of AGP-DMET. The two potential limiting steps are the cost of the full CI calculation and the cost of integral transformation (equation 5.24). For our case of one impurity site, the integral transformation is the rate limiting step. For  $N$  total orbitals and  $N_{imp}$  orbitals per embedded fragment, each fragment requires  $\mathcal{O}[N^3 \log N]$  work for this transformation, and there are  $\frac{N}{N_{imp}}$  fragments, resulting in a scaling of  $\mathcal{O}\left[\frac{N^4 \log N}{N_{imp}}\right]$ . In principle, this scaling compares favorably to other correlated methods.

## 5.5 Conclusions

The recently proposed density matrix embedding theory has proven successful for many strongly correlated systems. However, in its original formulation, the density matrix matching condition of DMET has a problem; for many systems, including some trivial cases, it cannot be exactly satisfied. This problem stems from the mean field nature of the underlying bath wave function; its idempotent density matrix cannot match the correlated density matrices of embedded wave

functions. To solve this problem, we have proposed to embed an impurity in a correlated wave function: the antisymmetrized geminal power in place of the mean field wave function, i.e. HF. The AGP reference has the advantages that it can have any one-particle density matrix, making the exact matching condition possible in theory, and that it is one step closer to the FCI-in-FCI embedding limit.

In order to perform DMET with the AGP bath, we have developed equations for Schmidt decomposition of the AGP wave function. The idea behind it is that AGP is regarded as number-projected HFB. Therefore, AGP-DMET essentially boils down to Schmidt decomposition of the HFB wave function followed by number symmetry projection. We applied this AGP embedding to several problems beyond the basic Hubbard model to demonstrate some of the strengths of AGP embedding. It was shown that the AGP bath can solve the two-electron system exactly, confirming the exactness of DMET mapping. AGP embedding is also able to yield the site energy correctly when interaction is zero (or very weak) between impurity and bath, while HF-DMET especially with two impurity sites breaks down due to the lack of proper self-consistency.

Moving forward, this chapter suggests a number of interesting directions for future research related to DMET. First, the ambiguous results with the existing matching condition suggest there is something wrong with the current DMET self-consistency conditions. In particular, it does not seem physically reasonable that mean field embedding should fail for non-interacting fragments. Is there a DMET matching condition that consistently improves the quality of results and is still exact for cases where DMET ought to be exact? Second, it will be interesting to look at DMET for excited states. In this light, projected wave functions like AGP are particularly interesting as it can be difficult to obtain excited wave functions that have the correct symmetry in HF, and projection can restore that symmetry, providing a good bath wave function for a particular excited state. Finally, it will be extremely interesting to apply these kinds of ideas to realistic molecular systems, as has been done with the original HF-DMET [176, 45].

## 5.6 Appendix: Second Quantized Matrix Elements for AGP Embedding

In section 5.3.3, we introduce equations for one-site embedding in AGP via the Thouless form of the HFB wave function. While this form is quick and numerically favorable, it does not provide a way to do embedding for more than one impurity site. For this, we need to reformulate the Schmidt decomposition in terms of the HFB quasiorbitals.

Any HFB state can be specified by its quasiparticle coefficients

$$\mathbf{W} = \begin{pmatrix} \mathbf{V}^* \\ \mathbf{U}^* \end{pmatrix} \quad (5.47)$$

Here  $\mathbf{W}$  is a  $2N \times N$  matrix that contains the coefficients of the  $N$  ‘‘occupied’’ quasi-orbitals in terms of the  $2N$  creation and destruction operators. To maintain normalization, we want  $\mathbf{W}$  to be unitary

$$\mathbf{W}^\dagger \mathbf{W} = \mathbf{V}^T \mathbf{V}^* + \mathbf{U}^T \mathbf{U}^* = \mathbf{1}. \quad (5.48)$$

In analogy to Hartree-Fock, we can also specify the HFB state in terms of its quasiparticle density matrix (qDM) [272]

$$\mathbf{R} = \mathbf{W}^\dagger \mathbf{W} = \begin{pmatrix} \mathbf{V}^* \mathbf{V}^T & \mathbf{V}^* \mathbf{U}^T \\ \mathbf{U}^* \mathbf{V}^T & \mathbf{U}^* \mathbf{U}^T \end{pmatrix} = \begin{pmatrix} \mathbf{P} & \boldsymbol{\kappa} \\ -\boldsymbol{\kappa}^* & \mathbf{1} - \mathbf{P}^* \end{pmatrix} = \begin{pmatrix} \langle \hat{a}^\dagger \hat{a} \rangle & \langle \hat{a} \hat{a} \rangle \\ \langle \hat{a}^\dagger \hat{a}^\dagger \rangle & \langle \hat{a} \hat{a}^\dagger \rangle \end{pmatrix} \quad (5.49)$$

where, in the last equality we have defined the density matrix ( $\mathbf{P}$ ) and the pairing matrix ( $\boldsymbol{\kappa}$ ) that determine the HFB state. The qDM is idempotent ( $\mathbf{R}\mathbf{R} = \mathbf{R}$ ) and has trace  $N$  (the number of quasi-particles) making it the analog of the DM familiar from HF theory.

Because the HFB state is completely determined by  $\mathbf{R}$ , every expectation value for a given HFB state is also determined by  $\mathbf{R}$  [272]. Thus, for example

$$\frac{\langle \Psi_{HFB} | \hat{H} | \Psi_{HFB} \rangle}{\langle \Psi_{HFB} | \Psi_{HFB} \rangle} = \sum_{pq} h_{pq} P_{qp} + \frac{1}{2} \sum_{pqrs} v_{pqrs} P_{rp} P_{sq} + \frac{1}{4} \sum_{pqes} v_{pqrs} \kappa_{pq}^* \kappa_{sr}. \quad (5.50)$$

Likewise, it is possible to work out every matrix element involving the Schmidt projection operators  $\mathcal{P}_{IJ}$  and  $\hat{H}$  in terms of  $\mathbf{R}$ .

Much as was the case for Hartree-Fock [258, 257, 176], we want to use the qDM to define some impurity orbitals and some entangled orbitals. In order to deal with the special status of the impurity orbitals, we will re-order the indices of  $\mathbf{R}$ . Specifically, we will re-order the indices so that particles and holes alternate and all the impurity operators ( $i, j, k, l, \dots$ ) come first followed by the bath operators ( $a, b, c, d, \dots$ ). Call the re-ordered  $\mathbf{R} \rightarrow \mathcal{R}$ .

Now, define  $\tau_{ai} = \mathcal{R}_{ai}$ .  $\boldsymbol{\tau}$  contains the portion of  $\mathcal{R}$  that describes coherence with the impurity. Thus,  $\vec{\tau}_i$  is a good candidate for the coefficients of the bath orbital that is entangled with the impurity  $i$ . Note that there are  $2N_{\text{imp}}$  vectors here, as there is one for each impurity creation operator and one for each destruction operator. These vectors are not orthonormal, but we can orthogonalize them

$$\mathbf{v} \equiv \mathbf{S}^{-1/2} \boldsymbol{\tau} \quad [\mathbf{S} \equiv \boldsymbol{\tau}^\dagger \boldsymbol{\tau}] \quad (5.51)$$

and then define the transformation to the impurity+entangled basis as

$$\mathbf{T} \equiv \begin{pmatrix} 1 & 0 \\ 0 & \mathbf{v} \end{pmatrix}. \quad (5.52)$$

We can then transform the density matrix into the impurity+entangled basis by

$$\mathcal{Q} \equiv \mathbf{T}^\dagger \mathcal{R} \mathbf{T} \quad (5.53)$$

Now,  $\mathcal{Q}$  is idempotent ( $\mathcal{Q}\mathcal{Q} = \mathcal{Q}$ ) and so we can make a unitary transformation to bring it into canonical form [272]

$$\bar{\mathcal{Q}} = \mathbf{U}^\dagger \mathcal{Q} \mathbf{U} = \begin{pmatrix} \mathcal{P} & \mathcal{K} \\ \mathcal{K} & \mathbf{1} - \mathcal{P} \end{pmatrix} \quad (5.54)$$

where

$$\begin{aligned} \mathcal{P}_{ij} &= n_i \delta_{ij} \\ \mathcal{K}_{ij} &= k_i \delta_{ij}. \end{aligned} \quad (5.55)$$

We can further transform the Hamiltonian into the canonical basis

$$\begin{aligned} \bar{\mathbf{h}} &\equiv \mathbf{U}^\dagger \mathbf{T}^\dagger \mathbf{h} \mathbf{T} \mathbf{U} \\ \bar{\mathbf{v}} &\equiv [\mathbf{U}^\dagger \mathbf{T}^\dagger \otimes \mathbf{U}^\dagger \mathbf{T}^\dagger] \mathbf{v} [\mathbf{T} \mathbf{U} \otimes \mathbf{T} \mathbf{U}] \end{aligned} \quad (5.56)$$

and also express the bath portion of the qDM

$$\bar{\mathcal{Q}}_{bath} \equiv \mathcal{R} - \mathbf{T} \mathbf{U} \bar{\mathcal{Q}} \mathbf{U}^\dagger \mathbf{T}^\dagger. \quad (5.57)$$

Note that all of this algebra is analogous to the Hartree-Fock case [46].

In terms of these quantities, the matrix elements of the full Hamiltonian in the Schmidt basis are reproduced by the reduced Hamiltonian

$$\hat{H}_{red} \equiv E[\bar{\mathcal{Q}}_{bath}] + \sum_{pq=1}^{4N_{imp}} f_{pq}[\bar{\mathcal{Q}}_{bath}] \hat{c}_p^\dagger \hat{c}_q + \sum_{pqrs=1}^{4N_{imp}} \bar{v}_{pqrs} \hat{c}_p^\dagger \hat{c}_q^\dagger \hat{c}_s \hat{c}_r \quad (5.58)$$

where  $E[\bar{\mathcal{Q}}_{bath}]$  is the HFB energy (Eq. 5.50) associated with the bath qDM and  $f[\bar{\mathcal{Q}}_{bath}]$  is the quasi-Fock matrix associated with the bath qDM [307]. Eq. 5.58 allows one to compute the matrix

elements of the Hamiltonian between any two Schmidt states for a single  $\Psi_{\text{HFB}}$ .

Now, in order to evaluate Eq. 5.24 we need to be able to evaluate matrix elements between the Schmidt states of two *different* HFB parent states (i.e. different states for the bra and the ket). Thankfully, as is the case for HF [200], the algebra here is only minorly different than the symmetric, bra=ket case. Assume these two states ( $\Phi$  and  $\Psi$ ) have quasiparticle coefficients  $\mathbf{W}^\Phi$  and  $\mathbf{W}^\Psi$ , respectively. Then the overlap between the occupied quasi-orbitals is

$$\mathbf{S}^{\Phi\Psi} = \mathbf{W}^{\Phi\dagger} \mathbf{W}^\Psi \quad (5.59)$$

If the states are individually normalized, then the overlap is then given by

$$\langle \Phi | \Psi \rangle = \text{Pf} \mathbf{S}^{\Phi\Psi} \quad (5.60)$$

where 'Pf' denotes the Pfaffian.

We can then go on to define the transition quasiparticle density matrix via

$$\mathbf{R}^{\Psi\Phi} \equiv \mathbf{W}^\Psi (\mathbf{S}^{\Phi\Psi})^{-1} \mathbf{W}^{\Phi\dagger} \equiv \begin{pmatrix} \mathbf{P}^{\Psi\Phi} & \boldsymbol{\kappa}^{\Psi\Phi} \\ \boldsymbol{\kappa}^{\Phi\Psi*} & \mathbf{1} - \mathbf{P}^{\Psi\Phi T} \end{pmatrix}. \quad (5.61)$$

Like the qDM, the transition qDM is idempotent and has trace  $N$ .<sup>1</sup> However, it is not Hermitian (i.e.  $\boldsymbol{\kappa}^{\Psi\Phi} \neq \boldsymbol{\kappa}^{\Phi\Psi(T)}$  and  $\mathbf{P}^{\Psi\Phi\dagger} \neq \mathbf{P}^{\Psi\Phi}$ ). Instead, the left and right vectors correspond, respectively, to the ket and bra states  $\Psi$  and  $\Phi$ .

In analogy to the symmetric case, in the asymmetric case, any normalized matrix element between  $\Phi$  and  $\Psi$  can be worked out in terms of the transition qDM. For example, Eq. (5.35) can be easily seen. One can therefore perform the same transformations as was done for the symmetric (bra=ket) case to compute matrix elements in the Schmidt space when the left and right states are distinct:

- Define left ( $\tau_{ai}^L = \mathcal{R}_{ia}$ ) and right ( $\tau_{ai}^R \equiv \mathcal{R}_{ai}$ ) entangled vectors and biorthogonalize them so that  $\boldsymbol{v}^L \boldsymbol{v}^R = \mathbf{1}$ .
- Build the left

$$\mathbf{T}^L \equiv \begin{pmatrix} \mathbf{1} & \mathbf{0} \\ \mathbf{0} & \boldsymbol{v}^L \end{pmatrix} \quad (5.62)$$

and right

$$\mathbf{T}^R \equiv \begin{pmatrix} \mathbf{1} & \mathbf{0} \\ \mathbf{0} & \boldsymbol{v}^R \end{pmatrix} \quad (5.63)$$

---

<sup>1</sup>Note that if  $\mathbf{S}$  has a zero eigenvalue, then the proper interpretation of  $\mathbf{S}^{-1}$  is as a pseudo-inverse. In this situation, the trace of  $\mathbf{R}$  will be equal to the rank of  $\mathbf{S}$ .

transformation matrices.

- Build the canonical system+impurity density matrix  $\bar{\mathcal{Q}}^{LR} = \mathbf{U}^{L\dagger} \mathbf{T}^{L\dagger} \mathcal{R}^{LR} \mathbf{T}^R \mathbf{U}^R$
- Transform the Hamiltonian into the canonical basis

$$\begin{aligned} \bar{\mathbf{h}}^{LR} &\equiv \mathbf{U}^{L\dagger} \mathbf{T}^{L\dagger} \mathbf{h} \mathbf{T}^R \mathbf{U}^R \\ \bar{\mathbf{v}}^{LR} &\equiv [\mathbf{U}^{L\dagger} \mathbf{T}^{L\dagger} \otimes \mathbf{U}^{L\dagger} \mathbf{T}^{L\dagger}] \mathbf{v} [\mathbf{T}^R \mathbf{U}^R \otimes \mathbf{T}^R \mathbf{U}^R] \end{aligned} \quad (5.64)$$

and also express the bath portion of the qDM

$$\bar{\mathcal{Q}}_{bath}^{LR} = \mathcal{R} - \mathbf{T}^L \mathbf{U}^L \bar{\mathcal{Q}} \mathbf{U}^{R\dagger} \mathbf{T}^{R\dagger}. \quad (5.65)$$

- Finally, evaluate Matrix elements in the Schmidt space using Eq. 5.58.

We have attempted to verify these results for more complicated cases than single site embedding but have thus far been stymied by the difficulty of maintaining the proper overall phase of the matrix elements in performing the grid integration. Thus, at this point the second quantized form of the equations is more of a curiosity than a real computational tool.

## 5.7 Acknowledgments

The work described in this chapter was undertaken with Takashi Tsuchimochi. He is listed as a co-author in reference [331].

## Chapter 6

# Bootstrap embedding

Strong correlation poses a difficult problem for electronic structure theory, with computational cost scaling quickly with system size. Fragment embedding is an attractive approach to this problem. By dividing a large complicated system into smaller manageable fragments "embedded" in an approximate description of the rest of the system, we can hope to ameliorate the steep cost of correlated calculations. While appealing, these methods often converge slowly with fragment size because of small errors at the boundary between fragment and bath. We describe a new electronic embedding method, dubbed "Bootstrap Embedding," a self-consistent wavefunction-in-wavefunction embedding theory that uses overlapping fragments to improve the description of fragment edges. We apply this method to the one dimensional Hubbard model and a translationally-asymmetric variant, and find that it performs very well for energies and populations. We find Bootstrap Embedding converges rapidly with embedded fragment size, overcoming the surface-area-to-volume-ratio error typical of many embedding methods. We anticipate that this method may find lead to a low-scaling, high accuracy treatment of electron correlation in large molecular systems.

### 6.1 Introduction

The computational cost of accurate electronic structure calculations typically rises superlinearly with system size. A potential approach to this problem is fragment embedding: divide the system into smaller fragments and treat each small fragment individually at a high level of theory. To account for the interaction of the fragment with its surroundings, each fragment is embedded in a bath that mimics the influence of the rest of the system on the fragment. Fragment embedding then amounts to a method for describing this bath and the fragment's interaction with it. There are many methods for fragment embedding, including fragment molecular orbital methods [171, 96, 97, 169, 367], divide and conquer [368, 110], partition density functional theory [90], frozen density embedding [66, 359], subsystem density functional theory [154, 114], and many more.

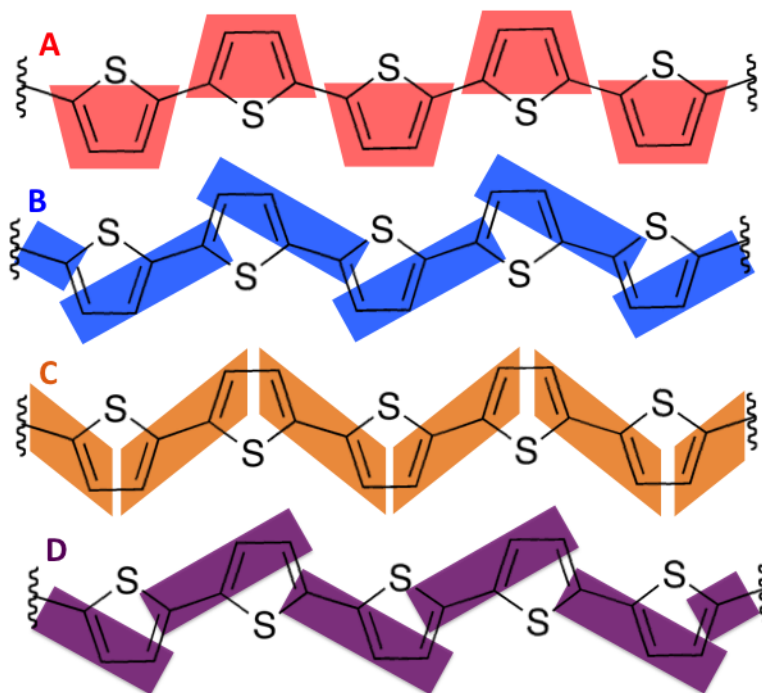


Figure 6-1: Four different fragment partitionings (A, B, C, D) for the same molecule. In Bootstrap Embedding, all four partitionings are used and the overlapping portions of the fragments are constrained to match.

One promising new method for fragment embedding is Density Matrix Embedding Theory (DMET) [175, 176], a wavefunction-in-wavefunction theory that treats the embedded fragment as an open quantum system entangled to its bath. A powerful feature of this approach is that fragments can in principle be chemically bonded to the bath, allowing for embedded calculations of large strongly coupled systems, such as molecules. DMET has shown great potential for treatment of strong correlation, in particular for the Hubbard model [149, 93] and for periodic systems [45].

As with many fragment embedding methods, much of DMET’s error arises from its description of the edges of the embedded fragment and their interaction with the bath. The center of the fragment, the “most embedded” part, is best described as it feels the effects of the approximate bath least. Meanwhile, the edges of the fragment, adjacent to the bath, can be as strongly coupled to the approximate bath as they are to the more accurate center of the fragment. The approximate nature of this edge-bath interaction then leads to a large and dominant source of error; we will later see numerically that the overall correlation energy error in DMET is proportional to the surface area to volume ratio of the embedded fragment. For a one dimensional system of length  $L$ , this results in a slow  $\frac{1}{L}$  convergence (see Figure 6-4). The convergence is even slower in higher dimensions ( $L^{-1/d}$  for  $d$  dimensions), leading to the common result that, while small fragments can give reasonable results, increasing fragment size produces only very slow convergence to the exact result.

In this chapter, we take a fragment embedding approach: divide a molecule into many separate

fragments, perform an embedded calculation on each fragment, and then recombine the results. At the outset, we must partition the molecule into fragments. There may be many such choices that have similar fragment size, similar surface-to-volume ratio, and thus similar accuracy (see Figure 6-1). Although similar in shape and size, the fragments in Figure 1 aren't equivalent: the atoms at the edge of fragment A sit at the center of fragment C. Therefore, they are better described in fragment C than in fragment A. The idea is then to improve the accuracy of fragment A by matching its edge atoms to their replicas in the center of fragment C. This leads to what we will call "Bootstrap Embedding": we partition the system in multiple ways, with overlapping fragments. Then, we use the centers of fragments in one partitioning to improve the edges of fragments in another partitioning. This way, we remove the inaccurate description of edge atoms. By matching centers to edges in various partitionings and requiring self-consistency, the fragment embedding calculation can "bootstrap" itself.

## 6.2 Theory

Before further describing Bootstrap Embedding, we will briefly summarize the key tools from DMET on which it is based. The fundamental idea underlying DMET is the Schmidt decomposition [257, 258, 174]. Given the exact wavefunction for a system with  $N$  states overall and  $N_f$  states chosen to comprise our fragment (which we assume to be a minority), we can decompose the full wavefunction as

$$|\Psi\rangle = \sum_i^{N_f} \lambda_i |\alpha_i\rangle |\beta_i\rangle, \quad (6.1)$$

where  $|\alpha_i\rangle$  are the fragment states and  $|\beta_i\rangle$  are an equal number of effective bath states. Remarkably, this new wavefunction is exact despite being represented by only  $N_f$  pairs of states. However, we do not in general know the exact wavefunction.

The key approximation of DMET is to describe the effective bath states at a lower level of theory, in this case mean field (MF). Then, these bath states,  $|\beta_i^{MF}\rangle$ , result from the Schmidt decomposition of the MF wavefunction for our system. We can then project the electronic Hamiltonian,

$$\hat{H} = \sum_{pq}^N h_{pq} \hat{a}_p^\dagger \hat{a}_q + \sum_{pqrs}^N v_{pqrs} \hat{a}_p^\dagger \hat{a}_q^\dagger \hat{a}_s \hat{a}_r, \quad (6.2)$$

onto the space of our chosen fragment states  $|\alpha_i\rangle$  and our MF approximate bath states  $|\beta_i^{MF}\rangle$ , resulting in a reduced Hamiltonian for the embedded fragment,

$$\hat{H}_{emb} = \sum_{pq}^{2N_f} \tilde{h}_{pq} \hat{c}_p^\dagger \hat{c}_q + \sum_{pqrs}^{2N_f} \tilde{v}_{pqrs} \hat{c}_p^\dagger \hat{c}_q^\dagger \hat{c}_s \hat{c}_r. \quad (6.3)$$

The second quantization operators,  $\hat{c}$ , are the union of the fragment and effective bath states. For a small number of fragment states, this embedded Hamiltonian can be solved exactly. The resulting Full Configuration Interaction [318] (FCI) wavefunction represents an embedding of a correlated wavefunction in a mean field bath. Its energy is evaluated as:

$$E_{emb} = \left\langle \sum_p^{N_f} \sum_q^N h_{pq} \hat{a}_p^\dagger \hat{a}_q + \sum_p^{N_f} \sum_{qrs}^N v_{pqrs} \hat{a}_p^\dagger \hat{a}_q^\dagger \hat{a}_s \hat{a}_r \right\rangle. \quad (6.4)$$

(The restriction on the sum prevents double-counting.) We then partition the system into disjoint fragments, perform this embedding calculation on each fragment, and sum their energies.

Unfortunately, naively performing this calculation gives poor results due to the approximate nature of the bath states. Density Matrix Embedding Theory draws its name from its solution to this problem. It seeks to improve the mean field bath states by matching the one-particle reduced density matrix (1RDM) of the FCI embedded wavefunction and that of the MF embedding wavefunction in the embedded space. That is

$$P_{FCI}^A = P_{MF}^A, \quad (6.5)$$

where  $A$  represents the embedded space corresponding to a fragment,  $A$ . This constraint is enforced by applying a one electron potential,  $\hat{\lambda}$ , and choosing the mean field embedding wavefunction to be the ground state of the system Hamiltonian (6.2) plus this potential:

$$|\Psi_{MF}\rangle = \arg \min_{|\Psi\rangle \in \text{determinants}} \langle \hat{H} + \hat{\lambda} \rangle. \quad (6.6)$$

The MF embedding wavefunction depends directly on  $\hat{\lambda}$ . Because the Hamiltonian for the embedded fragment (6.3) depends on the mean field, the embedded wavefunction also depends implicitly on  $\hat{\lambda}$ . It is now clear that the DMET matching condition represents a sort of self-consistency between the embedding (MF) and embedded (FCI) wavefunctions:

$$P_{FCI}^A(\hat{\lambda}) = P_{MF}^A(\hat{\lambda}) \quad (6.7)$$

In practice, this condition cannot be precisely met; different authors have remedied this by choosing to either satisfy equation 6.5 in a least squares sense [175], or choosing to exactly match subblocks of the 1RDM [46].

Previous efforts to extend DMET have focused on using an improved bath wavefunction to better satisfy the DMET matching condition (equation 6.5). These extensions have improved the description of the bath by using a more detailed, but still mean-field-like, wavefunction, including unrestricted Hartree Fock [46], Hartree Fock Bogoliubov [375], and the Antisymmetrized Geminal Power [331] (number-projected Hartree Fock Bogoliubov [307]) wavefunctions. In this chapter,

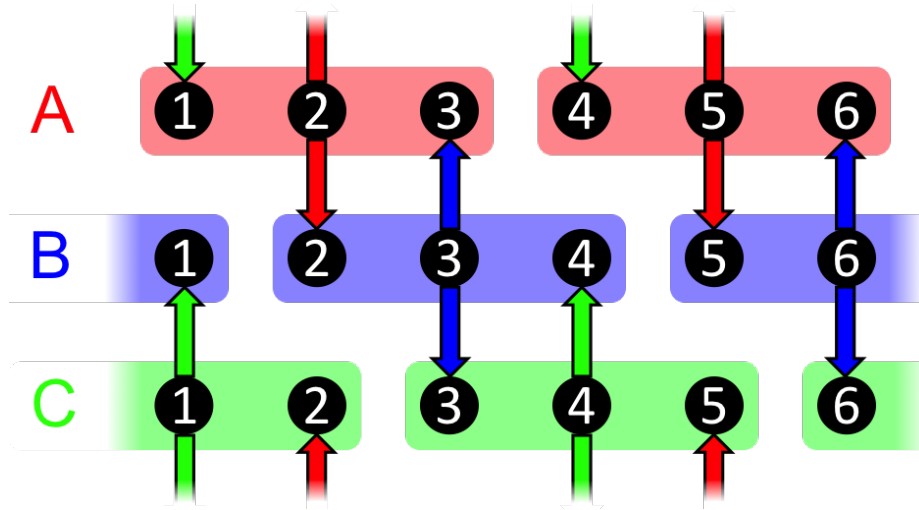


Figure 6-2: Illustration of the Bootstrap Embedding procedure for a lattice model with three sites per fragment. The three rows show the three possible partitionings of the lattice into fragments. The wavefunction of the center fragment site of each partitioning constrains the edge sites of the other two.

we use a Hartree Fock (HF) bath for simplicity, and focus instead on improving the embedded fragment directly. However, the new ideas presented can easily be combined with these improved bath wavefunctions.

Instead of the DMET matching condition, we propose an alternative: match the FCI 1RDM of the center of a fragment to the FCI 1RDM of the edge of a partially overlapping fragment from a different partitioning of the system (illustrated in Figure 6-2). We assume that the wavefunction on the central sites is more accurate than the wavefunction on the edge sites, and apply a potential to constrain the edge site wavefunction one fragment to match the central site wavefunction on another.

In this chapter, we match three properties of the wavefunction: (1) the one-electron populations, (2) the one-electron coherences, and (3) the on-top two-electron densities. That is, let  $A$  and  $B$  be overlapping fragments, and let  $e$  and  $e'$  index central sites of fragment  $A$  and at least one edge site of fragment  $B$ . Then, we want for all  $e$  and  $e'$ :

$$P_{ee'}^A = P_{ee'}^B \quad (6.8)$$

$$\Gamma_{eeee}^A = \Gamma_{eeee}^B, \quad (6.9)$$

where  $P$  and  $\Gamma$  are the FCI one- and two-electron density matrices of the embedded fragments in their respective embedded spaces.

We enforce these constraints with two potentials added to fragment  $B$ : a one-electron potential on its edge sites to constrain populations and coherences, and a diagonal two-electron potential on its edges to constrain diagonal elements of  $\Gamma^B$ . The Hamiltonian for embedded fragment  $B$  then

becomes

$$\hat{H}_{emb,cons} = \hat{H}_{emb} + \sum_{ee'}^{N_f} \Lambda_{ee'}^{(1)} \hat{c}_e^\dagger \hat{c}_{e'} + \sum_e^{N_f} \Lambda_e^{(2)} \hat{c}_e^\dagger \hat{c}_e \hat{c}_e^\dagger \hat{c}_e, \quad (6.10)$$

and  $\Lambda^{(1)}$  and  $\Lambda^{(2)}$  are optimized to satisfy the constraints in equations 6.8 and 6.9. These constraints are repeated for the edge sites of all fragments. Finally, we apply an overall one-electron chemical potential to constrain the total number of electrons on all fragments. The constraints are applied to all fragments and optimized simultaneously.

As an example, consider a lattice model with 3-site fragments (Figure 6-2). In partitioning  $B$ , the fragment spanning sites 2, 3, and 4 has a good center site and two edge sites. We wish to correct the edge sites (2 and 4) while leaving the center site (3) untouched. Notice that site 2 is a central site in partitioning  $A$  while site 4 is a central site in partitioning  $C$ . We can improve the fragment in  $B$  by making the population on its site 2 equal to that in partitioning  $A$  and by making the population on its site 4 equal to that in partitioning  $C$ . Concretely, we want:

$$P_{22}^B = P_{22}^A \quad (6.11)$$

$$P_{44}^B = P_{44}^C. \quad (6.12)$$

This is accomplished by applying potentials to sites 2 and 4 in partitioning  $B$ :

$$\hat{H}_{emb,cons}^B = \hat{H}_{emb}^B + \Lambda_{22}^B \hat{c}_2^\dagger \hat{c}_2 + \Lambda_{44}^B \hat{c}_4^\dagger \hat{c}_4. \quad (6.13)$$

Then, we simultaneously optimize  $\Lambda_{22}^B$  and  $\Lambda_{44}^B$  until conditions 6.11 and 6.12 are satisfied. Similar constraints are applied to sites 1 and 3 in partitioning  $A$  and to sites 3 and 5 in partitioning  $C$ . Finally, this can be extended to general one- and two-particle density matrix elements as following equations 6.8, 6.9, and 6.10.

Notice that in Eqs 6.8-6.10 the bath wave function has not been modified at all. All constraints are applied within the embedded FCI wave functions. Optimization of the mean field bath can thus be done completely separately from the bootstrap procedure, with bootstrap defining an optimal embedding for any approximate bath. We note that, unlike the original DMET problem, the bootstrap constraints can always be satisfied exactly. This is because in DMET, we attempt to match the less flexible MF to FCI, whereas in Bootstrap Embedding we match FCI to FCI. This also makes Bootstrap Embedding less sensitive to the initial choice of the embedding wavefunction because we are not matching the fragment to the bath, but rather to an embedded fragment in a different embedding.

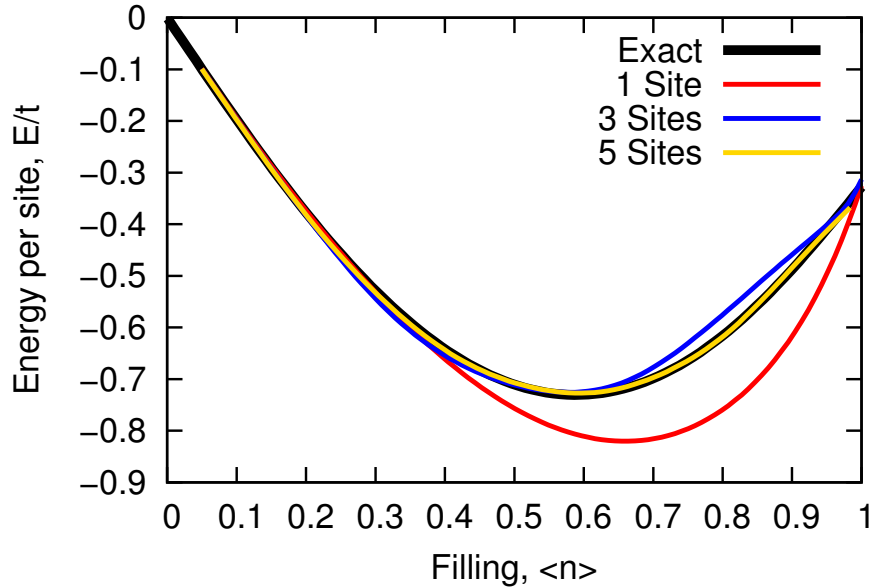


Figure 6-3: Energy per site of the one-dimensional Hubbard model as a function of electron filling with strong correlation ( $U/t = 8$ ). Even-numbered fragment sizes are omitted for visual clarity, but their errors are shown in Figure 6-4.

### 6.3 Results

As a first test of Bootstrap Embedding, we consider the one-dimensional Hubbard model [149, 93], a simple lattice model of electron correlation. The Hubbard Hamiltonian in the site basis for a lattice of  $N$  sites is

$$\hat{H}_{hub} = -t \sum_{\langle i,j \rangle} \sum_{\sigma \in \{1, \downarrow\}} \hat{a}_{i\sigma}^\dagger \hat{a}_{j\sigma} + U \sum_i \hat{n}_i \uparrow \hat{n}_i \downarrow. \quad (6.14)$$

The first term represents nearest-neighbor one-electron hopping. The second term represents on-site two electron repulsion.

Results for the one-dimensional Hubbard model are shown in Figure 6-3. Here, we examine qualitatively the convergence of Bootstrap Embedding as a function of the number of sites per embedded fragment over a range of electron fillings. The method shows good performance across the entire range of fillings and converges quickly with fragment size.

Figure 6-4 quantifies the rate of convergence of Bootstrap Embedding with fragment size, with comparison to DMET [175]. We see that the DMET energy error is inversely proportional to the fragment size ( $N_f$ ). This is consistent with the error being dominated by the surface sites adjacent to the bath. Meanwhile, Bootstrap Embedding converges at a far faster (possibly exponential) rate because the leading  $\frac{1}{N_f}$  error term has been eliminated. As an illustration of the disparity in convergence rates, DMET would require an (extrapolated) 174-site fragment to match Bootstrap's 6-site error.

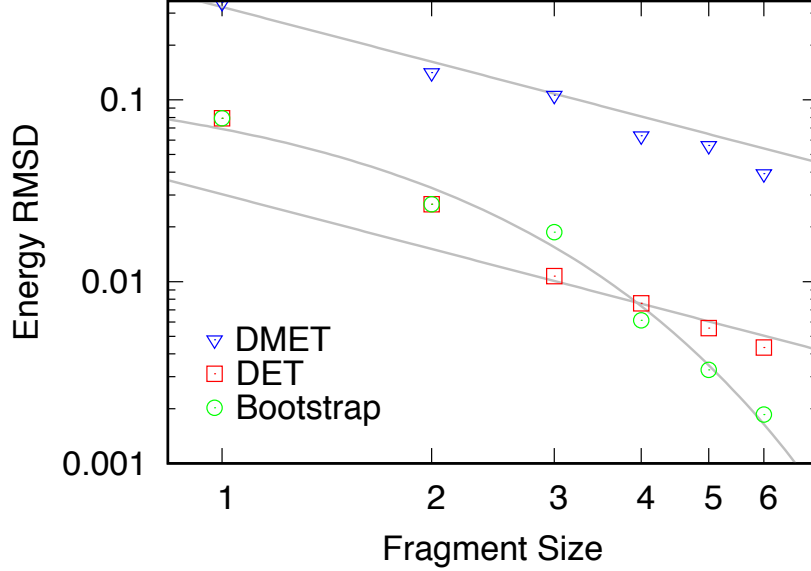


Figure 6-4: Convergence of two DMET-based methods and Bootstrap Embedding for the one-dimensional Hubbard model. Energy RMSDs are computed over the range of fillings from 0 to 1. DMET refers to the matching condition of reference [175]. DET refers to the matching condition of reference [46]. (For the matching condition in reference [176], we were unable to converge the calculation for fragments larger than three sites.) Grey trendlines are included to guide the eye. DMET and DET data are fit to a  $N_f^{-1}$  trendline. Bootstrap data are fit to an exponential trendline. (Note the axes are both logarithmic.)

In Figure 6-5, we examine the effect of bootstrapping different wavefunction properties. We start by matching only the one-electron populations at the edge,  $P_{ee}$ , as a baseline. Additionally matching either the one-electron coherences ( $P_{ee'}$ ) or the two-electron on-top pair densities ( $\Gamma_{eeee}$ ) results in a better answer. Matching all three quantities results in the best answer. As we constrain the embedded wavefunction at the edges of the fragment to look more like the wavefunction at the center, the energy improves.

To further explore the performance of the Bootstrap Embedding method, we consider a modified Hubbard model, which we dub the “ABAB model”

$$\hat{H} = \hat{H}_{hub} + \delta \sum_{i \in \text{odds}} \sum_{\sigma \in \{1, \downarrow\}} \hat{a}_{i\sigma}^\dagger \hat{a}_{i\sigma}. \quad (6.15)$$

This model adds a new dimensionless parameter,  $\delta/t$ , which can be thought of as an “electronegativity difference” between alternating “A” and “B” sites. This Hamiltonian can be thought of as a crude model of a one-dimensional ionic solid. The additional parameter creates a new and interesting observable of the wavefunction (in addition to the energy) that we do not know *a priori*: the population difference between the A and B sites. This is especially intriguing because the site populations are fundamental to the matching in Bootstrap Embedding. Figure 6-6 shows this population difference as a function of  $\delta/t$ .

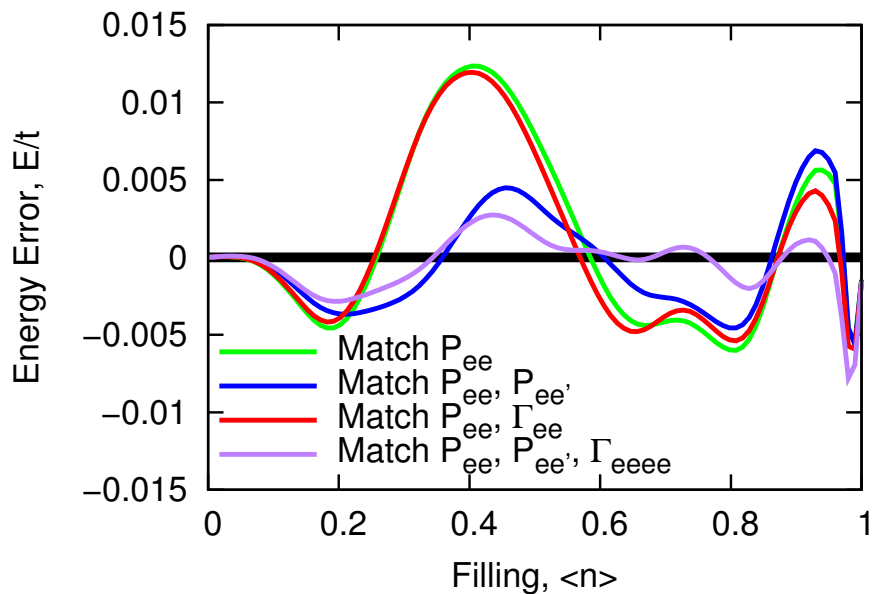


Figure 6-5: One-dimensional Hubbard model energy error for various constraint schemes. Fragments were 6 sites in size.

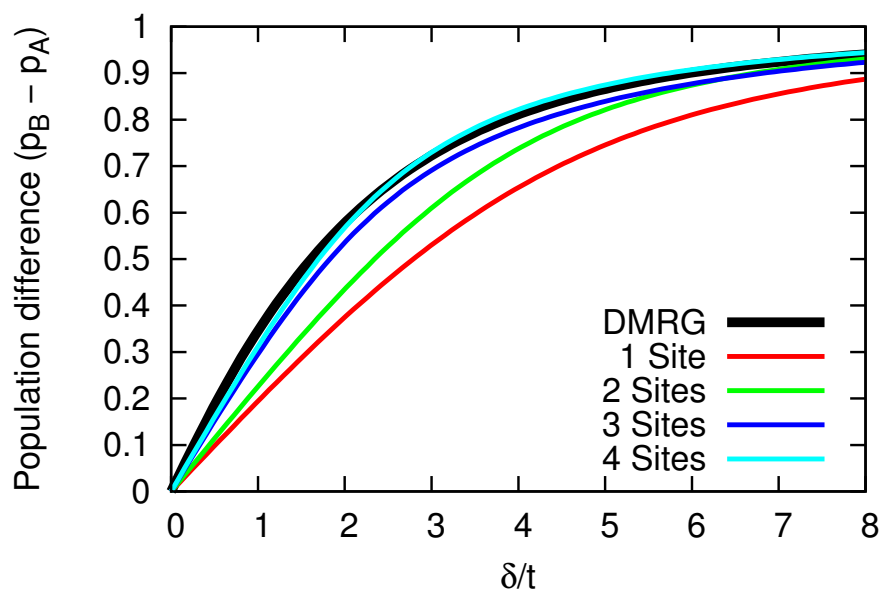


Figure 6-6: Population difference as a function of “electronegativity difference,”  $\delta/t$ , for the 1D ABAB Hubbard model at a filling of  $\langle n \rangle = 0.5$ . DMRG [52, 292] (on a lattice of 30 sites) is shown as a highly accurate answer for comparison.

## 6.4 Conclusions

In conclusion, we have described Bootstrap Embedding, a method which attempts to removed edge-based errors from embedding by matching the wavefunction at fragment edges to that at fragment centers. Bootstrap Embedding is based on the tools of DMET, but shows far faster convergence in the models tested: the Hubbard model and “ABAB” model. We have seen that matching more properties of the wavefunction leads to better energies, supporting the theory’s conceit.

Bootstrap Embedding has a number of additional advantages over previous schemes. First, it constrains exact wavefunctions to match exact wavefunctions, rather than matching exact wavefunctions to approximate ones. This allows the embedding boundary conditions to be satisfied exactly, rather than approximately satisfied by least squares. This also means that the embedding calculation is less sensitive to the choice of the approximate embedding wavefunction. Second, Bootstrap Embedding has a self-consistent choice for the boundary conditions of the fragments: match embedded fragments to embedded fragments. Third, Bootstrap embedding trivially allows for overlapping fragments. Fourth, Bootstrap Embedding is less sensitive to the choice of partitioning of the system into fragments; multiple partitionings are chosen and made consistent with each other.

In the future, Bootstrap Embedding can be extended in a number of directions. Up to this point, we have dealt only with the ground state. This chapter could be extended to handle excited states, either through direct excitation in the embedding and/or embedded wavefunction, or via linear response [36]. As another next step, this chapter can be extended to treat molecular systems (e.g. Figure 6-1). Both of these extensions could also involve iteratively improving the underlying mean field, perhaps by minimizing the embedded energy (equation 6.4) with respect to the mean field orbitals.

## 6.5 Acknowledgments

The work described in this chapter was undertaken with Takashi Tsuchimochi. He is listed as a co-author in a submitted manuscript.

## Chapter 7

# Why many semiempirical molecular orbital theories fail for liquid water and how to fix them

Water is an extremely important liquid for chemistry and the search for more accurate force fields for liquid water continues unabated. Neglect of diatomic differential overlap (NDDO) molecular orbital methods provide an intriguing generalization of classical force fields in this regard because they can account both for bond breaking and electronic polarization of molecules. However, we show that most standard NDDO methods fail for water because they give an incorrect description of hydrogen bonding, water's key structural feature. Using force matching, we design a reparameterized NDDO model and find that it qualitatively reproduces the experimental radial distribution function of water, as well as various monomer, dimer, and bulk properties that PM6 does not. This suggests that the apparent limitations of NDDO models are primarily due to poor parameterization and not to the NDDO approximations themselves. Finally, we identify the physical parameters that most influence the condensed phase properties. These results help to elucidate the chemistry that a semiempirical molecular orbital picture of water must capture. We conclude that properly parameterized NDDO models could be useful for simulations that require electronically detailed explicit solvent, including the calculation of redox potentials and simulation of charge transfer and photochemistry.

### 7.1 Introduction

Water is ubiquitous in nature. At the same time, water is notoriously difficult to model.[18] This has spawned not just a multitude of models of water, but even a spectrum of classes of models of water. On the more accurate end of the spectrum are *ab initio* molecular dynamics simulations,[189] which

are robust and (at least in principle) allow for simulation of chemical reactions and photochemistry. However, these methods are expensive for all but the smallest of model systems and even these methods do not always give physical results.[129, 192, 306, 337] This has led to the development of many computationally inexpensive empirical molecular mechanics models for water.[160, 121] However, these methods are limited in their applicability to reactions and electronically excited systems because they do not account for electronic degrees of freedom.

Between these extremes are polarizable force fields, which seek to describe the electronic physics of water via a phenomenological treatment of molecular polarizability. These methods include charge-on-spring Drude particles,[190, 347, 371] multipole expansions,[335] and fluctuating charge models.[271, 270] These methods have found successful application, but each presents its own difficulties.[352, 55]

Instead of attempting to classically reproduce the effects of polarizability, we can instead use a model that contains polarizability implicitly. Semi-empirical quantum chemical methods [373] approximate the Hartree Fock method and then recover accuracy with a set of empirical parameters. Because they are still quantum-mechanical at their core, these methods contain the physics of polarizability that is difficult to capture with a phenomenological classical interaction. In addition, they are undergirded by the same underlying mature algorithms used in quantum chemistry, giving them great numerical stability. At the same time, these methods are also faster than traditional electronic structure.

Within the set of semi-empirical methods, we examine the popular family of Neglect of Diatomic Differential Overlap (NDDO) methods.[262] These methods have been widely used to describe systems that include effects that cannot be easily captured by conventional force fields – such as bond breaking and charge transfer – but that are too large for a fully ab initio calculation. Often, NDDO methods are used in studies of properties of water, including hydrogen bonding,[181] solvation,[68] the structure of water clusters,[163] and water’s role in chemical reactions.[113, 186]

With this in mind, we wanted to understand how well NDDO methods perform for the description of bulk water. As a first test, we focus on a popular NDDO method, PM6,[311] and look at an important structural descriptor of water, the oxygen-oxygen pair distribution function (Figure 7-1). We find that the PM6 method gives a very poor description water’s structure, with nearest neighbor peaks that are too distant, too diffuse, and with overall understructuring. Since the pair distribution function serves as a proxy for important properties of water,[303] such as hydrogen bonding and solvation, this result calls into question the utility of PM6 as a model of bulk water.

Further, we look at the hydrogen bonding structure of PM6 water since hydrogen bonding is the most important effect in organizing water.[157] Figure 7-2(a) shows the binding potential energy between a water dimer. PM6 favors a hydrogen bond that is too long, and a bond angle far from the physical 180 degrees. Figure 7-2(c) shows a snapshot of hydrogen bonding in PM6 water, taken

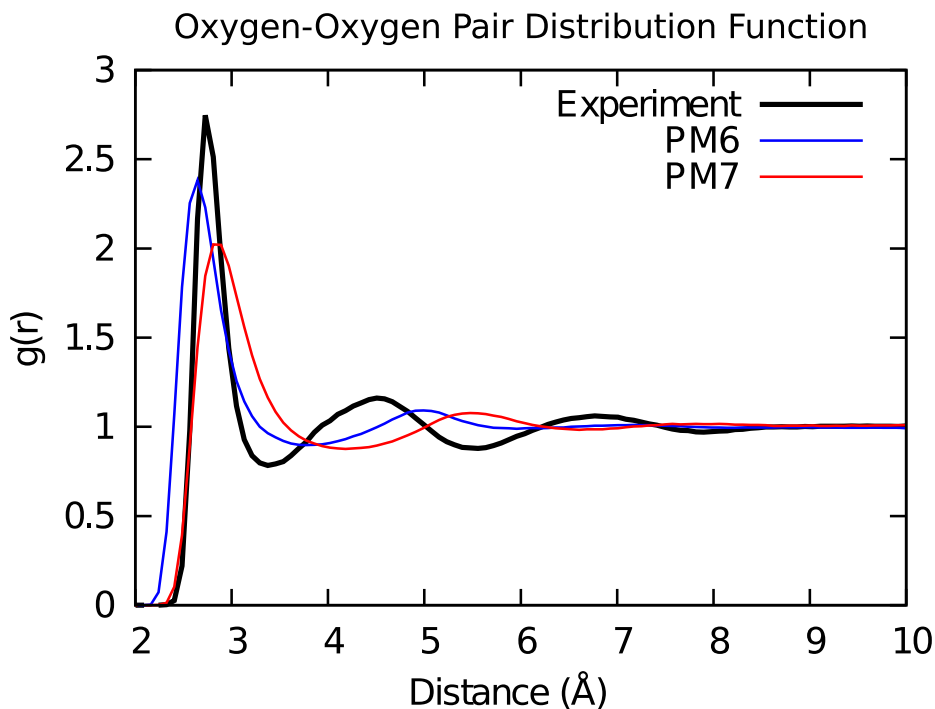


Figure 7-1: Oxygen-oxygen pair distribution function for two popular NDDO water models compared to experimental results.[303] While we focus on the PM6 method in this chapter, we include the successor to PM6, PM7, to show that it does not offer an improved description of the structure of water.

from MD. It is clear that PM6 water gets the radial and angular components of hydrogen bonding wrong, and that this in turn results in an incorrect pair distribution function.

This result raises the natural question: what is wrong with PM6? The PM6 model has two components: an approximate Hamiltonian and a set of empirical parameters for that Hamiltonian. PM6 is parameterized to describe chemistry in general, with a universal set of parameters per atom; it could be the case that, similar to MM force fields, a separate set of parameters is needed for oxygen and hydrogen in water molecules than in, say, organic molecules. On the other hand, it is possible that the PM6 Hamiltonian simply lacks the flexibility to describe water. Because of the minimal basis set used in PM6, it may have too little capacity for polarizability.[363] And since this is critical to the intermolecular interactions of water, it may be that PM6 cannot get water's structure right regardless of parameters.

To answer this question, we reparameterize the PM6 Hamiltonian specifically for water, an approach that has been explored recently.[376, 207] We first discuss the force-matching method for parameterization. Next, we present the properties of bulk water using our reparameterized PM6. Finally, we discuss the key differences between our parameters and those of the original PM6 model, and explain how reparameterization fixes the errors in PM6.

## 7.2 Reparameterizing PM6 for water

### 7.2.1 Force matching

Force matching [92, 153] uses a set of ab initio structures and attempts to fit a model to reproduce the energies and forces of those structures. Explicitly, this amounts to minimizing an objective function,  $\chi^2$ , which we define as the average residual of the force and energy,  $\mathbf{X}$ , for model parameters  $k$ , over some distribution of coordinates  $P$ . The energy and force are given weights  $w$  and  $1-w$ , respectively. This amounts to:

$$\chi^2 = \int P(\mathbf{r}; k) |\mathbf{X}(\mathbf{r}, k; w)|^2 d\mathbf{r} \quad (7.1)$$

$$|\mathbf{X}(\mathbf{r}, k; w)|^2 = \Delta\mathbf{Y}(\mathbf{r}, k)^T \text{Cov}(\mathbf{Y}_{QM})^{-1} \Delta\mathbf{Y}(\mathbf{r}, k) \quad (7.2)$$

$$\Delta\mathbf{Y} = \begin{pmatrix} w (E_{MM}(\mathbf{r}, k) - E_{QM}(\mathbf{r})) \\ \frac{1-w}{3N} \left( F_{MM}^{(1)}(\mathbf{r}, k) - F_{QM}^{(1)}(\mathbf{r}) \right) \\ \frac{1-w}{3N} \left( F_{MM}^{(2)}(\mathbf{r}, k) - F_{QM}^{(2)}(\mathbf{r}) \right) \\ \vdots \\ \frac{1-w}{3N} \left( F_{MM}^{(3N)}(\mathbf{r}, k) - F_{QM}^{(3N)}(\mathbf{r}) \right) \end{pmatrix} \quad (7.3)$$

$$\text{Cov}(\mathbf{Y}_{QM}) = \langle \mathbf{Y}_{QM} \otimes \mathbf{Y}_{QM} \rangle \quad (7.4)$$

where  $N$  is the number of atoms,  $F^{(i)}$  is the force on the  $i$ th coordinate, Cov denotes the covariance matrix, and  $\mathbf{Y}$  is a vector of weighted energy and force components. Improving on previous work,[348] we account for energy-force covariance in our residual, anticipating that it will give a more statistically rigorous objective function.

We use the PM6 [311] Hamiltonian for our model. We chose this semi-empirical method over the more recent PM6-DH+ [182] and PM7 [312] methods because initial tests showed that these gave worse results for the radial distribution function of water and because they are both slower than PM6. We also found that the greater flexibility of the PM6 model gave better results than the older, well-established PM3 [310] model.

We fit the parameters of the PM6 model to match quantum chemical forces and energies for clusters of 18 water molecules. Ab initio data were calculated at the RI-MP2 [353, 354]/aug-cc-pVTZ [86] level of theory using the frozen core and dual-basis [362] approximations. Ab initio calculations were performed using the Q-CHEM [291] quantum chemistry package. Semi-empirical calculations were performed using the MOPAC [309] package. 5100 structures were sampled from the Boltzmann ensemble at 300K by running molecular dynamics on the force field of Wang et. al.[348] with a harmonic restraining potential in the GROMACS [139] package. Samples were separated in time by 1ps to reduce statistical correlation. The energy and force were given equal weight. Local

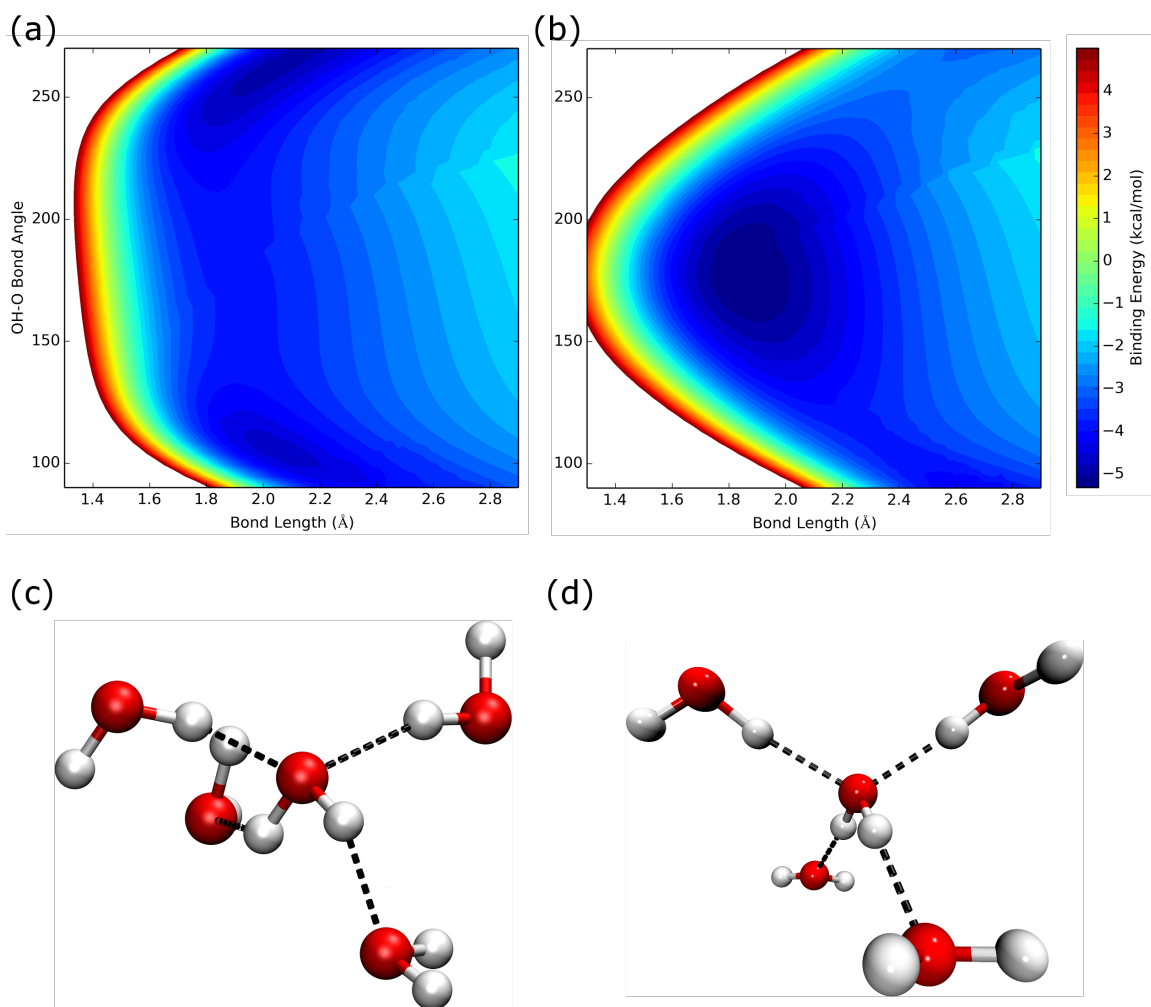


Figure 7-2: (a) and (b): Binding potential energy for a water dimer. The OH-O bond angle refers to the angle formed by the oxygen and hydrogen participating in the bond and the oxygen attached to said hydrogen. (c) and (d): Illustrative hydrogen bonding structures of water in bulk. PM6 water adopts hydrogen bonding geometry between the tetrahedral and see-saw configurations, while the force-matched model prefers the physical tetrahedral configuration. Further, the force-matched water has OH-O bond angles around 180 degrees, while the PM6 hydrogen bond angles are more disordered. These structures were taken directly from MD simulation discussed in section 7.2.2.

minimization of the objective function was performed using the BFGS [237] algorithm with finite difference first derivatives starting from the original PM6 parameters.[311]

Another model was created in which the energy, force, and net dipole moment of the clusters were all fit with equal weight, but the parameters and properties of this model did not change significantly. Because it offers no improvement, and the energy and force matching is conceptually simpler and has fewer parameters, we will use the energy and force matched PM6 parameters for the remainder of this discussion.

## 7.2.2 Comparison to experiment

To validate our water model, we compare its monomer, dimer, and bulk liquid properties to experimental data. Monomer and dimer properties were calculated at the model's equilibrium geometry using MOPAC. Liquid water properties were averaged over structures sampled using NVT molecular dynamics in a version of the GROMACS package modified to interface with MOPAC for energy and force calculations. Ten independent trajectories of 115 waters were simulated with periodic boundary conditions for 100 ps with a 1 fs time step. To allow for equilibration, samples were taken only after the first 5 ps. Simulations were run at 300K using the Nosé-Hoover thermostat [238, 145] at a density of  $999.50 \text{ kg/m}^3$  (corresponding to a square cell 1.51 nm on a side).

Figure 7-3 shows the radial distribution function (RDF) for our model as compared to neutron scattering experiments.[303] Table 7.1 provides a comparison between our model and experimental data for a variety of water properties. Results for the PM6,[311] dispersion and hydrogen bonding corrected PM6-DH+,[182] and PM7 [312]models are also included to provide a baseline for comparison. Finally, Figure 7-2(b) shows the dimer binding potential for our model and Figure 7-2(d) shows a sample taken from bulk simulation to illustrate its hydrogen bonding structure.

These observables break down into two classes: structural parameters that include the geometry of each water molecule as well as the geometry of hydrogen bonding, and electronic properties such as polarizabilities, dipoles, and dielectric constants. Our model shows consistent improvement of the former and scattered improvement of the latter. We note that none of the properties in these figures and tables were fit directly; they all arise as a consequence of force matching.

Our model does well for the simplest structural parameters of water, the gas phase bond length and angle. Often, these parameters are fit directly in force fields, but our force matching produces the same result. Figure 7-2 shows that the basic hydrogen bonding structure is correct in our model, with 180 degree O-H $\cdots$ O bond angles and tetrahedral packing in the bulk liquid. Meanwhile, as mentioned before, PM6 favors bond angles closer to 100 degrees, leading to a much more disordered hydrogen bonding network. This effect may also explain the discrepancy in self-diffusion constants: PM6 (and other NDDO methods) have too large self-diffusion constants, due to their disordered hydrogen bonding creating a weaker solvation cage around individual water molecules. Our repa-

parameterized method, with its improved hydrogen bonding structure, has a self-diffusion constant which is lower and much closer to experiment.

The radial distribution function shows that our model reproduces two body interactions well. The PM6, PM6-DH+, and PM7 models perform poorly in comparison, showing that our force matching is necessary to properly capture the basic structure of water. Surprisingly, the PM7 model is worse for the structure of water than PM6, despite having more parameters. Our model shows slight overstructuring in the oxygen-oxygen RDF and larger overstructuring in the oxygen-hydrogen and hydrogen-hydrogen RDFs. Since this effect grows as we look at lighter nuclei, we attribute this overstructuring to nuclear quantum effects which are not included in our classical molecular dynamics simulations. Again we note the hydrogen bonding seems to be the key effect distinguishing our model from standard PM6. Focusing on the oxygen-hydrogen RDF (Figure 7-3(b)), we notice that the first two hydrogen bonding peaks are understructured for PM6. This in turn creates the understructuring in the oxygen-oxygen RDF.

However, our model does not correctly describe the electronic properties of water in the gas phase, with too large dipole moments for the monomer and dimer. PM6 and NDDO methods are known to have too small a gas phase polarizability, and our method does not correct this. Despite having incorrect electronics in the gas phase, our model does reproduce the electronics of our target phase, liquid water. The low and high frequency dielectric constants are both in agreement with experiment. It is important to note that the PM6 model also does well for these observables. This supports our initial motivation to use semi-empirical methods because of their built-in treatment of polarization effects.

### 7.2.3 Why PM6 fails

In light of the improvement wrought by force matching, we now ask: why is the new model better? Specifically, we wish to understand which parameters are important to this new model and how these parameters affect the physical properties of our water model. We tackle this question by performing knockout experiments where we replace one parameter in our model with its PM6 value. We then look at the effect of this knockout on two key observables, the energy RMSD of this new set of parameters (averaged over ten thousand snapshots) and the oxygen-oxygen RDF (as simulated before). We find that 14 parameters cause the RMSD to rise substantially, 14 parameters result in an unphysical RDF, and that 12 of these parameters do both, indicating that they are key to the physics of our model.

These parameters fall into two classes: half concern core-core repulsion between oxygen and hydrogen and half concern the electronic structure of oxygen. In PM6, the core-core repulsion is handled using empirical potentials. We find that parameters involving the oxygen-hydrogen core-core repulsion are important to our model, and that the modifications made these parameters in our

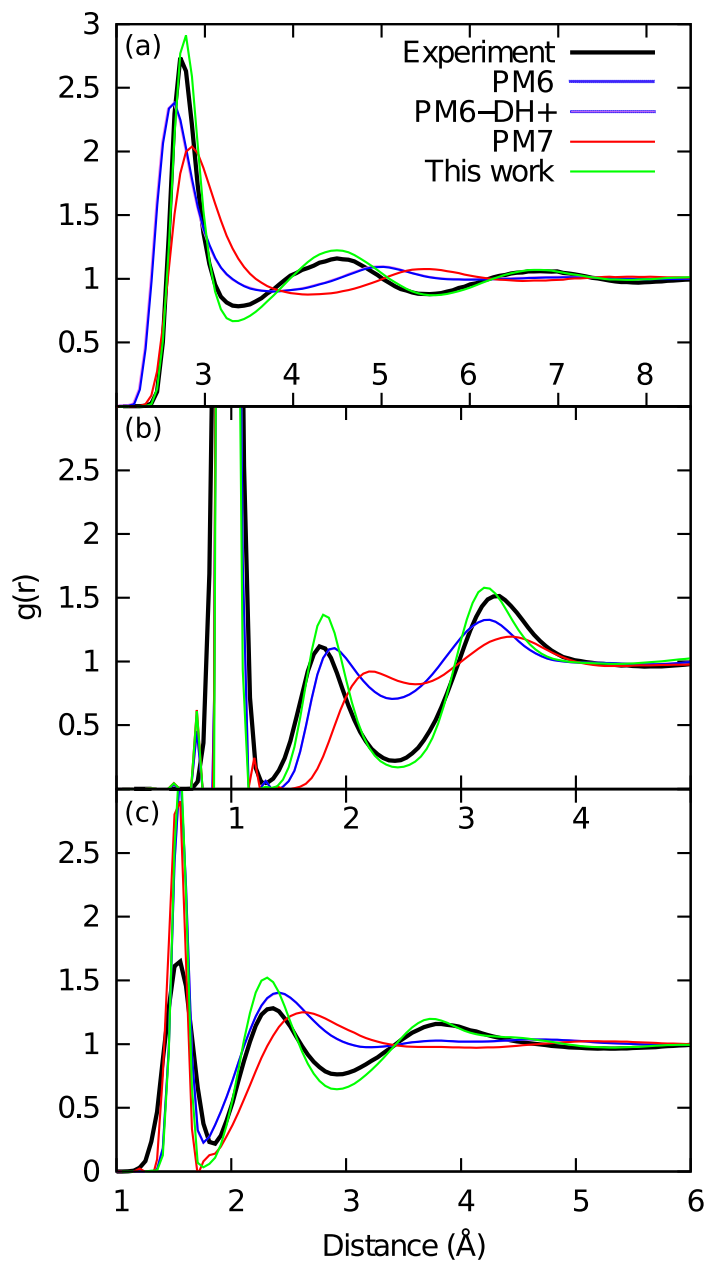


Figure 7-3: (a) O-O, (b) O-H, and (c) H-H radial distribution functions for water as predicted by PM6, PM6-DH+, PM7, and this work, and as measured in Ref [303]. Note that the horizontal scale differs between plots to show the region of interest.

Table 7.1: Calculated physical properties of PM6, PM6-DH+, PM7, and this work compared to experiment as well as the established AMOEBA and TIP4P/2005 force fields. Liquid water properties were calculated at 300K. Uncertainties, when appropriate, are given inside parenthesis and apply to the last significant figure.

	PM6	PM6-DH+	PM7	AMOEBA [268]	TIP4P/2005 [2]	This work	Experiment
<b>Monomer Properties</b>							
O-H Distance ( $\text{\AA}$ )	0.949	0.949	0.955	0.957 [268]	0.957 [2]	0.958	0.9575(5) [195]
Bond Angle	107.48	107.48	105.49	108.50 [268]	104.52 [2]	104.75	104.51 [195]
Dipole Moment ( $D$ )	2.071	2.071	2.128	1.773 [268]	2.305 [2]	2.104	1.85498(9) [297]
Polarizability ( $\text{\AA}^3$ )	1.35	1.35	1.43	1.421 [268]	N/A	1.34	1.470(6) [224]
<b>Dimer Properties</b>							
Binding Energy ( $\frac{\text{kcal}}{\text{mol}}$ )	-3.86	-3.81	-2.85	4.96 [268]	-7.06	-5.35	-5.4(7) [71]
$\theta_A$	47	53	39	57.2 [268]	77	48	58(6) [87]
$\theta_D$	48	54	46	N/A	28	50	51(6) [87]
O-O Distance( $\text{\AA}$ )	2.88	2.79	3.00	2.892 [268]	2.75	2.84	2.98(1) [87]
Dipole Moment ( $D$ )	2.095	2.817	3.359	2.54 [268]	3.22	3.08	2.64(5) [87]
<b>Liquid Properties (300K)</b>							
Static Dielectric Constant	65(2)	68.6(6)	78(2)	81.4(1) [349]	60 [2]	75(1)	78.4(1) [99]
High Frequency Dielectric Constant	1.8698(6)	1.8699(7)	1.8570(7)	N/A	N/A	1.8775(7)	1.79(1) [43]
Diffusion Constant( $10^{-5} \frac{\text{cm}^2}{\text{s}}$ )	12.7(2)	13.3(4)	14.1(6)	2.00 [349]	2.08 [2]	1.62(7)	2.299(5) [144]

model uniformly serve to weaken the oxygen-hydrogen repulsion. The core-core repulsion is summed pairwise and has both diatomic and monatomic parameters. The core-core repulsion between atoms  $i$  and  $j$  separated by  $R_{ij}$  is given by:

$$E_n(R_{ij}) = Z_i Z_j \left[ \langle s_i s_i | s_j s_j \rangle (1 + x_{ij} e^{-\alpha_{ij} R_{ij}}) + a_i^{b_i(R_{ij}-c_i)^2} + a_j^{b_j(R_{ij}-c_j)^2} \right] \quad (7.5)$$

where  $Z_i$  is the atomic number of atom  $i$  and  $x$ ,  $\alpha$ ,  $a$ ,  $b$ , and  $c$  are PM6 parameters. Of these, the diatomic parameter  $\alpha_{OH}$ , and the monatomic parameters  $a_H$  and  $c_H$  are the most important to our force matched model. In our parameterization,  $\alpha_{OH}$  decreases, resulting in reduced range of the oxygen-hydrogen repulsion.  $a_H$  and  $c_H$  also both decrease, creating a wider basin of attraction with a shorter radius. Since hydrogen-hydrogen core-core repulsion is not frequently encountered in liquid water, the changes in these three parameters change to correct the oxygen-hydrogen interaction. Both PM6 and our model describe the covalent OH bond well, so we conclude that this weaker and shorter cut-off core-core interaction between oxygen and hydrogen is necessary to get correct hydrogen bond energetics and geometries.

The second class of parameters concern the electronics of oxygen and determine approximate one- and two-electron integrals within the NDDO approximation. Of these, the three most important parameters to our model are  $G_{sp}$ ,  $U_{pp}$ , and  $U_{ss}$ , all for oxygen. The  $U$  parameters are the one electron integrals (site energies), while  $G_{sp}$  influences two electron integrals involving the  $sp$  combination of oxygen atomic orbitals. Scanning across  $G_{sp}$  shows that large values result in a linear water geometry while small values give too acute a bond angle. In our model,  $G_{sp}$  decreases by half. Taken at face value, this corrects water's bond angle in the gas phase. Looking deeper, we also see that the electronic geometry of water becomes more tetrahedral, resulting in correct hydrogen bonding network geometry. However,  $G_{sp}$  also controls the intra-atom two electron repulsion on oxygen and the coupling between oxygen and hydrogen. When this parameter decreases, *ceteris paribus*, oxygen becomes extremely electronegative and forms ionic bonds with hydrogen. To compensate for this behavior,  $U_{ss}$  and  $U_{pp}$  increase, decreasing the electronegativity of oxygen.

Considering the effects of all of these parameters, we can now understand the results in Figure 7-2. PM6 forms poor hydrogen bonding networks for two reasons. First, it has too much core-core repulsion between oxygen and hydrogen, which weakens hydrogen bonds. Second, the electronic geometry of oxygen is wrong, making tetrahedral hydrogen bonding networks energetically unfavorable.

## 7.3 Conclusions

NDDO methods offer an attractive alternative to polarizable force fields for capturing complex electronic phenomena in condensed phases at lower cost than fully *ab initio* methods. However,

these methods, specifically PM6, provide a poor description of the structure of liquid water as characterized by its pair distribution function and hydrogen bonding structure. We asked whether this result is due to a fundamental flaw in the PM6 Hamiltonian or whether the parameters for PM6 are just ill-suited for liquid water. To approach this question, we used force matching to reparameterize PM6 for liquid water. Comparing to experiment, we found that this new force-matched model had improved structural and electronic properties for water especially in the liquid phase, as well as in the gas phase. This led us to conclude that the PM6 Hamiltonian is in fact capable of describing liquid water. We then looked at which PM6 parameters effected this change and looked at their physical purpose. The main changes were a decreased oxygen-hydrogen core-core repulsion and electronic modifications to oxygen that promoted a tetrahedral electronic geometry. Both of these effects produced more physical hydrogen bonding and thus a better structure for liquid water.

This study allows us to understand the physics that are important to modeling water, and to show that NDDO methods are capable of capturing such physics. This opens up the possibility of applying these semi-empirical methods to the development of models that are cheaper than full ab initio simulations, but also capture the complex physics of water.

Because they treat electronic properties explicitly, NDDO models have great potential for describing complex condensed phase systems. For example, these methods could be used for calculation of redox potentials, solvation energies, and even excited state properties in solution, problems that are traditionally hard for molecular mechanics. While NDDO does not natively provide an accurate description of the condensed phase, we have shown that it still contains the essential physics and needs only to be reparameterized.

## 7.4 Appendix: Force field parameters

Table 7.2: NDDO parameters from force matching compared to original PM6 parameters [311].

Parameter	PM6 Value	Force-Matched Value	Percent Change
Hydrogen			
$U_{ss}$	-11.247	-10.709	4.78
$\beta_s$	-8.3530	-7.7084	7.72
$Z_s$	1.2686	1.3361	5.32
$g_{ss}$	14.449	15.701	8.66
$a$	.024184	0.17697	631
$b$	3.0560	3.9826	30.3

$c$	1.7860	1.2050	32.5
<hr/>			
Oxygen			
$U_{ss}$	-91.679	-67.069	26.8
$U_{pp}$	-70.261	-63.489	9.64
$\beta_s$	-65.635	-52.252	20.4
$\beta_p$	-21.623	-21.553	0.324
$Z_s$	5.4218	4.5999	15.2
$Z_p$	2.2710	1.8675	17.8
$g_{ss}$	11.304	12.865	13.8
$g_{sp}$	15.807	9.5353	39.7
$g_{pp}$	13.618	12.516	8.09
$g_{p2}$	10.333	11.052	6.96
$h_{sp}$	5.0108	3.6867	26.4
$a$	-0.017771	0.027321	254
$b$	3.058310	4.3324	41.7
$c$	1.8964	1.6071	15.3
<hr/>			
Diatomic			
$\alpha_{HH}$	3.5409	4.7169	33.2
$x_{HH}$	2.2436	2.6515	18.2
$\alpha_{OO}$	2.6240	2.5750	1.87
$x_{OO}$	0.53511	0.69485	29.9
$\alpha_{OH}$	1.2609	1.9896	57.8
$x_{OH}$	0.19230	0.22185	15.4

## 7.5 Appendix: Size extrapolation of static dielectric constants

Our simulation box is not large enough to directly calculate the static dielectric constants listed in Table I of the main text. Instead, we employ an extrapolation procedure. We cut random spheres of varying size ( $N=30-60$  in increments of 5) from our MD trajectory, and compute a dipole moment for each sphere. We then employ the formula for the dielectric constant of an isolated sphere [233] for each value of  $N$ . Finally, we extrapolate to infinite  $N$ . This extrapolation is shown in Figure 7-4. Errors in Table I of the main text are standard errors of the y-intercept of our fits. (We do

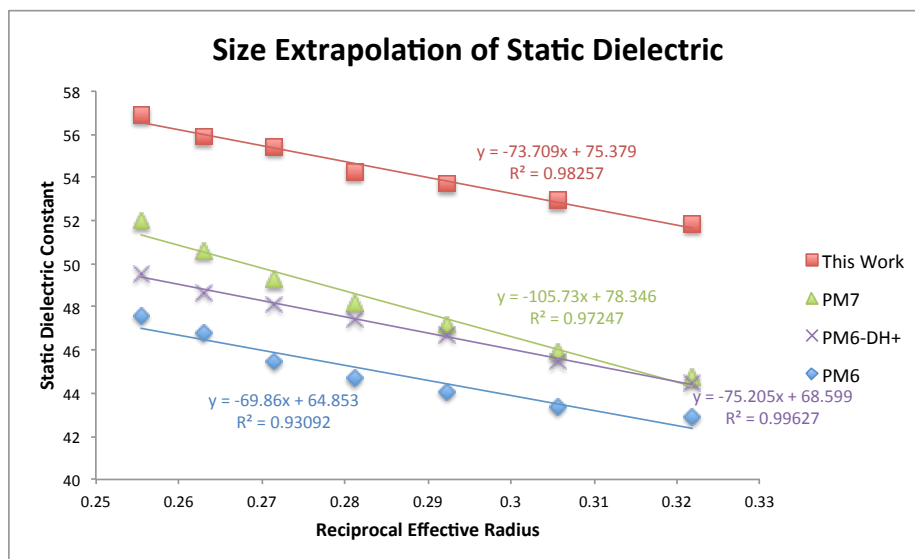


Figure 7-4: Size extrapolation of the static dielectric of water from our method as well as three common NDDO Hamiltonians.

not extrapolate the high-frequency dielectric of the molecule as we find that our simulation box is effectively the infinite limit for this shorter-range property.)

## 7.6 Acknowledgments

This work used force matching code written by Lee-Ping Wang and an interface to MOPAC written by Jiahao Chen. They are listed as coauthors in reference [357].



# Chapter 8

## Conclusions

In this thesis, we have explored many approaches to large systems. We studied subsets of experimental systems using density functional theory. We applied tools of random matrix theory to solve Anderson models. We developed embedding theories for strongly correlated systems. We employed semiempirical molecular orbital theory as a force field.

In Chapter 2, we saw the power of traditional approaches. Using molecular dynamics and density functional theory, we were able to corroborate experiments on site-specific cysteine arylation. We showed the  $\pi$ -clamp conformer forms under ambient conditions and that it promotes reactivity. We also explained trends in reactivity upon mutation of the  $\pi$ -clamp-forming residues and upon the addition of salts. Constrained density functional theory allowed us to compute the emission energies of exciplexes, but these energies only loosely match experiment. We also computed binding energies for these exciplexes. Finally, we modeled a crystalline rubrene/ $C_{60}$  interface. Using constrained density functional theory configuration interaction, we computed an electroluminescence peak and line shape that matched experiment. We also computed that charge separation is much more facile in this system compared to its disordered counterpart.

In Chapters 3 and 4, we employed random matrix theory to study disordered systems. We used free probability to approximate the density of states of the Anderson model, as well as some of its extensions. Qualitatively, we found the approximate density of states to be visually identical to the exact density of states. To quantify this, we developed an error analysis and found that in most cases, the leading error was in the eighth moment of the density of states.

Looking forward, this work could be extended in three ways. First, our error analysis allows us to compute the leading order correction to the density of states. This correction could be applied to cases where the free probability approximation is not sufficient, such as the case of off-diagonal disorder. Second, so far we have concerned ourselves with eigenvalues only; eigenvectors are also important for understanding disordered systems. Specifically, the localization length of particles in

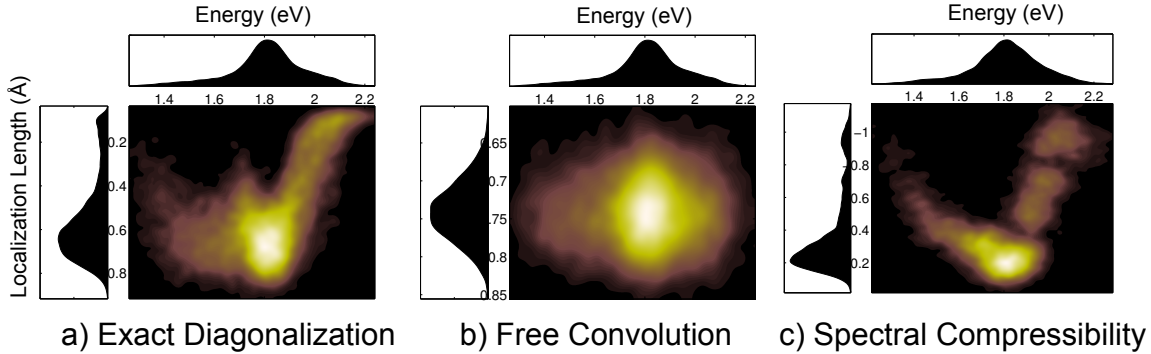


Figure 8-1: Comparison of methods for computing the density of states and localization length of excitons in metal-free phthalocyanine. Horizontal histograms at the top of each plot show the density of states. Vertical histograms at the left of each plot bin localization lengths, computed as the root variance of the position operator. The colored plots are heat maps of the cross-correlation of localization length and energy, smoothed with kernel density estimation. a) The exact result shows a relationship between energy and localization. b) Free convolution gets the correct density of states, but randomizes localization length and its correlation to energy. c) the spectral compressibility of the density of states predicted by free probability in (b) contains some information about localization.

disordered materials is a key property (e.g. exciton diffusion lengths in solar materials and charge conductivities in electroluminescent materials). Third, this work could be extended to describe real systems beyond the Anderson model. Preliminary results for the latter two directions are shown in Figure 8-1. From QM/MM simulations of disordered metal-free phthalocyanine under ambient conditions, an ensemble of one-exciton Hamiltonians was generated. These Hamiltonians were first exactly diagonalized, resulting in a cross-correlation between energy and localization length (panel *a*). Free convolution reproduces the density of states well, but gives incorrect localization lengths and destroys the cross-correlation (panel *b*). This is because the free approximation is equivalent to randomly rotating the eigenvectors, so all eigenvalue-eigenvector correlation is lost. It may be possible to recover information about localization from statistics of the density of states. Panel *c* shows the result of replacing the localization length with the spectral compressibility [173, 35, 245]: the cross-correlation is qualitatively restored. Other approaches to this problem may also prove fruitful [226, 26].

In Chapters 5 and 6, we extended Density Matrix Embedding Theory (DMET), an embedding theory for strongly correlated systems. First, we introduced an antisymmetrized geminal product (AGP) wavefunction to describe correlations in the bath. The resulting formalism has a number of advantages. First, it properly treats the *weak* correlation limit of independent pairs, which DMET is unable to do with a mean-field bath. Second, it associates a *size extensive* correlation energy with a given density matrix (for the models tested), which AGP by itself is incapable of providing. Third, it provides a reasonable description of charge redistribution in strongly correlated but non-periodic systems. We next introduced a new embedding theory that we call “Bootstrap Embedding”. It uses

overlapping fragments to improve the description of fragment edges. We found Bootstrap Embedding converges rapidly with embedded fragment size, overcoming the surface-area-to-volume-ratio error typical of many embedding methods.

Going forward, the grand challenge for these methods is generalization to molecules. A number of questions must first be answered:

- What is the optimal choice of fragments? Different choices of fragments will lead to different quality embeddings. In simple model systems, this choice is often intuitive, but for molecules the choice can be complex. One potential solution is to use the entanglement entropy of the Schmidt decomposition (equation 1.121) to quantify the quality of a partitioning. Following the bootstrap idea, another possibility is to use many overlapping partitionings, but this quickly grows expensive as the system grows larger.
- How should the energy be evaluated? Currently, energy is evaluated democratically — that is, each fragment’s contribution to the energy is given equal weight. This system fails when poorly chosen fragments are mixed in. Ideally, every added fragment should improve the energy because it carries new information about the system.
- Which fragment best describes a given site, atom, or orbital? Bootstrap embedding relies on a choice of a best fragment to match, but this choice is not always obvious in a molecule.
- How should the bath wavefunction be optimized? Multiple bath wavefunction self-consistency criteria have been proposed, and each can give significantly different results [364]. In order to be a general method, DMET needs an unambiguous best choice.

In Chapter 7, we employed semiempirical neglect of diatomic differential overlap (NDDO) methods as force fields for liquid water. Using force matching, we designed a reparameterized NDDO model and found that it qualitatively reproduces the experimental radial distribution function of water, as well as various monomer, dimer, and bulk properties that standard NDDO method do not. Next for this method is application. It could prove useful for simulations that require electronically detailed explicit solvent, including the calculation of redox potentials and simulation of charge transfer and photochemistry. Such a simulation could be performed by using NDDO water as the bath in a simple charge embedding or a more complicated density embedding [20].



# Bibliography

- [1] The nobel prize in physics 2014. [http://www.nobelprize.org/nobel\\_prizes/physics/laureates/2014/press.html](http://www.nobelprize.org/nobel_prizes/physics/laureates/2014/press.html), 2014.
- [2] J. L. F. Abascal and C. Vega. A general purpose model for the condensed phases of water: TIP4P/2005. *J. Chem. Phys.*, 123(23):234505, December 2005.
- [3] M. Abraham, T. Murtola, R. Schulz, J. C. Smith, B. Hess, and E. Lindahl. GROMACS: High performance molecular simulations through multi-level parallelism from laptops to supercomputers. *SoftwareX*, 1-2:19–25, 2015.
- [4] E. Abrahams, P. W. Anderson, D. C. Licciardello, and T. V. Ramakrishnan. Scaling Theory of Localization: Absence of Quantum Diffusion in Two Dimensions. *Phys. Rev. Lett.*, 42(10):673–676, 1979.
- [5] Energy Information Administration. Annual energy outlook. Technical report, US Dept. of Energy, 2014.
- [6] N. A. Afagh and A. K. Yudin. Chemoselectivity and the curious reactivity preferences of functional groups. *Angew. Chem. Int. Ed.*, 49(2):262–310, 2010.
- [7] G. Akemann, J. Baik, and P. Di Francesco, editors. *The Oxford Handbook of Random Matrix Theory*. Oxford University Press, Oxford; New York, 2011.
- [8] G. Allan. A linear prediction of the recursion coefficients. *J. Phys. C: Solid State Phys.*, 17(22):3945–3955, 1984.
- [9] M. P. Allen and D. J. Tidesley. *Computer Simulations of Liquids*. Oxford University Press, 1989.
- [10] P. W. Anderson. Absence of Diffusion in Certain Random Lattices. *Phys. Rev.*, 109(5):1492, 1958.
- [11] P. W. Anderson. Model for the Electronic Structure of Amorphous Semiconductors. *Phys. Rev. Lett.*, 34(15):953–955, 1975.

- [12] P. D. Antoniou and E. Economou. Absence of Anderson's transition in random lattices with off-diagonal disorder. *Phys. Rev. B*, 16(8):3768–3781, 1977.
- [13] E. Apol, R. Apostolov, H. J. C. Berendsen, A. van Buuren, P. Bjelkmar, R. van Drunen, A. Feenstra, S. Fritsch, G. Groenhof, C. Junghans, J. Hub, P. Kasson, C. Kutzner, B. Lambeth, P. Larsson, J. A. Lemkul, E. Marklund, P. Meulenhoff, T. Murtola, S. Pall, S. Pronk, R. Schulz, M. Shirts, A. Sijbers, P. Tieleman, C. Wennberg, M. Wolf, M. Abraham, B. Hess, D. van der Spoel, and E. Lindahl. Gromacs user manual. <ftp://ftp.gromacs.org/pub/manual/manual-5.0.7.pdf>.
- [14] K. Ardani, D. Seif, C. Davidson, J. Morris, S. Truitt, R. Tolbert, and R. Margolis. Preliminary non-hardware ('soft') cost-reduction roadmap for residential and small commercial solar photovoltaics. Technical report, NREL, 2013.
- [15] P. Y. Ayala and G. E. Scuseria. Linear scaling second-order mollerPlesset theory in the atomic orbital basis for large molecular systems. *J. Chem. Phys.*, 110:3660, 1990.
- [16] V. Bach, E. H. Lieb, and J. P. Solovej. Generalized Hartree-Fock theory and the Hubbard model. *J. Stat. Phys.*, 76(1-2):3–89, jul 1994.
- [17] J. Baker. An algorithm for the location of transition states. *J. Comput. Chem.*, 7(4):385–395, August 1986.
- [18] P. Ball. Water - an enduring mystery. *Nature*, 452(March):291–292, 2008.
- [19] E. Barkai, Y. Jung, and R. Silbey. Theory of single-molecule spectroscopy: beyond the ensemble average. *Annu. Rev. Phys. Chem.*, 55:457–507, January 2004.
- [20] T. A. Barnes, J. W. Kaminski, O. Borodin, and T. F. Miller. Ab Initio Characterization of the Electrochemical Stability and Solvation Properties of Condensed-Phase Ethylene Carbonate and Dimethyl Carbonate Mixtures. *J. Phys. Chem. C*, 119(8):3865, 2015.
- [21] R. N. Barnett and U. Landman. Born-Oppenheimer molecular-dynamics simulations of finite systems: structure and dynamics of (H<sub>2</sub>O)<sub>2</sub>. *Phys. Rev. B*, 48(4):2081, 1993.
- [22] R. J. Bartlett. Many-Body Perturbation Theory and Coupled Cluster Theory for Electron Correlation in Molecules. *Annu. Rev. Phys. Chem.*, 32(1):359–401, 1981.
- [23] A. D. Becke. A new mixing of Hartree-Fock and local density-functional theories. *J. Chem. Phys.*, 98(2):1372, 1993.
- [24] C. W. J. Beenakker. Applications of random matrix theory to condensed matter and optical physics. *arXiv:0904.1432*, 2009.

- [25] D. Belitz and T. R. Kirkpatrick. The Anderson-Mott transition. *Rev. Mod. Phys.*, 66(2), 1994.
- [26] F. Benaych-Georges and R. R. Nadakuditi. The eigenvalues and eigenvectors of finite, low rank perturbations of large random matrices. *Adv. Math.*, 227(1):494–521, 2011.
- [27] G. Bergmann. Weak localization in thin films: a time-of-flight experiment with conduction electrons. *Phys. Rep.*, 107(1):1–58, 1984.
- [28] P. Biane. Free probability for probabilists. In *Quantum probability communications*, volume 11, chapter 3, pages 55–71. 1998.
- [29] S. Biermann, A. Poteryaev, A. I. Lichtenstein, and A. Georges. Dynamical singlets and correlation-assisted peierls transition in vo2. *Phys. Rev. Lett.*, 94:026404, 2005.
- [30] K. Binder and A. P. Young. Spin glasses: Experimental facts, theoretical concepts, and open questions. *Rev. Mod. Phys.*, 58(4):801–976, 1986.
- [31] A. R. Bishop and A. Mookerjee. A new approach to the CPA and its generalizations. *J. Phys. C: Solid State Phys.*, 7:2165–2179, 1974.
- [32] J. Blackman, D. Esterling, and N. Berk. Generalized Locator–Coherent-Potential Approach to Binary Alloys. *Phys. Rev. B*, 4(8):2412–2428, October 1971.
- [33] J. M. Blatt. *Theory of Superconductivity*. Academic Press, New York, 1964.
- [34] S. Blinnikov and R. Moessner. Expansions for nearly Gaussian distributions. *Astron. Astrophys. Supp. Ser.*, 130(1):193–205, May 1998.
- [35] E. Bogomolny and O. Giraud. Eigenfunction Entropy and Spectral Compressibility for Critical Random Matrix Ensembles. *Phys. Rev. Lett.*, 106(4):6–9, 2011.
- [36] G. H. Booth and G. K.-L. Chan. Spectral functions of strongly correlated extended systems via an exact quantum embedding. *Phys. Rev. B*, 91(15):155107, April 2015.
- [37] M. Born and R. Oppenheimer. Zur quantentheorie der molekeln. *Ann. Phys.*, 20(84):457–484, 1927.
- [38] J.-P. Bouchaud and A. Georges. Anomalous diffusion in disordered media: Statistical mechanisms, models and physical applications. *Phys. Rep.*, 195(4-5):127–293, November 1990.
- [39] S. Bratož and P. Durand. Transposition of the theories describing superconducting systems to molecular systems. method of biorbitals. *J. Chem. Phys.*, 43:2670, 1965.
- [40] K. Brennan. *The Physics of Semiconductors: with Applications to Optoelectronic Devices*. Cambridge University Press, New York, 1999.

- [41] A. Brezini. Effects of off-diagonal disorder on the density of states. *Phys. Lett. A*, 147(4):179–183, 1990.
- [42] B. R. Brooks, C. L. Brooks, A. D. Mackerell, L. Nilsson, R. J. Petrella, B. Roux, Y. Won, G. Archontis, C. Bartels, S. Boresch, A. Caffisch, L. Caves, Q. Cui, A. R. Dinner, M. Feig, S. Fischer, J. Gao, M. Hodoscek, W. Im, K. Kuczera, T. Lazaridis, J. Ma, V. Ovchinnikov, E. Paci, R. W. Pastor, C. B. Post, J. Z. Pu, M. Schaefer, B. Tidor, R. M. Venable, H. L. Woodcock, X. Wu, W. Yang, D. M. York, and M. Karplus. CHARMM: the biomolecular simulation program. *J. Comput. Chem.*, 30(10):1545–614, July 2009.
- [43] A. D. Buckingham. A Theory of the Dielectric Polarization of Polar Substances. *Proc. R. Soc. A*, 238(1213):235–244, December 1956.
- [44] R. J. Buenker, S. D. Peyerimhoff, and W. Butscher. Applicability of the multi-reference double-excitation ci (mrd-ci) method to the calculation of electronic wavefunctions and comparison with related techniques. *Mol. Phys.*, 35(3):771–791, 1978.
- [45] I. W. Bulik, W. Chen, and G. E. Scuseria. Electron correlation in solids via density embedding theory. *J. Chem. Phys.*, 141(5):054113, 2014.
- [46] I. W. Bulik, G. E. Scuseria, and J. Dukelsky. Density matrix embedding from broken symmetry lattice mean fields. *Phys. Rev. B*, 89:035140, 2014.
- [47] F. A. Carey and R. J. Sundberg. *Advanced Organic Chemistry: Part A: Structure and Mechanisms*. Kluwer Academic, New York; London, 2002.
- [48] I. S. Carrico. Chemoselective modification of proteins: hitting the target. *Chem. Soc. Rev.*, 37:1423–1431, 2008.
- [49] A. H. Castro Neto, F. Guinea, and N. M. R. Peres. Edge and surface states in the quantum Hall effect in graphene. *Phys. Rev. B*, 73(20):1–8, 2006.
- [50] A. H. Castro Neto, N. M. R. Peres, K. S. Novoselov, and A. K. Geim. The electronic properties of graphene. *Rev. Mod. Phys.*, 81(1):109–162, 2009.
- [51] R. Catterall and N. F. Mott. Metal-ammonia solutions. *Adv. Phys.*, 18(76):665–680, 1969.
- [52] G. K.-L. Chan and M. Head-Gordon. Highly correlated calculations with a polynomial cost algorithm: A study of the density matrix renormalization group. *J. Chem. Phys.*, 116(11):4462, 2002.
- [53] J. Chen and A. Edelman. Partial freeness of random matrices. *arXiv:1204.2257*.

- [54] J. Chen, E. Hontz, J. Moix, M. Welborn, T. Van Voorhis, A. Suárez, R. Movassagh, and A. Edelman. Error Analysis of Free Probability Approximations to the Density of States of Disordered Systems. *Phys. Rev. Lett.*, 109(3):036403, 2012.
- [55] J. Chen and T. J. Martinez. *Advances in the Theory of Atomic and Molecular Systems*, volume 19 of *Progress in Theoretical Chemistry and Physics*. Springer Netherlands, Dordrecht, 2009.
- [56] M. S. Chen and M. C. White. A predictably selective aliphatic c-h oxidation reaction for complex molecule synthesis. *Science*, 318(5851):783–787, 2007.
- [57] D. M. Chipman. Reaction field treatment of charge penetration. *J. Chem. Phys.*, 112:5588, 2000.
- [58] T. Clark, J. Chandrasekhar, G. W. Spitznagel, and P. V. R. Schleyer. Efficient diffuse function-augmented basis sets for anion calculations. III. The 3-21+G basis set for first-row elements, Li-F. *J. Comput. Chem.*, 4(3):294–301, 1983.
- [59] A. J. Cohen, P. Mori-Sánchez, and W. Yang. Insights into current limitations of density functional theory. *Science*, 321:792, 2008.
- [60] A. J. Coleman. Structure of Fermion Density Matrices. II. Antisymmetrized Geminal Powers. *J. Math. Phys.*, 6(9):1425, 1965.
- [61] A. J. Coleman. The AGP model for fermion systems. *Int. J. Quantum Chem.*, 63(1):23–30, 1997.
- [62] A. J. Coleman and V. I. Yukalov. *Reduced Density Matrices: Coulson’s Challenge*. Springer, 2000.
- [63] B. Collins and P. Śniady. Integration with Respect to the Haar Measure on Unitary, Orthogonal and Symplectic Group. *Commun. Math. Phys.*, 264(3):773–795, March 2006.
- [64] K. D. Collins. Ion hydration: Implications for cellular function, polyelectrolytes, and protein crystallization. *Biophys. Chem.*, 119(3):271–281, February 2006.
- [65] Board on Energy Committee on Assessment of Solid State Lighting, Environmental Systems, Division on Engineering, and Physical Sciences. Assessment of advanced solid state lighting. Technical report, National Research Council, 2013.
- [66] P. Cortona. Self-consistently determined properties of solids without band-structure calculations. *Phys. Rev. B*, 44(16):8454–8458, October 1991.

- [67] M. Cossi, N. Rega, G. Scalmani, and V. Barone. Energies, structures, and electronic properties of molecules in solution with the C-PCM solvation model. *J. Comput. Chem.*, 24(6):669–81, 2003.
- [68] C. J. Cramer and D. G. Truhlar. PM3-SM3: A general parameterization for including aqueous solvation effects in the PM3 molecular orbital model. *J. Comput. Chem.*, 13(9):1089–1097, November 1992.
- [69] H. Cramér. *Random variables and probability distributions*. Cambridge Tracts in Mathematics and Mathematical Physics. Cambridge, Cambridge, UK, 3 edition, 1970.
- [70] J. C. Cressoni and M. L. Lyra. The nature of electronic states in a disordered chain with long-ranged hopping amplitudes. *Physica A*, 256(1-2):18–29, 1998.
- [71] L. A. Curtiss, D. J. Frurip, and M. Blander. Studies of molecular association in H<sub>2</sub>O and D<sub>2</sub>O vapors by measurement of thermal conductivity. *J. Chem. Phys.*, 71(6):2703, 1979.
- [72] P. Dai, C. Zhang, and B. L. Pentelute. personal communication, 2015.
- [73] H. T. Dang, X. Ai, A. J. Millis, and C. A. Marianetti. Density functional plus dynamical mean-field theory of the metal-insulator transition in early transition-metal oxides. *Phys. Rev. B*, 90:125114, 2014.
- [74] P. de Brito, E. Rodrigues, and H. Nazareno. Appearance of carrier propagations in the one-dimensional Anderson model with long-range hopping. *Phys. Rev. B*, 69(21):214204, 2004.
- [75] F. de Moura, A. Malyshev, M. Lyra, V. Malyshev, and F. Domínguez-Adame. Localization properties of a one-dimensional tight-binding model with nonrandom long-range intersite interactions. *Phys. Rev. B*, 71(17):174203, 2005.
- [76] P. G. Debenedetti and F. H. Stillinger. Supercooled liquids and the glass transition. *Nature*, 410(6825):259–67, 2001.
- [77] M. J. S. Dewar and W. Thiel. A semiempirical model for the two-center repulsion integrals in the NDDO approximation. *Theor. Chim. Acta*, 46(2):89–104, 1977.
- [78] M. J. S. Dewar, E. G. Zoebisch, Eamonn F. Healy, and J. J. P. Stewart. Development and use of quantum mechanical molecular models. 76. AM1: a new general purpose quantum mechanical molecular model. *J. Am. Chem. Soc.*, 107(13):3902–3909, June 1985.
- [79] P. Diaconis. What is a Random Matrix? *Not. Amer. Math. Soc.*, 52(11):1348–9, April 2005.
- [80] S. Difley, L.-P. Wang, S. Yeganeh, S. R. Yost, and T. Van Voorhis. Electronic Properties of Disordered Organic Semiconductors via QM/MM Simulations. *Acc. Chem. Res.*, 43(7):995–1004, 2010.

- [81] P. A. M. Dirac. A new notation for quantum mechanics. *Math. Proc. Cambridge Philos. Soc.*, 35(03):416, 1939.
- [82] G. Dolan and D. Osheroff. Nonmetallic Conduction in Thin Metal Films at Low Temperatures. *Phys. Rev. Lett.*, 43(10):721–724, 1979.
- [83] D. A. Drabold. Anderson transition and thermal effects on electron states in amorphous silicon. *J. Non-Cryst. Solids*, 269:211–217, 2000.
- [84] Y. Duan, C. Wu, S. Chowdhury, M. C. Lee, G. Xiong, W. Zhang, R. Yang, P. Cieplak, R. Luo, T. Lee, J. Caldwell, J. Wang, and P. Kollman. A point-charge force field for molecular mechanics simulations of proteins based on condensed-phase quantum mechanical calculations. *J. Comput. Chem.*, 24(16):1999–2012, December 2003.
- [85] J. S. Dugdale. *The Electrical Properties of Disordered Metals*. Cambridge Solid State Science Series. Cambridge, Cambridge, UK, 2005.
- [86] T. H. Dunning. Gaussian basis sets for use in correlated molecular calculations. I. The atoms boron through neon and hydrogen. *J. Chem. Phys.*, 90(2):1007, 1989.
- [87] T. R. Dyke, K. M. Mack, and J. S. Muentzer. The structure of water dimer from molecular beam electric resonance spectroscopy. *J. Chem. Phys.*, 66(2):498, 1977.
- [88] J. Dyre and T. Schröder. Universality of ac conduction in disordered solids. *Rev. Mod. Phys.*, 72(3):873–892, July 2000.
- [89] A. Edelman and N. R. Rao. Random matrix theory. *Acta Numerica*, 14:233–297, 2005.
- [90] P. Elliott, K. Burke, M. H. Cohen, and A. Wasserman. Partition density-functional theory. *Phys. Rev. A*, 82(2):1–4, 2010.
- [91] R. Elliott, J. Krumhansl, and P. Leath. The theory and properties of randomly disordered crystals and related physical systems. *Rev. Mod. Phys.*, 46(3):465–543, 1974.
- [92] F. Ercolessi and J. B. Adams. Interatomic Potentials from First-Principles Calculations: The Force-Matching Method. *Europhys. Lett.*, 26(8):583–588, June 1994.
- [93] F. H. L. Essler, H. Frahm, and V. E. Korepin. The one-dimensional Hubbard model. 2003.
- [94] D. M. Esterling. Simplified derivation of the matrix coherent-potential approximation for off-diagonal random alloys. *Phys. Rev. B*, 12(4):6–9, 1975.
- [95] F. Evers and A. Mirlin. Anderson transitions. *Rev. Mod. Phys.*, 80(4):1355–1417, October 2008.

- [96] D. G. Fedorov and K. Kitaura. The importance of three-body terms in the fragment molecular orbital method. *J. Chem. Phys.*, 120(15):6832–6840, 2004.
- [97] D. G. Fedorov and K. Kitaura. Extending the power of quantum chemistry to large systems with the fragment molecular orbital method. *J. Phys. Chem. A*, 111(30):6904–6914, 2007.
- [98] W. Feller. *An Introduction to Probability Theory and Its Applications, Vol. 2*. John Wiley, New York, 2nd edition, 1971.
- [99] D. P. Ferncindez, Y. Mulev, A. R. H. Goodwine, and J. M. H. L. Sengers. A Database for the Static Dielectric Constant of Water and Steam. *J. Phys. Chem. Ref. Data*, 24:33, 1995.
- [100] H. Fidder, J. Knoester, and D. A. Wiersma. Optical properties of disordered molecular aggregates: A numerical study. *J. Chem. Phys.*, 95(11):7880, 1991.
- [101] P. J. Ford. Spin glasses. *Contemp. Phys.*, 23(2):141–168, 1982.
- [102] S. R. Forest. The path to ubiquitous and low-cost organic electronic appliances on plastic. *Nature*, 428:911–918, 2004.
- [103] J. M. Fox, K. Kang, W. Sherman, A. Heroux, G. M. Sastry, M. Baghbanzadeh, M. R. Lockett, and G. M. Whitesides. Interactions between Hofmeister Anions and the Binding Pocket of a Protein. *J. Am. Chem. Soc.*, 137(11):3859–3866, March 2015.
- [104] D. Frenkel and B. Smit. *Understanding Molecular Simulation*. Academic Press, San Diego, 2002.
- [105] Z. C. Gao, Q. L. Hu, and Y. S. Chen. A convenient implementation of the overlap between arbitrary Hartree-Fock-Bogoliubov vacua for projection. *Phys. Lett. B*, 732:360–363, 2014.
- [106] A. Georges, G. Kotliar, W. Krauth, and M. J. Rozenberg. Dynamical mean-field theory of strongly correlated fermion systems and the limit of infinite dimensions. *Rev. Mod. Phys.*, 68:13, 1996.
- [107] A. Georges and W. Krauth. Numerical solution of the  $d = \infty$  hubbard model: Evidence for a moot transition. *Phys. Rev. Lett.*, 69:1240, 1992.
- [108] D. Gfeller, O. Michielin, and V. Zoete. Swisssidechain: a molecular and structural database of non-natural sidechains. *Nucleic Acids Res.*, 41(D1):D327–D332, 2013.
- [109] P. M. W. Gill, B. G. Johnson, and J. A. Pople. A standard grid for density functional calculations. *Chem. Phys. Lett.*, 209(5):506–512, July 1993.
- [110] S. Goedecker. Linear scaling electronic structure methods. *Rev. Mod. Phys.*, 71(4):1085–1123, 1999.

- [111] H. Goldstein, C. P. Poole Jr., and J. L. Safko. *Classical Mechanics*. Addison-Wesley, 2001.
- [112] G. H. Golub and C. F. van Loan. *Matrix Computations*. Johns Hopkins, Baltimore, MD, 3 edition, 1996.
- [113] A. Gonzalez-Lafont, T. N. Truong, and D. G. Truhlar. Direct dynamics calculations with NDDO (neglect of diatomic differential overlap) molecular orbital theory with specific reaction parameters. *J. Phys. Chem.*, 95(12):4618–4627, June 1991.
- [114] J. D. Goodpaster, T. A. Barnes, F. R. Manby, and T. F. Miller. Accurate and systematically improvable density functional theory embedding for correlated wavefunctions. *J. Chem. Phys.*, 140(18), 2014.
- [115] N. Govind, Y. A. Wang, and E. A. Carter. Electronic-structure calculations by first-principles density-based embedding of explicitly correlated systems. *J. Chem. Phys.*, 110(16):7677, 1999.
- [116] M. Gratzel. Photochemical cells. *Nature*, 414:338–334, 2001.
- [117] M. Gratzel. Photovoltaic and photoelectrochemical conversion of solar energy. *Philos. Trans. A Math. Phys. Eng. Sci.*, 365:993–1005, 2007.
- [118] D. J. Griffiths. *Introduction to Quantum Mechanics*. Prentice Hall, 1995.
- [119] S. Grimme, J. Antony, S. Ehrlich, and H. Krieg. A consistent and accurate ab initio parametrization of density functional dispersion correction (DFT-D) for the 94 elements H-Pu. *J. Chem. Phys.*, 132(15):154104, April 2010.
- [120] D. Grob, editor. *The Glass Transition and the Nature of the Glassy State*. New York Academy of Sciences, New York, 1976.
- [121] B. Guillot. A reappraisal of what we have learnt during three decades of computer simulations on water. *J. Mol. Liq.*, 101(1-3):219–260, November 2002.
- [122] L. Guttman. Order-Disorder Phenomena in Metals. *Solid State Phys.*, 3:145–223, 1956.
- [123] C. P. R. Hackenberger and D. Schwarzer. Chemoselective ligation and modification strategies for peptides and proteins. *Angew. Chem. Int. Ed.*, 47(52):10030–10074, 2008.
- [124] P. Hall. *The bootstrap and Edgeworth expansion*. Springer Series in Statistics. Springer-Verlag, New York, 1992.
- [125] B. Halperin. Green’s Functions for a Particle in a One-Dimensional Random Potential. *Phys. Rev.*, 139(1A):A104–A117, 1965.

- [126] N. Hamada, S.-I. Sawada, and A. Oshiyama. New one-dimensional conductors: Graphitic microtubules. *Phys. Rev. Lett.*, 68(10):1579–1581, 1992.
- [127] B. Hammer and J. K. Norskov. Theoretical Surface Science and Catalysis - Calculations and Concepts. *Adv. Catal.*, 45:71, 2000.
- [128] L. P. Hammett. Linear free energy relationships in rate and equilibrium phenomena. *J. Chem. Soc. Faraday Trans.*, 34:156–165, 1938.
- [129] J. R. Hammond, N. Govind, K. Kowalski, J. Autschbach, and S. S. Xantheas. Accurate dipole polarizabilities for water clusters  $n=2-12$  at the coupled-cluster level of theory and benchmarking of various density functionals. *J. Chem. Phys.*, 131(21):214103, December 2009.
- [130] C. Hampel and H.-J. Werner. Local treatment of electron correlation in coupled cluster theory. *J. Chem. Phys.*, 104:6286, 1996.
- [131] P. C. Hariharan and J. A. Pople. The influence of polarization functions on molecular orbital hydrogenation energies. *Theor. Chim. Acta*, 28(3):213–222, 1973.
- [132] D. R. Hartree. The Wave Mechanics of an Atom with a non-Coulomb Central Field. Part III. Term Values and Intensities in Series in Optical Spectra. *Math. Proc. Cambridge Philos. Soc.*, 24(03):426, 1928.
- [133] S. Havlin and D. Ben-Avraham. Diffusion in disordered media. *Adv. Phys.*, 51(1):187–292, 2002.
- [134] R. Haydock. The Recursive Solution of the Schrodinger Equation. *Solid State Phys.*, 35:215–294, 1980.
- [135] R. Haydock, V. Heine, and M. J. Kelly. Electronic structure based on the local atomic environment for tight-binding bands. *J. Phys. C: Solid State Phys.*, 5(20):2845–2858, 1972.
- [136] R. Haydock, V. Heine, and M. J. Kelly. Electronic structure based on the local atomic environment for tight-binding bands. II. *J. Phys. C: Solid State Phys.*, 8(16):2591–2605, 1975.
- [137] P. Henrici. *Applied and Computational Complex Analysis, vol. 3*. John Wiley & Sons, 1986.
- [138] A. Hernando. Magnetic properties and spin disorder in nanocrystalline materials. *J. Phys.: Condens. Matter*, 11(48):9455–9482, December 1999.
- [139] B. Hess, C. Kutzner, D. van der Spoel, and E. Lindahl. GROMACS 4: Algorithms for Highly Efficient, Load-Balanced, and Scalable Molecular Simulation. *J. Chem. Theory Comput.*, 4(3):435–447, March 2008.

- [140] S. Hirata. *Phys. Chem. Chem. Phys.*, 11:8397, 2009.
- [141] J. Hobson and W. Nierenberg. The Statistics of a Two-Dimensional, Hexagonal Net. *Phys. Rev.*, 89(3):662–662, 1953.
- [142] P. Hobza, M. Kabelac, J. Sponer, P. Mejzlik, and J. Vondrasek. Performance of empirical potentials (AMBER, CFF95, CVFF, CHARMM, OPLS, POLTEV), semiempirical quantum chemical methods (AM1, MNDO/M, PM3), and ab initio Hartree-Fock method for interaction of DNA bases: Comparison with nonempirical beyond Hartree-Fock results. *J. Comput. Chem.*, 18(9):1136–1150, 1997.
- [143] P. Hohenberg and W. Kohn. Inhomogeneous Electron Gas. *Phys. Rev.*, 136(3B):B864–B871, nov 1964.
- [144] M. Holz, S. R. Heil, and A. Sacco. Temperature-dependent self-diffusion coefficients of water and six selected molecular liquids for calibration in accurate  $^1\text{H}$  NMR PFG measurements. *Phys. Chem. Chem. Phys.*, 2(20):4740–4742, 2000.
- [145] W. Hoover. Canonical dynamics: Equilibrium phase-space distributions. *Phys. Rev. A*, 31(3):1695–1697, March 1985.
- [146] R. A. Horn and C. R. Johnson. *Matrix Analysis*. Cambridge, UK, 1990.
- [147] R. P. Hosteny, T. H. Dunning, R. R. Gilman, A. Pipano, and I. Shavitt. Abinitio study of the  $\pi$ -electron states of trans-butadiene. *J. of Chem. Phys.*, 62(12), 1975.
- [148] W. Hu, J. Dow, and C. Myles. Effects of diagonal and off-diagonal disorder on the Anderson-model densities of states in two and three dimensions. *Phys. Rev. B*, 30(4):1720–1723, 1984.
- [149] J. Hubbard. Electron Correlations in Narrow Energy Bands. *Proc. R. Soc. A Math. Phys. Eng. Sci.*, 276(1365):238–257, 1963.
- [150] W. J. Hunt, P. J. Hay, and W. A. Goddard III. Self-consistent procedures for generalized valence bond wavefunctions. applications h3, bh, h2o, c2h6, and o2. *J. Chem. Phys.*, 57:738, 1972.
- [151] A. C. Hurley, J. Lennard-Jones, and J. A. Pople. The molecular orbital theory of chemical valency. xvi. a theory of paired-electrons in polyatomic molecules. *Proc. R. Soc. A*, 220:446, 1953.
- [152] E. A. Hylleraas. *Z. Physik*, 54:347, 1929.
- [153] S. Izvekov, M. Parrinello, C. J. Burnham, and G. A. Voth. Effective force fields for condensed phase systems from ab initio molecular dynamics simulation: a new method for force-matching. *J. Chem. Phys.*, 120(23):10896–913, June 2004.

- [154] C. R. Jacob and L. Visscher. A subsystem density-functional theory approach for the quantum chemical treatment of proteins. *J. Chem. Phys.*, 128(15):155102, 2008.
- [155] D. Jacob, K. Haule, and G. Kotliar. Dynamical mean-field theory for molecular electronics: Electronic structure and transport properties. *Phys. Rev. B*, 82:195115, 2010.
- [156] D. Janzing. *Compendium of Quantum Physics*, chapter Entropy of Entanglement, pages 205–209. Springer Berlin Heidelberg, Berlin, Heidelberg, 2009.
- [157] G. Jeffrey. *An Introduction to Hydrogen Bonding*. Oxford University Press, New York, 1997.
- [158] C. A. Jimenez, T. M. Henderson, T. Tsuchimochi, and G. E. Scuseria. Projected Hartree-Fock Theory. (16), 2012.
- [159] W. L. Jorgensen, D. S. Maxwell, and J. Tirado-Rives. Development and Testing of the OPLS All-Atom Force Field on Conformational Energetics and Properties of Organic Liquids. *J. Am. Chem. Soc.*, 7863(15):11225–11236, 1996.
- [160] W. L. Jorgensen and J. Tirado-Rives. Potential energy functions for atomic-level simulations of water and organic and biomolecular systems. *Proc. Natl. Acad. Sci. U. S. A.*, 102(19):6665–70, 2005.
- [161] K. Jug and D. N. Nanda. SINDO1 II. Application to ground states of molecules containing carbon, nitrogen and oxygen atoms. *Theor. Chim. Acta*, 57(2):107–130, 1980.
- [162] K. Jug and D. N. Nanda. SINDO1 III. Application to ground states of molecules containing fluorine, boron, beryllium and lithium atoms. *Theor. Chim. Acta*, 57(2):131–144, 1980.
- [163] M. W. Jurema, K. N. Kirschner, and G. C. Shields. Modeling of magic water clusters (H<sub>2</sub>O)<sub>20</sub> and (H<sub>2</sub>O)<sub>21</sub>H<sup>+</sup> with the PM3 quantum-mechanical method. *J. Comput. Chem.*, 14(11):1326–1332, November 1993.
- [164] B. Kaduk. *Constrained Density Functional Theory - Configuration Interaction*. PhD thesis, 2012.
- [165] B. Kaduk, T. Kowalczyk, and T. Van Voorhis. Constrained density functional theory. *Chem. Rev.*, 112:321–370, 2012.
- [166] J. Kalinowski. Excimers and exciplexes in organic electroluminescence. *Mat. Sci.-Poland*, 27:735–756, 2009.
- [167] G. A. Kaminski, R. A. Friesner, J. Tirado-Rives, and W. L. Jorgensen. Evaluation and Reparameterization of the OPLS-AA Force Field for Proteins via Comparison with Accurate Quantum Chemical Calculations on Peptides. *J. Phys. Chem. B*, 105:6474–6487, 2001.

- [168] H. Kataura, Y. Endo, Y. Achiba, K. Kikuchi, T. Hanyu, and S. Yamaguchi. Dielectric constants of C60 and C70 thin films. *J. Phys. Chem. Solids*, 58(11):1913–1917, 1997.
- [169] R. Z. Khaliullin, M. Head-Gordon, and A. T. Bell. An efficient self-consistent field method for large systems of weakly interacting components. *J. Chem. Phys.*, 124(20):204105, May 2006.
- [170] J. Y. Kim, K. Lee, N. E. Coates, D. Moses, T.-Q. Nguyen, M. Dante, and A. J. Heeger. Efficient tandem polymer solar cells fabricated by all-solution processing. *Science*, 317:222–225, 2007.
- [171] K. Kitaura, E. Ikeo, T. Asada, T. Nakano, and M. Uebayasi. Fragment molecular orbital method: an approximate computational method for large molecules. *Chem. Phys. Lett.*, 313(3-4):701–706, 1999.
- [172] C. Kittel. *Introduction to Solid State Physics*. Wiley, Hoboken, NJ, 8th edition, 2005.
- [173] R. Klesse and M. Metzler. Spectral Compressibility at the Metal-Insulator Transition of the Quantum Hall Effect. *Phys. Rev. Lett.*, 79(4):721–724, 1997.
- [174] I. Klich. Lower entropy bounds and particle number fluctuations in a Fermi sea. *J. Phys. A. Math. Gen.*, 39(4):L85–L91, January 2006.
- [175] G. Knizia and G. K.-L. Chan. Density Matrix Embedding: A Simple Alternative to Dynamical Mean-Field Theory. *Phys. Rev. Lett.*, 109(18):186404, 2012.
- [176] G. Knizia and G. K.-L. Chan. Density Matrix Embedding: A Strong-Coupling Quantum Embedding Theory. *J. Chem. Theory Comput.*, 9(3):1428–1432, 2013.
- [177] A. Knutson and T. Tao. Honeycombs and Sums of Hermitian Matrices. *Notices Amer. Math. Soc.*, 48(2):175–186, 2001.
- [178] K. Koepernik, B. Velický, R. Hayn, and H. Eschrig. Analytic properties and accuracy of the generalized Blackman-Esterling-Berk coherent-potential approximation. *Phys. Rev. B*, 58(11):6944–6962, 1998.
- [179] W. Kohn and L. J. Sham. Self-Consistent Equations Including Exchange and Correlation Effects. *Phys. Rev.*, 140(4A):A1133–A1138, nov 1965.
- [180] M. Kolár, K. Berka, P. Jurecka, and P. Hobza. On the reliability of the AMBER force field and its empirical dispersion contribution for the description of noncovalent complexes. *Chemphyschem*, 11(11):2399–408, August 2010.
- [181] P. A. Kollman and L. C. Allen. Hydrogen bonded dimers and polymers involving hydrogen fluoride, water, and ammonia. *J. Am. Chem. Soc.*, 92(4):753–759, February 1970.

- [182] M. Korth. Third-Generation Hydrogen-Bonding Corrections for Semiempirical QM Methods and Force Fields. *J. Chem. Theory Comput.*, 6(12):3808–3816, December 2010.
- [183] T. Kowalczyk, L.-P. Wang, and T. Van Voorhis. Simulation of solution phase electron transfer in a compact donor-acceptor dyad. *J. Phys. Chem. B*, 115(42):12135–12144, 2011. PMID: 21961889.
- [184] C. Kraus. Solutions of metals in non-metallic solvents; I. General properties of solutions of metals in liquid ammonia. *J. Am. Chem. Soc.*, 29(11):1557–1571, 1907.
- [185] R. Krishnan, J. S. Binkley, R. Seeger, and J. A. Pople. Self-consistent molecular orbital methods. XX. A basis set for correlated wave functions. *J. Chem. Phys.*, 72:650, 1980.
- [186] E. R. Kuechler and D. M. York. Quantum mechanical study of solvent effects in a prototype SN2 reaction in solution: Cl- attack on CH3Cl. *J. Chem. Phys.*, 140(5):054109, March 2014.
- [187] W. Kutzelnigg. Direct Determination of Natural Orbitals and Natural Expansion Coefficients of Many-Electron Wavefunctions. I. Natural Orbitals in the Geminal Product Approximation. *J. Chem. Phys.*, 40(12):3640, 1964.
- [188] W. Kutzelnigg. On the validity of the electron pair approximation for the beryllium ground state. *Theor. Chim. Acta.*, 3:241, 1965.
- [189] K. Laasonen, M. Sprik, M. Parrinello, and R. Car. "Ab initio" liquid water. *J. Chem. Phys.*, 99(11):9080, 1993.
- [190] G. Lamoureux, A. D. MacKerell, and B. Roux. A simple polarizable model of water based on classical Drude oscillators. *J. Chem. Phys.*, 119(10):5185, 2003.
- [191] V. I. Lebedev. No Title. *Sib. Mat. Zh.*, 18:132, 1977.
- [192] H.-S. Lee and M. E. Tuckerman. Dynamical properties of liquid water from ab initio molecular dynamics performed in the complete basis set limit. *J. Chem. Phys.*, 126(16):164501, April 2007.
- [193] R. Lee. The outlook for population growth. *Science*, 333:569–573, 2011.
- [194] C. A. Lewis and S. J. Miller. Site-selective derivatization and remodeling of erythromycin a by using simple peptide-based chiral catalysts. *Angew. Chem. Int. Ed.*, 45(34):5616–5619, 2006.
- [195] D. R. Lide. *CRC Handbook of Chemistry and Physics*. CRC Press, 93 edition, 2012.
- [196] E. H. Lieb and F. Y. Wu. The one-dimensional Hubbard model: a reminiscence. *Phys. A Stat. Mech. its Appl.*, 321:1–27, 2003.

- [197] N. Lin, C. A. Marianetti, A. J. Millis, and D. R. Reichman. Dynamical mean-field theory for quantum chemistry. *Phys. Rev. Lett.*, 106:096402, 2011.
- [198] P. Lloyd. Exactly solvable model of electronic states in a three-dimensional disordered Hamiltonian: non-existence of localized states. *J. Phys. C: Solid State Phys.*, 2(10):1717–1725, 1969.
- [199] P.-O. Löwdin. On the Non-Orthogonality Problem Connected with the Use of Atomic Wave Functions in the Theory of Molecules and Crystals. *J. Chem. Phys.*, 18(3):365–375, 1950.
- [200] P.-O. Löwdin. Quantum Theory of Many-Particle Systems. I. Physical Interpretations by Means of Density Matrices, Natural Spin-Orbitals, and Convergence Problems in the Method of Configurational Interaction. *Phys. Rev.*, 97(6):1474–1489, 1955.
- [201] P.-O. Löwdin. Quantum theory of many-particle systems. ii. study of the ordinary hartree-fock approximation. *Phys. Rev.*, 97, 1955.
- [202] M. W. Mahoney and W. L. Jorgensen. A five-site model for liquid water and the reproduction of the density anomaly by rigid, nonpolarizable potential functions. *J. Chem. Phys.*, 112(20):8910, 2000.
- [203] T. Maier, M. Jarrell, T. Pruschke, and M. H. Hettler. Quantum cluster theories. *Rev. Mod. Phys.*, 77:1027, 2005.
- [204] A. Malyshev, V. Malyshev, and F. Domínguez-Adame. Monitoring the localization-delocalization transition within a one-dimensional model with nonrandom long-range interaction. *Phys. Rev. B*, 70(17):172202, 2004.
- [205] R. A. Marcus. On the Theory of Oxidation-Reduction Reactions Involving Electron Transfer. I. *J. Chem. Phys.*, 24(5):966, 1956.
- [206] C. A. Marianetti, K. Haule, G. Kotliar, and M. J. Fluss. Electronic coherence in  $\delta$ -pu: A dynamical mean-field theory study. *Phys. Rev. Lett.*, 101:056403, 2008.
- [207] A. Marion, G. Monard, M. F. Ruiz-López, and F. Ingrosso. Water interactions with hydrophobic groups: assessment and recalibration of semiempirical molecular orbital methods. *J. Chem. Phys.*, 141(3):034106, July 2014.
- [208] G. Markopoulos and T. Swager. personal communication, 2015.
- [209] S. Matsuishi, Y. Toda, M. Miyakawa, K. Hayashi, T. Kamiya, M. Hirano, I. Tanaka, and H. Hosono. High-density electron anions in a nanoporous single crystal:  $[\text{Ca}_{24}\text{Al}_{28}\text{O}_{64}]_{4+}(4e^-)$ . *Science*, 301(5633):626–9, 2003.

- [210] M. G. Mavros, D. A. Micha, and D. S. Kilin. Optical Properties of Doped Silicon Quantum Dots with Crystalline and Amorphous Structures. *J. Phys. Chem. C*, 115(40):19529–19537, 2011.
- [211] D. A. Mazziotti. Geminal functional theory: A synthesis of density and density matrix methods. *J. Chem. Phys.*, 112(23):10125, 2000.
- [212] D. P. McMahon, D. L. Cheung, L. Goris, J. Dacuna, A. Salleo, and A. Troisi. Relation between Microstructure and Charge Transport in Polymers of Different Regioregularity. *J. Phys. Chem. C*, 115(39), 2011.
- [213] D. P. McMahon, D. L. Cheung, and A. Troisi. Why Holes and Electrons Separate So Well in Polymer/Fullerene Photovoltaic Cells. *J. Phys. Chem. Lett.*, 2(21):2737–2741, 2011.
- [214] D. A. McQuarrie. *Statistical Mechanics*. University Science Books, 2000.
- [215] M. L. Mehta. *Random matrices*. Pure and Applied Mathematics. Elsevier/Academic Press, Amsterdam ; San Diego, CA, 3rd edition, 2004.
- [216] M. Mestechkin, G. Whyman, and G. Klimko. Molecular viewpoint on high-temperature superconductivity importance of orbital degeneracy. *Mol. Phys.*, 82(6):1079–1098, 1994.
- [217] W. Metzner and D. Vollhardt. Correlated lattice fermions in  $d = \infty$  dimensions. *Phys. Rev. Lett.*, 62:324, 1989.
- [218] T. Mizusaki and M. Oi. A new formulation to calculate general HFB matrix elements through the Pfaffian. *Phys. Lett. B*, 715(1-3):219–224, 2012.
- [219] S.-K. Mo, J. D. Denlinger, H.-D. Kim, J.-H. Park, J. W. Allen, A. Sekiyama, A. Yamasaki, K. Kadono, S. Suga, Y. Saitoh, T. Muro, P. Metcalf, G. Keller, K. Held, V. Eyert, V. I. Anisimov, and D. Vollhardt. Prominent quasiparticle peak in the photoemission spectrum of the metallic phase of  $v_2o_3$ . *Phys. Rev. Lett.*, 90:186403, 2003.
- [220] J. E. Moore. The birth of topological insulators. *Nature*, 464(7286):194–8, 2010.
- [221] N. F. Mott and H. Jones. *The Theory of the Properties of Metals and Alloys*. Dover Publications, New York, 1958.
- [222] R. Movassagh and A. Edelman. Isotropic Entanglement. December.
- [223] R. Movassagh and A. Edelman. Density of States of Quantum Spin Systems from Isotropic Entanglement. *Phys. Rev. Lett.*, 107(9):097205, August 2011.

- [224] W. F. Murphy. The Rayleigh depolarization ratio and rotational Raman spectrum of water vapor and the polarizability components for the water molecule. *J. Chem. Phys.*, 67(12):5877, 1977.
- [225] E. D. Murray, K. Lee, and D. C. Langreth. Investigation of Exchange Energy Density Functional Accuracy for Interacting Molecules. *J. Chem. Theory Comput.*, 5(10):2754–2762, October 2009.
- [226] R. R. Nadakuditi. *Applied Stochastic Eigen-Analysis*. PhD thesis, 2007.
- [227] K.-i. Nakamura. Two-Body Correlation of Interacting Fermions. *Prog. Theor. Phys.*, 21(5):713–726, 1959.
- [228] D. N. Nanda and K. Jug. SINDO1. A semiempirical SCF MO method for molecular binding energy and geometry I. Approximations and parametrization. *Theor. Chim. Acta*, 57(2):95–106, 1980.
- [229] P. Neu and R. Speicher. Spectra of Hamiltonians with generalized single-site dynamical disorder. *Z. Phys. B*, 95(1):101–111, 1994.
- [230] P. Neu and R. Speicher. Random matrix theory for CPA: generalization of Wegner’s n-orbital model. *J. Phys. A*, 79:L79–L83, 1995.
- [231] P. Neu and R. Speicher. Rigorous mean-field model for coherent-potential approximation: Anderson model with free random variables. *J. Stat. Phys.*, 80(5-6):1279–1308, September 1995.
- [232] J. Neugebauer. Chromophore-specific theoretical spectroscopy: From subsystem density functional theory to mode-specific vibrational spectroscopy. *Phys. Rep.*, 489(1-3):1–87, 2010.
- [233] M. Neumann and O. Steinhauser. On the calculation of the frequency-dependent dielectric constant in computer simulations. *Chem. Phys. Lett.*, 102(6):508–513, December 1983.
- [234] A. Nica and R. Speicher. *Lectures on the combinatorics of free probability*. Cambridge University Press, Cambridge, 2006.
- [235] A. Nica and R. Speicher. *Lectures on the Combinatorics of Free Probability*. London Math. Soc. Lecture Note Ser. London, 2006.
- [236] V. A. Nicely and J. F. Harrison. Geminal product wavefunctions: A general formalism. *J. Chem. Phys.*, 54:4364, 1971.
- [237] J. Nocedal and S. J. Wright. *Numerical Optimization*. Springer, New York, 2 edition, 2006.

- [238] S. Nose. A unified formulation of the constant temperature molecular dynamics methods. *J. Chem. Phys.*, 81(1):511, 1984.
- [239] NREL. Best Research-Cell Efficiencies. [http://www.nrel.gov/ncpv/images/efficiency\\_chart.jpg](http://www.nrel.gov/ncpv/images/efficiency_chart.jpg). Accessed: 2016-04-06.
- [240] J. O. Oelerich, D. Huemmer, and S. D. Baranovskii. How to Find Out the Density of States in Disordered Organic Semiconductors. *Phys. Rev. Lett.*, 108(22):226403, 2012.
- [241] M. Oi and T. Mizusaki. New Pfaffian formulae for an overlap of multiple quasiparticle states. *EPJ Web Conf.*, 66:02075, mar 2014.
- [242] S. Olver. Computing the hilbert transform and its inverse. *Math. Comp.*, 80(275):1745–1767, 2011.
- [243] S. Olver and R. R. Nadakuditi. Numerical computation of convolutions in free probability theory. *arXiv*.
- [244] N. Onishi and S. Yoshida. Generator coordinate method applied to nuclei in the transition region. *Nucl. Phys.*, 80(2):367–376, 1966.
- [245] A. Ossipov, I. Rushkin, and E. Cuevas. Level-number variance and spectral compressibility in a critical two-dimensional random-matrix model. *Phys. Rev. E*, 85(2):021127, February 2012.
- [246] R. G. Palmer. Broken ergodicity. *Adv. Phys.*, 31(6):669–735, December 1982.
- [247] S. H. Park, A. Roy, S. Beaupre, S. Cho, N. Coates, J. S. Moon, D. Moses, M. Leclerc, K. Lee, and A. J. Heeger. Bulk heterojunction solar cells with internal quantum efficiency approaching 100%. *Nat. Photonics*, 3:297–302, 2009.
- [248] R. G. Parr and W. Yang. *Density-Functional Theory of Atoms and Molecules*. Oxford University Press, 1994.
- [249] R. G. Parr and W. Yang. Density-Functional Theory of the Electronic Structure of Molecules. *Annu. Rev. Phys. Chem.*, 46(1):701–728, oct 1995.
- [250] A. Pathak. *Elements of Quantum Computation and Quantum Communication*. Taylor and Francis, 2003.
- [251] T. P. Pathak and S. J. Miller. Site-selective bromination of vancomycin. *J. Am. Chem. Soc.*, 134(14):6120–6123, 2012. PMID: 22462775.

- [252] E. Pavarini, S. Biermann, A. Poteryaev, A. I. Lichtenstein, A. Georges, and O. K. Andersen. Mott transition and suppression of orbital fluctuations in orthorhombic 3d1 perovskites. *Phys. Rev. Lett.*, 92:176403, 2004.
- [253] S. Peddibhotla, Y. Dang, J. O. Liu, and D. Romo. Simultaneous arming and structure/activity studies of natural products employing o-h insertions: An expedient and versatile strategy for natural products-based chemical genetics. *J. Am. Chem. Soc.*, 129(40):12222–12231, 2007. PMID: 17880073.
- [254] J. Peet, A. J. Heeger, and G. C. Bazan. "Plastic" solar cells: self-assembly of bulk hetero-junction nanomaterials by spontaneous phase separation. *Acc. Chem. Res.*, 42(11):1700–8, November 2009.
- [255] J. P. Perdew. Density functional theory and the band gap problem. *Int. J. Quantum Chem.*, 28:497, 1985.
- [256] J. P. Perdew, K. Burke, and M. Ernzerhof. Generalized Gradient Approximation Made Simple. *Phys. Rev. Lett.*, 77(18):3865–3868, October 1996.
- [257] I. Peschel. Special Review: Entanglement in Solvable Many-Particle Models. *Brazilian J. Phys.*, 42(3-4):267–291, 2012.
- [258] I. Peschel and V. Eisler. Reduced density matrices and entanglement entropy in free lattice models. *J. Phys. A Math. Theor.*, 42(50):504003, 2009.
- [259] K. S. Pitzer, M. C. P. De Lima, and D. R. Schreiber. Critical point and phase separation for an ionic system. *J. Phys. Chem.*, 89(10):1854–1855, 1985.
- [260] I. Popescu. personal communication, 2011.
- [261] J. A. Pople. Approximate Self-Consistent Molecular-Orbital Theory. V. Intermediate Neglect of Differential Overlap. *J. Chem. Phys.*, 47(6):2026, 1967.
- [262] J. A. Pople, D. P. Santry, and G. A. Segal. Approximate Self-Consistent Molecular Orbital Theory. I. Invariant Procedures. *J. Chem. Phys.*, 43(10):S129, 1965.
- [263] J. A. Pople and G. A. Segal. Approximate Self-Consistent Molecular Orbital Theory. II. Calculations with Complete Neglect of Differential Overlap. *J. Chem. Phys.*, 43(10):S136–S151, 1965.
- [264] J. A. Pople and G. A. Segal. Approximate Self-Consistent Molecular Orbital Theory. III. CNDO Results for AB<sub>2</sub> and AB<sub>3</sub> Systems. *J. Chem. Phys.*, 44(9):3289, 1966.

- [265] Z. D. Pozun, S. E. Rodenbusch, E. Keller, K. Tran, W. Tang, K. J. Stevenson, and G. Henkelman. A Systematic Investigation of p-Nitrophenol Reduction by Bimetallic Dendrimer Encapsulated Nanoparticles. *J. Phys. Chem. C. Nanomater. Interfaces*, 117(15):7598–7604, 2013.
- [266] P. Pulay. Localizability of dynamic electron correlation. *Chem. Phys. Lett.*, 100:151, 1983.
- [267] D. Rabuka. Chemoenzymatic methods for site-specific protein modification. *Curr. Opin. Chem. Biol.*, 14(6):790 – 796, 2010. Model Systems/Biomolecular Synthesis and Modification.
- [268] P. Ren and J. W. Ponder. Polarizable Atomic Multipole Water Model for Molecular Mechanics Simulation. *J. Phys. Chem. B*, 107(24):5933–5947, June 2003.
- [269] T. Richards, M. Bird, and H. Sirringhaus. A quantitative analytical model for static dipolar disorder broadening of the density of states at organic heterointerfaces. *J. Chem. Phys.*, 128(23):234905, 2008.
- [270] S. W. Rick and S. J. Stuart. Potentials and algorithms for incorporating polarizability in computer simulations. *Rev. Comput. Chem.*, 18:89–146, 2003.
- [271] S. W. Rick, S. J. Stuart, and B. J. Berne. Dynamical fluctuating charge force fields: Application to liquid water. *J. Chem. Phys.*, 101(7):6141, 1994.
- [272] P. Ring and P. Schuck. *The Nuclear Many-Body Problem*. Springer, Berlin, 1980.
- [273] A. Rodríguez, V. Malyshev, G. Sierra, M. Martín-Delgado, J. Rodríguez-Laguna, and F. Domínguez-Adame. Anderson Transition in Low-Dimensional Disordered Systems Driven by Long-Range Nonrandom Hopping. *Phys. Rev. Lett.*, 90(2):027404, 2003.
- [274] B. O. Roos, P. R. Taylor, and P. E. M. Siegbahn. A complete active space SCF method (CASSCF) using a density matrix formulated super-CI approach. *Chem. Phys.*, 48(2):157–173, 1980.
- [275] P. J. Rossky and J. Schnitker. The hydrated electron: quantum simulation of structure, spectroscopy, and dynamics. *J. Phys. Chem.*, 92(15):4277–4285, 1988.
- [276] H. Rouhaninejad and J. Yoccoz. Champ self-consistent et methode de projection. *Nucl. Phys.*, 78(2):353 – 368, 1966.
- [277] S. Saebø and P. Pulay. Local treatment of electron correlation. *Annu. Rev. Phys. Chem.*, 44:213, 1993.
- [278] R. Saito, G. Dresselhaus, and M. S. Dresselhaus. *Physical Properties of Carbon Nanotubes*. Imperial College Press, London, 1999.

- [279] D. K. Samarakoon and X.-Q. Wang. Tunable band gap in hydrogenated bilayer graphene. *ACS Nano*, 4(7):4126–30, 2010.
- [280] V. R. Saunders and J. H. van Lenthe. The direct ci method. *Mol. Phys.*, 48(5):923–954, 1983.
- [281] J. Sawada. Generating Bracelets in Constant Amortized Time. *SIAM J. Comput.*, 31(1):259, 2001.
- [282] M. W. Schmidt and M. S. Gordon. The construction and interpretation of mscf wave functions. *Annu. Rev. Phys. Chem.*, 49:233, 1998.
- [283] U. Schollwöck. The density-matrix renormalization group. *Rev. Mod. Phys.*, 77(1):259–315, 2005.
- [284] K. Schönhammer and W. Brenig. D.C. conductivity and Anderson transition in disordered systems. *Phys. Lett. A*, 42(6):447–448, 1973.
- [285] E. Schrödinger. An undulatory theory of the mechanics of atoms and molecules. *Phys. Rev.*, 28(6):1049–1070, 1926.
- [286] L. D. Schuler, X. Daura, and W. F. van Gunsteren. An improved GROMOS96 force field for aliphatic hydrocarbons in the condensed phase. *J. Comput. Chem.*, 22(11):1205–1218, August 2001.
- [287] L. Schwartz, H. Krakauer, and H. Fukuyama. Random Transfer Integrals and the Electronic Structure of Disordered Alloys. *Phys. Rev. Lett.*, 30(16):746–749, 1973.
- [288] L. Schwartz and E. Siggia. Pair Effects in Substitutional Alloys. I. Systematic Analysis of the Coherent-Potential Approximation. *Phys. Rev. B*, 5(2):383–396, January 1972.
- [289] G. E. Scuseria, C. A. Jiménez-Hoyos, T. M. Henderson, K. Samanta, and J. K. Ellis. Projected quasiparticle theory for molecular electronic structure. *J. Chem. Phys.*, 135(12):124108, 2011.
- [290] Y. Shao, Z. Gan, E. Epifanovsky, A. T. B. Gilbert, M. Wormit, J. Kussmann, A. W. Lange, A. Behn, X. Feng, D. Ghosh, M. Goldey, P. R. Horn, L. D. Jacobson, I. Kaliman, R. Z. Khaliullin, T. Kuś, J. Liu, E. I. Proynov, Y. M. Rhee, R. M. Richard, A. Rohrdanz, R. P. Steele, E. J. Sundstrom, L. H. Woodcock, M. Zimmerman, D. Zuev, B. Albrecht, E. Alguire, B. Austin, G. J. O. Beran, Y. A. Bernard, E. Berquist, K. Brandhorst, B. Bravaya, S. T. Brown, D. Casanova, C.-M. Chang, S. H. Chien, K. D. Closser, D. L. Crittenden, R. A. Distasio Jr, H. Do, A. D. Dutoi, G. Edgar, S. Fatehi, L. Fusti-Molnar, A. Ghysels, A. Golubeva, J. Gomes, M. W. D. Hanson-Heine, H. P. Philipp, A. W. Hauser, E. G. Hohenstein, Z. C. Holden, T. Jagau, H. Ji, B. Kaduk, K. Khistyayev, J. Kim, J. Kim, R. A. King, P. Klunzinger, D. Kosenkov, T. Kowalczyk, C. M. Krauter, K. U. Lao, A. D. Laurent, K. V. Lawler,

V. Levchenko, C. Y. Lin, F. Liu, E. Livshits, R. C. Lochan, A. Luenser, P. Manohar, S. F. Manzer, S.-P. Mao, A. V. Marenich, S. A. Maurer, N. J. Mayhall, E. Neuscammann, C. M. Oana, R. Olivares-Amaya, P. O. Neill, J. A. Parkhill, T. M. Perrine, R. Peverati, D. R. Rehn, E. Rosta, N. J. Russ, S. M. Sharada, S. Sharma, D. W. Small, A. Sodt, T. Stein, D. Stück, Y.-C. Su, A. J. W. Thom, T. Tsuchimochi, V. Vanovschi, O. Vydrov, T. Wang, M. A. Watson, J. Wenzel, A. White, C. F. Williams, J. Yang, S. Yeganeh, S. R. Yost, I. Y. Zhang, X. Zhang, Y. Zhao, B. R. Brooks, K. L. Chan, D. M. Chipman, C. J. Cramer, W. A. Goddard, M. S. Gordon, W. J. Hehre, A. Klamt, H. F. Schaefer, M. W. Schmidt, C. D. Sherrill, D. G. Truhlar, A. Warshel, X. Xu, A. Aspuru-Guzik, R. Baer, A. T. Bell, N. A. Besley, D. Chai, A. Dreuw, B. D. Dunietz, T. R. Furlani, R. Steven, C.-P. Hsu, Y. Jung, J. Kong, D. S. Lambrecht, W. Liang, C. Ochsenfeld, V. A. Rassolov, V. Lyudmila, J. E. Subotnik, T. Van Voorhis, J. M. Herbert, A. I. Krylov, P. M. W. Gill, M. Head-Gordon, Y. Shao, Z. Gan, E. Epifanovsky, and A. T. B. Gilbert. Advances in molecular quantum chemistry contained in the Q-Chem 4 program package. *Mol. Phys.*, 113:184–215, 2015.

- [291] Y. Shao, L. F. Molnar, Y. Jung, J. Kussmann, C. Ochsenfeld, S. T. Brown, A. T. B. Gilbert, L. V. Slipchenko, S. V. Levchenko, D. P. O’Neill, R. A. DiStasio, R. C. Lochan, T. Wang, G. J. O. Beran, N. A. Besley, J. M. Herbert, C. Y. Lin, T. Van Voorhis, S. H. Chien, A. Sodt, R. P. Steele, V. A. Rassolov, P. E. Maslen, P. P. Korambath, R. D. Adamson, B. Austin, J. Baker, E. F. C. Byrd, H. Dachsel, R. J. Doerksen, A. Dreuw, B. D. Dunietz, A. D. Dutoi, T. R. Furlani, S. R. Gwaltney, A. Heyden, S. Hirata, C.-P. Hsu, G. Kedziora, R. Z. Khalliulin, P. Klunzinger, A. M. Lee, M. S. Lee, W. Liang, I. Lotan, N. Nair, B. Peters, E. I. Proynov, P. A. Pieniazek, Y. M. Rhee, J. Ritchie, E. Rosta, C. D. Sherrill, A. C. Simmonett, J. E. Subotnik, H. L. Woodcock, W. Zhang, A. T. Bell, A. K. Chakraborty, D. M. Chipman, F. J. Keil, A. Warshel, W. J. Hehre, H. F. Schaefer, J. Kong, A. I. Krylov, P. M. W. Gill, and M. Head-Gordon. Advances in methods and algorithms in a modern quantum chemistry program package. *Phys. Chem. Chem. Phys.*, 8(27):3172–91, July 2006.
- [292] S. Sharma and G. K.-L. Chan. Spin-adapted density matrix renormalization group algorithms for quantum chemistry. *J. Chem. Phys.*, 136(12):124121, 2012.
- [293] S. J. Sheather. Density Estimation. *Stat. Sci.*, 19(4):588–597, November 2004.
- [294] J. A. Sheikh and P. Ring. *Nucl. Phys. A*, 665(1-2):71–91, 2000.
- [295] H. Shiba. A Reformulation of the Coherent Potential Approximation and Its Applications. *Progr. Theoret. Phys.*, 46(1):77–94, 1971.
- [296] M. F. Shlesinger, G. M. Zaslavsky, and J. Klafter. Strange kinetics. *Nature*, 363(6424):31–37, 1993.

- [297] S. L. Shostak, W. L. Ebenstein, and J. S. Muentzer. The dipole moment of water. I. Dipole moments and hyperfine properties of H<sub>2</sub>O and HDO in the ground and excited vibrational states. *J. Chem. Phys.*, 94(9):5875, 1991.
- [298] D. M. Silver. Natural orbital expansion of interacting geminals. *J. Chem. Phys.*, 50:5108, 1969.
- [299] J. C. Slater. The theory of complex spectra. *Phys. Rev.*, 34(10):1293–1322, 1929.
- [300] J. C. Slater. Atomic shielding constants. *Phys. Rev.*, 36:57–64, Jul 1930.
- [301] E. M. Sletten and C. R. Bertozzi. Bioorthogonal chemistry: Fishing for selectivity in a sea of functionality. *Angew. Chem. Int. Ed.*, 48(38):6974–6998, 2009.
- [302] S. A. Snyder, A. Gollner, and M. I. Chiriac. Regioselective reactions for programmable resveratrol oligomer synthesis. *Nature*, 474(7352):461–466, 06 2011.
- [303] A. K. Soper. The radial distribution functions of water and ice from 220 to 673 K and at pressures up to 400 MPa. *Chem. Phys.*, 258(2-3):121–137, August 2000.
- [304] R. Speicher. Free probability theory and random matrices. In A. M. Vershik, editor, *Asymptotic Combinatorics with Application to Mathematical Physics*, number July, pages 53–73, St. Petersburg, 2003.
- [305] C. D. Spicer and B. G. Davis. Selective chemical protein modification. *Nat. Commun.*, 5, sep 2014.
- [306] M. Sprik, J. Hutter, and M. Parrinello. Ab initio molecular dynamics simulation of liquid water: Comparison of three gradient-corrected density functionals. *J. Chem. Phys.*, 105(3):1142, 1996.
- [307] V. N. Staroverov and G. E. Scuseria. Optimization of density matrix functionals by the Hartree-Fock-Bogoliubov method. *J. Chem. Phys.*, 117(24):11107, 2002.
- [308] F. D. Stefani, J. P. Hoogenboom, and E. Barkai. Beyond quantum jumps: Blinking nanoscale light emitters. *Phys. Today*, 62(2):34–39, 2009.
- [309] J. J. P. Stewart. MOPAC. <http://openmopac.net/>.
- [310] J. J. P. Stewart. Optimization of parameters for semiempirical methods I. Method. *J. Comput. Chem.*, 10(2):209–220, March 1989.
- [311] J. J. P. Stewart. Optimization of parameters for semiempirical methods V: modification of NDDO approximations and application to 70 elements. *J. Mol. Model.*, 13(12):1173–213, December 2007.

- [312] J. J. P. Stewart. Optimization of parameters for semiempirical methods VI: more modifications to the NDDO approximations and re-optimization of parameters. *J. Mol. Model.*, 19(1):1–32, January 2013.
- [313] G. Strang. The discrete cosine transform. *SIAM Rev.*, 41(1):135–147, 1999.
- [314] A. Stuart and J. K. Ord. *Kendall's advanced theory of statistics*. Edward Arnold, London, 1994.
- [315] M. M. C. Sun, K. S. Beam, C. G. Cervený, K. G. Hamblett, R. S. Blackmore, M. Y. Torgov, F. G. M. Handley, N. C. Ihle, P. D. Senter, and S. C. Alley. Reduction-alkylation strategies for the modification of specific monoclonal antibody disulfides. *Bioconjugate Chem.*, 16(5):1282–1290, 2005. PMID: 16173809.
- [316] P. R. Surjan, A. Szabados, P. Jeszenszki, and T. Zoboki. Strongly orthogonal geminals: size-extensive and variational reference states. *J. Math. Chem.*, 50:534, 2012.
- [317] A. P. Sutton, M. W. Finnis, D. G. Pettifor, and Y. Ohta. The tight-binding bond model. *J. Phys. C: Solid State Phys.*, 21(1):35–66, 1988.
- [318] A. Szabo and N. S. Ostlund. *Modern Quantum Chemistry: Introduction to Advanced Electronic Structure Theory*. Dover, Mineola, 1996.
- [319] O. Tal, Y. Rosenwaks, Y. Preezant, N. Tessler, C. Chan, and A. Kahn. Direct Determination of the Hole Density of States in Undoped and Doped Amorphous Organic Films with High Lateral Resolution. *Phys. Rev. Lett.*, 95(25):256405, 2005.
- [320] T. Tanaka, K. Moorjani, and S. M. Bose. Coherent Potential Theory of Off-Diagonal Randomness. *Bull. Am. Phys. Soc.*, 16(1), 1971.
- [321] W. Tang and G. Henkelman. Charge redistribution in core-shell nanoparticles to promote oxygen reduction. *J. Chem. Phys.*, 130(19):194504, 2009.
- [322] T. Tao. 245a, notes 5: Free probability. <https://terrytao.wordpress.com/2010/02/10/245a-notes-5-free-probability/>.
- [323] S. Tavazzi, L. Silvestri, M. Campione, A. Borghesi, A. Papagni, P. Spearman, A. Yassar, A. Camposeo, S. Tavazzi, L. Silvestri, M. Campione, A. Borghesi, and A. Papagni. Generalized ellipsometry and dielectric tensor of rubrene single crystals. *J. Appl. Phys.*, 102:023107, 2007.
- [324] N. Tessler, Y. Preezant, N. Rappaport, and Y. Roichman. Charge Transport in Disordered Organic Materials and Its Relevance to Thin-Film Devices: A Tutorial Review. *Adv. Mater.*, 21(27):2741–2761, 2009.

- [325] N. Tessler and Y. Roichman. Amorphous organic molecule/polymer diodes and transistors- Comparison between predictions based on Gaussian or exponential density of states. *Org. Electron.*, 6(5-6):200–210, 2005.
- [326] D. J. Thouless. Stability conditions and nuclear rotations in the Hartree-Fock theory. *Nucl. Phys.*, 21:225–232, 1960.
- [327] D. J. Thouless. Electrons in disordered systems and the theory of localization. *Phys. Rep.*, 13(3):93–142, October 1974.
- [328] E. Titchmarsh. *Introduction to the theory of Fourier integrals*. Oxford University Press, 1986.
- [329] J. Tomasi, B. Mennucci, and R. Cammi. Quantum Mechanical Continuum Solvation Models. *Chem. Rev.*, 105(8):2999–3094, August 2005.
- [330] F. Torricelli, Z. M. Kovács-Vajna, and L. Colalongo. The role of the density of states on the hole mobility of disordered organic semiconductors. *Org. Electron.*, 10(5):1037–1040, 2009.
- [331] T. Tsuchimochi, M. Welborn, and T. Van Voorhis. Density matrix embedding in an antisymmetrized geminal power bath. *J. Chem. Phys.*, 143(2):024107, 2015.
- [332] A. M. Tsel'ick and P. B. Wiegmann. Exact results in the theory of magnetic alloys. *Adv. Phys.*, 32(4):453–713, 1983.
- [333] V. Turkowski, A. Kabir, N. Nayyar, and T. S. Rahman. Dynamical mean-field theory for molecules and nanostructures. *J. Chem. Phys.*, 136:114108, 2012.
- [334] C. Uttamapinant, K. A. White, H. Baruah, S. Thompson, M. Fernandez-Suarez, S. Puthenveetil, and A. Y. Ting. A fluorophore ligase for site-specific protein labeling inside living cells. *Proc. Natl. Acad. Sci. USA*, 107(24):10914–10919, 2010.
- [335] D. Van Belle, M. Froeyen, G. Lippens, and S. J. Wodak. Molecular dynamics simulation of polarizable water by an extended Lagrangian method. *Mol. Phys.*, 77(2):239–255, October 1992.
- [336] T. Van Voorhis, T. Kowalczyk, B. Kaduk, L.-P. Wang, C.-L. Cheng, and Q. Wu. The diabatic picture of electron transfer, reaction barriers, and molecular dynamics. *Annu. Rev. Phys. Chem.*, 61:149–70, March 2010.
- [337] J. VandeVondele, F. Mohamed, M. Krack, J. Hutter, M. Sprik, and M. Parrinello. The influence of temperature and density functional models in ab initio molecular dynamics simulation of liquid water. *J. Chem. Phys.*, 122(1):14515, January 2005.

- [338] B. Verreet, P. Heremans, A. Stesmans, and B. P. Rand. Microcrystalline organic thin-film solar cells. *Adv. Mater.*, pages 5504–5507.
- [339] D. J. Vinyard, G. M. Ananyev, and G. C. Dismukes. Photosystem ii: The reaction center of oxygenic photosynthesis. *Annu. Rev. of Biochem.*, 82(1):577–606, 2013. PMID: 23527694.
- [340] D. Voiculescu. Symmetries of some reduced free product  $C^*$ -algebras. In Huzihiro Araki, Calvin Moore, Serban-Valentin Stratila, and Dan-Virgil Voiculescu, editors, *Operator algebras and their connections with topology and ergodic theory*, volume 1132 of *Lecture Notes in Mathematics*, pages 556–588. Springer, 1985.
- [341] D. Voiculescu. Addition of certain non-commuting random variables. *J. Funct. Anal.*, 66(3):323–346, 1986.
- [342] D. Voiculescu. Limit laws for Random matrices and free products. *Invent. Math.*, 104(1):201–220, December 1991.
- [343] D. Voiculescu. Free probability theory: random matrices and von Neumann algebras. In *Proceedings of the International Congress of Mathematicians*, pages 227–241, Zürich, Switzerland, 1994. Birkhäuser Verlag.
- [344] O. A. Vydrov and T. Van Voorhis. Nonlocal van der Waals density functional: the simpler the better. *J. Chem. Phys.*, 133(24):244103, December 2010.
- [345] D. C. Walker. The hydrated electron. *Q. Rev. Chem. Soc.*, 21(1):79–108, 1967.
- [346] D. L. Wallace. Asymptotic approximations to distributions. *Ann. Math. Stat.*, 29(3):635–654, 1958.
- [347] F. Wang and K. D. Jordan. Application of a Drude model to the binding of excess electrons to water clusters. *J. Chem. Phys.*, 116(16):6973, 2002.
- [348] L.-P. Wang, J. Chen, and T. Van Voorhis. Systematic parameterization of polarizable force fields from quantum chemistry data. *J. Chem. Theory Comput.*, November 2012.
- [349] L.-P. Wang, T. Head-Gordon, J. W. Ponder, P. Ren, J. D. Chodera, P. K. Eastman, T. J. Martinez, and V. S. Pande. Systematic improvement of a classical molecular model of water. *J. Phys. Chem. B*, 117(34):9956–72, August 2013.
- [350] L.-P. Wang and T. Van Voorhis. Direct-coupling o2 bond forming a pathway in cobalt oxide water oxidation catalysts. *J. Phys. Chem. Lett.*, 2(17):2200–2204, 2011.
- [351] L.-P. Wang and T. Van Voorhis. A polarizable qm/mm explicit solvent model for computational electrochemistry in water. *J. Chem. Theory Comput.*, 8(2):610–617, 2012. PMID: 26596609.

- [352] A. Warshel, M. Kato, and A. V. Pisiakov. Polarizable Force Fields: History, Test Cases, and Prospects. *J. Chem. Theory Comput.*, 3(6):2034–2045, November 2007.
- [353] F. Weigend and M. Haser. RI-MP2 : First derivatives and global consistency. *Theor. Chem. Acc.*, 97:331–340, 1997.
- [354] F. Weigend, A. Kohn, and C. Hattig. Efficient use of the correlation consistent basis sets in resolution of the identity MP2 calculations. *J. Chem. Phys.*, 116(8):3175, 2002.
- [355] B. Weiner and O. Goscinski. Excitation operators associated with antisymmetrized geminal-power states. *Phys. Rev. A*, 27(1):57–71, 1983.
- [356] M. Welborn, J. Chen, and T. Van Voorhis. Densities of states for disordered systems from free probability. *Phys. Rev. B*, 88:205113, 2013.
- [357] M. Welborn, J. Chen, L.-P. Wang, and T. Van Voorhis. Why Many Semiempirical Molecular Orbital Theories Fail for Liquid Water and How to Fix Them. *J. Comp. Chem.*, 36:934, 2015.
- [358] P. A. Wender, M. H. Hilinski, and A. V. W. Mayweg. Late-stage intermolecular ch activation for lead diversification: A highly chemoselective oxyfunctionalization of the c-9 position of potent bryostatin analogues. *Org. Lett.*, 7(1):79–82, 2005. PMID: 15624982.
- [359] T. Wesolowski and A. Warshel. Ab Initio Free Energy Perturbation Calculations of Solvation Free Energy Using the Frozen Density Functional Approach. *J. Phys. Chem.*, 98(3):5183–5187, 1994.
- [360] S. R. White. Density matrix formulation for quantum renormalization groups. *Phys. Rev. Lett.*, 69(19):2863–2866, 1992.
- [361] E. P. Wigner. Random Matrices in Physics. *SIAM Rev.*, 9(1):1–23, 1967.
- [362] K. Wolinski and P. Pulay. Second-order Moller-Plesset calculations with dual basis sets. *J. Chem. Phys.*, 118(21):9497, 2003.
- [363] D. E. Woon and T. H. Dunning. Gaussian basis sets for use in correlated molecular calculations. IV. Calculation of static electrical response properties. *J. Chem. Phys.*, 100(4):2975, 1994.
- [364] S. Wouters, C. A. Jiménez-Hoyos, Q. Sun, and G. Kin-Lic Chan. A practical guide to density matrix embedding theory in quantum chemistry. *ArXiv e-prints*, March 2016.
- [365] Q. Wu, C.-L. Cheng, and T. Van Voorhis. Configuration interaction based on constrained density functional theory: a multireference method. *J. Chem. Phys.*, 127(16):164119, October 2007.

- [366] Q. Wu, B. Kaduk, and T. Van Voorhis. Constrained density functional theory based configuration interaction improves the prediction of reaction barrier heights. *J. Chem. Phys.*, 130(3):034109, January 2009.
- [367] W. Xie, L. Song, D. G. Truhlar, and J. Gào. The variational explicit polarization potential and analytical first derivative of energy: Towards a next generation force field. *J. Chem. Phys.*, 128(23), 2008.
- [368] W. Yang and T.-S. Lee. A density-matrix divide-and-conquer approach for electronic structure calculations of large molecules. *J. Chem. Phys.*, 103(13):5674, 1995.
- [369] F. Yonezawa and K. Morigaki. Coherent Potential Approximation. *Progr. Theoret. Phys. Suppl.*, 53:1–76, 1973.
- [370] S. R. Yost, L.-P. Wang, and T. Van Voorhis. Molecular Insight Into the Energy Levels at the Organic Donor/Acceptor Interface: A Quantum Mechanics/Molecular Mechanics Study. *J. Phys. Chem. C*, 115(29):14431–14436, July 2011.
- [371] H. Yu and W. F. van Gunsteren. Accounting for polarization in molecular simulation. *Comput. Phys. Commun.*, 172(2):69–85, November 2005.
- [372] A. Zee. Law of addition in random matrix theory. *Nucl. Phys. B*, 474(3):726–744, September 1996.
- [373] M. C. Zerner. Semiempirical Molecular Orbital Methods. In K Lipkowitz and D Boyd, editors, *Rev. Comput. Chem. Vol. 2*, volume 2, chapter 8, pages 313–365. Wiley, New York, 1991.
- [374] C. Zhang, M. Welborn, T. Zhu, N. J. Yang, M. S. Santos, T. Van Voorhis, and B. L. Pentelute.  $\pi$ -clamp-mediated cysteine conjugation. *Nat. Chem.*, 8(2):120–128, 02 2016.
- [375] B.-X. Zheng and G. K.-L. Chan. Ground-state phase diagram of the square lattice Hubbard model from density matrix embedding theory. *Arxiv*, 2015.
- [376] Y. Zhou and J. Pu. Reaction Path Force Matching: A New Strategy of Fitting Specific Reaction Parameters for Semiempirical Methods in Combined QM/MM Simulations. *J. Chem. Theory Comput.*, 10(8):3038–3054, August 2014.
- [377] J. M. Ziman. *Models of Disorder: The Theoretical Physics of Homogeneously Disordered Systems*. Cambridge University Press, Oxford, 1979.